ISBN 978-82-326-1554-4 (printed ver.)
ISBN 978-82-326-1555-1 (electronic ver.)
ISSN 1503-8181

Doctoral theses at NTNU, 2016:108

Camilla Sommerseth

The Effect of Production Parameters on the Performance of Carbon Anodes for Aluminium Production

Camilla Sommerseth
Doctoral thesis

NTNU
Norwegian University of
Science and Technology
Thesis for the Degree of
Philosophiae Doctor
Faculty of Natural Sciences and Technology
Department of Materials Science and
Engineering

Doctoral theses at NTNU, 2016:108

NTNU

NTNU
Norwegian University of
Science and Technology

NTNU
Norwegian University of
Science and Technology

Camilla Sommerseth

The Effect of Production Parameters on the Performance of Carbon Anodes for Aluminium Production

Thesis for the Degree of Philosophiae Doctor

Trondheim, April 2016

Norwegian University of Science and Technology
Faculty of Natural Sciences and Technology
Department of Materials Science and Engineering

NTNU
Norwegian University of
Science and Technology

NTNU
Norwegian University of Science and Technology

Thesis for the Degree of Philosophiae Doctor

Faculty of Natural Sciences and Technology
Department of Materials Science and Engineering

ISBN 978-82-326-1554-4 (printed ver.)
ISBN 978-82-326-1555-1 (electronic ver.)
ISSN 1503-8181

IMT-report 2016:225

Doctoral theses at NTNU, 2016:108

Printed by NTNU Grafisk senter

In memory of my Grandfather, Michael.

Preface

This thesis is part of the Research Council of Norway supported innovation project called Hydro Aluminium Ultra Performance Aluminium Cell (HAL UP). The project is a collaboration between Hydro Aluminium, NTNU and SINTEF. It was financed by the Norwegian Research Council (NFR). Hydro Aluminium supplied the project with the pilot anode materials used for testing.

All the experimental work in the thesis has been performed by the author except: XRF analysis and physical parameters experiments performed by technicians at Hydro Årdalstangen (Tables 3.2, 3.3, 4.2, 4.3, 5.1 and 5.2). The operation of the confocal microscope was performed by Research Assistant Cristian Torres Rodriguez (NTNU) (Figures 3.2-3.9, 5.15 and 5.16). The operation of the X-ray computed tomography (CT) was performed by Staff Engineer Ole Tore Buset (NTNU) (Figures 3.12-3.17 and Figures 5.7-5.13). Hg porosimetry was performed by Senior Engineer Jannicke Hatlø Kvello (SINTEF) (Figures 4.2 and 5.4). The electrochemical measurements in Chapter 5 was performed in collaboration with Postdoctoral Fellow Wojciech Gebarowski (NTNU) (Figures 5.17, 5.18 and 5.20).

All data processing obtained by experimental work was performed by the author, except the processing of the CT data and creation of the contour images from the confocal microscopy data (Figures 3.2-3.9 b), 3.12-3.17, 5.7-5.13 and 5.15-5.16 b), d), f) and h)). This was performed by Research Scientist Stein Rørvik (SINTEF).

My main supervisor Ann Mari Svensson, co-supervisors Arne Petter Ratvik, Lorentz Petter Lossius and Egil Skybakmoen, as well as other participants in the project including Rebecca Thorne, Espen Sandnes, Hogne Linga and Wojciech Gebarowski have all contributed to the discussion of the results in Chapters 3-5.

Camilla Sommerseth
Trondheim, 17 December 2015

Acknowledgement

The time has come to wrap up this thesis and the past four years of work. Of course this work has been a process where many people have been involved, and this is the time to send out a thank you to those people! I could not have done it without you.

First I would like to thank my supervisor Professor Ann Mari Svensson. You came into this project in 2012 with new eyes and lots of essential competence on electrochemistry and carbon materials. I have enjoyed our discussions regarding the topic and you have always shown interest in my work. I really appreciate it and I have enjoyed learning all the quirks of impedance from you. A warm thank you for all guidance, help and support!

A great thank you is also due to my co-supervisors Egil Skybakmoen (SINTEF), Arne Petter Ratvik (SINTEF) and Lorentz Petter Lossius (Hydro Aluminium). You have all fulfilled various parts of the supervision. Egil, mainly in the beginning when the project was starting up, but also through an open door policy for whatever question I may have had during these four years. Arne Petter, for many valuable discussions on the results obtained in the laboratory and for the helping direct the road ahead. Petter, for sharing your enormous knowledge on anode manufacturing, for answering my numerous questions concerning anodes and for facilitating the production of the pilot anodes.

Rebecca Thorne (then NTNU, now NILU), the post-doctoral fellow on the "sister-project": NextGenAnodes. If it hadn't been for you, this thesis would never have happened. You have taught me everything I know concerning laboratory skills, you have been an excellent discussion partner and you really paved the way for me. I will always appreciate everything you have taught me and all the help, guidance and support! Also, thank you for being a friend!

Espen Sandnes (NTNU and Hydro Aluminium) and Hogne Linga (Hydro Aluminium) deserves a thank you for the way you have engaged yourselves in this project and for the fruitful discussions we have had.

Odd-Arne Lorentsen (then Hydro Aluminium and NTNU, now Yara) who was my supervisor the first year of this PhD work deserves a thank you for being a strong participant in initiating the direction this project ended up taking with overpotential measurements and electrochemical testing of the carbon anodes.

Stein Rørvik (SINTEF) has been essential when it comes to help with the imaging techniques: CT, processing of the data from confocal microscopy and training in optical microscopy. Thank you for that!

Aksel Alstad (NTNU) at the workshop deserves a great thank you for all the hours spent in manufacturing all the tiny parts for the anode assembly. Without his expertise and skills in carbon materials processing, this work would never have been possible! I have also enjoyed all the great conversations we've had!

Kristian E. Einarsrud (HIST) deserves a thank you for the discussions we have had

concerning bubble generation at the carbon anode and for patiently answering my many questions concerning this topic.

I would like to direct a warm thank you to all the SINTEF Materials and Chemistry staff at the Department of Industrial Process Technology. You have all been so supportive and this thesis is also a result of the great collaboration I have had with all of you, really all the way back since I started my Master thesis. I would especially like to mention Asbjørn Solheim, Henrik Gudbrandsen and Ole Kjos.

Thanks are also due to the staff at Hydro Aluminium Årdalstangen for producing the pilot anodes and for performing all the physical testing and doing XRF measurements. I would especially like to mention Kirsti Gulbrandsen and Lars Sørhage.

I have had many great colleagues and friends among the staff, PhD students, post-doctoral fellows and students at the Department of Materials Science and Engineering at NTNU. I cannot mention them all, but I would like to thank Axel Holene, Henrik Åsheim, Wojciech Gebarowski and Julian Tolchard (then NTNU, now SINTEF) especially. I would also like to thank those of you from Class '11 who stayed behind and continued the university life with a PhD. It's been great to have some people around who knows exactly what you're going through.

To my colleagues, lunch mates, but foremost my great friends Sigrid Lædre and Karen Nessler Seglem: You guys have been travelling this journey with me from start to end and I'm so thankful for having you two around!

To all my friends and to my extended family - I cannot mention you all, but thank you all for being in my life!

To my parents, you have always been so supportive of me and let me find my own way in this world. I'm forever grateful for the opportunities you have given me in life: Sending me off to various parts of the world from a young age. It must have taken some courage to do that. Thank you for letting me be me!

Finally I would like to thank my husband Finn and my little daughter and sunshine, Live. You two are everything to me. Finn you have been with me on this entire journey, you have been so supportive, you have listened to my frustrations and you have waited patiently for me to end this thesis with everything that comes along with it. To Live who has helped me out of the office, I love picking you up in kindergarten and seeing your happy smiling face. You are the one that really matter in life. You two are the "Wonders of you", and for that I love you.

Abstract

Carbon anodes used in aluminium electrolysis cells are produced from a blend of calcined petroleum cokes, recycled anode butts and using a coal tar pitch as a binder. As cokes are the main constituents of carbon anodes, their properties are important for the quality of the final anode product. Coke is produced from petroleum crude oil and there are three main types of cokes: anisotropic needle coke, anisotropic sponge coke and isotropic cokes. Isotropic cokes have similar properties in all directions and they have a fine grained texture. Anisotropic cokes have a coarser texture and a more layered structure. The anisotropic sponge coke is a mixture of fine and coarse texture and has a heterogeneous structure. Traditionally, anisotropic cokes have been regarded as anode grade cokes, but due to changes in the petroleum production the future supply of anisotropic cokes is expected to be insufficient, making isotropic cokes a raw material for coke blends.

Two pilot anode lines have been produced where one varied in isotropic to anisotropic coke content (0 %, 7.2 %, 14.2 %, 35.0 %, 49.0 % and 100 % isotropic coke content) while the other varied in mixing (150 °C and 210 °C) and baking temperature (1150 °E, 1260 °E and 1350 °E). The second pilot anode line was produced with anisotropic coke only. Both pilot anode lines were produced of fresh coke only, i.e. no butts were introduced. These two pilot anode lines have been investigated thoroughly in the present work.

The anodes were characterised electrochemically, with the aim of determining differences in overpotential for anode setups both designed for maximum (horizontal anode setup) and minimum (vertical anode setup) bubble retention on the anode surface. A small reduction of the reaction overpotential was observed upon introduction of isotropic cokes. Also, a significant reduction in potential oscillation of ~0.19 V related to bubble formation and release was found for the blended anodes (7.2 %-49.0 % isotropic coke), and correspondingly a lower screening of the surface by the bubbles formed. A suggested explanation for the lowered potential oscillation amplitude is the increased wettability between anode and electrolyte observed when using the immersion-emersion technique. Increased wettability lowers the contact angle, and helps remove gas bubbles from the anode surface more efficiently.

Some obvious problems concerning use of isotropic cokes in carbon anodes is the low porosity of the coke grains. This gives problems with pitch penetration and hence problems with producing a dense carbon anode. Results obtained by imaging techniques and porosity measurements show that producing anodes entirely from isotropic cokes is not feasible. When using isotropic coke in blends with anisotropic coke, the higher coefficient of thermal expansion of isotropic coke needs to be taken into consideration. There is a threshold for how much isotropic coke it is possible to blend in the anodes before cracking will occur. X-ray computed tomography has shown that this threshold for this pilot anode line is between 14.2 and 35.0 % isotropic coke. For the 35.0 % anode cracking is visible, while for the 49.0 % anode extensive cracking is observed. Another issue with isotropic coke is the increased amount of impurities, both metal impurities and sulfur. The metal impurities will end up in the aluminium metal and

cause increased impurity levels in the final products. The metal impurities will have to either be removed or tolerated. The increased sulfur content will give increased SO_2 emissions and will need to be removed from the off-gases by wet scrubbing.

When investigating the effect of baking and mixing temperature, the mixing temperature was found to be the most influential of the anode properties. A too low mixing temperature is detrimental to anode density creating anodes with increased porosity, and this in turn affects properties like specific electrical resistivity and air permeability. However, the increased anode porosity for the low mixing temperature anodes did not affect the electrochemical performance in terms of reaction overpotential. A slight increase in capacitance was seen for the low mixing temperature anodes, and this was attributed to the higher surface roughness caused by the increased porosity. The anisotropic coke used for producing this pilot anode line was a low sulfur coke, which probably explains why little effect of the various baking temperatures was observed, as desulfurisation is not expected for these cokes.

Contents

1 Introduction

1.1 Motivation

The aluminium industry has moved towards larger higher amperage cells to increase production. This has led to a need for larger carbon anodes, as well as high quality anodes in order to avoid increased anode failures in the potrooms. Anode failures include cracking, overheating of anodes and spikes. China's demand for aluminium has increased exponentially since year 2000 [1], and increased production led to an increasing demand for calcined petroleum coke for anode production. Calcined petroleum coke is produced from crude oils and the quality of the crudes in terms of impurities and structure depend on geography of the oil wells, more than calciner production parameters. Crude oils extracted from the North Sea and North and West Africa produce high quality, low impurity and highly anisotropic cokes. Isotropic cokes are produced from crudes extracted from oil wells in the Mexican Gulf and Venezuela. Isotropic cokes have previously been disregarded by the aluminium industry due to its high impurity level and less developed structure. However, with the increased demand for petroleum coke due to China's expansion as an aluminium producer and consumer, isotropic coke has become an extra source of anode grade petroleum coke, despite its short-comings [2, 3].

The coke producers have strongly encouraged the aluminium industry to accept the use of isotropic cokes in blends for carbon anodes [3–5]. This in turn leads to the need for research with the aim to investigate the effect of isotropic cokes in anodes in terms of their baking properties, like increased risk of cracking due to the higher coefficient of thermal expansion these cokes inhibit in relation to the blending ratios. Also, in order to produce high quality anodes, correct tuning of baking and mixing temperatures is important. These production parameters have a great effect on the resulting baked anode density and hence parameters like the specific electrical conductivity, air permeability, resistance to crack propagation and resistance to thermal shock [6]. Low density anodes of poor quality can cause excess carbon consumption and increase the risk of higher emission of greenhouse gases due to increased air and CO_2 reactivity [7]. Traditionally, the mixing temperature used during anode production has been ~50 °C above the Mettler softening point of the pitch, but scientists have questioned if this procedure has been questioned [8–10] since the wettability of pitch towards coke has been shown to improve drastically at much higher temperatures above the Mettler softening point.

Moreover, the effect these cokes have on electrochemical performance of the anode like reaction overpotential, wetting behaviour between anode and electrolyte and the effect on bubble generation and release on the anode surface, needs to be investigated.

1.2 Aim of work

The main aim of the work in this thesis has been to investigate the effect of various production parameters like coke quality, blending ratio of isotropic to anisotropic coke, mixing temperature and baking temperature on anode performance. Two pilot anode lines were produced from <2 mm coke aggregate. The first pilot anode line varied in isotropic coke content, ranging from 0 % isotropic coke (100 % anisotropic coke), 7.2 %, 14.2 %, 35.0 %, 49.0 % and 100 % isotropic coke. All other production parameters were kept constant for this line. For the second pilot anode line, the production parameters were varied in terms of mixing temperature (150 °C and 210 °C) and baking temperature (1150 °E, 1260 °E and 1350 °E). The anodes in this production line were made from 100 % anisotropic coke and all other production parameters were kept constant.

These sets of pilot anodes were then characterised to reveal differences in the overall electrochemical reactivity, both with respect to evaluation of reactions rate, as well as additional overvoltage related to bubble formation and release. Differences in local consumption rates between grains of different composition, as well as the pitch phase, was addressed by means of various imaging techniques. Imaging techniques have also been applied to gain valuable knowledge about the internal morphology of the anodes. The electrode-electrolyte wetting properties were investigated and used to provide further insights to the results from electrochemical characterisations. Furthermore, the findings are correlated to the results from conventional anode tests, like content of impurity, baked anode density, specific electrical resistivity, air permeability, coefficient of thermal expansion, air and CO_2 reactivity.

1.3 About the Structure of the Thesis

Chapter 2 gives a general introduction to the field of aluminium production, carbon anodes and calcined petroleum cokes. Chapters 3, 4 and 5 are the main chapters of the thesis, and includes the results from the experimental work. These chapters address the electrochemical reactivity of anodes varying in isotropic coke content (Chapter 3), as well as the anodic bubble behaviour for the same anodes (Chapter 4). In the last main chapter, Chapter 5, effects of baking and mixing temperatures on the performance of the anodes have been investigated. These three chapters have been written as individual papers. They may be read separately, and will later be submitted to relevant journals. Selected results have been included in two publications in Light Metals, and these are included in Appendices E.3 and E.4.

References

[1] World Aluminium. *Primary Aluminium Production*. 2015. URL: http://www.world-aluminium.org/statistics/#linegraph (visited on 12/08/2015).

[2] B. Vitchus, F. Cannova, and H. Childs. "Calcined Coke from Crude Oil to Customer Silo". *Light Metals* (2001), pp. 589–596.

[3] L. Edwards, F. Vogt, M. Robinette, R. Love, A. Ross, M. McClung, R.J. Roush, and W. Morgan. "Use of Shot Coke as an Anode Raw Material". *Light Metals* (2009), pp. 985–990.

[4] L. Edwards. "Evolution of Anode Grade Quality and Calcining Technology". *Proc. 10th AASTC* (2011). Ed. by B. Welch, G. Stephens, J. Metson, and M. Skyllas-Kazacos.

[5] L. Edwards, N. Backhouse, H. Darmstadt, and M.-J. Dion. "Evolution of anode grade coke". *Light Metals* (2012), pp. 1207–1212.

[6] S. Wilkening. "Maintaining Consistent Anode Density using Varying Carbon Raw Materials". *Light Metals* (2009), pp. 991–997.

[7] D. Kocaefe, A. Sarkar, S. Das, S. Amrani, D. Bhattacharyay, D. Sarkar, and Y. Kocaefe. "Review of Different Techniques to Study the Iteractions between Coke and Pitch in Anode Manufacturing". *Light Metals* (2013), pp. 1045–1050.

[8] A. Sarkar, D. Kocaefe, Y. Koceafe, D. Sarkar, and Bhattacharyay. "Coke-pitch interactions during anode preparation". *Fuel* (2014), pp. 598–607.

[9] A.A. Mirchi, G. Savard, J.P. Tremblay, and M. Simard. "Alcan Characterisation of Pitch Performance for Pitch Binder Evaluation and Process Changes in an Aluminium Smelter". *Light Metals* (2002), pp. 525–533.

[10] V.G. Rocha, C. Blanco, R. Santamaría, E.I. Diestre, R. Menéndez, and M. Granda. "Pitch/coke wetting behaviour". *Fuel* (2005), pp. 1550–1556.

2 Carbon Anodes for Aluminium Production

2.1 The Hall-Héroult Process

Aluminium is produced in the "Hall-Héroult" process [1]. This process was patented in 1886 by two independent scientists: the American Charles Martin Hall and the Frenchman Paul Héroult. They both suggested the electrochemical reduction of aluminium oxide (Al_2O_3) in a an electrolyte mainly consisting of molten cryolite (Na_3AlF_6) according to the general reaction given in Equation 2.1. Cryolite was chosen for its rare ability to dissolve Al_2O_3. Overall, Al^{3+} is reduced at the cathode, while carbon is oxidised at the carbon anode forming CO_2. In reality, the reaction scheme is a little more complicated, and the anode reaction will be discussed further in later chapters.

$$2Al_2O_3(diss) + 3C(s) = 4Al(l) + 3CO_2(g) \tag{2.1}$$

Figure 2.1 shows a sketch of a modern Hall-Héroult cell with prebaked carbon anodes. The electrolyte and anodes are covered by crust and anode cover material. The electrolyte is covered in order to avoid excess reaction between electrolyte and air, forming e.g. HF. The coverage of anodes is done in order to avoid excess air reactivity of the carbon anode (i.e. airburn). Modern cells are usually point fed with Al_2O_3. The electrolysis cell consists of a steel casing lined with refractory bricks. A current collector bar is cast into the carbon cathode block at the bottom of the cell. The sides of the electrolysis cell are protected by frozen cryolite - the sideledge. Molten electrolyte is placed on top of the cathode. When aluminium is formed, this is collected at the bottom of the cell. Hence once formed, aluminium works as the real cathode of the cell towards the electrolyte. Steel rods are cast into the anodes and the steel rod is connected to the anode beam. Prebaked anodes are consumed and have to be changed every 2-4 weeks depending on anode size and current density. Approximately 75 % of the anode is consumed before anode change needs to take place and the remaining part is called butt. The butts are cleaned, crushed and used as raw material for new carbon anodes. [2]

Ever since the electrochemical production route of aluminium metal was invented, a carbothermic reduction route has been investigated. However, no success has been made to date on this field in order to replace the high energy intensive Hall-Héroult process (13 kWh/kg Al in modern cells) on an industrial scale.

2.2 Carbon Anodes for Aluminium Electrolysis

A typical prebake potline consists of several hundred electrolysis cells and each cell consists typically of 20-40 anodes. The technology including cell amperage, size of anodes and number of anodes per cell vary from plant to plant. Nevertheless, carbon anodes are an important component in aluminium electrolysis. Carbon anodes are produced from coal tar pitch and calcined petroleum coke, usually a blend of various

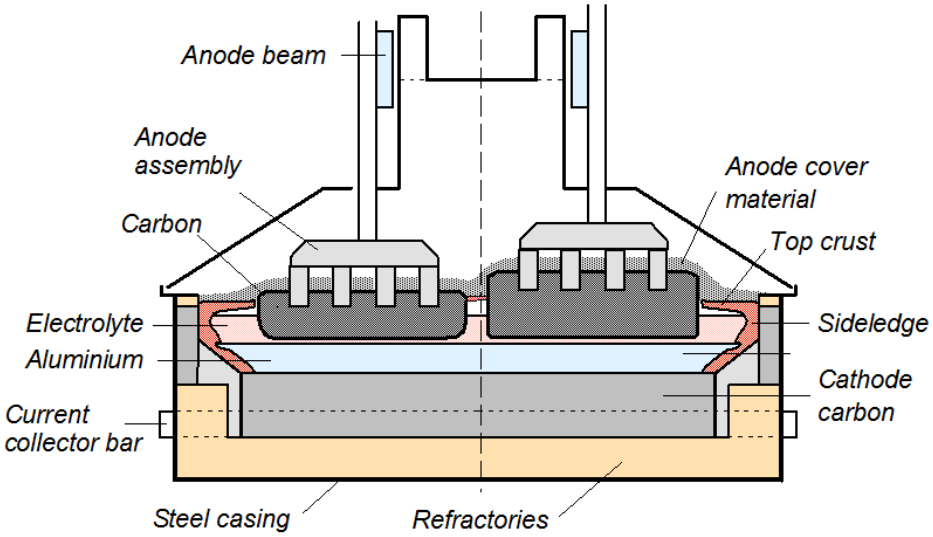

Figure 2.1: A sketch of the Hall-Héroult cell.

qualities. The cokes are fractioned and sieved to the desired distribution of aggregates. The coke is then mixed at an elevated temperature with pitch (usually >50 °C above the pitch Mettler softening point). Then forming and pressing takes place. Finally the anodes are baked at about 1100-1150 °C. The total baking time including preheating, firing, cooling, unloading of the baking furnace and maintenance of refractory bricks is about two weeks [3]. The baking level of the anodes depends on both the maximum temperature the anode sees, but also the hold time at this temperature. Lossius et al. [4] has developed a method for determining the degree of graphitization of the anode material, determined by measurements of crystallite size, L_c. The unit for baking temperature is called the equivalent temperature, °E, when using the method of measuring the crystallite size [4]. The typical range of L_c for carbon anodes is 20-40 Å [3]. Figure 2.2 shows the thermostructural evolution for carbon-rich materials *vs.* temperature [3, 5], including the carbonisation process below 2000 °C, and graphitisation at higher temperatures.

The overall objective of the baking process is to transform the binder pitch structure into a more graphitized form that is closer to the petroleum coke, through decomposition and carbonisation. When increasing the amperage in the potroom, the industry have experienced problems with anode quality (excess anode consumption and anode cracking) [7, 8]. Excess consumption happens in terms of CO_2 and air reactivity and Equations 2.2-2.4 show these processes [9].

$$C_{anode} + CO_2(g) = 2CO(g) \tag{2.2}$$

$$C_{anode} + O_2(g) = 2CO_2(g) \tag{2.3}$$

$$2C_{anode} + O_2(g) = 2CO(g) \tag{2.4}$$

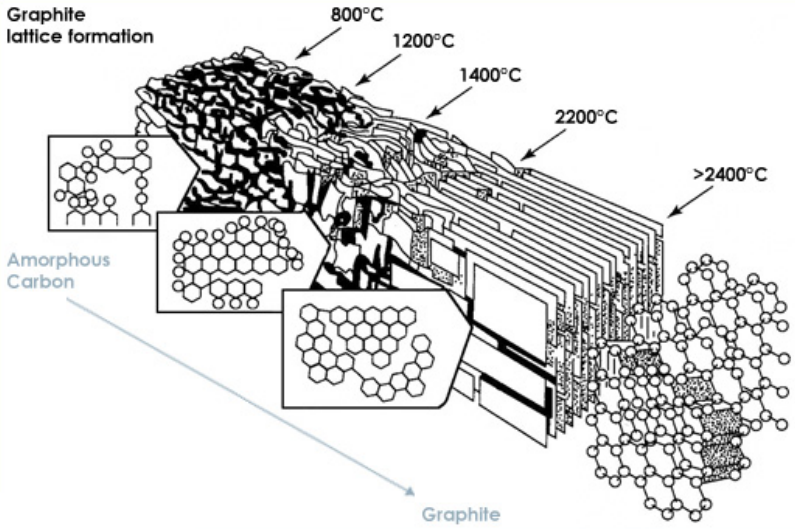

Figure 2.2: Degree of crystallographic orientation as a function of temperature extracted from [6]. The structure resembling carbon anodes are typically found around 1100-1300 °C [3, 5].

Optimization of the baking process is required for high-quality anodes. For high baking tempreatures, better crystallite orientation will result in better electrical conductivity and higher resistance towards attack by ambient air and CO_2 . However, overbaking will cause desulfurisation and microporosity, and hence, an optimum baking temperature exist. This optimum baking temperature will differ according to coke qualities and their original sulfur content. Microporosity increases both the air permeability and the air reactivity [3]. Air reactivity is a problem when carbon anodes come in contact with air, since excess consumption of the anodes will take place due to airburn. In industry, this problem is mainly solved through good coverage of the anodes using alumina and frozen electrolyte as shown in Figure 2.1. In contrast, CO_2 reactivity is relevant for the anode:gas:electrolyte interface. When CO_2 is formed electrochemically, gas bubbles may reside on the surface of the anode and react to form CO, as described in Equation 2.2. At Hydro Årdalstangen air and CO_2 reactivity tests are used regularly to monitor anode quality [9].

Table 2.1 show worldwide ranges for a carbon anodes, and target values for various physical parameters [3].

2.3 Pilot Scale Anode Production

Hydro Aluminium has long experience in producing pilot anodes for experimental purposes. Pilot scale anodes are valuable for experimental purposes, but only if the pilot scale anodes have physical properties similar to industrial scale anodes. The pilot line at Hydro Årdalstangen has been tuned to simulate industrial scale anodes

Table 2.1: Preferred targets for good anodes extracted from [3].

Property	Method	Unit	Worldwide ranges	Mean target for good anodes
Baked apparent density	ISO 12985-1	kg/dm^3	1.50-1.62	≥ 1.58
Spec. el. resistance	ISO 11713	$\mu\Omega$m	51-74	≤ 55
Flexural strength	ISO 12986-1	MPa	4-14	≥ 12
Compressive strength	ISO 18515	MPa	30-65	≥ 45
Coeff. of th. expansion	ISO 14420	10^{-6}K^{-1}	3.6-4.6	≤ 4.1
Thermal conductivity	ISO 12987	W/mK	3-5	4.2
Air permeability	ISO 15906	nPm	0.3-8	≤ 0.9
CO_2 reactivity	ISO 12988-1			
Residue		%	75-96	≥ 92
Dust		%	0.2-14	≤ 2
Loss		%	4-15	≤ 6
Air reactivity	ISO 12989-1			
Residue		%	55-95	≥ 80
Dust		%	1-12	≤ 3
Loss		%	4-35	≤ 15

and Table 2.2 has been extracted from Lossius et al. [10] to show that it is possible to make pilot anodes that are similar to industrial scale anodes. After tuning was established, a series of pilot anodes were made by Lossius et al. [10] using full scale production coke, butts fractions and pitch. The table shows averages from 9 pilot anodes and 13 industrial anodes with the same coke and butts fractions and the same pitch. Generally, the properties matched well, although the Young's Modulus was somewhat lower and the permeability was a little higher for the pilot line anodes. The full scale anode properties represent typical anode properties of a modern anode production plant.

2.4 The Origin of Petroleum Cokes

As cokes are the main constituents of carbon anodes, their properties are important for the quality of the final anode product. Cokes are produced from petroleum crude oil and there are three main types of cokes: anisotropic needle coke, anisotropic sponge coke and isotropic cokes. The isotropic coke has similar properties in all directions and a fine grained texture. Anisotropic cokes have a coarser texture and a more layered structure. The anisotropic sponge coke is a mixture of fine and coarse texture and has a heterogeneous structure [11]. Differences in the coke quality originates from differences in the crude oil residues, which in turn depends on where the crude oil originates from geographically, more than the production parameters. Asphaltenes are complex polyaromatic compounds in the crude oil [12]. A significant amount of asphaltenes in the crude is essential in order to produce cokes with high bulk density. However,

Table 2.2: Anode property comparison after tuning the pilot anode line to simulate industrial scale anodes. The work was performed at Hydro Årdalstangen [10].

Anode property	Unit	Pilot scale anodes	Production anodes
Reactivity, R_{CO_2}	mg/cm^{2}h	14.9	15.3
Reactivity, Dust index	%	3.2	2.0
Reactivity, R_{Air}	mg/cm^{2}h	33.7	30.0
Density	g/cm^3	1.582	1.582
Resistivity, SR	m	52.9	52.7
Young's Modulus, YM	MPa	9394	10273
Strength, CCS	MPa	44.1	45.5
Permeability	nPm	0.8	0.3
Expansion, CTE	1/K·10^6	4.5	4.7
Thermal Shock, TSR		19.6	18.1

asphaltenes also have a high amount of metal impurities like vanadium, nickel and iron. Some crude oil high in sulfur and with a significant amount of asphaltenes, produces cokes with a high bulk density, high particle strength and high concentration of impurities like vanadium and nickel. These cokes are known as isotropic coke, including shot coke. Characteristic of asphaltenes that tend to produce shot coke is that they have a higher number of heteroatoms per aromatic carbon. Heteroatoms are defined as an atom other than carbon in a ring structure. Additionally, asphaltenes that produce shot coke are associated with higher solubility parameter to polynuclear aromatic (PNA) cores. A higher solubility parameter of PNA cores favour more rapid phase separation and promote self-coking molecular weight growth reactions that inhibit mesophase development and particle agglomeration during the coking process. Mesophase and particle agglomeration characterises anisotropic coke formation [12]. It is especially crude oil from Mexico and Venezuela that exhibit these properties [13]. Shot coke has a fine texture and uniform properties. The particles are usually spherical and uniform in size and with little open porosity [11].

Crudes from the North Sea and North and West Africa have low concentrations of metal and sulfur impurities and are also low in asphaltenes. These crude oils produce anisotropic cokes with lower bulk density and lower impurity concentrations. Raw material for anisotropic sponge coke are heavy hydrocarbons, in containing an appropriate ratio of aromatics and asphaltenes. Needle coke is produced from aromatic crude oil with no asphaltenes and metal impurities. This coke is not used as anode grade coke due to its low bulk density, high porosity, poor particle strength and size [11, 13].

References

[1] J. Thonstad, P. Fellner, G.M. Haarberg, J. Hives, H. Kvande, and Å. Sterten. *Aluminium Electrolysis: Fundamentals of the Hall-Heroult Process*. 3rd. Dusseldorf: Aluminium-Verlag, 2001.

[2] K.L. Hulse. *Anode Manufacture*. 1st. Sierre: R&D Carbon Ltd., 2000.

[3] F. Keller and P.O. Sulger. *Anode Baking*. 2nd. Sierre: R & D Carbon Ltd., 2008.

[4] L.P. Lossius, I. Holden, and H. Linga. "The Equivalent Temperature Method for Measuring the Baking Level of Anodes". *Light Metals* (2006), pp. 609–613.

[5] K. Grjotheim and H. Kvande. *Introduction to Aluminium Electrolysis*. 2nd. Dusseldorf: Aluminium-Verlag, 1993.

[6] H. Marsh and J. Griffiths. "A high resolution electron microscopy study of graphitization of graphitizable carbons". *Proc. Intern. Symp. on Carbon, New Processes and New Applications* (1982), p. 81.

[7] L.P. Lossius, J. Chmelar, I. Holden, H. Linga, and M. Tkac. "Pilot Scale Anodes for Raw Material Evolution and Process Improvement". *Light Metals* (2013), pp. 1177–1182.

[8] V. Piffer, P. Miotto, C. Kato, M. Meier, R. Perruchoud, and P. Sulger. "Process Optimization in Bake Furnace". *Light Metals* (2007), pp. 959–964.

[9] T.E. Jentoftsen, H. Linga, I. Holden, B.E. Aga, V.G. Christensen, and F. Hoff. "Correlation between Anode Properties and Cell Performance". *Light Metals* (2009), pp. 301–304.

[10] L.P. Lossius, K.J. Neyrey, and L. Edwards. "Coke and Anode Desulfurization Studies". *Light Metals* (2008), pp. 881–886.

[11] L. Edwards, F. Vogt, M. Robinette, R. Love, A. Ross, M. McClung, R.J. Roush, and W. Morgan. "Use of Shot Coke as an Anode Raw Material". *Light Metals* (2009), pp. 985–990.

[12] M. Siskin, S.R. Kelemen, C.P. Eppig, L.D. Brown, and M. Afeworki. "Asphaltene Molecular Structure and Chemical Influences on the Morphology of Coke Produced in Delayed Coking". *Energy Fuels* (2006), pp. 1227–1234.

[13] B. Vitchus, F. Cannova, and H. Childs. "Calcined Coke from Crude Oil to Customer Silo". *Light Metals* (2001), pp. 589–596.

3 Electrochemical Performance of Anodes Varying in Isotropic Coke Content

Abstract

As the aluminium industry faces a shift towards utilizing previously rejected isotropic cokes, it becomes increasingly important to understand the impacts of this coke in carbon anodes. In this work, the effects of isotropic cokes on electrochemical reactivity, both by electrochemical methods and by various imaging techniques (3D confocal optical microscopy, SEM/EDS and computed tomography) were investigated. For the investigation, a set of anodes containing various fractions of isotropic cokes: 0 % isotropic coke (i.e. 100 % anisotropic coke), 7.2 %, 14.2 %, 35.0 % and 49.0 % isotropic coke to anisotropic coke including an anode made from 100 % isotropic coke, were tested and characterised. The study also includes effects on physical parameters including density, specific electrical resistivity, air permeability, coefficient of thermal expansion, air and CO_2 reactivity and dust index. Electrochemical methods used were chronopotentiometry, polarisation curves (very slow cyclic voltammetry scan) and electrical impedance spectroscopy (EIS) in laboratory scale cells. Capacitance was extracted from the EIS data. The experimental setup was chosen as to minimize effects of bubble retention on the anode surface using a vertical anode working surface. A minor increase in the electrochemical reactivity in terms of reduction in reaction overpotential and an increase of the double layer capacitance were observed upon addition of isotropic coke. The latter is a clear indication of improved electrolyte wetting of the isotropic cokes.

Scanning electron microscopy (SEM) and energy dispersive spectroscopy (EDS) showed that sulfur is mainly bound to carbon in cokes; hence metal sulphides are of minor importance in cokes, both isotropic and anisotropic. Confocal microscopy images taken before and after electrolysis showed that pitch is the more reactive phase in anodes, and is faster consumed than coke particles. Both confocal microscopy and X-ray computed tomography (CT) have been used to show that isotropic and anisotropic coke particles are consumed at approximately the same rate. CT images also showed that even large pores are not penetrated by the electrolyte during electrolysis. CT images of the interior of the anodes showed cracks for anodes containing $\geq$35.0 %. This is due to the higher coefficient of thermal expansion for the isotropic cokes.

The above findings suggest that using isotropic coke in anodes is possible, and can even be beneficial for the electrochemical performance of the anodes. However, due to thermal strain cracking issues, and the high amount of sulfur and metal impurities, there is a threshold for maximum amount of isotropic coke possible to use in anodes. For this pilot anode line, this blending ratio limit is found between 14.2 % and 35.0 %.

3.1 Introduction

Production of aluminium is a high energy intensive process and the best cells today run at about 13 kWh/kg Al. The electrolysis cells are run at constant current and a total cell voltage of 4.1-4.2 V is common in modern cells, although the decomposition voltage of Al_2O_3 including overvoltages related to the anode and cathode is typically ~1.8 V. The cell voltage is hence a decisive factor concerning the energy consumption (kWh/kg Al). In addition, the cell voltage is important for keeping the correct heat balance of the cell and maintaining good cell stability. These are the most important factors when choosing the operational target cell voltage in aluminium electrolysis cells [1].

3.1.1 Use of Isotropic Coke in Anodes

As the aluminium industry faces a shift towards utilizing previously rejected isotropic coke, it becomes increasingly important to understand the impacts of this coke in carbon anodes.

Anode grade coke has normally been defined as delayed petroleum coke with an anisotropic sponge structure. These cokes are relatively low in metal impurities like vanadium (<400 ppm) and nickel (<250 ppm), and also low in sulfur (0.5-4.0 %) [2]. Today, a range of cokes of different qualities and a wide range of properties, anisotropic and isotropic, including shot coke, are blended and used as anode grade coke [2]. This is due to shortage of traditional anode grade coke, which in turn is due to a higher demand for coke for anode production, refining technology and available crude oil quality. Many of the new oil fields extract crude oil of higher specific gravity and with higher sulfur content. Cokes produced from these crudes typically have an isotropic character [3]. Shot coke is an isotropic coke type with some special features. The coke has a fine texture and more uniform properties. The particles are usually spherical, uniform in size and with little open porosity [4].

Edwards et al. [2, 4] have investigated the effect of using isotropic shot coke in anodes in collaboration with several aluminium producers. Isotropic shot coke has generally a higher coefficient of thermal expansion compared to anisotropic sponge cokes. This makes anodes containing isotropic shot coke more susceptible to cracking. There is a threshold for how much isotropic shot coke it is possible use in anodes before cracking occurs. Plant trials have found that 20 % isotropic shot coke is below this limit. The baked density of anodes containing isotropic shot coke is found to be higher than the purely anisotropic sponge coke anodes. As isotropic cokes are typically higher in impurities, this puts limitations on the fraction of isotropic coke that may be used in the baked anode.

Increased sulfur content in anodes will give higher SO_2 emissions and most smelters around the world have to handle this in a way where they still manage to stay below the SO_2 emission limit set by the authorities. This can partly be taken care of by blending with low sulfur cokes into the coke aggregate or by wet scrubbing the off gases from the potroom [2, 4–6]. Removing sulfur by increasing coke calcination temperature and/or

increasing residence time in the coker is possible, but will produce coke that is not suitable for anode manufacturing due to decreased bulk density due to the increased desulfurisation that will take place at higher calcining temperatures/residence times [5]. On the other hand, sulfur has the desirable effect that it acts as an inhibitor to CO_2 reactivity by forming inactive metal-sulfur complexes with metal catalysts [7].

High contents of V and Ni will give increased impurity levels in the final aluminium metal product [8]. Removing V from the final metal product is possible and is done by many aluminium producers. Ni on the other hand is difficult to remove and can only be achieved by the "three-layer electrolytic refining method". However, this approach will double the production cost of the aluminium metal. As a consequence, producers and consumers of aluminium metal may have to accept higher impurity specifications [7, 9, 10]. Vanadium is found to destabilise the surrounding carbons in the ring structure and hence act as an air reactivity catalyst [7]. Increased airburn give increased carbon consumption of the anodes. However, good process control and good crust coverage of the anodes reduce the extent of this problem [10].

3.1.2 Anodic Reaction Mechanisms

In an aluminium electrolysis cell, aluminium oxide, Al_2O_3, is dissolved into a cryolitic electrolyte, oxyfluoroaluminate ions ($Al_2O_xF_y^{6-2x-y}$ [11]) are formed by chemical reaction between the electrolyte and the Al_2O_3 and these ions are then oxidised on the anode. Mainly carbon dioxide gas is then formed on the anode at normal operating conditions, while a reduction reaction is taking place on the cathode forming aluminium [12]. Equation 3.1 shows the generalised total cell reaction when aluminium is produced [13]:

$$2Al_2O_3(diss) + 3C(s) = 4Al(l) + 3CO_2(g) \tag{3.1}$$

Raman spectroscopy and cryoscopic measurements have shown bridging Al-O-Al bonds and even double bridged bonds between aluminium and oxygen atoms in cryolitic melts when Al_2O_3 is dissolved [14–16]. Haupin [11] suggested the following reactions occurring in the electrolyte during Al_2O_3 dissolution.

$$4AlF_6^{3-} + Al_2O_3 = 3Al_2OF_6^{2-} + 6F^- \tag{3.2}$$

$$2AlF_6^{3-} + 2Al_2O_3 = 3Al_2O_2F_4^{2-} \tag{3.3}$$

In Equations 3.2 and 3.3 AlF_6^{3-} results from the dissociation of Na_3AlF_6 according to Equation 3.4 [11].

$$Na_3AlF_6 = 3Na^+ + AlF_6^{3-} \tag{3.4}$$

Sterten [17] used thermodynamic calculations to verify that both $Al_2OF_6^{2-}$ and $Al_2O_2F_4^{2-}$ species are probable. $Al_2OF_6^{2-}$ was found to be the dominating ion at lower Al_2O_3 concentrations. However, he also found that species like $Al_2OF_{10}^{6-}$ and $Al_2O_2F_6^{4-}$ had to be present at higher Al_2O_3 concentrations in order to justify the observed solubility ratio of Al_2O_3 in cryolitic melts.

Equations 3.5-3.7 show a generalised anodic reaction mechanism suggested by Picard et al. [18] as a three-step electrochemical reaction. Equation 3.5 describes the diffusion of oxyfluoroaluminate species from the bulk of the electrolyte to the anode surface. Equation 3.6 describes the formation of an intermediate adsorbed CO compound on the anode surface.

$$AlOF_x^{1-x}(electrolyte) \rightarrow AlOF_x^{1-x}(anode) \tag{3.5}$$

$$AlOF_x^{1-x} + C \rightarrow CO_{ads} + AlF_x^{3-x} + 2e^- \tag{3.6}$$

Lastly, Equation 3.7 describes the desorption of gaseous CO_2.

$$AlOF_x^{1-x} + CO_{ads} \rightarrow CO_2 + AlF_x^{3-x} + 2e^- \tag{3.7}$$

Kisza, Thonstad and Eidet [19] argues that a two-step reaction scheme is sufficient for describing the anode reaction process, and that diffusion of the oxyfluoroaluminate species from the bulk to the surface is fast in a saturated cryolite melt. They suggested that the $Al_2O_2F_6^{4-}$ anion was the most likely specie in Al_2O_3 rich electrolytes, although this could not be deduced from the electrochemical measurements. Equations 3.8 and 3.9 show their suggested reaction mechanism. The first step is the charge transfer step with an adsorbed intermediate (Equation 3.8). This step was found to be rate determining. The second step (Equation 3.9) involved electrochemical desorption.

$$Al_2O_2F_6^{4-} \rightarrow Al_2OF_6^{2-} + CO_{ads} + 2e^- \tag{3.8}$$

$$Al_2O_2F_6^{4-} + CO_{ads} \rightarrow CO_2 + Al_2O_2F_6^{2-} + 2e^- \tag{3.9}$$

However, in a later work, Kisza et al. [20] suggested a three-step reaction mechanism, where reactions 3.8 and 3.9 are preceded by the chemical step given below:

$$Al_2OF_{10}^{6-} \rightarrow Al_2O_2F_6^{4-} + 4F^- \tag{3.10}$$

Thus, although all details of the anodic reaction mechanism are still not fully understood, it seems to be generally agreed that the sequence includes the oxidation of an oxyfluoroaluminate species, and an intermediate adsorption process, most likely a CO compound [13, 16].

3.1.3 Anodic Overpotential

The anodic contribution to the total cell voltage is in the range of 0.4-0.7 V including the additional voltage caused by gas bubbles [1, 12]. Equation 3.11 shows the components that make up the measured potential, $E_{anode,measured}$ [13, 21–24].

$$E_{anode,measured} = E^{rev} + \eta_c + \eta_r' + \eta_h + I(R_s' + \delta R_s) \tag{3.11}$$

Here, E^{rev} is the reversible potential for the CO_2 forming reaction. η_c is the concentration overpotential caused by concentration gradients of Al_2O_3 in the electrolyte close to the anode. η_r' is the reaction overpotential when no gas bubbles are screening the anode surface and η_h is the additional reaction overpotential on the anode due to increased local current density caused by the reduced effective surface area when bubbles are screening the anode. η_h is also denoted as hyperpolarisation [24–26]. The total reaction overpotential is hence $\eta_r = \eta_r' + \eta_h$, and is related to charge transfer reactions where intermediate adsorption/desorption processes takes place on the electrode surface, as described in the previous section. $I(R'_s + \delta R_S)$ is related to the increase in ohmic resistance when bubbles are screening the anode surface. R'_s gives the ohmic series resistance with no bubbles screening the anode and R_S denotes the increase in ohmic series resistance due to partial blocking of the anode.

It is generally agreed that the concentration overpotential is negligible in a saturated melt, but also generally small even in industrial cells (estimated to ∼0.02 V). The anodic reaction overpotential is ∼0.5 V and the extra voltage caused by bubbles is ∼0.2 V [12].

In laboratory studies, graphite has typically been found to have higher overvoltage than baked carbon anodes [13]. Recent work has also given strong indications that single coke source anodes fabricated from isotropic cokes have a slightly higher electrochemical reactivity than anodes fabricated from anisotropic cokes, and thus a lower reaction overpotential. In these studies, a vertical anode design was used in order to minimise the bubble retention on the anode surface [21, 23, 27]. Leistra and Sides [25] found hyperpolarisation on baked carbon anodes to be approximately 15 mV using a rotating disk at 1.0 A/cm^2.

Traditionally, researchers have fitted experimental current-overvoltage data to the semi-logarithmic Tafel equation when studying the anodic overpotential. However, as reviewed by Thonstad et al. [13], there is a large scatter between results with numerical values ranging from 0.09 V/dec to 0.55 V/dec for the Tafel slope. Sørensen and Kjelstrup [28] has pointed out that producing Tafel plots are challenging since the Tafel equation is a limiting case of the Butler-Volmer equation. Due to the two possible reactions that can take place on the anode surface (the two electron transfer reaction producing CO, mainly at low current densities but also as a competing reaction to the CO_2 evolving reaction at higher current densities [29], and the four electron transfer reaction producing CO_2), the true current-overvoltage relationship is not likely to obey the Tafel approximation. Also, COS has been detected during electrolysis [30] and at lower concentrations of Al_2O_3 the production of several other

anodic gases is also possible, mainly COF_2 and CF_4 [31]. Hence, due to the complexity of the anodic reaction and difficulties in setting the current density correctly e.g. due to bubble noise, the parameters determined from the Tafel approximation are difficult to compare and interpret from one experiment to another. Factors like experimental design affects the resulting Tafel curve and the parameters are hence specific of the given electrochemical conditions in each laboratory setup.

3.1.4 Electroactive Surface Area determined by the Capacitance

For the determination and comparison of electrochemical activity of different anodes, it is crucial that variations in surface area are corrected for. It is generally agreed that the capacitance provides a measure of the active electrode surface area [19, 32, 33] as it reflects the ability of the surface to store electric charge by polarisation. Electrochemical impedance spectroscopy (EIS) can be used to extract the capacitance of an electrode. Eidet [16] (Sections 2-5) gives a good introduction to the use of EIS in cryolitic systems. The capacitance can be used as an in situ measure of the wetted surface area. Typical values for double layer capacitance for graphite is reported in the range 45-75 $\mu F/cm^2$. Thonstad [34] found a double layer capacitance for baked carbon anodes, in the range 150-600 $\mu F/cm^2$, however, the most commonly capacitance range for carbon anodes reported by various scientists is 150-280 $\mu F/cm^2$ [19, 32, 33, 35]. In a recent work, Gebarowski et al. [36] found double layer capacitance for graphite after polarisation of 30 $\mu F/cm^2$. For two anode samples varying in coke quality, they found ranges between 50-70 $\mu F/cm^2$ at potentials above 1.3 V. At potentials below 1.3 V the capacitance was somewhat higher. Nevertheless, Gebarowski et al. [36] show lower capacitance values than previously reported. It is assumed that for sufficiently high frequencies no faradaic reactions occur (or occur at negligible rate), such that the only contributions to the imaginary impedance are the double layer capacitance and the inductance from the external leads. In Gebarowski et al. [36] the effect of the frequency range was investigated in order to be able to use this assumption and it was shown that a higher frequency range is needed for this assumption to be true.

In general, the large variety in capacitance measured for baked carbon anodes is attributed to the variation in porosity and the inhomogeneity in surface roughness between samples [33, 34, 37]. Varying production parameters of these anodes in terms of e.g. coke and pitch quality, mixing and baking temperatures will affect the porosity and surface roughness. The surface roughness will also change during electrolysis due to uneven electrolytic consumption of the anodes. Thonstad [37] found an increase in double layer capacitance of 45 % when comparing a fresh baked carbon anode sample with the same anode after it had been electrolysed for a time corresponding to anode consumption of 2 mm at 1.0 A/cm^2. However, Jarek and Orman [35] found no such increase in capacitance for baked carbon anodes before and after polarisation.

3.1.5 The Effect of Carbon Structure on the Electrochemical Anodic Reactivity

The amount of active sites on carbon surfaces depends on crystallite size, crystallite orientation, vacancy concentration in the basal plane and type and location of impurities [38]. It has been shown that edges of carbon crystallites have higher oxygen reactivity than basal plane surfaces, as edge carbon atoms have unpaired electrons available for bonding (so-called "dangling bonds", i.e. the incomplete σ-bonds) . Edge-planes have also been shown to be electrochemically more active for various carbon materials: more edge-planes gives higher electrochemical activity [39]. The effect of basal planes has also been shown on overpotential measurements on pyrolytic graphites (perpendicular and parallel to basal plane), graphite and baked carbons by Thonstad [40]. The pyrolytic graphite with parallel basal planes showed higher overpotential than pyrolytic graphite with perpendicular basal planes. Regular graphite showed lower overpotential compared with the near perfect ordered structure pyrolytic graphite. Lastly, the least structured baked carbon anodes showed the lowest anodic overpotential.

Thorne et al. [21] determined the amount of edge sites, basal planes and defects for crushed graphite, isotropic and anisotropic cokes and for crushed anodes made from isotropic and anisotropic coke. It was found that the coverage of edge sites increased with isotropy and that the coverage of defect sites decreased with isotropy. The graphite anode showed a substantial amount of basal planes, while the petroleum cokes showed a basal plane fraction less than 10 %, Thorne et al. [21] observed that the anodes made from isotropic cokes with a higher fraction of edge sites also exhibited a slightly lower polarization resistance and overpotential as compared to the anodes made from anisotropic cokes.

3.1.6 Purpose of this Work

Based on the changes in the raw material situation for anode cokes, with a shift towards blending in isotropic cokes into the coke aggregate, the purpose of this work is to improve the understanding of the impact of this coke in carbon anodes. The main objective of the work is to study the effects of isotropic cokes on electrochemical reactivity, both by electrochemical methods, and by various imaging techniques (3D confocal optical microscopy, SEM/EDS and computed tomography). The imaging techniques provide information on local consumption of the various phases, on distribution of impurities, as well as the morphology and quality of the anodes in terms of porosity and presence of cracks.

The properties of anodes containing various fractions of isotropic cokes, i.e 0 % anode (i.e. 100 % anisotropic coke), 7.2 %, 14.2 %, 35.0 % and 49.0 % isotropic coke to anisotropic coke including also an anode made from 100 % isotropic coke are investigated. The study includes effects on physical parameters (including density, specific electrical resistivity, air permeability, coefficient of thermal expansion, air and CO_2 reactivity and dust index) and electrochemical reactivity, determined by chronopotentiometry, polarisation curves (very slow cyclic voltammetry scan) and by electrical

impedance spectroscopy (EIS) in laboratory scale cells. EIS is used in order to determine the capacitance and the charge transfer resistance. A vertical anode assembly is chosen to minimise effects of bubble retention on the anode surface during bubble build-up and release.

Confocal microscopy is used to study the consumption and the true area of anode surfaces before and after electrolysis. X-ray computed tomography is used to study the interior of anodes before and after electrolysis, and also in order to study the electrolyte-anode surface interaction in terms of intrusion of electrolyte into pores. By combining electrochemical and imaging techniques, differences in the reactivity of the cokes are assessed, and some considerations regarding the optimum amounts of isotropic coke are made.

3.2 Materials and Methods

3.2.1 Pilot Anode Materials and Electrolyte

Pilot scale anodes (Ø = 130 mm, h = 180 mm) were produced by Hydro Aluminium from one single source sponge petroleum coke of anisotropic character, one single source isotropic petroleum coke and an industrial grade coal tar pitch. The particle size of the aggregate was 0-2 mm and the grain size distribution was comparable in the aggregates; this aggregate sizing was chosen to ensure a representative and fairly homogeneous surface area in laboratory scale experiments. The recipe for producing the anodes was varied throughout the series in terms of blending ratio of isotropic to anisotropic coke and was based on combining 1-2 mm, 0-1 mm and a ball mill dust fraction ($< 63\ \mu$m). Six different pilot anodes were produced to varying blending ratios. Table 3.1 shows the compositions of the anodes in this study, and the anode name refers to the total isotropic coke content in the anode. The anode names referred to in Table 3.1 will be used consistently throughout this chapter. A graphite material from Svensk Specialgrafit AB (Ultrapure grade CMG) was used for comparison and is denoted as "graphite" throughout the chapter. The pitch binder used for production of the anodes had a Mettler softening point of 119.1°C and a quinoline insoluble (QI) level of 7.8%. Mixing and baking temperatures during anode fabrication were kept constant throughout the entire anode series at 168 °C and 1230 °E, respectively. See [41] for details on equivalent baking temperature, °E.

For clarity, Anodes 0 % and 100 % in this work are sampled from the same pilot anodes as Anode A and B in Sommerseth et al. [23, 42], respectively. Also, Anode 0 % and Anode 100 % are sampled from the same pilot anodes as Anode 1 and Anode 4 in [21, 22, 27, 36], respectively. However, new samples were made for the electrochemical tests reported here.

The electrolyte was a cryolitic melt with a molar ratio of NaF to AlF_3 of 2.3, saturated in aluminium oxide. The cryolite was from Sigma Aldrich (>97% purity) with an excess of AlF_3 of 9.8 wt% (industrial grade, sublimed in-house) and 9.4 wt% γ-Al_2O_3 from Merck (>99.4 % purity). The same electrolyte composition was used for all experiments.

Table 3.1: Pilot anodes. Coke type denotes anisotropic, A, and isotropic, I, coke.

Anode name	Coke type	0-1 mm aggregate	1-2 mm aggregate	Ball mill product	Pitch content
		wt%	wt%	wt%	wt%
0 %	A	35.0	38.0	27.0	15.0
	I	0			
7.2 %	A	32.4	32.4	28.0	14.0
	I	3.6	3.6	0	
14.2 %	A	28.0	28.8	29.0	14.0
	I	7.0	7.2	0	
35.0 %	A	17.5	17.5	30.0	14.0
	I	17.5	17.5	0	
49.0 %	A	10.5	10.5	30.0	14.0
	I	24.5	24.5	0	
100 %	A	0	0	0	15.0
	I	35.0	38.0	27.0	

3.2.2 Physical Analysis

The anodes were characterised using International Organization for Standardization (ISO) methods used in the industry for density (ISO 12985-1:2000), specific electrical resistivity (SER) (ISO 11713:2000), permeability (in house method at Hydro comparable to ISO 15906:2007) and coefficient of thermal expansion (ISO 14420:2005, but the temperature range was extended to 300-700°C and a sample size of Ø = 20 mm, height = 75 mm). Air and CO_2 reactivity tests were performed using in-house thermogravimetric analysis methods developed at Hydro Aluminium similar to ISO 12989-1 and ISO 12988-1, respectively. Additionally, the levels of metal and sulfur impurities in the carbon anodes were determined using X-Ray fluorescence (XRF). The methodology is described in ISO 12980:2000. All these measurements are performed as routine measurements at Hydro Aluminium Årdalstangen.

3.2.3 Surface Investigations through Microscopy Imaging Techniques

Cores of 10 mm diameter samples were drilled from the 0 %, 49.0 % and 100 % pilot anodes and the horizontal surface was ground down stepwise to P#4000 using SiC paper. A low vacuum SEM, Hitachi S-3400N with EDS was used in order to perform elemental analysis on the anodes. The entire horizontal surface of the anodes was assembled from over 400 scans. The software Aztec from Oxford Instruments was used in order to display the distribution of impurities on the anode surface. Surface roughness investigations of the same horizontal anode surface were performed us-

ing an Infinitefocus confocal microscope from Alicona 3D. The resolution was 410 nm. The microscope scanned the entire surface, creating a 3D image of the anode surface including pits and voids. The instrument measured and reported the surface roughness of the anode as true area over projected area (TA/PA), where true area included all pits and voids and projected area was the geometric surface area. The rod samples were then electrolysed at 1.0 A/cm^2 for 1500 s. After electrolysis the remaining electrolyte on the anode surface was removed by soaking in a solution saturated in $AlCl_3$. Confocal microscopy was then repeated in order to investigate the changes in surface roughness (TA/PA) after electrolysis. The images of the anode surfaces obtained by confocal microscopy before and after electrolysis are used to investigate differences in local consumption rates along the surface. Confocal microscopy images as well as the SEM images are oriented in the same direction and used to investigate the consumption of sulfur-rich grains.

3.2.4 X-Ray Computed Tomography

CT was used to investigate the interior of anodes and the intrusion of electrolyte into anodic pores after electrolysis. Tomographs were recorded before and after electrolysis at 1.0 A/cm^2 for 1800 s. The anodes were withdrawn from the electrolyte with current still on (hot-pulled). Figure 3.1 shows the anode assembly and the electrolysis setup used when investigating the anodes using CT. The anode setup gave a well-defined surface area of 1.52 cm^2. The anode test piece was shielded with a BN piece on the top and bottom creating a vertical anode surface area. A graphite rod in the middle served as electrical contact. This anode assembly was also used during the electrochemical measurements, as described below.

CT was performed with a Nikon XT H225 ST. A molybdenum reflection target was used. Settings for the imaging were 110 kV and 200 μA. Integration time was 1 second, 1440 projections per revolution, distance from source to sample was 35.1 mm, distance from source to detector was 1124.8 mm and the voxel dimension (combination of "volume" and "pixel" to denote the resolution) was 6.25 μm x 6.25 μm x 6.25 μm. Three different software programs from Nikon Metrology were used to create the CT images: Inspect-X (used to control the x-ray generator, sample table and collecting images), CT Pro 3D (used to edit parameter files for reconstruction of CT images) and CT Agent (used for reconstruction of CT images). The images were exported as a stack of 2000 single 2D images sliced in the XY (transverse) direction. These were loaded and post processed in ImageJ by cropping, translating and rotating the images so that the after electrolysis scans matched the before electrolysis scans. These images were merged into side-by-side images allowing easy comparison of the before and after electrolysis scans. All these steps were done automatically by a custom written macro. The translation and rotation parameters were determined manually.

3.2.5 Texture Analysis

Optical microscopy is used to investigate the texture of the anodes varying in isotropic coke content. 10 mm cores of anode samples were mounted in epoxy resin under vacuum (Epofix two-component epoxy with Epodye fluorescent dye from Struers, Denmark). When set, samples were ground and polished stepwise down to 1 μm and studied in an optical microscope. When analysing the texture of the anodes a custom written macro for the NIH software [43] was used in order to characterise the anodes in terms of mosaic and fiber index. The mosaic and fiber index can be related to the degree of isotropy and anisotropy. A magnification of x250 was used and a representative area (total sample area of 4.6 x 4.6 mm^2) of the samples was investigated under polarised light (192 images stitched together).

3.2.6 Electrochemical Measurements

All electrochemical tests were performed using a Zahner IM6 potentiostat with a built in frequency analyser for electrochemical impedance spectroscopy (EIS) measurements. The potentiostat had a PP201 20 A booster from Zahner-Elektrik.

The anodes were characterised electrochemically by chronopotentiometry, cyclic voltammetry (CV) and EIS. An aluminium reference electrode produced in-house was used and all potentials were measured between the anode and the reference electrode. The reference electrode is more thoroughly described in Appendix A. The carbon anode was the working electrode, the graphite crucible walls acted as the counter electrode. Figure 3.1 shows the anode assembly and the laboratory electrolysis cell. The anodes were investigated by first preconditioning the anode by electrolysing at 1.0 A/cm^2 for 200 s. Then chronopotentiometry was performed at 1.0 A/cm^2 200 s and the voltage output between anode and reference electrode was recorded. The average potential of the last 50 s was reported as the voltage output for each tested sample. CV was run for three consecutive runs from open circuit potential (OCP) to 2.5 V at 0.1 V/s. The scan was so slow that it was considered equivalent with polarisation curves.

Impedance spectra were recorded at OCP and 1.5 V (non IR corrected) in the frequency range 100000-0.1 Hz. The amplitude was 50 mV. The potential has then been IR corrected using the series resistance, R_S, as obtained from the high frequency intercept of the Nyquist plots. From the 1.5 V Nyquist plots the capacitance, C_{dl} or C_{eff} (depending on the equivalent circuit used), was extracted. The Nyquist plots were fitted to equivalent circuits using the software Zview 3.4e by Scribner Associates, Inc. The EIS spectra have been modelled using two circuits: the simple LR(CR) circuit and the more complex LR(Q(R(LR))) circuit as described by Harrington and Conway [44], except that the ideal double layer capacitance has been replaced by a constant phase element, Q (or often denoted as CPE). The first resistance in the equivalent circuits denotes the ohmic resistance of the electrolyte including the leads to the electrode, also known as the series resistance, R_s, and the first L is the inductance of external wires. The second and third resistances are the charge transfer resistances of the first and second half spheres in the Nyquist spectras, R_{CT_1} and R_{CT_2}, respectively. The last

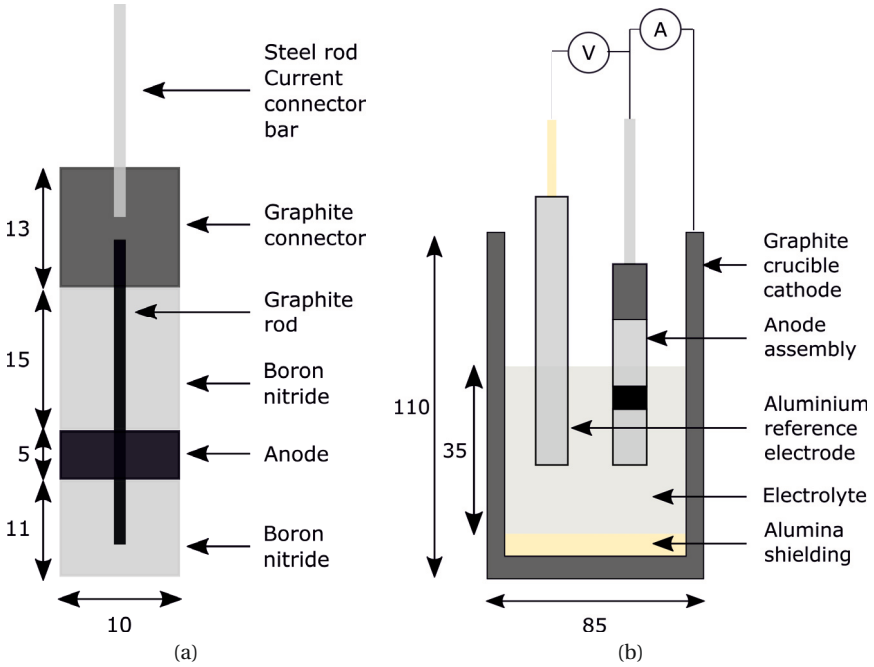

Figure 3.1: Electrochemical experimental setup used when electrolysing samples for CT scanning and during general electrochemical testing, including overpotential measurements, cyclic voltammetry and electrical impedance spectroscopy. All measures indicated in the figure are in mm. a) Vertical anode assembly. b) A principle sketch of the electrolysis cell used with the aluminium reference electrode, the graphite crucible acting as the cathode, the vertical anode assembly and the electrolyte.

L is denoted as the inductance of adsorbed species, L_{ads}. In [44], the LR(Q(R(LR))) equivalent circuit was derived for a general reaction sequence involving intermediately adsorbed species. Introduction of the constant phase element is reasonable, since the anodes studied here have a relatively high surface roughness [45]. Different methods were used in order to determine the double layer capacitance. It was extracted directly using the equivalent circuit LR(CR). The effective capacitance was modelled using the equivalent circuit LR(Q(R(LR))). The effective capacitance, C_{eff}, was calculated using Equation 3.12 (same as Equation 15 in Orazem et al. [46] developed for Faradaic systems). The effective capacitance is also denoted interfacial capacitance and may be considered to be a good approximation for the double layer capacitance.

$$C_{eff} = Q^{1/\alpha}\left(\frac{R_s(R_{CT_1}+R_{CT_2})}{R_s+R_{CT_1}+R_{CT_2}}\right)^{(1-\alpha)/\alpha} \tag{3.12}$$

α is the dimensionless constant phase element exponent in Equation 3.12. The remaining symbols have been described above.

In addition, the capacitance was extracted using the high frequency range (100000-

5000 Hz) assuming the simple circuit LRC to apply. L represents the inductance of the leads to the cell, R represents the resistance of the electrolyte between the anode and the reference electrode (including leads to the working electrode) and C_{dl} (later denoted $C_{dl,high\,frequency}$) is the capacitance of the anode. It was assumed that for high frequencies, no or negligible faradaic reactions occur, hence the only contributions to the imaginary impedance are inductance from the external leads and double layer capacitance.

The inductance, L, was extracted from the raw data from EIS at 1.5 V at the highest frequency (100000 Hz) according to Equation 3.13:

$$L_{100000\,Hz} = \frac{Z_{Im,100000\,Hz}}{2\pi f} \tag{3.13}$$

In Equation 3.13, f is the frequency and Z_{Im} is the imaginary impedance. The inductance was then used to calculate the capacitance using Z_{Im} for each frequency step according to Equation 3.14.

$$C_{dl,high\,frequency} = \frac{1 \cdot 10^6}{1.52 \cdot 2\pi f(2\pi f L - Z_{Im})} \tag{3.14}$$

$C_{dl\,frequency}$ was then plotted *vs.* frequency and from the graph a horizontal capacitance range was found in the high frequency region. This horizontal range was used to determine $C_{dl,high\,frequency}$. This method is described in [33, 34, 36].

All three equivalent circuits described above are more thoroughly described and explained in Appendix C.

3.3 Results and Discussion

3.3.1 Physical Parameters for the Test Anodes

Table 3.2 shows impurity levels in the graphite anode, 0 % isotropic coke anode (made of 100 % traditional anisotropic coke) and 100 % isotropic coke anode. The impurity levels were found by analysing using an X-ray fluorescence spectrometer. From the table it is evident that the ultrapure graphite is very low in all impurities, as expected. The 0 % anode (i.e. 100 % anisotropic) is also fairly low in all impurities both metal and sulfur. The 100 % anode is made from a high impurity coke, especially in terms of sulfur, calcium, vanadium, nickel and to some extent, iron.

Table 3.3 shows physical parameters for the anodes, including density, specific electrical resistivity, permeability, coefficient of thermal expansion, air and CO_2 reactivity and dust index. The density is similar for the 7.2 %, 14.2 % and 100 % anodes. The 0 % anode is slightly denser, while the 35.0 % and 49.0 % anodes are significantly denser than the rest of the pilot anode series. This indicates that with the coke aggregate recipe used for these pilot anodes, there is a threshold between 14.2 % isotropic coke

and 35.0 % isotropic coke where the packing between the isotropic and anisotropic cokes become more optimum and hence denser anodes are produced. The specific electrical resistivity generally reflects the density of the coke. A denser anode gives lower specific electrical resistivity i.e. better conductivity. However, this does not include the 0 % and the 100 % anodes, indicating that the coke quality also affects the resistivity. The 100 % anode shows a significantly lower specific electrical resistivity compared with the density. This has been seen in other studies as well, when using isotropic coke for pilot anode production [47]. The air permeability reflects the density, except for the 100 % anode. This anode exceeded the limit for the air permeability measuring equipment; hence, 6.9 nPm only reflects that the equipment reached the maximum measurable level. A high air permeability has also been seen by Lossius et al. [47] when producing an anode from 100 % isotropic coke. This indicates that the 100 % isotropic coke anode has a large array of open porosity, due to poor pitch wetting between coke and pitch and/or due to the high density of isotropic coke grains and difficulties in finding a dense optimum packing between coke grains. The coefficient of thermal expansion follows a near linear increase depending on the weight percent isotropic coke present. This was also seen by Edwards et al. [4].

In Table 3.3 it is seen that CO_2 reactivity generally decreases with isotropic coke present compared with the anode purely made of anisotropic coke. This is due to the increased sulfur content in anodes containing isotropic coke and sulfur is a known inhibitor for CO_2 reactivity [7]. The air reactivity increase with increasing isotropic coke content from 7.2 % all through to 100 % isotropic coke content. It is reasonable to conclude that this is due to the increasing amount metal impurities like vanadium [9, 10]. Graphite shows a very low air and CO_2 reactivity, and this can be attributed to the high amount of basal planes compared with edge and defect sites and also the very low impurity levels [21]. Edge and defect sites have been found to be more reactive than basal planes [38]. The dust index is also observed to reduce drastically with introduction of isotropic coke. Dust reduction is desirable in the electrolysis cell, as dust eventually has to be removed from the electrolyte manually [48] and dust can increase the ohmic resistance through the electrolyte as they act as insulators once the carbon particles has detached from the anode [1].

The anodes produced for this work represent specialised, tailor-made anode aggregates. They are produced in a pilot scale anode production line that has been tuned to simulate full scale anode production. A fair level of agreement with actual anode properties is expected, but there are deviations compared with typical industrial an-

Table 3.2: XRF elemental results for graphite and the baked 0 % and 100 % isotropic coke anodes.

Anode	Na ppm	Si ppm	P ppm	S %	Ca ppm	V ppm	Fe ppm	Ni ppm	Zn ppm	Pb ppm
Graphite	10	10	1	0.00	11	1	25	3	1	1
0 %	56	108	11	0.94	25	70	287	45	5	7
100 %	115	284	4	4.45	227	883	393	372	38	20

Table 3.3: Physical parameters for the anodes. The tests were performed at Hydro Aluminium Årdalstangen. SER = Specific el. resistivity, Perm. = Permeability, CTE = Coefficient of thermal expansion and TC = Thermal conductivity, CO_2, air reactivity and dust index.

Anode	Density	SER	Perm.	CTE	R_{CO_2}	R_{Air}	Dust index
	g/cm^3	$\mu\Omega$m	nPm	μm/mK	mg/cm^{2}h	mg/cm^{2}h	mg/cm^2
Graphite	1.771	12.7	0.20	N/A	2.5	0.3	0.4
0 %	1.603	55.2	0.8	4.14	19.0	39.0	15.3
7.2 %	1.597	58.3	1.1	4.19	11.9	21.5	4.8
14.2 %	1.595	59.4	1.5	4.48	11.4	25.2	4.4
35.0 %	1.651	51.9	0.9	5.07	14.4	30.9	2.2
49.0 %	1.674	50.7	0.6	5.44	18.1	37.2	2.1
100 %	1.596	50.5	6.9*	7.07	7.4	70.1	0.2

*This was the maximum measurable level of the equipment, indicating that the measurement is out of range.

ode parameters (*cf.* Table 2.1 and [49]), especially for the 100 % anode with the high porosity. Some of these deviations are due to a higher pitch content compared to the ability of the isotropic coke to absorb pitch as well as the unusual coke aggregate used. Also, it is fairly common that pilot scale anodes show a slightly lower density, a little higher air permeability and electrical resistivity than industrial scale anodes [47].

3.3.2 Scanning Electron Microscopy, Energy Dispersive Spectroscopy, Confocal Microscopy and Surface Roughness Investigations

The surface for the anodes with 0 %, 49.0 % and 100 % isotropic coke content were investigated using SEM and EDS for element distribution and using confocal microscopy for surface roughness investigations. SEM was used to create a surface map of the entire sample surface. Carbon, sulfur, iron, vanadium and silicon elemental maps were obtained by EDS. The samples investigated were Ø = 10 mm and 2-4 anode parallels were studied for each pilot anode. The surface map was stitched together from over 400 individual images as the SEM screened the entire sample surface. The same anodes, including the remaining pilot anodes (the 7.2 %, 14.2 % and 35.0 % anodes) of the isotropic coke content series, were also investigated using confocal microscopy to create contour images of the surfaces before and after electrolysis at 1.0 A/cm^2 for 25 mins. The confocal microscope was used to measure true area over projected area (TA/PA).

Figures 3.2-3.9 show a) confocal microscopy surface map, b) confocal microscopy contour map before electrolysis, c) sulfur EDS map and d) confocal microscopy contour map after electrolysis and after the electrolyte had been removed for the anodes with 0 %, 49.0 % and 100 % isotropic coke content. In the confocal microscopy contour

images, the colour red denotes “hills in the landscape” and green denotes “valleys in the landscape”. SEM/EDS investigations were compared with contour images from confocal microscopy in order to evaluate the electrochemical consumption on a carbon surface with different coke grains containing various impurities, in particular the high-sulfur grains.

Figures B.1-B.8 in Appendix B show surface maps and elemental analysis maps (C, S, Fe, V and Si) of the anodes varying in isotropic coke content, 0 %, 49.0 % and 100 %, respectively.

By investigating the EDS images in Figures 3.2-3.9 and Figures B.1-B.8 in Appendix B, it is evident that sulfur is bound to carbon, and not to other metal impurities like iron. This applies both for the isotropic and anisotropic coke particles. For the pure anisotropic anode (the 0 % anode), the sulfur is distributed in single high sulfur coke grains only, randomly distributed. For the isotropic coke it is evident that all isotropic coke grains contain a certain amount of sulfur, evenly distributed throughout each coke grain. It has been suggested in literature that most sulfur in coke occurs in organic form in five or six ring carbon structures in the coke, derived from thiophene and thiopyran [50, 51]. Vanadium also appears to be evenly distributed in the isotropic coke grains as evident from Figures B.5 e) and B.6 e). In these images the isotropic coke grains show different contrast compared to the anisotropic coke grains. However, vanadium was not detected by EDS for the 0 % anode samples, and could not be distinguished to a large extent for the 100 % anode. This implies that EDS is not able to identify vanadium in ppm levels unless there is a contrast difference between two phases. Iron and silicon are randomly distributed on the anode surfaces suggesting that they are oxide impurities not bound to the carbon structure.

By inspection of the contour images before and after electrolysis in Figures 3.2, 3.3 and 3.5, the most pronounced difference in consumption on various coke particles on the anode surface, is coke particles high in porosity. Particles high in porosity (so-called “bubble coke”) are visible for all anodes containing anisotropic coke (Figures 3.2-3.7) and these coke particles are consumed at a slower rate than the matrix. This is either due to a lower electrical conductivity through these grains and/or due to poorer wetting between electrolyte and anode surface during electrolysis. The former is considered more likely. It could not be determined, however, whether grains high in sulfur are consumed at a higher or slower rate than the bulk coke.

For all the anode samples in Figures 3.2-3.9 an increased consumption can be seen for the filler between larger coke grains. Many scientists have found increased air reactivity for pitch compared with coke, and many have also suggested that pitch is more reactive than coke during electrolysis [12, 13, 32, 34]. Thonstad [37] found by EIS that the double layer capacitance increased by 45 % after electrolysis compared with an unpolarised fresh sample. He suggested that the pitch had been preferably consumed. The contour images before and after electrolysis support these earlier findings.

For the 49.0 % anode samples (Figure 3.6-3.7) any significant differences in consumption between isotropic and anisotropic coke grains is not observed. This is supported by CT images in Figures 3.13-3.16.

For Figures 3.8 and 3.9, an array of large pores is visible. This is also seen in cross-section tomographs (Figure 3.17). This array of large pores, creating a significant amount of open porosity can explain the high value for air permeability for the 100 % anode as seen in Table 3.3. These pores are most likely due to an inappropriate amount of pitch to the amount of coke used, and/or poor wetting between coke and pitch, and/or non optimum packing of the coke particles. The coke is, as already mentioned, highly isotropic. Isotropic cokes are known for having a low amount of open porosity and hence little pitch penetrates into the coke grains. This also implies that less pitch is needed when producing pure isotropic coke anodes compared with anisotropic coke anodes [47]. An inappropriate mixing temperature used when mixing the coke and the pitch is also reasonable to suspect. Sessile drop tests of the wettability between the cokes used (the anisotropic sponge coke and the isotropic coke) and the pitch was not performed before production and the same mixing temperature was used for the entire anode pilot line. The coke aggregate sizing and packing for the 100 % anode also looks non-optimum. Problems with producing anodes of purely isotropic cokes has also been discussed elsewhere and the conclusion is that making anodes from isotropic coke only, is not realistic [47].

Figure 3.10 shows TA/PA for the entire series of anodes varying in isotropic coke content. Square points show TA/PA for anode surfaces before electrolysis and circle points show TA/PA after electrolysis and removal of electrolyte. TA/PA reflects the geometric surface roughness of the anodes. Figure 3.11 shows the average ratio between the area increases of the anode surface after electrolysis compared with the polished anode surface before electrolysis. An increase of 30-50 % in surface area is observed for the electrolysed sample compared with the fresh, ground anode sample. This is in good agreement with the EIS measurements performed by Thonstad, where he observed an increase in surface area of 45 % [37]. TA/PA and the increase in surface roughness after electrolysis are higher for both the 0 % and 100 % anodes compared with the blended anodes. This is most likely due to the high amount of “bubble coke” in the 0 % anode samples and the high amount of large open porosity in the 100 % anode samples.

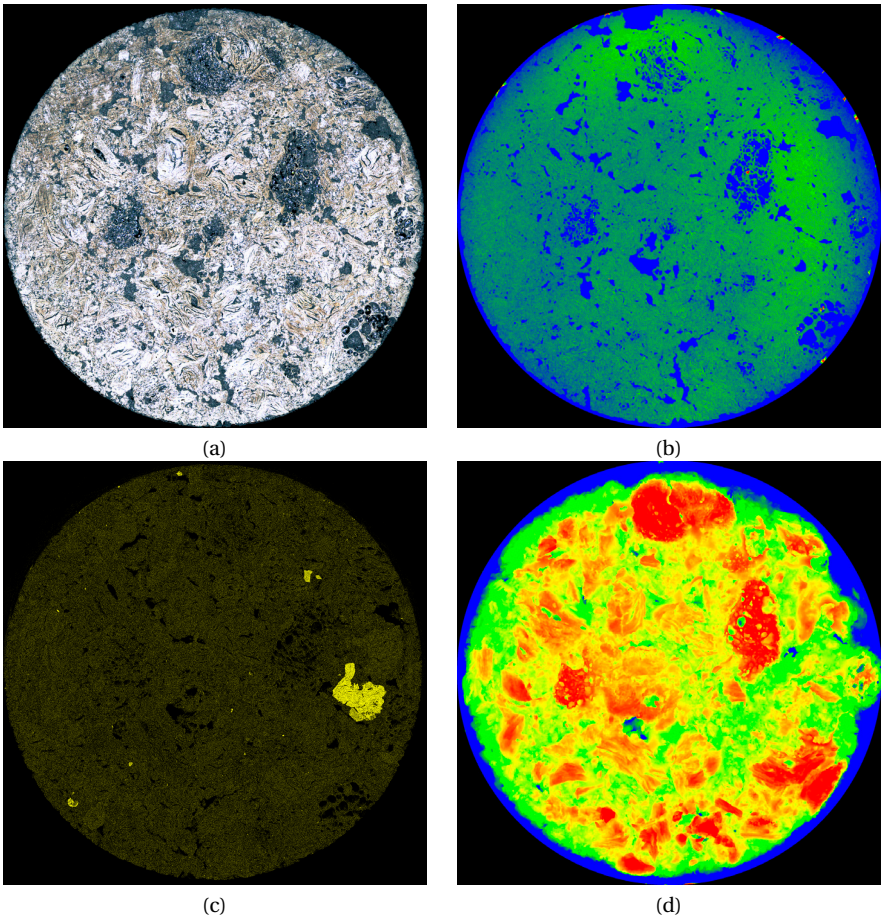

(a) (b) (c) (d)

Figure 3.2: Anode made of 100 % traditional anisotropic coke (0 % isotropic coke), sample 1. a) Confocal microscopy surface map before electrolysis, b) Confocal microscopy contour image of the surface before electrolysis, c) Sulfur map obtained by SEM/EDS, and d) Contour image of the surface after electrolysis.

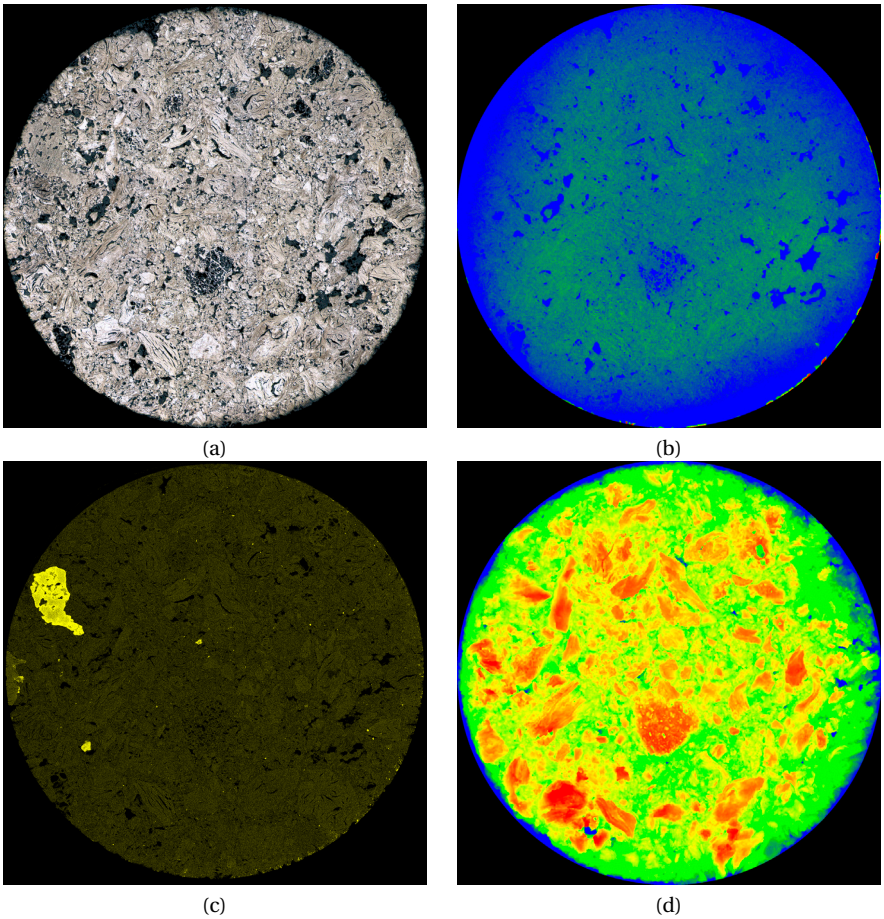

Figure 3.3: Anode made of 100 % traditional anisotropic coke (0 % isotropic coke), sample 2. a) Confocal microscopy surface map before electrolysis, b) Confocal microscopy contour image of the surface before electrolysis, c) Sulfur map obtained by SEM/EDS, and d) Contour image of the surface after electrolysis.

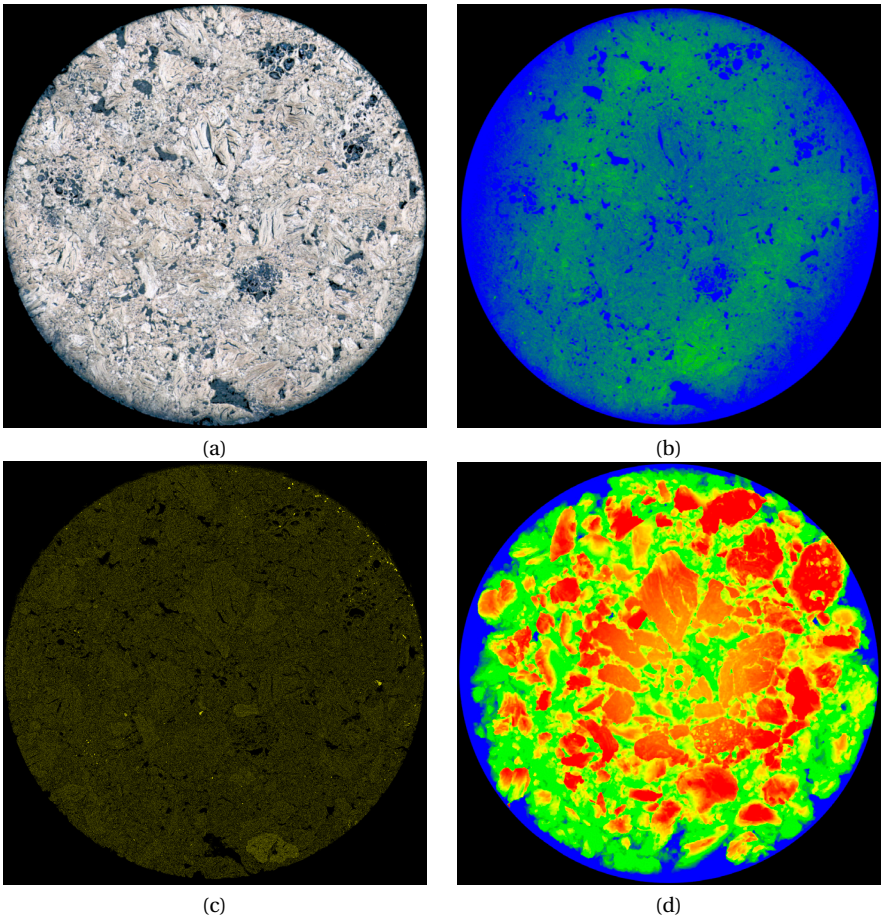

(a) (b) (c) (d)

Figure 3.4: Anode made of 100 % traditional anisotropic coke (0 % isotropic coke), sample 3. a) Confocal microscopy surface map before electrolysis, b) Confocal microscopy contour image of the surface before electrolysis, c) Sulfur map obtained by SEM/EDS, and d) Contour image of the surface after electrolysis.

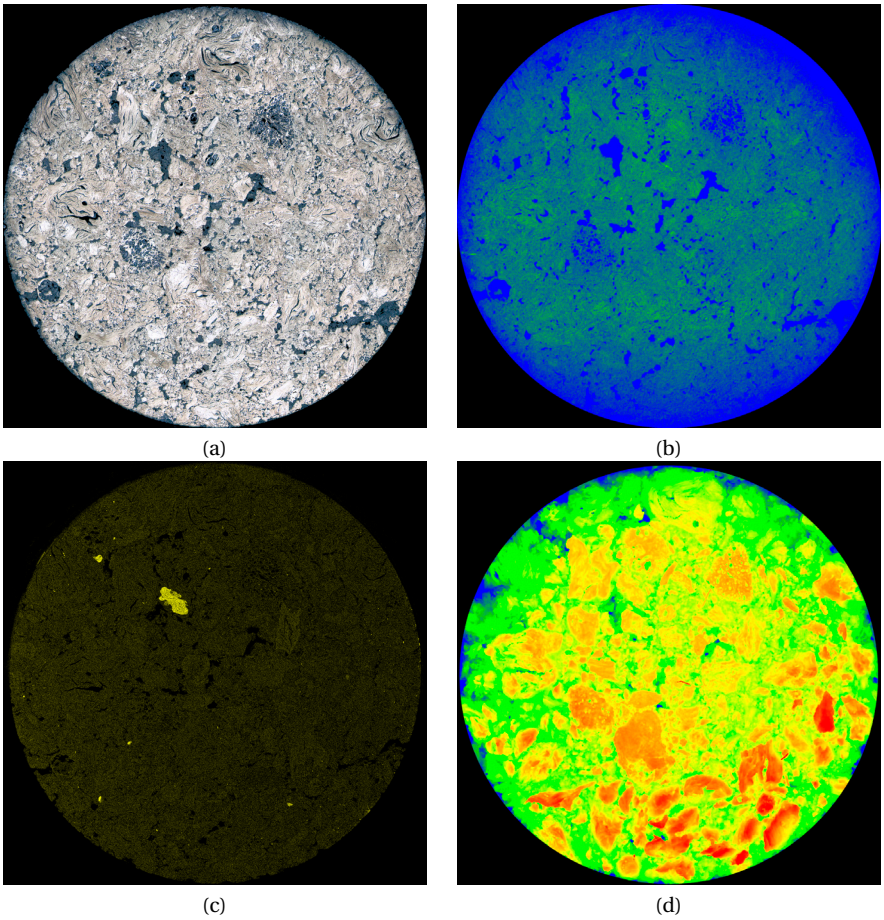

(a) (b) (c) (d)

Figure 3.5: Anode made of 100 % traditional anisotropic coke (0 % isotropic coke), sample 4. a) Confocal microscopy surface map before electrolysis, b) Confocal microscopy contour image of the surface before electrolysis, c) Sulfur map obtained by SEM/EDS, and d) Contour image of the surface after electrolysis.

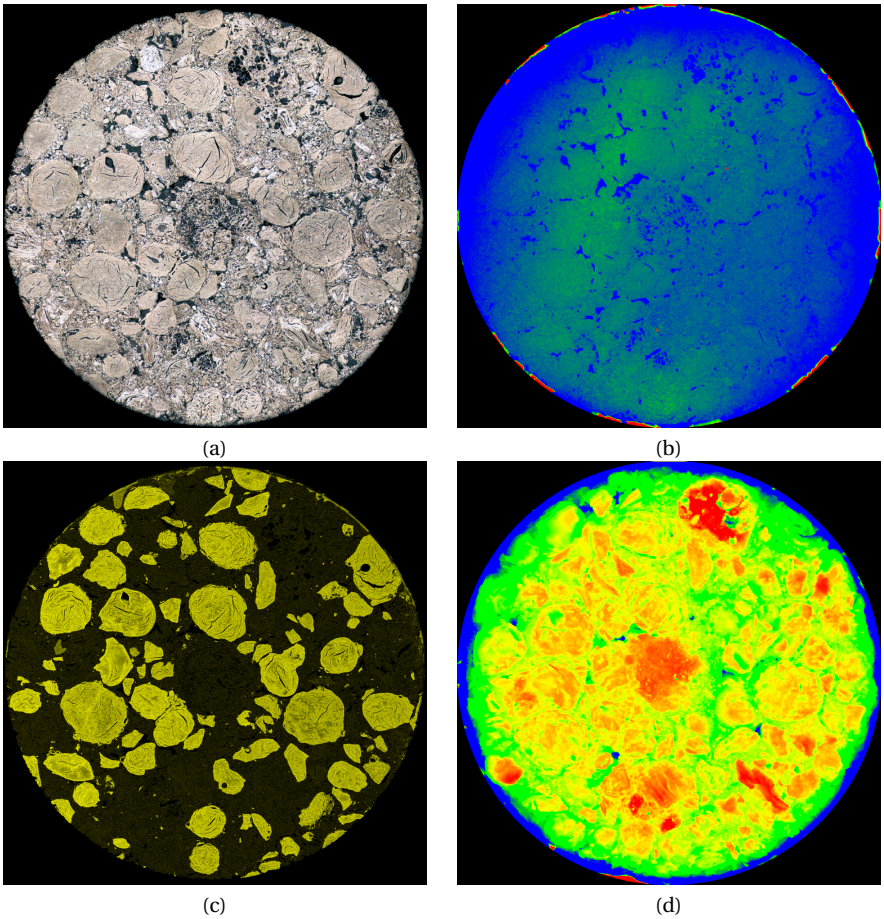

Figure 3.6: Anode made of 49.0 % isotropic coke, sample 1. a) Confocal microscopy surface map before electrolysis, b) Confocal microscopy contour image of the surface before electrolysis, c) Sulfur map obtained by SEM/EDS, and d) Contour image of the surface after electrolysis.

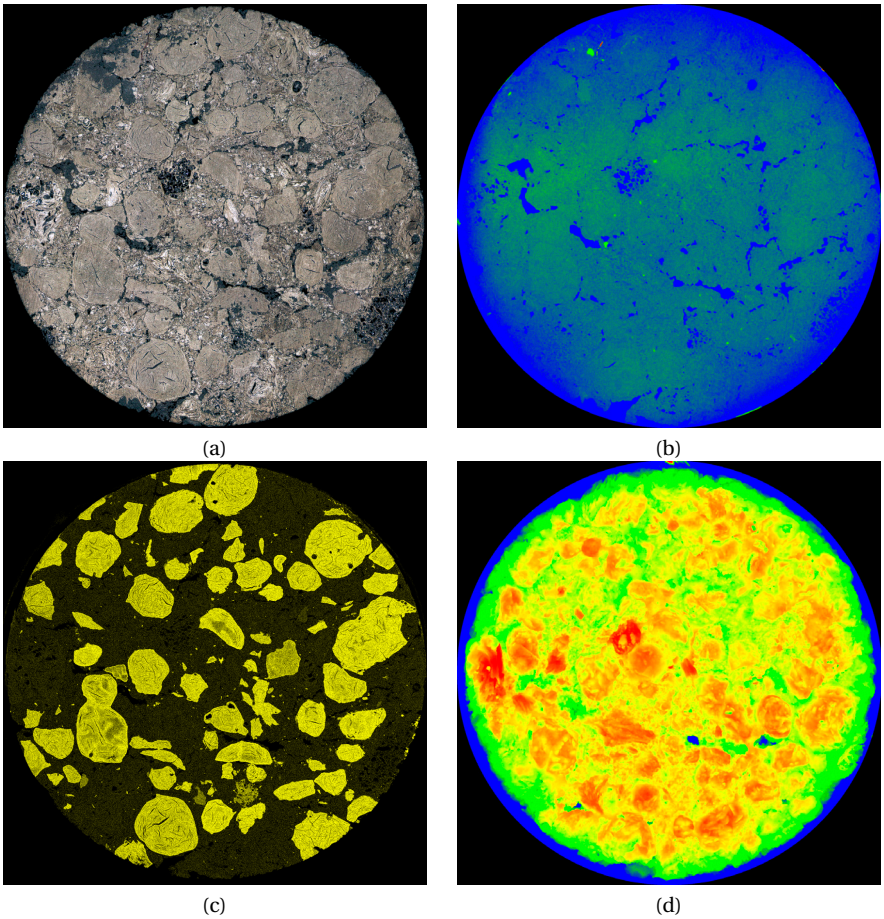

Figure 3.7: Anode made of 49.0 % isotropic coke, sample 2. a) Confocal microscopy surface map before electrolysis, b) Confocal microscopy contour image of the surface before electrolysis, c) Sulfur map obtained by SEM/EDS, and d) Contour image of the surface after electrolysis.

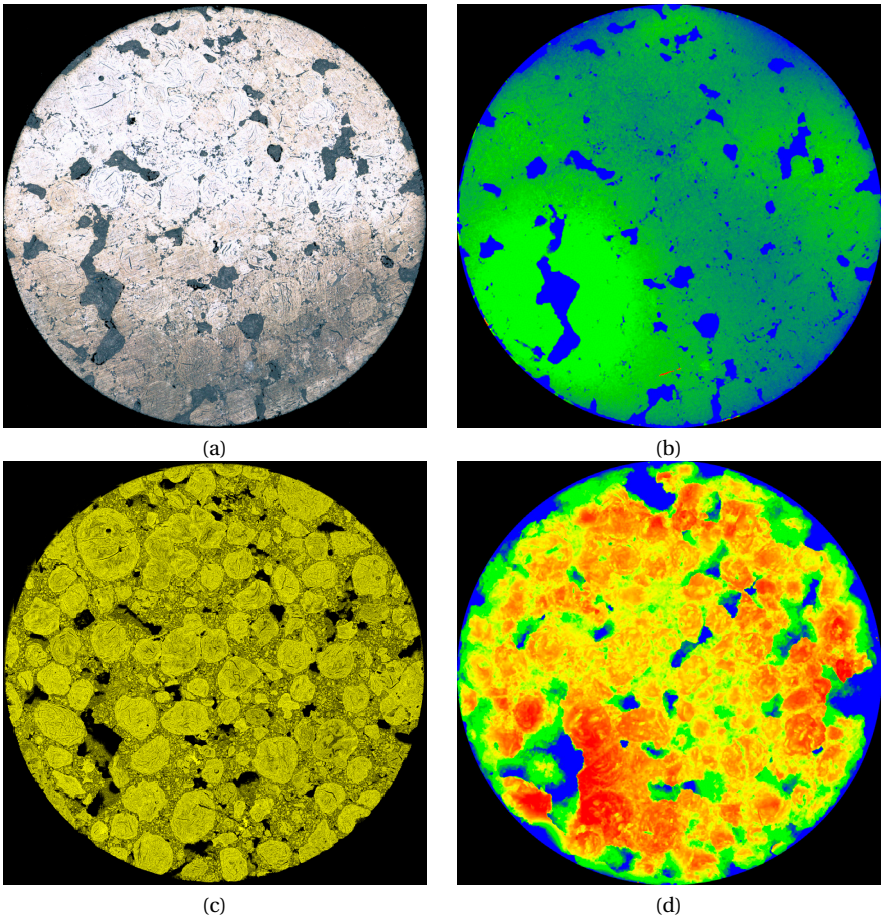

Figure 3.8: Anode made of 100 % isotropic coke, sample 1. a) Confocal microscopy surface map before electrolysis, b) Confocal microscopy contour image of the surface before electrolysis, c) Sulfur map obtained by SEM/EDS, and d) Contour image of the surface after electrolysis.

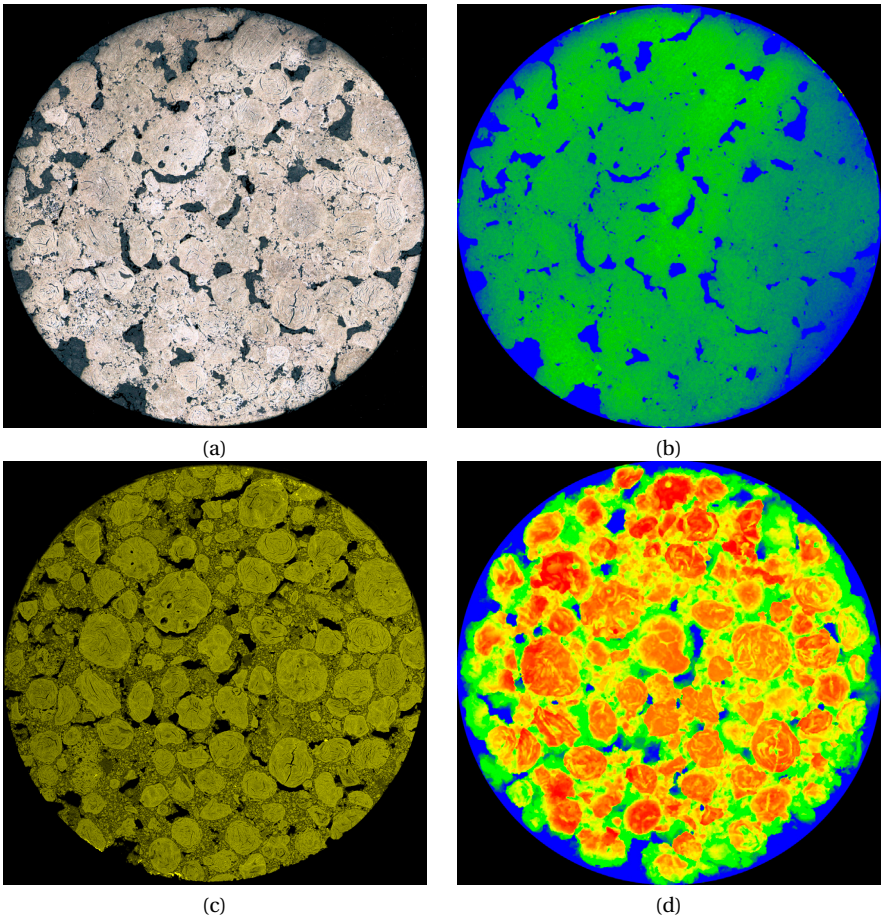

(a) (b) (c) (d)

Figure 3.9: Anode made of 100 % isotropic coke, sample 2. a) Confocal microscopy surface map before electrolysis, b) Confocal microscopy contour image of the surface before electrolysis, c) Sulfur map obtained by SEM/EDS, and d) Contour image of the surface after electrolysis.

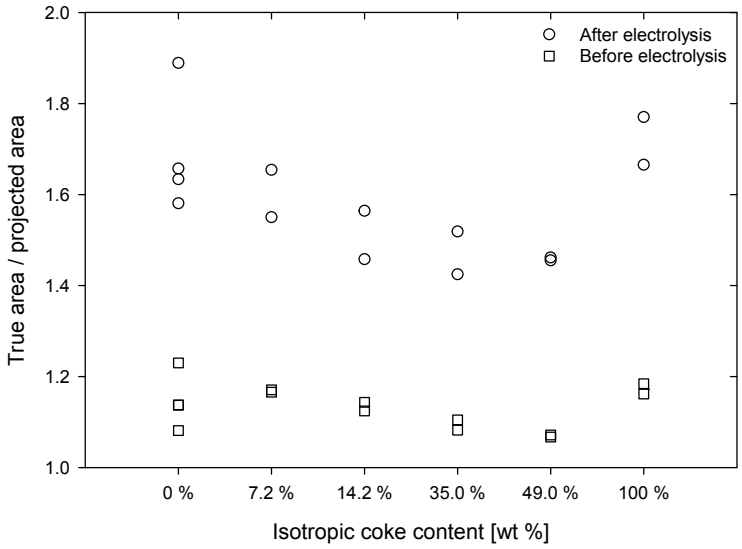

Figure 3.10: Ratio of true area over projected area obtained by using confocal microscopy on freshly cut samples ground with SiC paper down to P#4000 (squares) and electrolysed samples (circles) at 1.0 A/cm^2 for 25 mins.

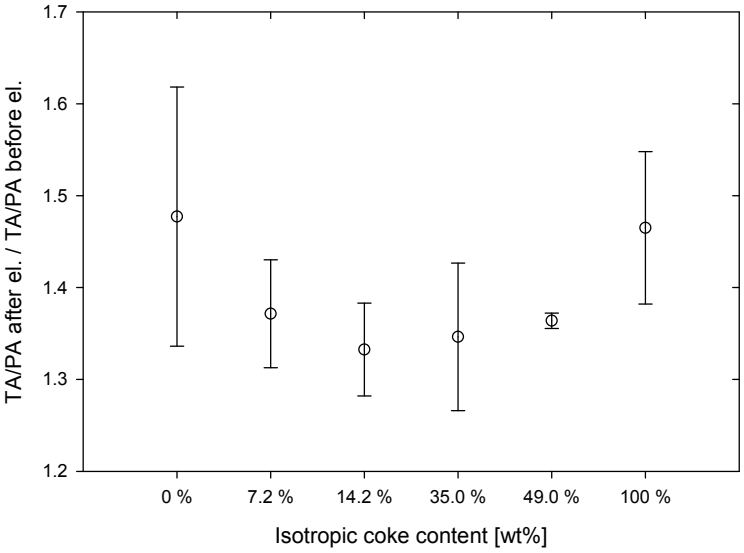

Figure 3.11: Average area increase between non electrolysed and electrolysed sample obtained by TA/PA measurements using confocal microscopy. Average results are given with one standard deviation.

3.3.3 X-Ray Computed Tomography

Figures 3.12-3.17 show CT images of cross-sections of all the test anodes. Two parallels of each anode is shown, before and after electrolysis at 1.0 A/cm^2 for 30 mins. One cross-section per anode sample is shown in the following to show some interesting features of the consumption of the anode surfaces after electrolysis. "Hot-pulling" of the anodes was done in order to avoid electrolyte penetration into pores after electrolysis was ended, and to create after electrolysis images that recreate the conditions at the anode/electrolyte interface during electrolysis. It is obvious that little electrolyte penetrates the pores of the anodes. Pores have to be concave for the electrolyte to wet the pore wall. This is for instance seen to the left in Figure 3.17 b). For comparison, the large, but more narrow pore to the upper right in Figure 3.17 a) was not penetrated by electrolyte. Several of the same features can be seen here as already discussed for the confocal microscopy images in Figures 3.2-3.9: "bubble" coke sticking out of the matrix coke and pitch after electrolysis for anodes containing anisotropic coke and the 100 % anode having a large amount of open porosity. For the blended anodes (7.2 %-49.0 %), a contrast difference is observed between isotropic and anisotropic coke particles. This is due to the difference in density between the coke particles; isotropic coke being denser than anisotropic coke.

Figures 3.15 and 3.16 show tomographs of cross-sections inside the 35.0 % and 49.0 % isotropic coke anodes. These images show significant cracking inside the anodes surrounding the isotropic coke particles, especially for the 49.0 % anode. This is due to the difference in coefficient of thermal expansion between the anisotropic and isotropic coke particles as indicated in Table 3.3, where a near linear increase in CTE is seen when isotropic coke is introduced into the anodes. In Figure 3.14 cracking around the isotropic coke grains is not visible. This suggests that there is a threshold of isotropic to anisotropic coke content in order for the anodes to sustain a strong structure without cracks. This threshold is somewhere between 14.2 % and 35.0 % isotropic coke. This is also in accordance with Edwards et al. [2], where a suggested threshold for isotropic coke in blends with more traditional anisotropic coke is set to 20 %. However, cracking problems in potrooms can be significantly reduced when increasing the coke grain to fines ratio [52]. This suggests that the exact threshold for isotropic cokes to anisotropic coke blends should be investigated further in terms of optimisation of the coke aggregate recipe.

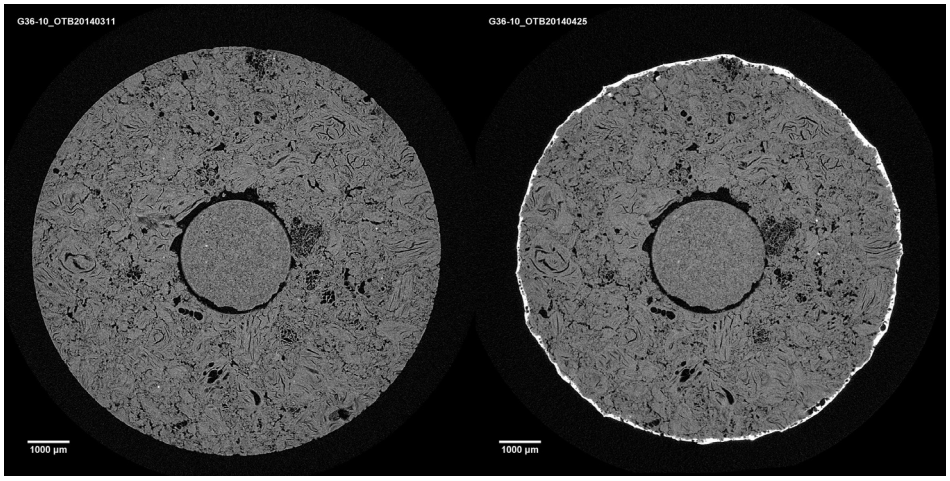

(a)

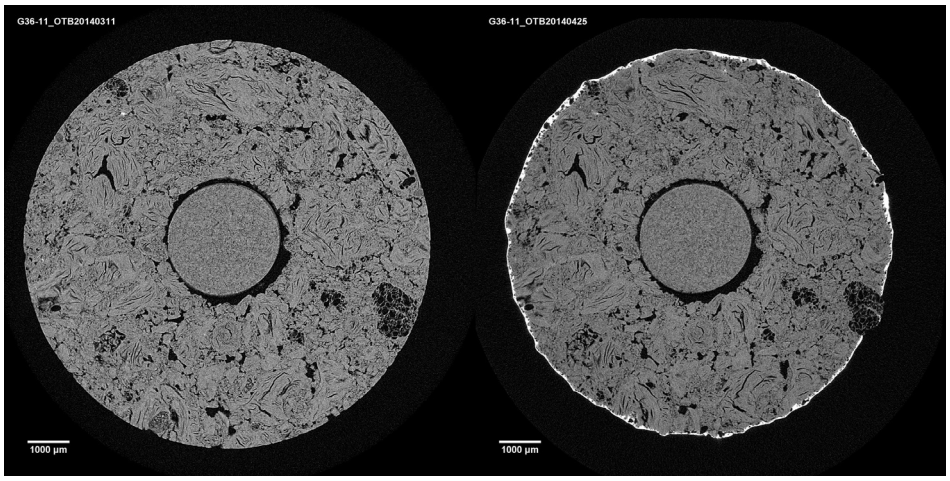

(b)

Figure 3.12: CT images of an interior cross-section of anodes before and after electrolysis. a) and b) show the anode made of 100 % anisotropic coke, parallels 1 and 2, respectively.

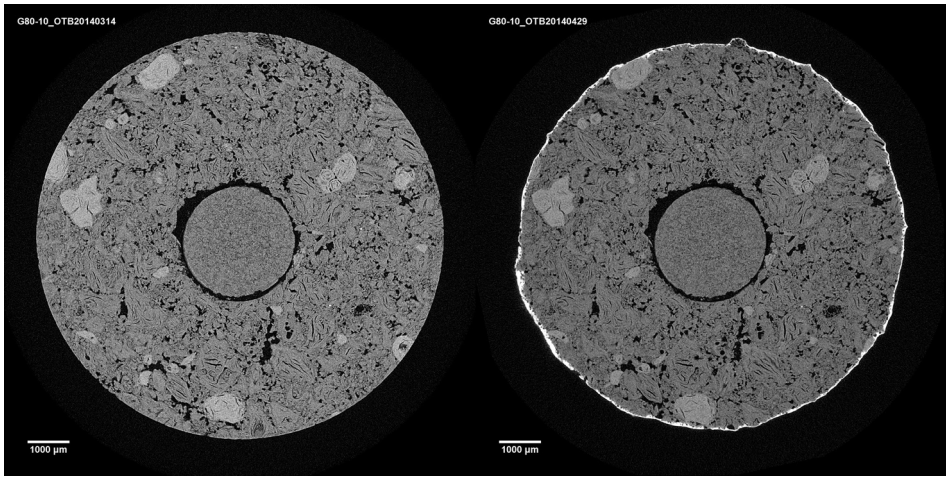

(a)

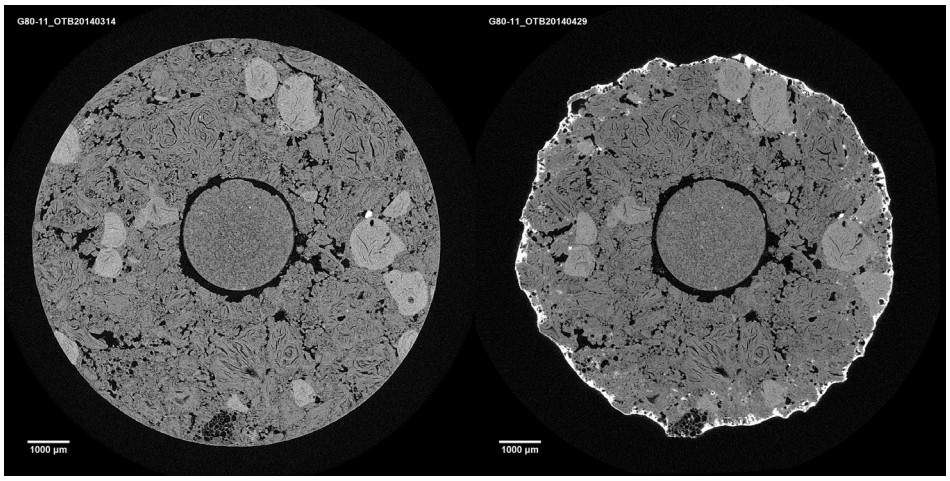

(b)

Figure 3.13: CT images of an interior cross-section of anodes before and after electrolysis. a) and b) show the anode made of 7.2 % isotropic coke, parallels 1 and 2, respectively.

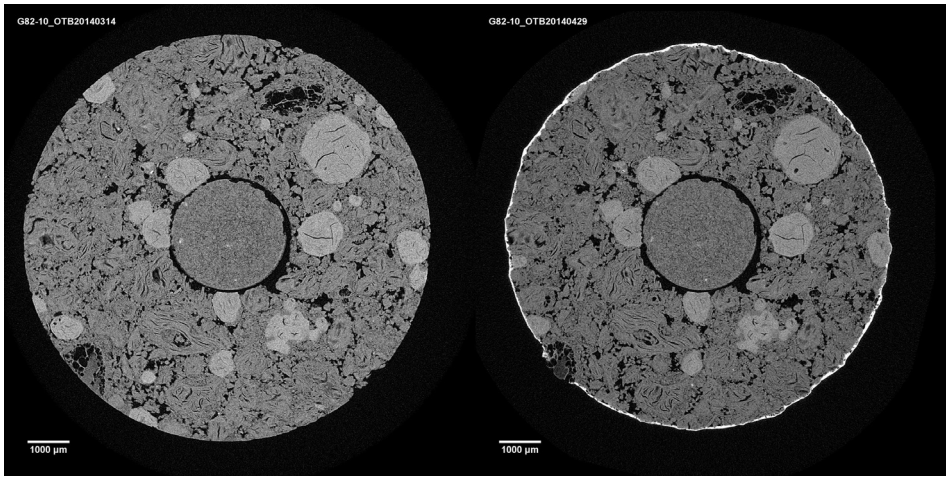

(a)

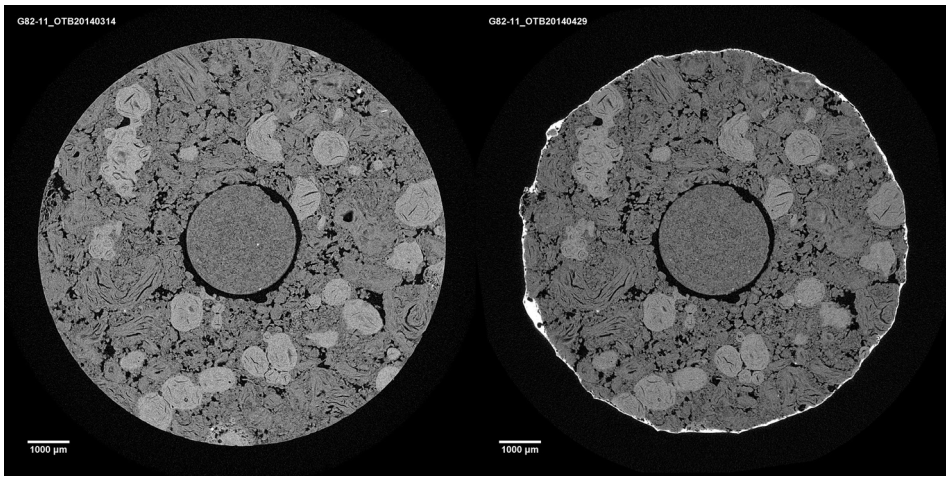

(b)

Figure 3.14: CT images of an interior cross-section of anodes before and after electrolysis. a) and b) show the anode made of 14.2 % isotropic coke, parallels 1 and 2, respectively.

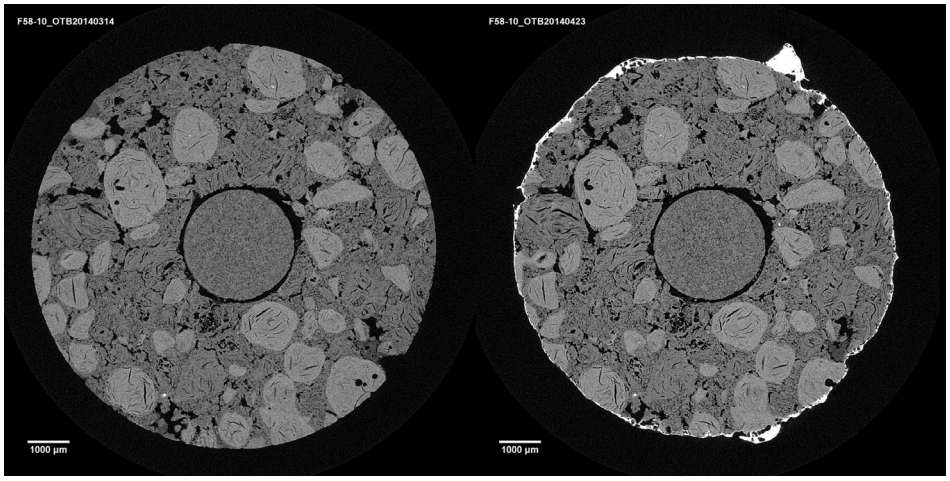

(a)

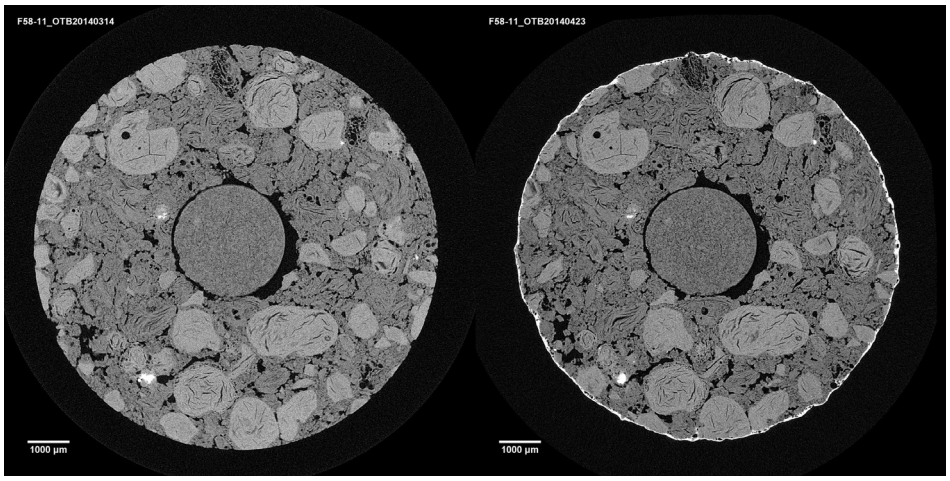

(b)

Figure 3.15: CT images of an interior cross-section of anodes before and after electrolysis. a) and b) show the anode made of 35.0 % isotropic coke, parallels 1 and 2, respectively.

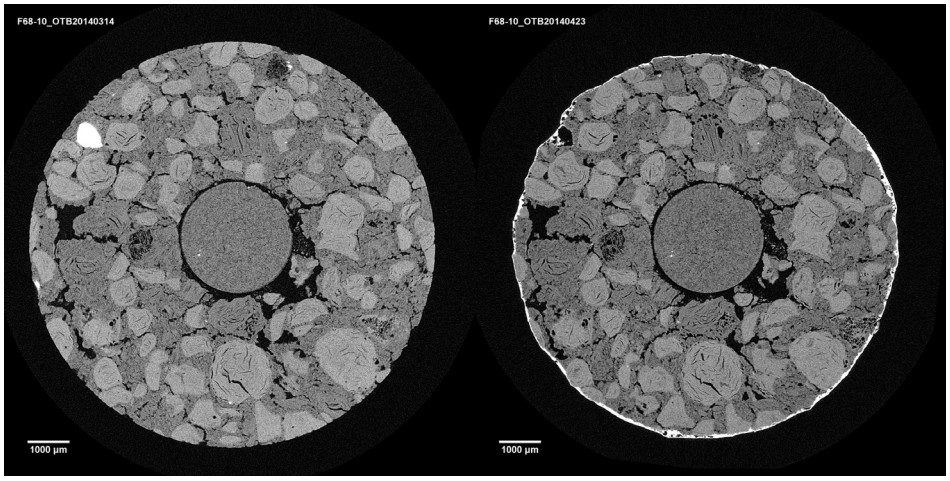

(a)

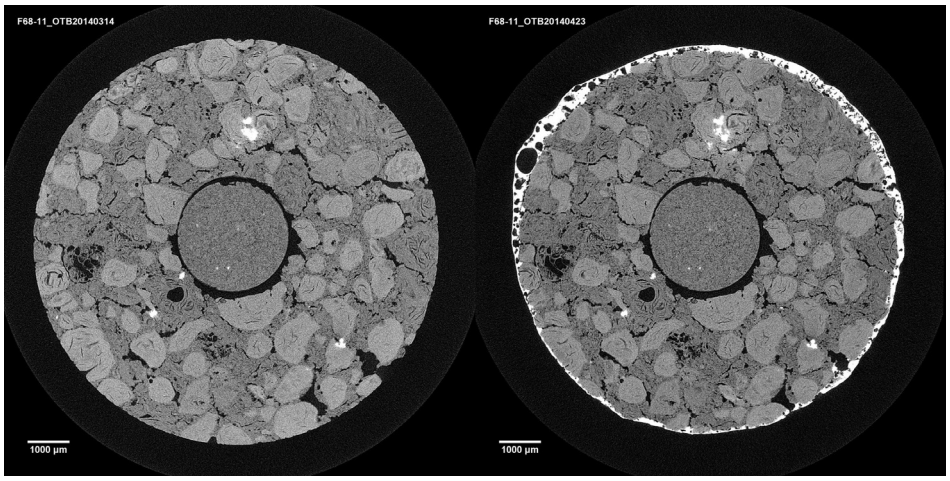

(b)

Figure 3.16: CT images of an interior cross-section of anodes before and after electrolysis. a) and b) show the anode made of 49.0 % isotropic coke, parallels 1 and 2, respectively.

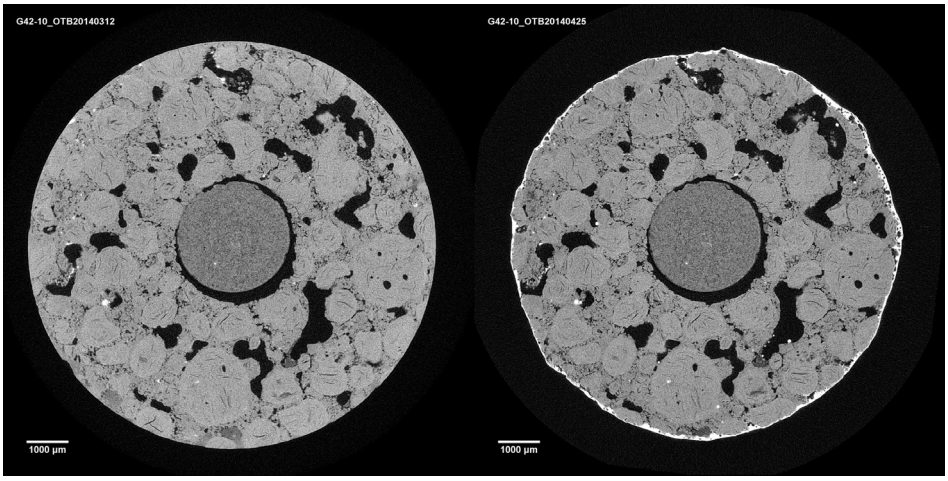

(a)

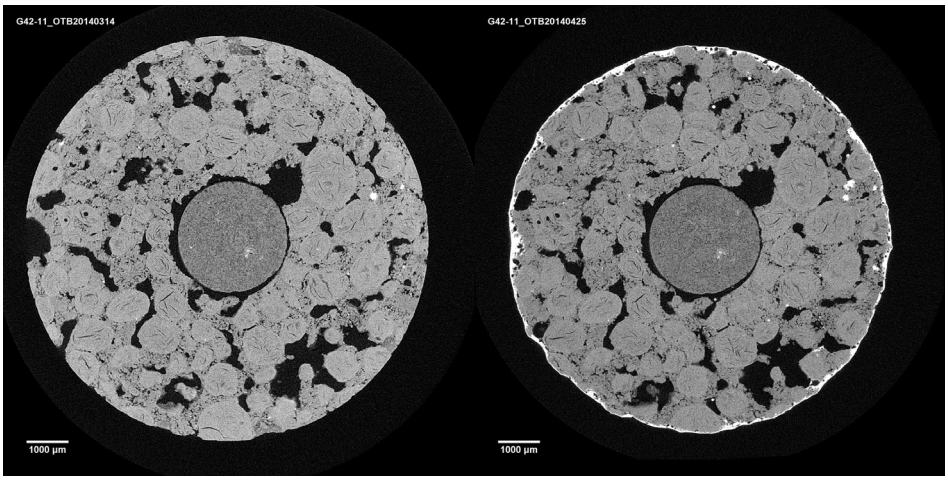

(b)

Figure 3.17: CT images of an interior cross-section of anodes before and after electrolysis. a) and b) show the anode made of 100 % isotropic coke, parallels 1 and 2, respectively.

3.3.4 Texture Analysis using Optical Microscopy

The mosaic index and fiber index relate to the fineness and alignment of optical domains, respectively, meaning that fiber index is a measure of the anisotropy and mosaic index is a measure of the fineness of the coke structure [43]. Figure 3.18 shows mosaic index and fiber index of the anodes varying in isotropic coke content. The fiber index is seen to decrease with increasing isotropic coke content in the anodes, while the mosaic index increases with increasing isotropic coke content. Generally, a high mosaic index correlates to a low fiber index.

Figure 3.19 shows examples of optical microscopy images that were used to extract the fiber and mosaic indexes. From the optical microscopy images a more disordered structure with more optical activity is seen in areas with anisotropic coke (Figure 3.19 a)). A finer, more ordered structure is visible for the isotropic coke grains (Figure 3.19 c)). The isotropic coke grains are optically inactive, meaning that no clear features are visible due to the fine-grained microtexture. This is also observed in [53, 54]. For the blended anode (Figure 3.19 b)), a clear contrast can be seen between isotropic coke grains an anisotropic coke grains due to the difference in microstructure.

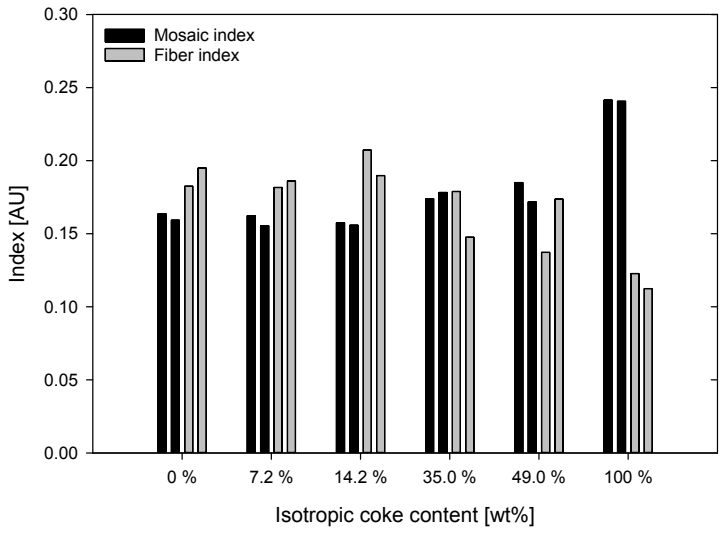

Figure 3.18: Mosaic index and fiber index of the anodes obtained by optical microscopy under polarised light. Measurements were performed on two parallels.

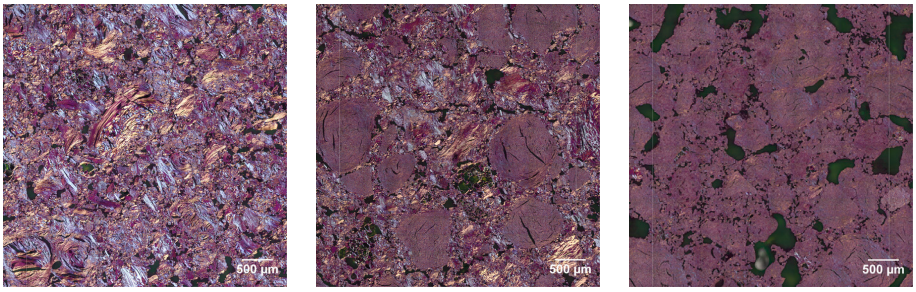

(a) (b) (c)

Figure 3.19: Optical microscopy images under polarised light of pilot anodes with a) 0 %, b) 35.0 % and c) 100 % isotropic coke content. The anode samples were mounted in epoxy and polished down to 1 μm.

3.3.5 Electrochemical Measurements

Figure 3.20 shows IR corrected polarisation curves of graphite and anodes with 0 wt%, 14.2 wt% and 100 wt% isotropic coke content. The polarisation curve was obtained by very slow cyclic voltammetry (0.1 V/s). Graphite is seen to have a higher potential corresponding to current density when comparing with anodes made from anisotropic and isotropic coke. This is in accordance with [18, 21, 27] and in accordance with the results obtained with chronopotentiometry in Figure 3.21.

Figure 3.21 shows overpotential reduction at 0.6 A/cm^2, 0.8 A/cm^2 and 1.0 A/cm^2 quoted relative to graphite. Two parallel samples of the entire anode series, including graphite, were run in each duplicate run except the first run, where the anodes with 35.0 wt% and 49.0 wt% isotropic coke content were excluded. In the figure average results from polarisation curves (slow sweep cyclic voltammetry at 0.1 V/s) at 0.6 A/cm^2, 0.8 A/cm^2 and 1.0 A/cm^2 with one standard deviation (n=4-6 from 3 duplicate runs) along with average values of chronopotentiometry results where 1.0 A/cm^2 was applied along with error bars for one standard deviation (n=6-8 from 4 duplicate runs). From Figure 3.21 it can be seen that the overpotential values are fairly similar for the 0 % and 7.2 % anode. For the 14.2 %, 35.0 %, 49.0 % anodes and to a certain extent the 100 % anode, lower reaction overpotential, η'_r, was found for increasing isotropic coke content. Compared to the 0 % anode a reduction in overpotential of 15-20 mV is seen for anodes blended with ≥14.2 % isotropic coke. A decrease in overpotential when making anodes from isotropic coke has also been reported elsewhere [18, 21, 23, 27]. The decrease in overpotential may be attributed to the increased amount of metal impurities in isotropic coke (*cf.* Table 3.2 and the increased amount of edge sites found for isotropic coke in [21]. Increased amounts of certain metal oxides (e.g. Fe, Mg, Ca, Li, Na) [13] and edge sites will give a higher concentration of active sites on the reacting anode surface.

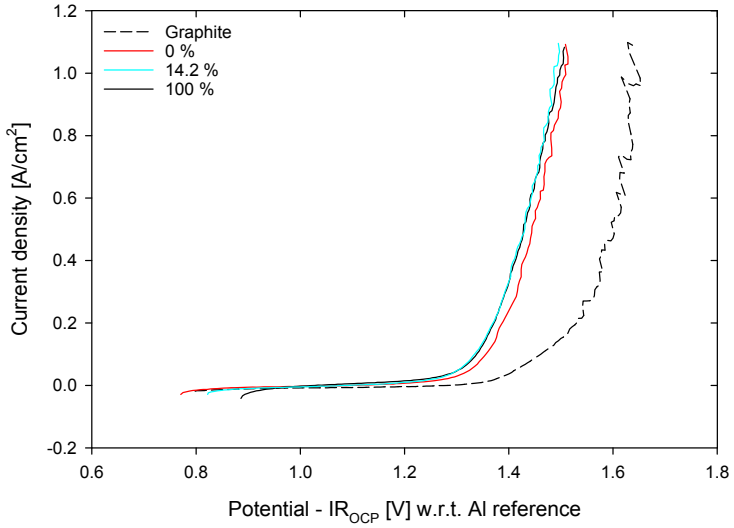

Figure 3.20: IR corrected polarisation curves of graphite and anodes with 0 wt%, 14.2 wt% and 100 wt% isotropic coke content. The second forward scan of three consecutive forward and backward scans is shown for each anode.

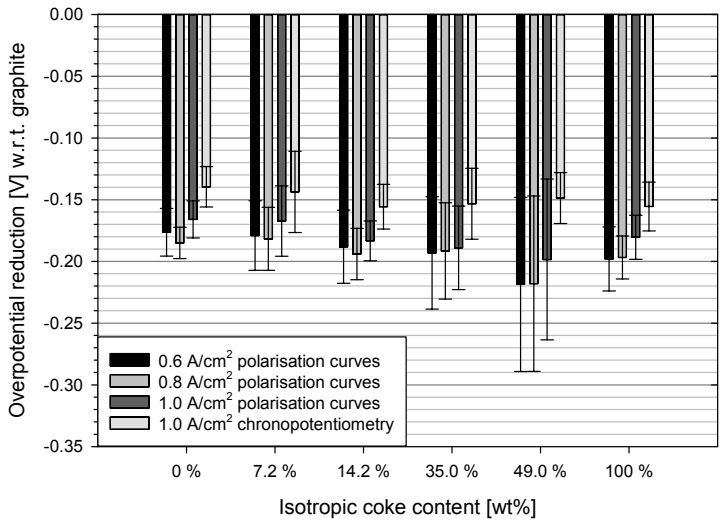

Figure 3.21: Anode overpotential reduction at 0.6 A/cm^2, 0.8 A/cm^2 and 1.0 A/cm^2 recorded by polarisation curves and 1.0 A/cm^2 recorded by chronopotentiometry for anodes varying in isotropic coke content quoted relative to graphite. To the right, average overpotential reduction with error bars obtained at 1.0 A/cm^2 by chronopotentiometry and polarisation curves. The error bars show one standard deviation where n=4-8 from 3-4 duplicate runs.

Nyquist plots with impedance raw data and modelled data with equivalent electrical circuits LR(CR) and LR(Q(R(LR))) are shown for the anodes in Figures 3.22 and 3.23. The two figures show impedance data for one parallel for two consecutive duplicate runs with new electrolytes and reference electrodes. In total two parallel anodes were investigated per duplicate runs. The impedance data was recorded at 1.5 V non-IR corrected. From Figures 3.22 and 3.23 an inductive loop at the lower frequencies can be seen. This is attributed to the charge transfer reaction as described in e.g. Equations 3.6 and 3.8. The vertical part of the curve at high frequencies was used to extract the double layer capacitance from the LRC-circuit as described earlier. In this frequency range it is assumed that no Faradaic reactions take place. Since these experiments were run in an electrolyte saturated in Al_2O_3 it is also assumed that diffusion processes as described in Equation 3.5 are negligible and that the diffusion double layer is small. Hence, it is assumed that the reaction is charge transfer controlled. The reason why the polarization resistance is so different between run 1 and run 2 is due to a difference in current density as can be seen in Tables D.5-D.6 in Appendix D. The current density difference affects the resistance to charge transfer, R_{CT}, obtained by modelling of the LR(Q(R(LR))) circuit. The difference in current density is due to slight variations in the in-house produced reference electrodes between runs.

Figure 3.24 shows average double layer capacitance, C_{dl} (n = 3), and effective capacitance, C_{eff} (n = 4), for all parallel anodes for the two duplicate runs. For the first parallel anodes, second duplicate run, the C_{dl} parameters was considered anomaly, due to poor curve fit, explaining why n = 3 for C_{dl}. The effective capacitance was calculated using Equation 3.12 and parameters given in Appendix D. The high frequency C_{dl} was calculated using the LRC circuit at high frequencies. The values for the capacitances are within the ranges reported previously by Thonstad [34], yet slightly lower than that reported elsewhere [19, 32, 33, 35]. The capacitance values for graphite are also slightly lower than that reported previously. This is most likely due to inhomogeneity in the materials used. C_{eff} and $C_{dl,LRC}$ are very similar to each other, and they are considered more reliable. The LR(CR) model gives poorer curve fit to the obtained experimental results, and this is reflected in an overestimation of the capacitances reported. The capacitances are similar for the 0 %-35.0 % anodes within the standard deviations given. However, from Figure 3.24 it is evident that both the 49.0 % and 100 % anodes show a higher capacitance than the remaining pilot anode series. The capacitance values were then corrected for real surface area obtained by confocal microscopy (*cf.* Figure 3.10) in order to verify that the capacitance difference seen for the 49.0 % and 100 % anodes are not merely due to real area differences after electrolysis. Figure 3.25 shows capacitance over true area/projected area *vs.* isotropic coke content after electrolysis. An increase in capacitance is still seen after correction for the ratio of true area over projected area. This implies that the capacitance increase seen for the 49.0 % and 100 % anodes, but also to a certain extent the 35.0 % anode, are due to a difference in surface wetting properties of these anodes towards the electrolyte. At 49.0 % isotropic coke, the effect of isotropic coke on the electrochemical reactivity is more pronounced. The isotropic coke used in this study is more reactive and better wetted by the electrolyte compared with the anisotropic coke. This was also found in [21, 23, 36].

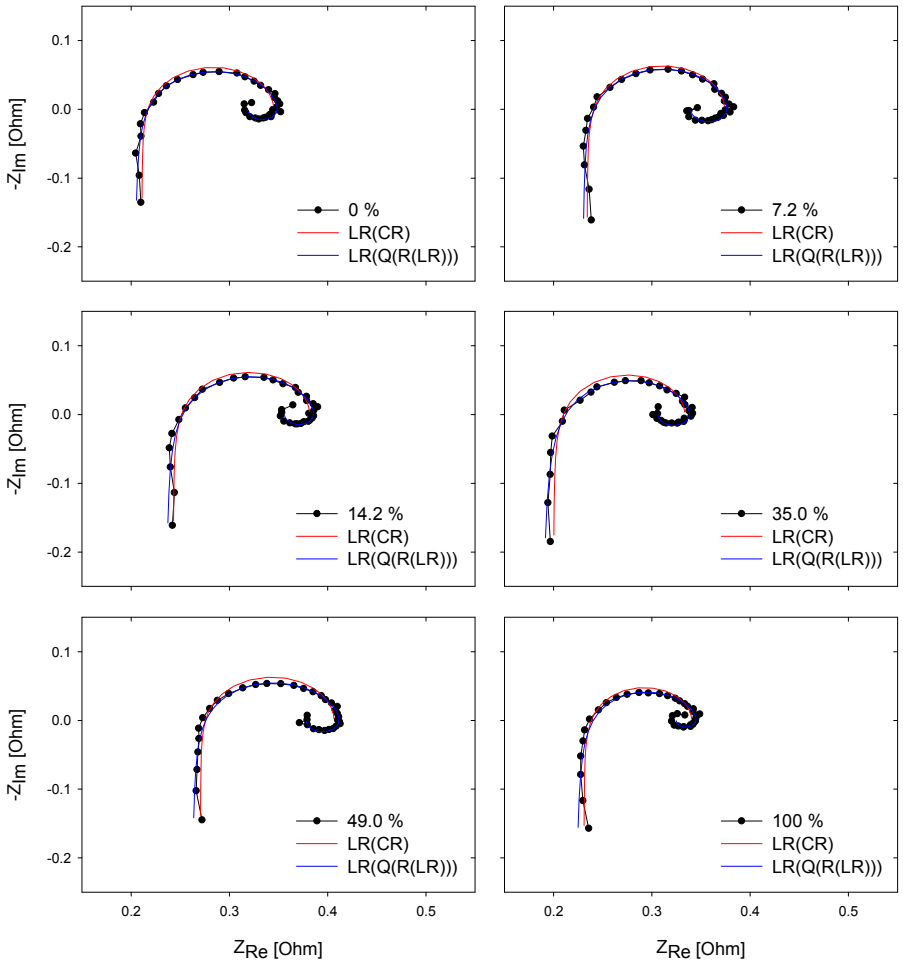

Figure 3.22: Raw data from EIS at 1.5 V (non-IR corrected), LR(CR) and LR(Q(R(LR))) modelled circuits for the corresponding raw data for anodes varying in isotropic coke content, run 1, parallel 1.

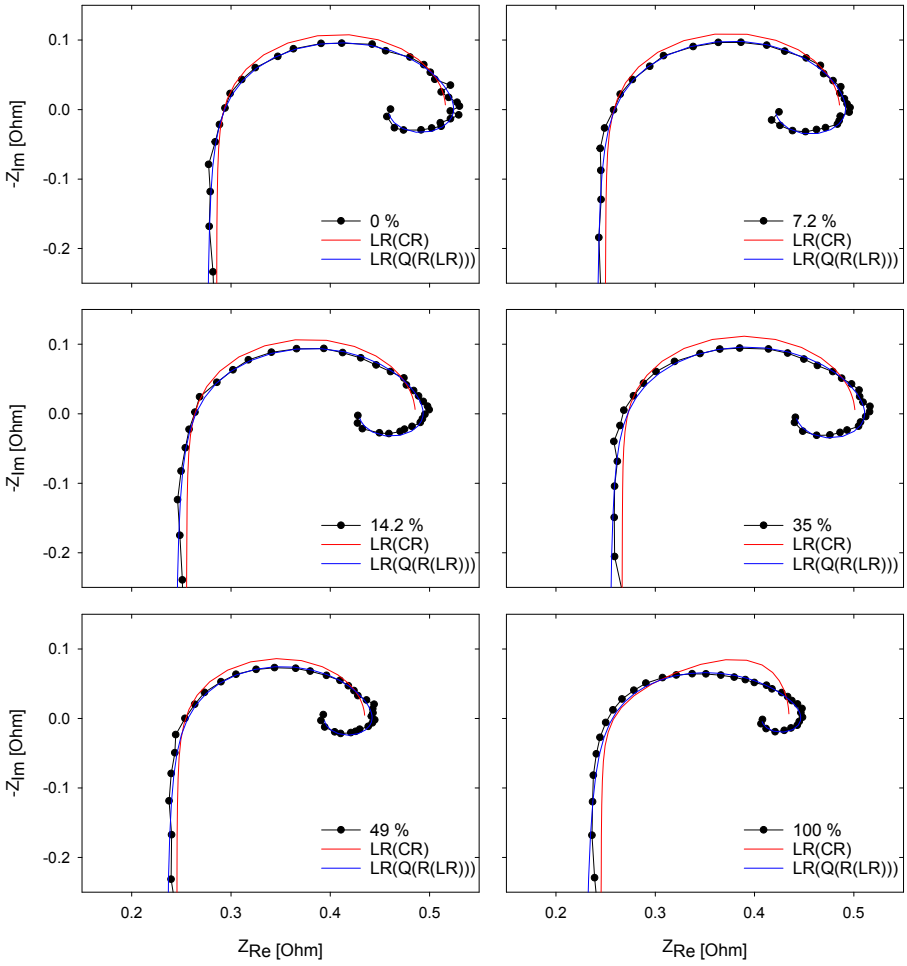

Figure 3.23: Raw data from EIS at 1.5 V (non-IR corrected), LR(CR) and LR(Q(R(LR))) modelled circuits for the corresponding raw data for anodes varying in isotropic coke content, run 2, parallel 1.

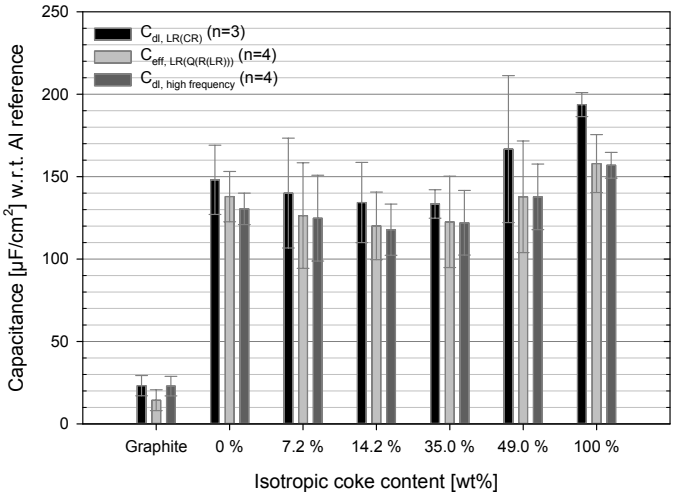

Figure 3.24: Average double layer capacitance extracted from LR(CR), average calculated effective capacitance from LR(Q(R(LR))) and average double layer capacitance from the LRC circuit at high frequencies, along with one standard deviation. The impedance data was recorded at 1.5 V w.r.t. Al reference, non-IR corrected.

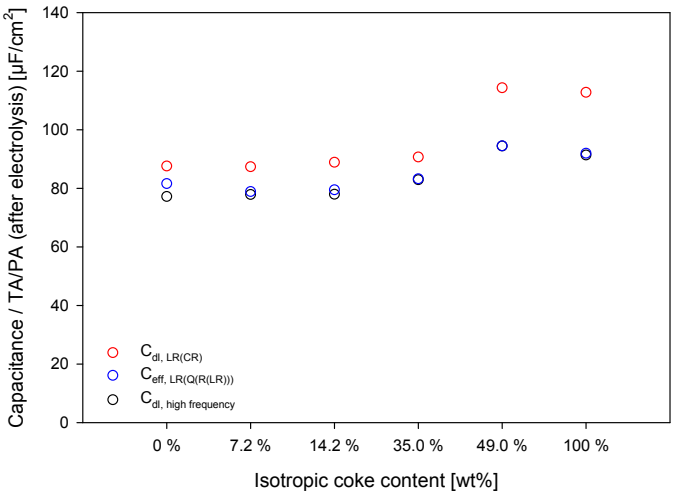

Figure 3.25: Capacitance modelled in three different ways ($C_{dl,LR(CR)}$, $C_{eff,LR(Q(R(LR)))}$ and $C_{dl,high\,frequency}$ over true area/projected area after electrolysis from confocal microscopy *vs.* isotropic coke content.

3.4 Conclusion

The effect of various blending ratios of isotropic coke to anisotropic coke in carbon anodes have been investigated both by imaging and electrochemical techniques. By imaging techniques like CT, cracking around isotropic coke grains could be observed for blended anodes containing ≥35.0 % isotropic coke. Sulfur was found by EDS to be distributed in carbon rich coke grains, and not as metal sulphides. For isotropic coke, sulfur was visible throughout all coke grains.

A gradual decrease in reaction overpotential was observed as isotropic coke was introduced into the anodes. Capacitance measurements also showed an increased electrochemical reactivity and increased electrochemically wetted surface area towards the electrolyte for anodes containing ≥49.0 % isotropic coke. It is reasonable to believe that metal oxides and increased amount of edge sites for isotropic coke is affecting the electrochemical performance of the anodes.

Confocal microscopy images taken before and after electrolysis showed that pitch is the more reactive phase in anodes, and are faster consumed than coke particles. Both confocal microscopy and X-ray computed tomography (CT) have been used to show that isotropic and anisotropic coke particles are consumed at approximately the same rate. CT images also showed that even large pores are not penetrated by the electrolyte after electrolysis.

This work shows that using isotropic coke in carbon anodes for the aluminium industry works well and can even be beneficial in terms of electrochemical performance. However, there is a threshold to the maximum amount of isotropic coke that can be used in anodes. This threshold is due to the cracks that will occur due to the difference in coefficient of thermal expansion between isotropic and anisotropic coke. This work has shown that the threshold is somewhere between 14.2 % and 35.0 % isotropic coke. The aluminium industry also has to take the increased amount of metal impurities that follow the isotropic coke, into account when blending this coke in anodes. These metal impurities report to the metal and have to either be removed or tolerated within the specifications of the metal. Increased sulfur content will also affect the amount of SO_2 produced in the smelters and without sufficient wet scrubbing, it will be difficult to meet authority regulations for maximum release of SO_2 to the atmosphere.

Acknowledgement

The work was financed by Hydro Aluminium and The Research Council of Norway through the research program called “HAL Ultra Performance Aluminium Cell”. Thanks are due to Aksel Alstad at the NTNU workshop for fabricating the experimental parts. Cristian Torres Rodriguez, Stein Rørvik, Julian Tolchard and technicians at Hydro Aluminium Årdalstangen also deserve a great thank you for help with various experimental techniques.

References

[1] H. Kvande and W. Haupin. “Cell Voltage in Aluminum Electrolysis: A Practical Approach”. *JOM* (2000), pp. 31–37.

[2] L. Edwards, N. Backhouse, H. Darmstadt, and M.-J. Dion. “Evolution of anode grade coke”. *Light Metals* (2012), pp. 1207–1212.

[3] L. Edwards. “Evolution of Anode Grade Quality and Calcining Technology”. *Proc. 10th AASTC* (2011). Ed. by B. Welch, G. Stephens, J. Metson, and M. Skyllas-Kazacos.

[4] L. Edwards, F. Vogt, M. Robinette, R. Love, J.A. Ross, M. McClung, R.J. Roush, and W. Morgan. “Use of Shot Coke as an Anode Raw Material”. *Light Metals* (2009), pp. 985–990.

[5] A. Gagnon, N. Backhouse, H. Darmstadt, E. Ryan, L. Dyer, and D.G. Dixon. “Impurity Removal from Petroleum Coke”. *Light Metals* (2013), pp. 1057–1062.

[6] S.J. Lindsay. “Raw Material Impurities and the Challenge Ahead”. *Light Metals* (2013), pp. 5–8.

[7] K.N. Tran, A.J. Berkovich, A. Tomsett, and S.K. Bhatia. “Influence on Sulfur and Metal Microconstituents on the Reactivity of Carbon Anodes”. *Energy Fuels* (2009), pp. 1909–1924.

[8] M.A. Rhamdhani, J.F. Grandfield, A. Khaliq, and G. Brooks. “Management of Impurities in Cast House with Particular Reference to Ni and V”. *Light Metals* (2013), pp. 33–38.

[9] C.T. Leach, D.G. Brooks, and R.E. Gehlbach. “Correlation of Coke Properties, Anode Properties, and Carbon Consumption”. *Light Metals* (1997), pp. 481–488.

[10] C. Coney, L. Crabtree, J. Gavin, W. Marcrum, A. Weber, and L. Edwards. “Impact of Higher Vanadium Levels on Smelter Operations”. *Light Metals* (2013), pp. 21–25.

[11] W.E. Haupin. “Electrochemistry of the Hall-Heroult Process for Aluminium Smelting”. *J. Chem. Educ.* (1983), pp. 279–282.

[12] K. Grjotheim and H. Kvande. *Introduction to Aluminium Electrolysis*. 2nd. Dusseldorf: Aluminium-Verlag, 1993.

[13] J. Thonstad, P. Fellner, G.M. Haarberg, J. Hives, H. Kvande, and Å. Sterten. *Aluminium Electrolysis: Fundamentals of the Hall-Heroult Process*. 3rd. Dusseldorf: Aluminium-Verlag, 2001.

[14] B. Gilbert, G. Mamantov, and G.M. Begun. “Raman Spectra of Al_2O_3 Solutions in Molten Cryolite and Other Aluminum Fluoride Containing Melts”. *Inorg. Nucl. Chem. Letters* (1976), pp. 415–423.

[15] T. Førland and S.K. Ratkje. “Aluminium-Oxygen Containing Species in Fluoride Melts”. *Acta. Chem. Scand.* (1973), pp. 1883–1890.

[16] T. Eidet. “Reactions on carbon anodes in aluminium electrolysis”. PhD thesis. Norwegian University of Science and Technology, 1997.

[17] Å. Sterten. “Structural Entities in NaF-AlF_3 Melts Containing Alumina”. *Electrochim. Acta* (1980), pp. 1673–1677.

[18] G.S. Picard, E.C. Prat, Y.J. Bertaud, and M.J. Leroy. “Evidencing the Electrochemical Mechanism at Carbon/Bath Interface by Means of Impedance Measurement:

An Improved Approach to the Aluminum Reduction Process". *Light Metals* (1987), pp. 507–517.

[19] A. Kisza, J. Thonstad, and T. Eidet. "An Impedance Study of the Kinetics and Mechanism of the Anodic Reaction on Graphite Anodes in Saturated Cryolite-Alumina Melts". *J. Electrochem. Soc.* (1996), pp. 1840–1847.

[20] A. Kisza, J. Kazmierczak, J. Thonstad, T. Eidet, and J. Hives. "The Kinetics and Mechanism of the Electrode Reactions in Aluminium Electrolysis". *Light Metals* (1999), pp. 423–429.

[21] R.J. Thorne, C. Sommerseth, A.P. Ratvik, S. Rørvik, E. Sandnes, L.P. Lossius, H. Linga, and A.M. Svensson. "Correlation between Coke Type, Microstructure and Anodic Reaction Overpotential in Aluminium Electrolysis". *J. Electrochem. Soc.* (2015), E296–E306.

[22] R.J. Thorne, C. Sommerseth, A.P. Ratvik, S. Rørvik, E. Sandnes, L.P. Lossius, H. Linga, and A.M. Svensson. "Bubble Evolution and Anode Surface Properties in Aluminium Electrolysis". *J. Electrochem. Soc.* (2015), E104–E114.

[23] C. Sommerseth, R.J. Thorne, A.P. Ratvik, E. Sandnes, L.P. Lossius, H. Linga, and A.M. Svensson. "Electrochemical Reactivity and Wetting Properties of Anodes Made from Anisotropic and Isotropic Cokes". *Light Metals* (2016), In press.

[24] J.A. Leistra and P.J. Sides. "Voltage Components at Gas Evolving Electrodes". *J. Electrochem. Soc.* (1987), pp. 2442–2446.

[25] J.A. Leistra and P.J. Sides. "Hyperpolarization at gas evolving electrodes-II. Hall-Heroult electrolysis". *Electrochim. Acta* (1988), pp. 1761–1766.

[26] J.A. Leistra and P.J. Sides. "Anode Polarization in the Hall Cell". *Light Metals* (1986), pp. 473–478.

[27] R.J. Thorne, C. Sommerseth, A.M. Svensson, E. Sandnes, L.P. Lossius, H. Linga, and A.P. Ratvik. "Understanding Anode Overpotential". *Light Metals* (2014), pp. 1213–1217.

[28] T.S. Sørensen and S. Kjelstrup. "A Two Electron Process Producing CO and a Four Electron Process Producing CO_2 during Aluminium Electrolysis". *Light Metals* (1999), pp. 415–422.

[29] R. Farr-Wharton, B.J. Welch, R.C. Hannah, R. Dorin, and H.J. Gardner. "Chemical and Electrochemical Oxidation of Heterogeneous Carbon Anodes". *Electrochim. Acta* (1980), pp. 217–221.

[30] T.A. Aarhaug, O.S. Kjos, H. Gudbrandsen, A. Ferber, and A.P. Ratvik. "Evaluation of Gas Composition from Laboratory Scale Electrolysis Experiments with Anodes of Different Sulphur Contents". *Light Metals* (2016), In press.

[31] O.S. Kjos, T.A. Aarhaug, E. Skybakmoen, and A. Solheim. "Studies of Perfluorocarbon Formation on Anodes in Cryolite Melts". *Light Metals* (2012), pp. 623–626.

[32] S. Jarek and J. Thonstad. "Wetted Surface Area and Polarization Potential of Carbon Anodes in Cryolite-Alumina Melts". *Light Metals* (1987), pp. 399–407.

[33] S. Jarek and J. Thonstad. "Double-layer capacitance and polarization potential of baked carbon anodes in cryolite-alumina melts". *J. Appl. Electrochem.* (1987), pp. 1203–1212.

[34] J. Thonstad. "The Electrode Reaction on the C, CO_2 Electrode in Cryolite-Alumina Melts-II. Impedance Measurements". *Electrochim. Acta* (1970), pp. 1581–1595.

[35] S. Jarek and Z. Orman. “The Faradaic Impedance of the Carbon Anode in Cryolite-Alumina Melt”. *Electrochim. Acta* (1985), pp. 341–345.
[36] W. Gebarowski, C. Sommerseth, A.P. Ratvik, E. Sandnes, L.P. Lossius, H. Linga, and A.M Svensson. “Interfacial Boundary between Carbon Anodes and Molten Salt Electrolyte”. *Light Metals* (2016), In press.
[37] J. Thonstad. “Double layer capacity of graphite in cryolite-alumina melts and surface area changes by electrolyte consumption of graphite and baked carbon”. *J. Appl. Electrochem.* (1973), pp. 315–319.
[38] N.R. Laine, F.J. Vastola, and P.L. Walker Jr. “The Importance of Active Surface Area in the Carbon-Oxygen Reaction”. *J. Phys. Chem.* (1963), pp. 2030–2034.
[39] C.E. Banks, T.J. Davies, G.G. Wildgoose, and R.G. Compton. “Electrocatalysis at graphite and carbon nanotube modified electrodes: edge-plane sites and tube ends are the reactive sites”. *Chem. Commun.* (2004), pp. 829–841.
[40] J. Thonstad. “The Electrode Reaction on the C, CO_2 Electrode in Cryolite-Alumina Melts-I. Steady State Measurements”. *Electrochim. Acta* (1970), pp. 1569–1580.
[41] L.P. Lossius, I. Holden, and H. Linga. “The Equivalent Temperature Method for Measuring the Baking Level of Anodes”. *Light Metals* (2006), pp. 609–613.
[42] C. Sommerseth, R.J. Thorne, S. Rørvik, E. Sandnes, A.P. Ratvik, L.P. Lossius, H. Linga, and A.M. Svensson. “Spatial Methods for Characterising Carbon Anodes for Aluminium Production”. *Light Metals* (2015), pp. 1141–1146.
[43] S. Rørvik, M. Aanvik, M. Sørlie, and H.A. Øye. “Characterization of Optical Texture in Cokes by Image Analysis”. *Light Metals* (2000), pp. 549–554.
[44] D.A. Harrington and B.E. Conway. “ac Impedance of Faradaic Reactions Involving Electrosorbed Intermediates - I. Kinetic Theory”. *Electrochim. Acta* (1987), pp. 1703–1712.
[45] M.E. Orazem and B. Tribollet. *Electrochemical Impedance Spectroscopy*. 1st. New Jersey: Wiley, 2008.
[46] M. Orazem, I. Frateur, B. Tribollet, V. Vivier, S. Marcelin, N. Pebere, A.L. Bunge, E.A. White, D.P. Riemer, and M. Musiani. “Dielectric Properties of Materials Showing Constant-Phase-Element (CPE) Impedance Response”. *J. Electrochem. Soc.* (2013), pp. C215–C225.
[47] L.P. Lossius, M. Lubin, L. Edwards, and J. Wyss. “Relationships between Coke Properties and Anode Properties - Round Robin 19”. *Light Metals* (2013), pp. 1183–1188.
[48] M. Jensen, T.B. Pedersen, and K. Kalgraf. “Bubble Noise from Söderberg Pots”. *Light Metals* (2007), pp. 353–356.
[49] L.P. Lossius, K.J. Neyrey, and L. Edwards. “Coke and Anode Desulfurization Studies”. *Light Metals* (2008), pp. 881–886.
[50] H. Al-Haj-Ibrahim and B.I. Morsi. “Desulfurization of Petroleum Coke: A Review”. *Ind. Eng. Chem. Res.* (1992), pp. 1835–1840.
[51] L. Edwards, K.J. Neyrey, and L.P. Lossius. “A Review of Coke and Anode Desulfurization”. *Light Metals* (2007), pp. 895–900.
[52] J.G. Ameeri, C. Dreyer, and B. Samanos. “An Approach for a Complete Evaluation of Resistance to Thermal Shock”. *Light Metals* (1997), pp. 591–596.

[53] A. Innus, A. Jomphe, and H. Darmstadt. “A Method for the Rapid Characterization of Petroleum Coke Microstructure using Polarized Light Microscopy”. *Light Metals* (2013), pp. 1069–1073.

[54] K.J. Neyrey, L. Edwards, J.A. Ross, and F. Vogt. “A Tool for Predicting Anode Performance of Non-Traditional Calcined Cokes”. *Light Metals* (2005), pp. 607–612.

4 Anodic Bubble Behaviour and Wetting Properties of the Anode:Electrolyte Interface in Aluminium Electrolysis Cells

Abstract

A pilot carbon anode line was made with various blending ratios of isotropic to anisotropic coke. These anodes were then studied in terms of the anode voltage oscillation related to bubble formation and release, and the wettability interaction between anode and electrolyte. It was found that the voltage noise caused by gas bubbles was strongly reduced with a moderate addition of isotropic coke (7.2 wt%). For anodes with blending ratios of isotropic to anisotropic coke of 7.2 %-49.0 %, the potential oscillation amplitude was reduced by ~0.19 V, compared to an anode made from 100 % anisotropic coke. The regular voltage oscillations observed for a pure anisotropic coke and graphite were less pronounced for the anodes containing isotropic coke, with the pattern becoming less sawtooth-like. In general, the percentage of the anode screened by gas bubbles was also reduced as isotropic coke was added to the anodes. Increased wettability between the electrolyte and the anodes containing isotropic coke, compared with the pure anisotropic coke anode, can go some way towards explaining the lower potential oscillation amplitude and the decreased bubble screening observed.

4.1 Introduction

When producing aluminium, aluminium oxide, Al_2O_3, is dissolved in the electrolyte to form oxyfluoroaluminate ions. These are oxidised electrochemically on the carbon anode surface to produce CO_2, and to some extent, CO gas [1, 2]. Carbon anodes are made from calcined petroleum coke, usually a blend of different cokes, and a coal tar pitch binder. Thermodynamically, the production of CO gas at the anode is more favourable, although kinetically, CO_2 gas production is more favourable. Aluminium is formed on the cathode.

Aluminium production is an energy intensive process, and the energy demand is about 13 kWh/kg Al. The specific electric energy consumption is related to both the total cell voltage and the current efficiency of the cell (i.e. the actual amount of produced aluminium per theoretical amount of aluminium as given by the current applied) [3]. The aluminium industry has worked continuously towards reducing the energy consumption in aluminium production. Since current efficiency has been significantly improved during the last decades, reducing the cell voltage is where possible energy savings can be made today. The total cell voltage of an aluminium electrolysis cell is typically around 4.1-4.2 V, and consists of three main contributions [4, 5]:

1. The decomposition voltage, or reversible potential, deriving from the standard Gibbs energy for the total reaction.

2. Voltages induced from the polarisation of both the anode and cathode interfaces (concentration overpotentials on anode and cathode as well as anode reaction overpotential).

3. Ohmic voltage drops throughout the entire cell including the ohmic voltage drop through the electrolyte, anode and cathode, the voltage drop through external leads and connectors, as well as the additional ohmic voltage drop related to anodic gas bubble evolution.

The overpotential related to the anode surface makes a significant contribution to the overall voltage loss [6]. The various contributions that make up the measured anode voltage are provided in Equation 4.1, see also [3, 7–9].

$$E_{anode,measured} = E^{rev} + \eta_c + \eta'_r + \eta_h + I(R'_s + \delta R_s) \tag{4.1}$$

Here, E^{rev} is the reversible potential for the CO_2 forming reaction, and η_c is the concentration overpotential caused by concentration gradients of Al_2O_3 in the electrolyte close to the anode. The concentration overpotential is usually small, except at low concentrations of Al_2O_3. η'_r is the anode reaction overpotential with no bubbles screening the anode surface and η_h is the additional reaction overpotential due to the reduced effective surface area when bubbles are screening the anode, also known as hyperpolarisation [10]. The total reaction overpotential can be considered as η_r=η'_r+η_h and this is related to charge transfer reactions where intermediate adsorption/desorption processes takes place on the electrode surface. The last term of Equation 4.1 is related to the increase in ohmic resistance due to bubbles blocking the anode surface: R'_s gives the ohmic series resistance with no bubbles screening the surface and δR_s denotes the increase in ohmic series resistance due to partial anode blockage.

The total anodic overpotential is typically in the range of 0.4-0.7 V. It is generally agreed that the concentration overpotential is negligible in a saturated melt, but also generally small even in industrial cells (estimated to ∼0.02 V). The anodic reaction overpotential is ∼0.5 V and the extra ohmic resistance caused by bubbles is ∼0.2 V [1]. Typically graphite has been determined to have higher overvoltage than baked carbon anodes in laboratory studies [3], and recent work has given strong indications that single source anodes fabricated from isotropic cokes are slightly more electrochemically active than anodes fabricated from anisotropic cokes [7, 9, 11], as shown in Chapter 3 in the present thesis. Leistra and Sides showed that hyperpolarisation is measurable on baked carbon anodes by using a rotating disk, and quantified it to be approximately 15 mV at 1 A/cm^2 [10]. As bubble generation is a fairly large contribution to the cell voltage, reducing this parameter also means reducing the total energy consumption in Hall-Héroult cells [6].

4.1.1 Gas Bubbles in Industrial Cells

In industrial cells, the carbon anodes face downwards into the electrolyte. Thus, gas bubbles that grow on the anode surface are pressed upwards due to buoyancy and will remain there until the drag force induced by the velocity of the electrolyte exceeds

the interfacial tension between the gas bubble and the anode [12, 13]. The velocity of the electrolyte is governed by movement caused by the formation of gas bubbles [14], but in industrial electrolysis cells, electrolytic motion induced by the strong current and magnetic fields (magnetohydrodynamics) also has to be accounted for, although the effect of magnetohydrodynamics has been shown to be of one order of magnitude lower than the gas bubble induced velocity [15, 16]. A slight tilt of the anode of as low as 1° increases the bubble velocity substantially and remarkably changes the premises for bubble coverage on the anode surface [13, 14, 17]. Increased electrochemical consumption of the anode near the edges of the anode (the edge effect) can also create naturally tilted anode surfaces on industrial anodes [18].

Bubble build-up under the anode causes an increased ohmic resistance through the cell as well as increased hyperpolarisation on the anode. This extra resistance and hyperpolarisation causes increased cell voltage as well as increased voltage noise in the cell. Due to the highly corrosive environment of the cryolitic melts, bubble behaviour has been investigated in laboratory experiments in numerous ways. This includes use of water models e.g. [14, 19–23], indirect study using chronoamperometry and/or chronopotentiometry mainly in labscale cells and/or using transparent cells in cryolite based melts e.g. [8, 17, 21, 23–27]. Some industrial experiments have also been performed to investigate bubble behaviour e.g. [28–30]. Computer modelling by, for instance, computational fluid dynamics (CFD) is also a powerful tool to describe the bubble behaviour inside an electrolysis cell. Work in this field has been performed by e.g. [15, 16, 18, 20, 30, 31], and is further described in the sections below.

4.1.2 Bubble Formation Mechanisms

According to the classical theory, for nucleation of gas bubbles to proceed in a bulk liquid, the solution has to be supersaturated with gas [32]. According to Einarsrud [30], the most relevant bubble nucleation model for carbon anodes in cryolite melts is the Type IV model by Jones, Evans and Galvin [32]. According to this theory, there are no energy barriers related to formation of gas bubbles on nucleation sites. The substrate (anode) has cavities (pores), and bubbles will preferably nucleate at these imperfections on the surface. The pores will constantly be filled, and further gas production will happen in pre-existing gas cavities. The process is mass transfer driven and related to the concentration difference of dissolved CO_2 between the bulk and the bubble surface. When the bubble reaches a critical radius in a given pore, the growth of the bubble at the nucleation site is terminated. The bubble will then detach and start moving along the anode surface. Further growth of the gas bubbles occurs by coalescence, and this process is likely the main mechanism for bubble growth [33, 34]. In laboratory scale experiments with transparent cells [24, 25] the time interval between bubble release from the anode surface to generation of new bubbles was found to be very short. This indicates that little supersaturation is needed in order to initiate bubble nucleation, supporting that the process is mass transfer driven. Pores are filled with gas from the anode reaction and this is where new bubbles are nucleating. Pores on the anode surface are hence important as nucleation sites for gas bubbles. Einarsrud [30] modelled the effect of the pore size at a constant pore density, and

found that smaller pores give a higher release frequency and higher voltage oscillation amplitude than larger pores. More bubbles are formed, more gas volume is produced and hence, screening of bubbles on the anode surface is higher and a higher overall voltage oscillation amplitude is seen.

Using CFD modelling, the behaviour of gas bubble build-up and release has been calculated and compared with experimental results. By careful tuning of the physical parameters, modelling is a powerful tool to explain and confirm trends seen during laboratory investigations. The importance of parameters like bubble growth, bubble coalescence, wetting of the electrolyte:anode interface as well as wetting behaviour of electrolyte:gas:anode interfaces, current density, inclination of anode, porosity of the anode, bath chemistry, electrical conductivity, magnetic field motion, viscosity and surface tension have been investigated in works like [15, 16, 18, 30, 31, 35]. Modelling shows the complexity and sensitivity of the bubble behaviour in a Hall-Héroult cell. For instance, Einarsrud et al. [31] showed the importance of surface tension and wetting behaviour in terms of contact angle in order to fully reflect laboratory findings. Current density has also been shown to affect the bubble build-up and release. Increasing current density was shown to increase the bubble frequency and the voltage amplitude [8, 24, 36], which was confirmed by models [31].

4.1.3 Effect on Cell Voltage

The contribution to cell voltage from gas bubbles produced at the anode surface is increasingly important as aluminium producers attempt to decrease the total energy consumption of the electrolysis process [6]. The CO_2 gas bubbles form a local electrically insulating layer, owing to the negligible electrical conductivity of the bubbles, hindering current to flow to the anode surface from the electrolyte [14] and hence increasing current density locally in uncovered anode areas. This increased local current density also leads to hyperpolarisation as described above [10].

Most works on bubble formation, e.g. [8, 15, 17, 24, 25, 30, 31, 36–38], reports a quasi-periodical dynamic pattern of voltage oscillations, related to the additional voltage induced by the gas bubbles. The lowest potential during the voltage oscillations are attributed to an anode surface free of bubbles. Kiss and Ponscák [33] found through mathematical modelling that the voltage oscillations are mainly governed by coalescence, and that the nucleation stage is completely overshadowed by coalescence. The size of the anodes will also affect the voltage oscillations. Larger anodes give higher amplitudes and lower characteristic frequency. This is attributed to the increased length the bubbles have to travel, giving the bubbles more time to coalesce. Einarsrud and Sandnes [39] observed bubbles evolving from an industrial sized anode in a real Hall-Héroult cell, and their findings suggest that several large bubbles are escaping the anodes producing a more noisy voltage response, as opposed to laboratory experiments where the voltage oscillations can be attributed to one single bubble. Qian, Chen and Chen [21] found that the resistivity related to bubbles formed by electrolysis at a given current density in a cryolite based melt was about 20 % higher compared to the corresponding resistivity in a water model system. They concluded that water model systems cannot be directly compared to electrochemically formed bubbles [21].

However, they did not report important information such as the cryolite electrolyte composition or parameters like the viscosity or surface tension of the two baths used, making it difficult to determine the reasons for their findings. Hyde and Welch [40] used a lead chloride/sodium chloride melt with ceramic beads as "gas bubbles" and they found that the increased ohmic resistance is primarily dependent on bubble volume, not on bubble shape. However, this is probably only correct for a limited range in anode cathode distance. Dorin and Frazer in a laboratory experiment using a cryolite based melt and graphite anode [36] found that the overall voltage amplitude increased with increasing current density, which was explained in terms of the increased rate of gas generation, and that inclination of the anode reduced the screening by the bubbles.

4.1.4 Laboratory Experiments Related to Bubble Formation

Fortin et al. [14] used a full scale water model for investigations of the bubble build-up and release. They suggested a bubble build-up regime where small bubbles are formed at nucleation sites, spherical growth takes place, followed by lateral spread, mutual impingement and coalescence into a single gas sheet with a so-called head and a tail. The gas sheet is finally released rapidly at the edge of the anode. The authors suggest that gas bubble release is a hydrodynamic phenomenon, where large gas bubbles induce a velocity in the electrolyte that helps move gas bubbles along the anode surface, coalescing and enabling gas release. The velocity of larger gas bubbles along an anode surface in the water model experiment was determined to be 0.3 m/s [14, 20]. The suggested bubble build-up regime described by Fortin et al. was confirmed by the works of Xue and Øye [24] and Zhao et al. [25] who both used a transparent quartz cell and a video camera to visualise real time bubble behaviour under an anode during a laboratory scale electrolysis experiment in a cryolite melt. Aaberg et al. [17] measured gas bubble parameters by measuring the volume change of the electrolyte during bubble oscillations, their findings also support the water model of Fortin et al. [14].

The experiments conducted in the transparent laboratory cell by Xue and Øye [24], with a cryolite melt, showed that even small bubbles attached to the anode surface are subject to oscillations. However, these oscillations were not large enough to cause significant movement along the anode surface. The observed oscillation motion is suggested to be caused by a combination of the force of buoyancy, reaction force due to impingement surface tension, bath flow and turbulence. Larger bubbles detach from the anode and move across the anode surface, coalesce with neighbouring bubbles and finally reach the edge of the anode where they are released [15]. Cassayre et al. [23, 27] observed in a transparent cell, that at low current density, bubbles nucleate on specific nucleation sites. With increasing current density, the amount of nucleation sites increases. They also found that the average bubble diameter before release was not affected by Al_2O_3 content.

4.1.5 Size and Screening of Bubbles

A bubble layer thickness of about 4-6 mm is reported from transparent laboratory cells where the bubble build-up and release was investigated [23–25]. Dewing [41] reports a bubble thickness of 5 mm. Aaberg et al. [17] calculates the bubble thickness to be 5 mm, based on a method where the change in volume of electrolyte during bubble build-up and release is determined coupled with the monitoring of voltage fluctuations. Dorin and Frazer [36] also report a bubble layer thickness of 5 mm in a laboratory cell when investigating the effect of the ACD on the ohmic voltage drop through the electrolyte, while Kasherman and Skyllas-Kazacos [42] found a bubble layer thickness of 1 cm in a similar laboratory experiment. In industrial cells a bubble layer thickness of 1 cm was found based on electrolyte resistance measurements when varying the ACD [43]. Haupin [29] found that the measured voltage response became "noisy" at a distance of 2 cm under an anode in a 10 kA cell when using a dedicated reference scanning probe. This noisy voltage response was attributed to gas bubble noise. CFD modelling suggest that the flow patterns under the anode is not affected by changes in ACD between 2-4 cm, suggesting that the bubble layer thickness is less than 2 cm [16].

The bubble layer coverage of the anode surface in laboratory scale experiments was determined to be on average 45 % by Aaberg et al. [17], 50 % anode coverage is suggested by Dewing [41] while Zhao et al. [25] reported bubble coverage in the range of 50-90 %. However, Zhao et al. showed that the surface coverage of bubbles and the corresponding voltage oscillations is reduced drastically when slots are introduced at current densities lower than 1.3 A/cm^2. At 1.3 A/cm^2, the estimated anode coverage with and without slots reach similar values. At increasing current densities the bubble coverage was observed to decrease, probably due to increased velocity of the electrolyte, facilitating movement of bubbles across the anode surface. Increasing current density has been found to give increasing bubble screening and the same was found for decreasing Al_2O_3 content [44]. Thorne et al. [8] showed that the screening of the anode surface was highly dependent on the anode material, with graphite showing the highest values, anodes made from anisotropic coke show intermediate values and anodes made from isotropic cokes show the lowest bubble coverage. The bubble coverage in this work ranged from 10 % to 75 %.

4.1.6 Role of Pores

One possible transport route for gas bubbles from the anode surface is through pores in the anode [1, 30, 33]. The observation that pores are not filled with electrolyte as long as current is applied [45], supports the suggested transport route of gas filling pores. The degree of open porosity and air permeability will affect the rate of transport through pores. It has been shown for Söderberg anodes that the bubble noise on the anode surface is affected by the height of the electrolyte surrounding the anode [46, 47]. A higher bath height around the anode was shown to lower the bubble noise, but also increase the frequency of anode problems, such as pieces of the anode breaking off and falling into the bath. It was concluded that more CO_2 gas was transported through the anode rather than sliding along the anode surface when the bath height

was increased. Söderberg anodes are known to have higher porosity and higher air permeability than prebake anodes due to the excess amount of pitch used (about 13-15 % in prebake anodes compared to about 25 %-35 % in Söderberg anodes [48]).

4.1.7 Wetting between Anode and Electrolyte

Wetting properties can affect important parameters like bubble size, screening of the anode surface and hence, the additional ohmic resistance, as well as the hyperpolarisation, due to the gas bubble layer. The Young's equation relates surface tension (σ) between liquid-gas (lg), surface-liquid (sl) and surface-gas (sg) with contact angle (θ), as shown in Equation 4.2.

$$cos(\theta) = \frac{\sigma_{sg} - \sigma_{sl}}{\sigma_{lg}} \tag{4.2}$$

If $\sigma_{sg} < (\sigma_{sl} + \sigma_{lg})$, the liquid droplet will spread out on the surface, forming a wetted state between liquid and surface, i.e. $\theta < 90°$. And opposite, if $\sigma_{sg} > (\sigma_{sl} + \sigma_{lg})$, a dewetted state will occur, where the liquid droplet will be sphere shaped resenting gravity, i.e. $\theta > 90°$.

Cassayre et al. [23, 27] investigated the wetting properties and bubble behaviour in a transparent cell with both a graphite anode and an oxygen evolving SnO_2 anode. The wetting angle upon heating was measured between a flat anode substrate with an electrolyte sample on top using the sessile drop method. The SnO_2 anode showed full wetting with the cryolitic sample (0°). The graphite:cryolite test showed a wetting angle of about 120-130°, i.e. poor wetting. It was also observed that the gas bubbles (i.e. oxygen) formed on the anode surface were small and detached easily from the SnO_2 surface, forming a froth of tiny gas bubbles. On the graphite anode, the bubbles grew larger at their nucleation sites before they detached. They concluded that wetting properties is important for gas bubble behaviour. Wetting of anode:electrolyte was also investigated using the sessile drop technique by Thorne et al. [8], and it was found that anodes made from isotropic coke showed better wetting toward the electrolyte (θ<90°), than anodes made from anisotropic coke (θ>90°).

The sessile drop method is an equilibrium measurement, where the size of the electrolyte droplet is small and the anode sample is not polarized. Solheim et al. [49] used an immersion-emersion technique where the wetting properties between an industrial baked carbon anode and electrolyte were investigated before and after polarisation. It was found that wetting is permanently improved after polarisation and this may be attributed to adsorbed species on the anode surface. It was also found that increasing Al_2O_3 concentration improves the wetting between anode and electrolyte. Also, it was observed that after the experiment had been terminated, solidified cryolite adheres to the anode sample after high Al_2O_3 content experiments. This was not the case during low Al_2O_3 content experiments. The effect of low Al_2O_3 concentration on the wetting angle has also been investigated by Vogt in relation to the anode effect [12]. An electrolyte containing a low Al_2O_3 concentration showed poor wetting towards the

anode. Anodes that had been subjected to the anode effect were investigated and C-F bonds were observed [50, 51]. These C-F bonds create a smooth, nearly polished, anode surface, which has even been observed on anode surfaces run at normal Al_2O_3 concentration conditions. A fluoridised anode surface deteriorates wetting between anode and electrolyte, consequently increasing the bubble screening of the anode. A lower wetting angle i.e. better wetting conditions between electrolyte and carbon anode, which in-turn enhances the removal of gas bubbles on the anode surface. Additionally, a higher Al_2O_3 concentration was found to enhance the wetting angle of the electrolyte towards the anode.

4.1.8 Purpose of this Work

Studies on the effect of properties of the carbon anode on the gas bubble behaviour are limited in the open literature. Many studies have used graphite of various qualities e.g. [23–25, 27, 36], but studies where the anode coke material is varied are rather scarce. Kasherman and Skyllas-Kazacos [42] made two anodes of the same coke and pitch, making one anode more porous than the other. They found that the ohmic voltage drop through the electrolyte is lower for a more porous anode compared to a denser anode. They suggested that the size of the bubbles is smaller for a more porous anode, and further suggested that the porosity affects the anode:electrolyte interface. The latter was not confirmed by specific wetting experiments.

Thorne et al. [8] studied anodes made with different cokes. Two anodes were made from anisotropic cokes and two anodes were made from isotropic cokes. The authors found that the frequency of bubble release, voltage oscillation magnitude, bubble volume and degree of bubble screening is affected by the coke quality. Anodes made from isotropic cokes show a lower bubble release frequency, have lower potential oscillations, a larger bubble volume and a lower degree of bubbles screening the anode surface than anodes made from anisotropic cokes. The anodes made from isotropic cokes show a lower wetting angle as obtained by the sessile drop method and one of them had significantly larger pores.

This work seeks to further investigate the effect of isotropic cokes in anodes. Due to the coke raw material situation in the world, trials of introducing isotropic coke into anodes have been performed by several major industrial aluminium producers [52, 53]. Isotropic coke has traditionally been regarded as fuel grade coke and rejected by the anodes producers. In this work, a series of pilot anodes were made with blends of two single source cokes; one anisotropic coke and one isotropic coke. The content of isotropic coke to anisotropic coke was varied (0 %, 7.2 %, 14.2 %, 35.0 %, 49.0 % and 100 % isotropic coke content). The anodes have been characterised with respect to impurities, density, specific electrical resistivity, air permeability, coefficient of thermal expansion, air and CO_2 reactivity and dust index by conventional methods applied by the industry. The porosity of the anodes was studied by Hg porosimetry and optical microscopy.

The anodes were investigated by electrochemical techniques in laboratory scale experiments in order to study the build-up, coverage and release of gas bubbles. The wetting

properties of the anode were studied under polarisation by the immersion-emersion technique mentioned above [49, 54]. The main purpose of the work was to improve the understanding on the effect of various anode properties on the electrochemically produced gas bubble build-up behaviour and the wetting properties using the immersion-emersion technique.

4.2 Materials and Methods

4.2.1 Pilot Anodes and Electrolyte

Pilot scale anodes (Ø = 130 mm, h = 180 mm) were produced by Hydro Aluminium from one single source industrial sponge type petroleum coke of anisotropic character, one single source isotropic petroleum coke and an industrial grade coal tar pitch. The particle size of the aggregate was 0-2 mm, which was chosen to ensure a representative and homogeneous surface area in laboratory scale experiments. The recipe for producing the anodes was varied throughout the series in terms of blending ratio of isotropic to anisotropic coke. The coke aggregate had coke particle fractions of 1-2 mm, 0-1 mm and ball mill dust of less than 0.125 mm size. Six different pilot anodes were produced to varying blending ratios. Table 4.1 shows production details of the anodes in this study where the anode name reflects the total isotropic coke content. The anode names referred to in Table 4.1 will be used consistently throughout this chapter. A graphite material from Svensk Specialgrafit AB (Ultrapure grade CMG) was used for comparison and is denoted as “graphite” throughout the entire chapter. The pitch binder used for production of the anodes had a Mettler softening point of 119.1°C and a QI level of 7.8 %. Mixing and baking temperatures during anode fabrication were kept constant.

For clarity, Anodes 0 % and 100 % in this work were sampled from the same pilot anodes as Anode A and B in Sommerseth et al. [9, 45], respectively. Also Anode 0 % and Anode 100 % are sampled from the same pilot anodes as Anode 1 and Anode 4 in [7, 8, 11, 55], respectively. However, new samples were made for all electrochemical tests, and new electrochemical tests were performed.

The electrolyte used was a cryolitic melt with a molar ratio of NaF to AlF_3 of 2.3, saturated in aluminium oxide. The cryolite was from Sigma Aldrich (>97% purity) with an excess of AlF_3 of 9.8 wt% (industrial grade, sublimed in-house) and 9.4 wt% γ-Al_2O_3 from Merck (>99.4 % purity). The same electrolyte composition was used for all electrochemical tests.

4.2.2 Physical Analysis

The anodes were characterised using the industry International Organization for Standardization (ISO) methods for density (ISO 12985-1:2000), specific electrical resistivity (SER) (ISO 11713:2000), permeability (in house method at Hydro comparable to ISO 15906:2007) and coefficient of thermal expansion (ISO 14420:2005, but

Table 4.1: Pilot anodes. Under coke type, A and I denote anisotropic and isotropic coke, respectively.

Anode name	Coke type	0-1 mm aggregate	1-2 mm aggregate	Ball mill product	Pitch content
		wt%	wt%	wt%	wt%
0 %	A	35.0	38.0	27.0	15.0
	I	0			
7.2 %	A	32.4	32.4	28.0	14.0
	I	3.6	3.6	0	
14.2 %	A	28.0	28.8	29.0	14.0
	I	7.0	7.2	0	
35.0 %	A	17.5	17.5	30.0	14.0
	I	17.5	17.5	0	
49.0 %	A	10.5	10.5	30.0	14.0
	I	24.5	24.5	0	
100 %	A	0	0	0	15.0
	I	35.0	38.0	27.0	

the temperature range was extended to 300-700°C and a sample size of Ø = 20 mm, height = 75 mm). Air and CO_2 reactivity tests were performed using in-house thermogravimetric analysis methods developed at Hydro Aluminium similar to ISO 12989-1 and ISO 12988-1, respectively. Additionally, the levels of metal and sulfur impurities in the carbon anodes were determined using X-Ray fluorescence (XRF). The methodology is described in ISO 12980:2000. All these tests were performed as routine measurements at Hydro Aluminium Årdalstangen.

4.2.3 Porosity and Texture

A Micrometrics Autopure IV 9500 Mercury Porosimeter was used to investigate the microporosity (typically <1 μm[1]) of the carbon anode samples. Hg was filled into anode bulk samples of ~2.2 g at pressures 0.50-60 000 psia ($3.45 \cdot 10^3$-$4.14 \cdot 10^8$ Pa). The pore diameter range measured by mercury intrusion was 0.003-360 μm [58].

Porosity was also investigated using an optical microscope (high-end Leica/Relchert MeF3A metallurgical optical reflecting light microscope) and a custom written macro

[1]Note that the IUPAC definition of porous materials deviate from the definition used in aluminium industry for microporosity: Microporous materials have pore diameter <2 nm, mesoporous materials have pore diameter in the range 2-50 nm and macroporous materials have pore diameters >50 nm [56]. This definition is not applied here. There is no consensus on the definition of microporosity within aluminium industry, although in the present work a definition for microporosity will include pores with diameter <1 μm, corresponding to the definition in [57].

for the NIH software as described by Rørvik and Øye [59]. The resolution range for porosity measurements using this method was 5-10000 μm diameter. Ø = 10 mm core anode samples were mounted in epoxy resin under vacuum (two-component Epofix epoxy with Epodye green fluorescent dye from Struers, Denmark). After setting of the epoxy, the samples were ground and polished step-wise down to 1 μm. The samples were then studied in the optical microscope using a selective fluorescent light filter (named B5) that only include wavelengths equal to or shorter than blue light. The fluorescent light ensured good contrast between the fluorescent epoxy filled pores and the carbon sample. The magnification used was x100. The optical microscope was set to take 192 individual frames of the entire sample surface. These images were then stitched together. The NIH software then determined the porosity *vs.* pore diameter, where the pore diameter is set equal to the diameter of the largest circle that will fill the pore.

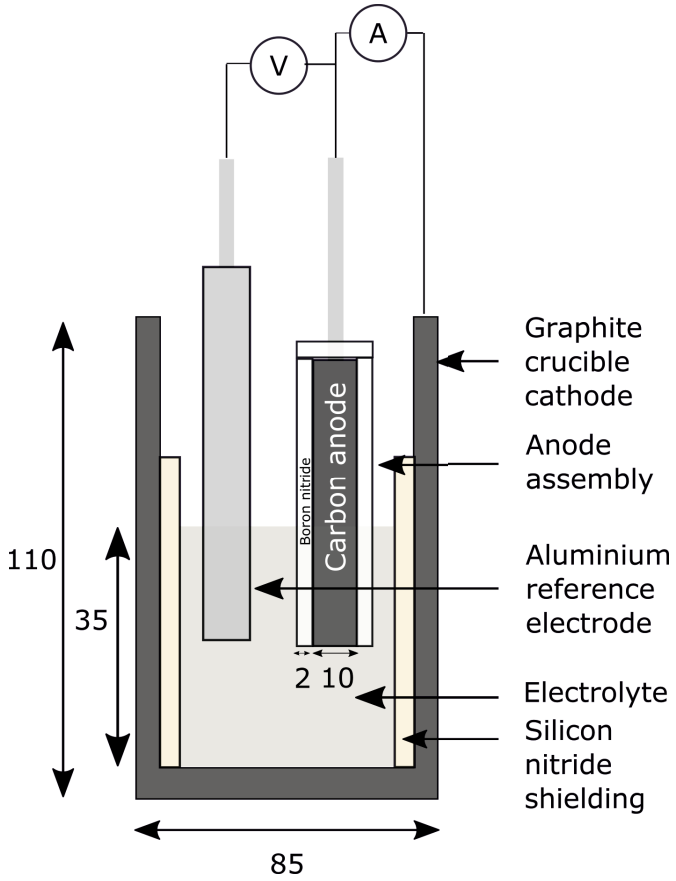

Figure 4.1: Electrochemical experimental setup used when investigating the bubble build-up and release of the different carbon anode materials. All measures are in mm.

4.2.4 Electrochemical Bubble Evolution

The electrochemical bubble behaviour of the anode materials varying in isotropic coke content, and a reference graphite material, was investigated using a flat horizontal anode surface. 10 mm core anodes were placed inside a boron nitride tube (wall thickness of 2 mm) in order to maintain a completely flat surface with no vertical anode area (0.79 cm^2) exposed to the electrolyte. The anode sample was immersed approximately 0.5 cm into the electrolyte. A graphite crucible was used to hold the electrolyte. A silicon nitride tube was used to shield the walls of the crucible and the bottom of the graphite crucible was used as the cathode to obtain as straight current lines as possible. The anode sample with the boron nitride shielding was threaded onto a Ø = 3 mm stainless steel rod for electrical contact. An aluminium reference electrode, which was produced in-house, was used in order to measure the anode (working electrode) potential. All potentials referred to in this work are quoted with respect to the Al reference electrode. A new reference electrode was used for every duplicate experimental run. Figure 4.1 shows a sketch of the experimental setup. The experiments were performed in a tube furnace at 1000 °C in an argon atmosphere. A Parstat 4000 potentiostat/galvanostat/EIS analyzer from Princeton Applied Research with a minimum/maximum current range of ±40 pA/±4 A was used for the electrochemical testing.

A current density of 1.0 A/cm^2 was applied for 2x200 s and the voltage response measured. The first 200 seconds was used as a preconditioning of the anode surface, until a pseudo-steady potential state was obtained. The experimental design allowed for maximum bubble retention under the anode surface, and distinctive potential oscillations were seen as the bubbles built up and eventually release. The amplitude and frequency of these oscillations are thus directly related to the formation and release of bubbles on the surface. The volume of released bubbles was calculated using the average of five time intervals (Δt) for complete bubble oscillations, related to the charge passed according to Faraday's law:

$$V_{bubble} = \frac{I \cdot \Delta t \cdot R \cdot T}{n \cdot F \cdot P} \cdot 10^3 \tag{4.3}$$

In Equation 4.3, I is current, F is Faraday constant and n is number of electrons passed, i.e. 4, R is the gas constant (0.0821 L atm/mol K) and T is temperature (1273.15 K). The pressure, P, is assumed to be 1 atm and it is also assumed that the ideal gas law applies.

By applying a constant potential of 2.5 V for 200 s, while the current was recorded, the bubble coverage, also denoted as bubble screening, on the anode surface was determined by calculating the ratio between the maximum and minimum current values.

Three or more samples were tested for each anode material with the exception of the 7.2 % isotropic coke content anode. This anode was tested once, and then it was excluded from the series. The test sequence of the anode series was randomised during the experiments in order to eliminate possible changes in the properties of the melt over the time of the experiment.

4.2.5 Wetting Properties of Polarised Anode Samples in a Cryolitic Melt

A dedicated apparatus for investigating the wetting properties of carbon anode samples towards cryolitic melts before and after polarisation was built by SINTEF in collaboration with Hydro Aluminium. This apparatus has been thoroughly described in [49, 54]. In the present work the anode shape was modified to an outer diameter was 30 mm and inner diameter was 22 mm. The sequence of the measurements was:

- **Step 1**: Start with the sample 8 mm above the electrolyte. The dry sample was immersed 40 mm into the cryolitic melt at a rate of 0.2 mm/s by raising the crucible holding the electrolyte. The sample was left at this position for 10 mins. After 10 mins the crucible was lowered 5 mm at a rate of 0.2 mm/s and left at this position (anode immersed 35 mm) for another 10 mins until the crucible was lowered at a rate of 0.2 mm/s until the entire anode was out of the electrolyte.
- **Step 2**: The same procedure as above was repeated immediately with the wet sample.
- **Step 3**: Start with the sample 8 mm above the electrolyte. The anode was immersed 40 mm into the electrolyte at a rate of 0.2 mm/s, and then held for 10 mins. An anodic current of 0.7 A/cm^2 (50 A, maximum current for the current supplier) was applied for 10 s. The crucible was then lowered at a speed of 0.2 mm/s till the anode was out of the electrolyte.
- **Step 4**: Start with the sample 8 mm above the electrolyte. The anode was immersed 40 mm into the electrolyte at a rate of 0.2 mm/s, and then the direction of the crucible motion was immediately reversed at the same rate.

According to Martinez et al. [54], the total measured weight of the anode sample during an experiment is a combination of 1) the free weight [g] of the anode sample, m_0 (i.e. hanging freely over the electrolyte), 2) the buoyancy of the immersed part of the anode sample, m_b and the weight of the meniscus, m_σ. m_σ is the reported value, and m_0 and m_b are used to correct the measured raw data weight, m_m, according to Equation 4.4.

$$m_\sigma = m_m - m_0 - m_b = m_m - m_t \tag{4.4}$$

Theoretical weight m_t is given as the sum of the buoyancy and the free weight. Equation 4.5 gives the force [N], F, acting on the anode sample in the vertical direction.

$$F = L \cdot \sigma \cdot cos\theta \tag{4.5}$$

In the Equation, L is the length of the meniscus [m] (=π(diameter$_{outer}$+diameter$_{inner}$), σ is the surface tension [N/m] between the liquid and the gas and θ is the calculated wetting angle between the electrolyte and the anode sample. σ was found to be 0.1131 N/m by assuming that Equation 4.6 applies [3].

$$\sigma = c - d \cdot t \tag{4.6}$$

Equation 4.6 is identical with Equation 5.2.7 in "Aluminium Electrolysis" p. 101 [3]. The parameters c=205.2 N/m and d=0.0921 N/m·°C are found in Table 5.2.2 (p. 101 [3]). t denotes the temperature (in °C) during experiment and is 1000 °C. Equation 4.7 shows the dependency between the force and the weight of the meniscus.

$$m_\sigma = F/g \tag{4.7}$$

In Equation 4.7, g is the standard acceleration of gravity (9.81 m/s^2). Equations 4.5 and 4.7 were used to calculate the wetting angle.

4.3 Results and Discussion

4.3.1 Physical Parameters for the Test Anodes

Table 4.2 shows impurity levels for various elements as determined by XRF. The ultra-pure graphite sample is as expected, low in all impurity elements. The anisotropic coke anode (0 %) is intermediate in most impurities. Note especially the low sulfur and vanadium contents. The 100 % isotropic coke anode is generally high in all impurities compared to the 0 % anode (except phosphorus). Note especially the high sulfur and vanadium contents. The coke type is responsible for the increased impurity content in the 100 % anode compared with the 0 % anode, since the pitch is the same throughout the anode series. It is assumed that the anodes containing 7.2-49.0 % isotropic coke show linear increase in impurities dependent on the amount of isotropic coke present.

Table 4.3 shows physical properties for the entire anode series, including density, specific electrical resistivity (SER), air permeability, coefficient of thermal expansion (CTE), air and CO_2 reactivity and dust index. The 35.0 % and 49.0 % anodes are higher in density than all the other anodes. In general, SER and air permeability reflects the density of the anodes, except for the 100 % anode. As seen by further porosity investigations of these anodes (Figures 4.2, 4.3 and 4.4), the 100 % anode shows a network of large open pores and this is the reason for the high air permeability. The value 6.9 indicates that the air permeability test exceeds the limit for the permeability equipment used. CTE increases linearly with increasing isotropic coke content, suggesting that isotropic coke will expand more than anisotropic coke upon heating. A consequence of this is seen in Figure 4.4 where cracks around the isotropic coke particles are clearly visible for the 35.0 % and 49.0 % baked anodes. This was also reported by Sommerseth

Table 4.2: XRF elemental results for graphite and the baked 0 % and 100 % isotropic coke anodes.

Anode	Na ppm	Si ppm	P ppm	S %	Ca ppm	V ppm	Fe ppm	Ni ppm	Zn ppm	Pb ppm
Graphite	10	10	1	0.00	11	1	25	3	1	1
0 %	56	108	11	0.94	25	70	287	45	5	7
100 %	115	284	4	4.45	227	883	393	372	38	20

Table 4.3: Physical properties of the anodes. SER = Specific el. resistivity, Perm. = Permeability, CTE = Coefficient of thermal expansion and TC = Thermal conductivity, CO_2, air reactivity and dust index.

Anode	Density	SER	Perm.	CTE	R_{CO_2}	R_{Air}	Dust index
	g/cm^3	$\mu\Omega$m	nPm	μm/mK	mg/cm^{2}h	mg/cm^{2}h	mg/cm^2
Graphite	1.771	12.7	0.20	N/A	2.5	0.3	0.4
0 %	1.603	55.2	0.8	4.14	19.0	39.0	15.3
7.2 %	1.597	58.3	1.1	4.19	11.9	21.5	4.8
14.2 %	1.595	59.4	1.5	4.48	11.4	25.2	4.4
35.0 %	1.651	51.9	0.9	5.07	14.4	30.9	2.2
49.0 %	1.674	50.7	0.6	5.44	18.1	37.2	2.1
100 %	1.596	50.5	6.9*	7.07	7.4	70.1	0.2

*This was the maximum measurable level of the equipment, indicating that the measurement is out of range.

et al. [45]. The isotropic coke expands more and when the amount of isotropic coke content reaches a certain fraction (somewhere between 14.2 and 35.0 %), cracking is visible by microscopy. A decrease in CO_2 reactivity was generally seen for all anodes containing isotropic coke, compared to the pure anisotropic coke anode (the 0 % anode). This is in agreement with Edwards et al. [52] where a slight improvement in CO_2 reactivity was seen when isotropic coke was introduced to anodes. This is due to sulphur forming inactive metal-sulphur complexes with metal catalysts, which in turn inhibit the CO_2 forming reaction [60].

In anodes containing isotropic coke, an increasing trend of air reactivity was seen with increasing isotropic coke content. There is reason to believe that the increased content of metal impurities may be responsible for this [61]. Dusting is, however, reduced with an increasing isotropic coke content. Dust in potrooms must be removed manually [47], and this causes increased labour costs as well as instability in the pots. Hence, reducing carbon dusting from anodes is desirable. The graphite anode is clearly different from the carbon anodes in terms of physical properties. It is denser, has lower SER and air permeability and very low CO_2 and air reactivity as well as dust index. The low air and CO_2 reactivity can be explained by the high amount of basal planes compared to edge planes and defects in the crystal lattice and the absence of impurities.

The anodes produced for the thesis work represent specialised, tailor-made anode aggregates and they are produced on a pilot scale anode production line that has been tuned to simulate full scale anode production. A fair level of agreement with actual anode properties is expected, but there are deviations compared with typical industrial anode parameters (*cf.* Table 2.1 and [57]), especially for the 100 % anode with the exaggerated porosity. These deviations were due to a too high pitch content in relation to the ability of isotropic coke to absorb pitch, and the unusual coke aggregate

used. Also, it is fairly common that pilot scale anodes show a slightly lower density, and a higher air permeability and electrical resistivity than industrial scale anodes [62].

4.3.2 Porosity Measurements

Microporosity was measured using Hg porosimetry. Figure 4.2 shows the differential intrusion of mercury *vs.* pore size diameter of the anodes. Only one parallel was run of each sample. The graphite sample shows very little porosity except in the range between 0.3-1 μm. The porosity of graphite assessed by Hg porosimetry corresponds to the volume fraction of pores formed between single grains of carbon particles. The pilot anode series show that the 100 % anode has higher differential porosity around 100 μm. Such wide pores are not observed for the other pilot anodes. The presence of large pores in the 100 % anode is due to non-optimal packing of the coke grains, non-optimal mixing temperature between the isotropic coke and the pitch and also a non-optimal pitch content, leaving the coke grains unwetted. For anodes 0-49.0 %, the fines were purely anisotropic coke as shown in Table 4.1 and this appears to have a significant effect on the quality of the anode as the coke/pitch interaction depends on the type of coke. In the 1-10 μm range the 0-49.0 % anodes show some porosity, while the 100 % anode has very little porosity in this range. In general, the porosity in the range 10-100 μm appears to be due to the packing between the isotropic and anisotropic coke particles. The 49.0 % anode shows a particularly small amount of pores in this range, suggesting that the packing between the coke grains at this mixing range is very good.

Figure 4.3 shows the porosity analysis of the anodes *vs.* pore size diameter, as obtained by optical microscopy. The results are an average of two parallels for each anode sample. Graphite was not investigated due to difficulties in getting epoxy to penetrate the pore structure, due to the very small size of the pores. The characterisation of porosity by optical microscopy support the findings from Hg porosimetry in terms of the 100 % anode having large pores peaking at 300 μm that are not present in the other anodes. Also, the effect of packing between the isotropic and anisotropic coke particles can be seen in the 30-100 μm range. Neither the 0 % nor the 100 % anodes have peaks of porosity in this range. The packing between the isotropic and anisotropic coke grains is good in the range of 7.2 % to 49.0 % isotropic coke content. This was also seen in the Hg porosimetry measurements. Figure 4.4 shows a collage of each anode sample where the porosity was measured by optical microscopy. The red colour is the carbon sample and the yellow colour is the epoxy penetrated into pores and voids in the sample. The epoxy creates a good contrast between the carbon and the pores. Only open pores are filled with epoxy. In Figure 4.4 the large pores that appear for the 100 % anode are very visible.

Porosity investigations using optical microscopy have some advantages compared to Hg porosimetry. The optical microscopy method is a “maximum” measuring technique, that measures a pore as the largest circle that can fit into a void filled with epoxy. This gives a more realistic measure of the size of the pores. Hg porosimetry on the other hand measures the pressure needed to penetrate the bottleneck of the pore, and

relates this to the pore size. It provides no information about the size of the pore inside the bottleneck [59]. The size of the samples measured during Hg porosimetry is very small, causing some uncertainty as to whether the samples are representative. Optical microscopy on the other hand is challenging in terms of successful filling of all the open pores with epoxy. Both methods only measures open porosity.

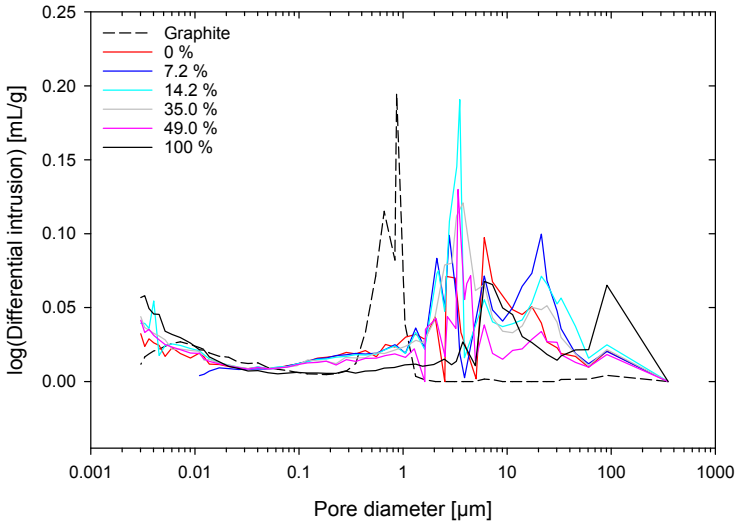

Figure 4.2: Differential intrusion of mercury into pores *vs.* pore size diameter.

4.3.3 Electrochemical Bubble Evolution

The anodes were characterized electrochemically in a laboratory cell as shown in Figure 4.1. A current density of 1.0 A/cm^2 was applied and the voltage was recorded. An example of the voltage obtained at 1.0 A/cm^2 for one parallel of each sample in the anode series, is shown in Figure 4.5. As was also seen in several other works [8, 15, 17, 24, 25, 30, 31, 36–38], a quasi-periodical dynamic pattern of bubble build-up and release was observed. Figure 4.6 shows a summary of voltage oscillation amplitudes for all samples tested during three individual duplicate runs with one or two parallel samples of each pilot anode. For each sample the average of five bubble build-up and release cycles sampled towards the end of the 200 s measuring period, was used to determine the amplitudes. In Figure 4.6 b), the average of all the pilot anode samples are shown together with the corresponding standard deviations. The two high points for 14.2 wt% and 35.0 wt% isotropic coke content have been considered as anomalous due to obvious irregularities in the voltage output obtained. Hence, n = 3-5, except for the 7.2 wt% anode which was only tested once. The values for the maximum and minimum voltages, as well as the time period between maximum and minimum points, were extracted manually. When introducing isotropic coke, the regularity of

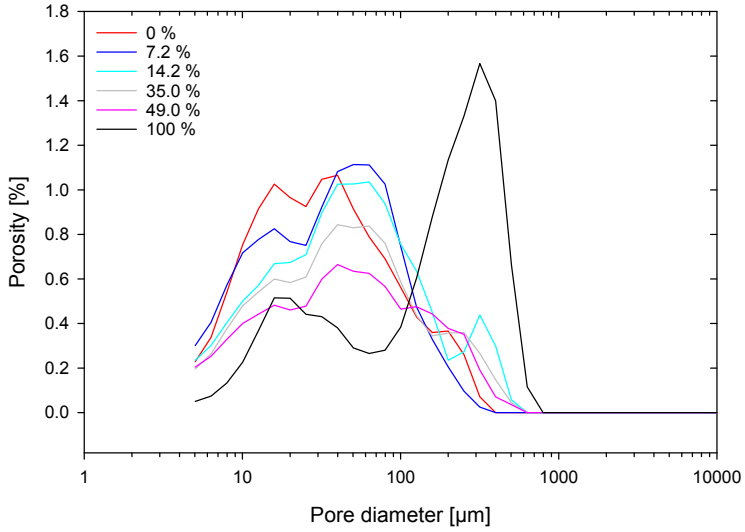

Figure 4.3: Porosity [%] *vs.* diameter of pores obtained by optical microscopy, average of two duplicate runs of each sample.

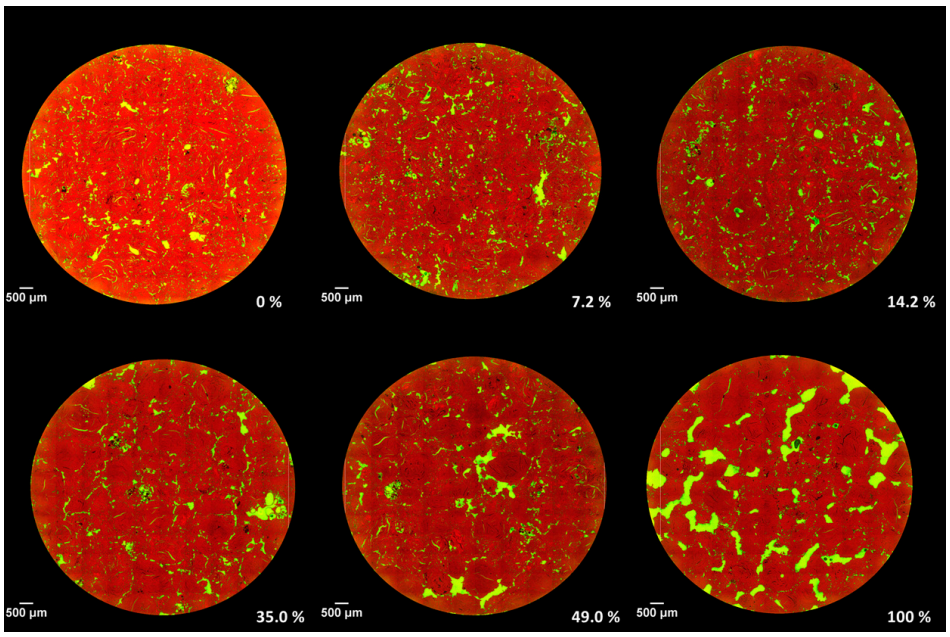

Figure 4.4: Optical microscopy images showing pores (yellow) in the different anode materials.

the oscillation patterns become disrupted and the patterns become more noisy, less regular and more sawtooth-like, as seen in Figure 4.5. Due to a lack of regularity in the voltage signal for these anodes, FFT analysis could not be used (only for the graphite and anisotropic anode).

From Figure 4.6 it is obvious that graphite has much higher voltage oscillation amplitudes than the pilot anodes. A suggested reason for the high potential oscillation amplitudes of graphite is the very dense and nearly polished surface, which tends to facilitate nucleation of a large number of small bubbles in the micropores which screens a high fraction of the surface before coalescing.

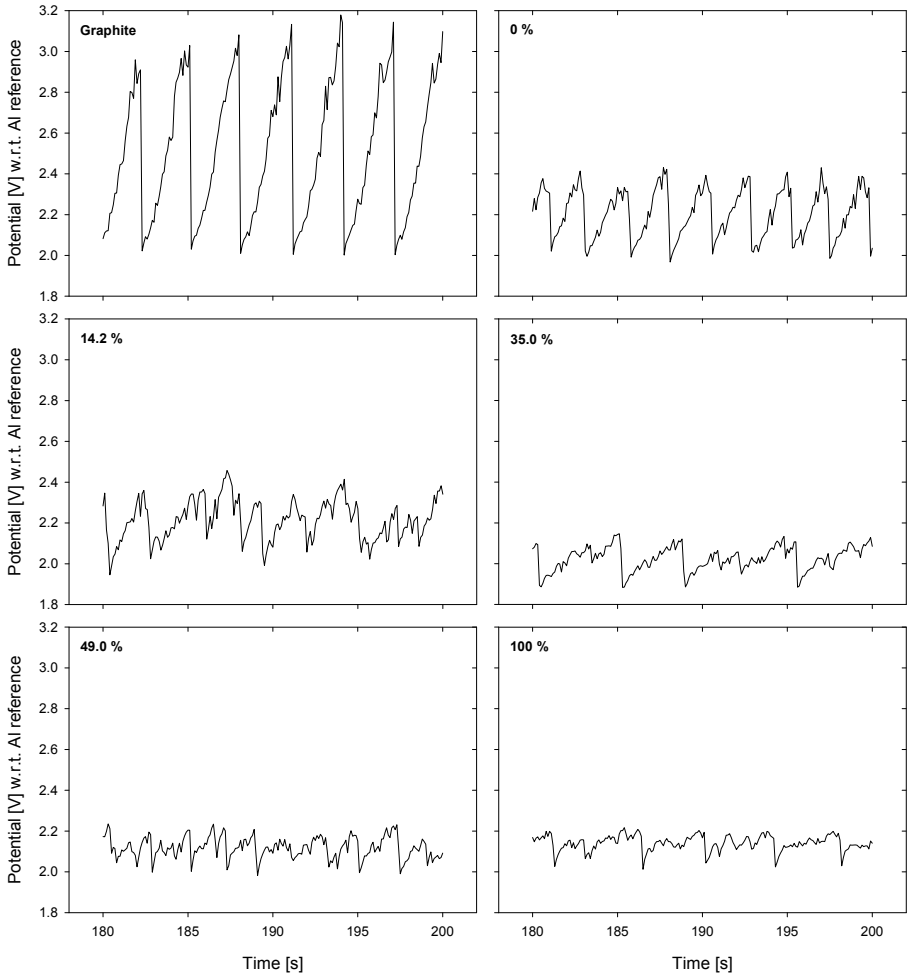

Figure 4.5: Example of potential *vs.* time for graphite and the pilot anodes where 1.0 A/cm^2 was applied for 200 seconds. The last 20 seconds of the 200 s long measurements are shown.

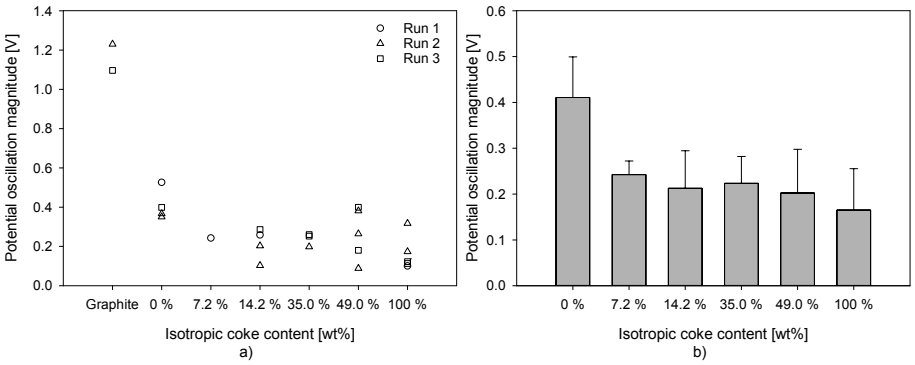

Figure 4.6: Potential oscillation magnitude of bubbles evolved during electrolysis at 1.0 A/cm^2 of anodes varying in isotropic coke content. a) All results including graphite from three duplicate runs. b) Average results with error bars for all anodes except graphite.

For both graphite and the 0 % anode, the oscillations are very regular with a fairly constant time interval between the minimum and maximum points. As already mentioned, this regularity breaks down when isotropic coke is introduced into the anode series. It is evident that introducing isotropic coke lowers the potential oscillation amplitude and this effect appears already with only a small addition of isotropic coke (7.2 %). The reduction in potential oscillation amplitudes when blending in isotropic coke to anisotropic coke, is remarkably high, around ∼0.19 V. This suggests a great potential for energy savings in potrooms if the findings can be confirmed using industrial scale anodes. The reduction in ohmic resistance caused by bubbles can be utilized further by either lowering the ACD [44], or alternatively running at the same ACD as before, but with a more stable potline with less back-reactions and hence increased current efficiency. The findings in this work for the 0 % and 100 % anodes are also confirmed in [8].

The lack of porosity may have an important role in the bubble oscillation amplitude observed for the graphite samples compared with the pilot anode samples, as pores are nucleation sites for bubble formation [24, 25, 30, 32]. Also, the 100 % isotropic coke anode has an even lower bubble potential amplitude than the blended anodes. The large array of open pores present in the 100 % anode and the high air permeability shown in Table 4.3, may suggest that more gas is susceptible to enter the pores instead of escaping from the anode surface. Transport of bubbles through pores as a means of reducing surface screening has also been suggested by [1, 30, 33]. However, the amount of gas entering pores is not confirmed or quantified by testing for example the effect of ACD and hence, increased pressure on the anode sample as described in [46, 47].

For the blended anodes it is more difficult to draw any conclusion on how porosity affects the bubble potential amplitudes. However, the porosity differences between these anodes are not so great compared with graphite and the 100 % anode. The

nucleation and coalescence of bubbles appears to be fairly similar for all the blended isotropic to anisotropic coke anodes, explaining why all these anodes show similar potential oscillation amplitudes within the standard deviations given.

The bubble volume was calculated according to Faraday's law, as given by Equation 4.3. Figure 4.7 shows the calculated bubble volume for the anodes, including graphite. These results, however, do not correlate with the potential oscillation amplitudes as anodes with higher calculated bubble volumes have lower potential oscillation amplitudes. Due to the breakdown of the regularity of the voltage oscillations when isotropic coke is blended in, there is some difficulty in determining Δt accurately, and this is reflected in the fairly high standard deviations for the blended anodes. According to Einarsrud [30], the bubble release should be faster (i.e. lower Δt) with higher potential oscillation amplitudes. Despite the problems determining Δt, the frequency of bubble release is slightly higher for the 0 % anode compared with the remaining pilot anode series. However, the results for graphite which has the highest potential oscillation amplitude, does not confirm this since Δt for graphite and the 0 % anode are similar. An explanation related to bubble screening of the anode surface is given below.

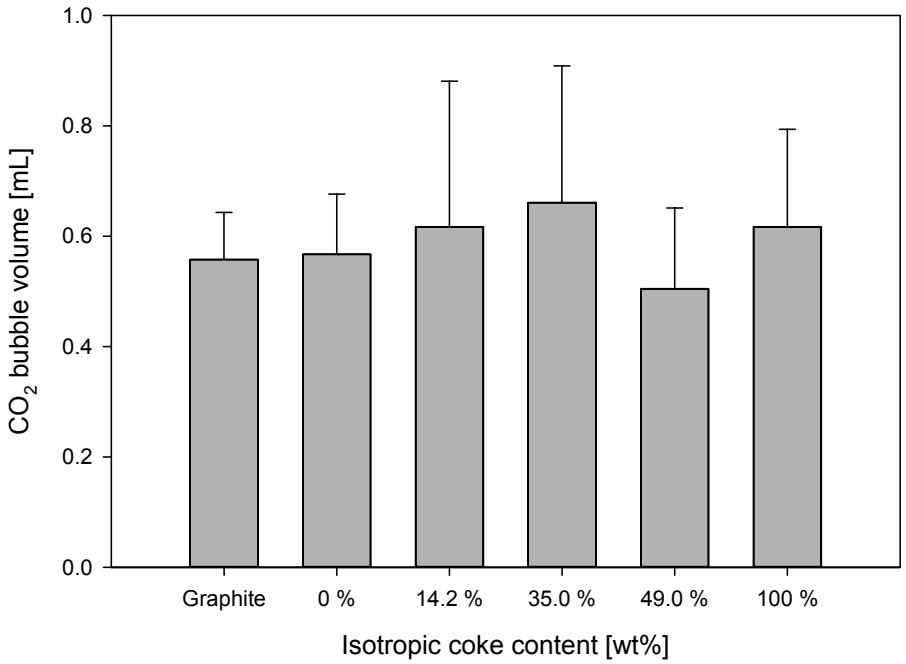

Figure 4.7: Average bubble volume per bubble evolved during electrolysis at 1.0 A/cm^2 with error bars. For graphite n = 2 and for the remaining anodes, n = 3-5. For each sample the average of 5 bubbles are reported and included in the calculations.

Figure 4.8 shows current *vs.* time for graphite and the pilot anodes. These raw data results were used in order to calculate the bubble screening on the anode. Figure 4.9 shows the percentage of bubbles covering the anode surface calculated by using the maximum over the minimum current amplitude observed for each anode sample when a constant voltage of 2.5 V was applied. The fraction of the anode surface screened by bubbles ranges from 14-90 %, depending on the anode material in use, and this is in fair agreement with [8]. This suggests that bubble screening is highly material dependent. Other work has shown a smaller range of bubble screening [17, 25, 41] , however, these works were performed using different anode sizes and materials making it difficult to directly compare these results with the present work.

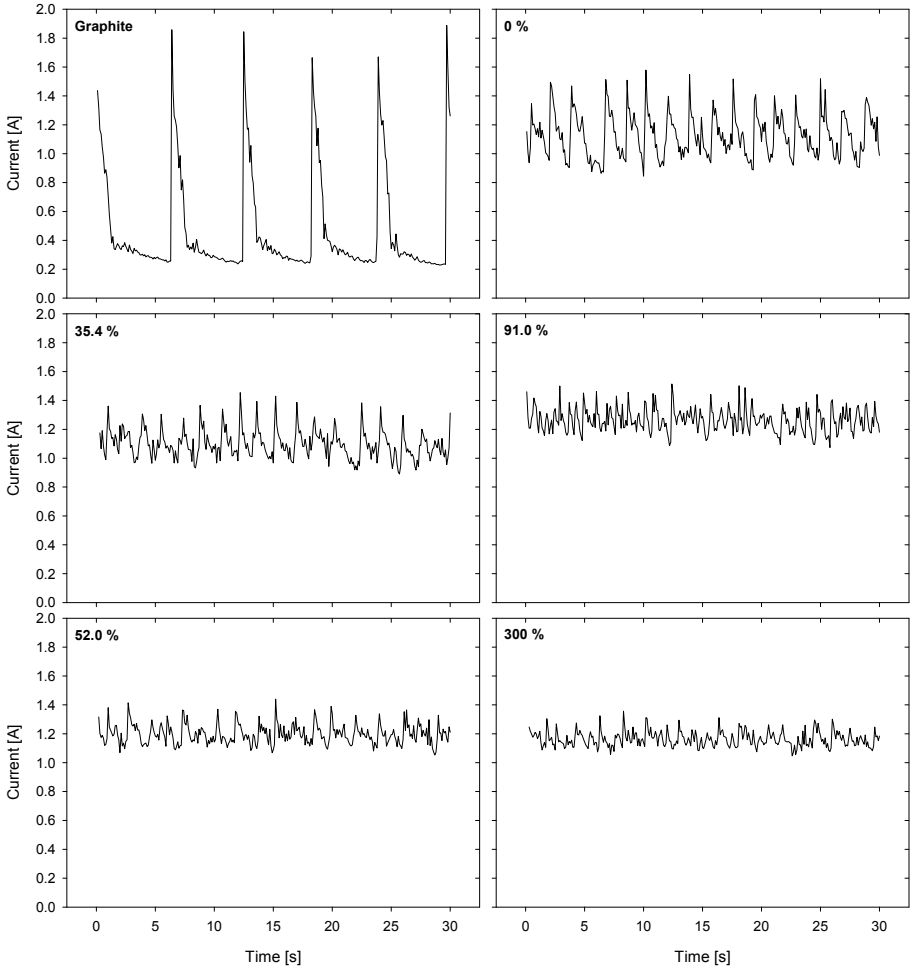

Figure 4.8: Example of current *vs.* time for graphite and the pilot anodes where 2.5 V was applied for 200 seconds. The first 30 seconds of the 200 s long measurements are shown.

As can be seen from Figure 4.9, graphite has a much higher bubble screening than the pilot anodes. The standard deviation for graphite also suggests a maximum coverage above 100 % which of course is not possible. From the 14.2 % anode and towards the 100 % anode the bubble screening decreases from 42.6 % to 14.5 % and the 35.0-100 % anodes all have lower bubble screening than the 0 % anode. Exactly why the bubble screening for the 14.2 % anode seems to be higher than the 0 % anode, is not fully understood, but considering the standard deviation, they may be considered almost similar.

When comparing the present results with Thorne et al. [8] it may seem that the 0 % anode is a little underestimated in the present work. About ∼38 % screening of the 0 % anode was found in the present work compared with ∼50 % in Thorne et al. One possible source of error during anode screening experiments may be underestimating the screening due to a slight tilt under anodes. A tilt of the anodes will change the buoyancy effect underneath the anode and hence change the velocity regime for bubble release [13, 14, 17]. The graphite and 100 % anodes are similar to the results obtained in [8] within the standard deviations. Also, in [8], the size of the anodes is slightly smaller, 8 mm.

It can be questioned, as mentioned previously that gas may enter the large array of open pores in the 100 % anode suggesting that the bubble screening reported here is lower than what it might have been if the anode had been more optimised in terms of packing between larger coke grains and fines. However, there is a downward trend towards the 100 % anode suggesting that this trend is real since both the 35.0 % and 49.0 % are the more dense anodes in this pilot anode series. This supports the hypothesis/explanation that the decrease observed in bubble screening when isotropic coke is introduced in anodes, is a material property of the cokes.

A suggested explanation as to why the bubble screening in general is lower for anodes containing isotropic coke is the increased electrolyte wettability for the anodes containing isotropic coke compared with anodes only containing anisotropic coke. Better wetting between anode and electrolyte implies a reduced contact angle, and a correspondingly higher gas-solid contact angle. In literature, it has been found that increased wetting between anode and electrolyte enhances the bubble release from the anode surface and the anode screening was reduced [23, 27]. Cassayre et al. [23, 27] also observed a reduction in the additional ohmic resistance caused by bubbles. A simple assessment of the wetting between anode and electrolyte is shown in [8] where the 100 % anode (denoted Anode 4 in the paper) showed significantly better wettability than the 0 % anode (denoted Anode 1) using the sessile drop method. However, the measurements were not conducted under polarisation and polarisation is known to affect the anode:electrolyte wetting behaviour. Therefore, the in-house design wetting apparatus, as described in Section 4.2.5 was used for determination of wetting angle for the anode *vs.* electrolyte before and after polarisation, as discussed below.

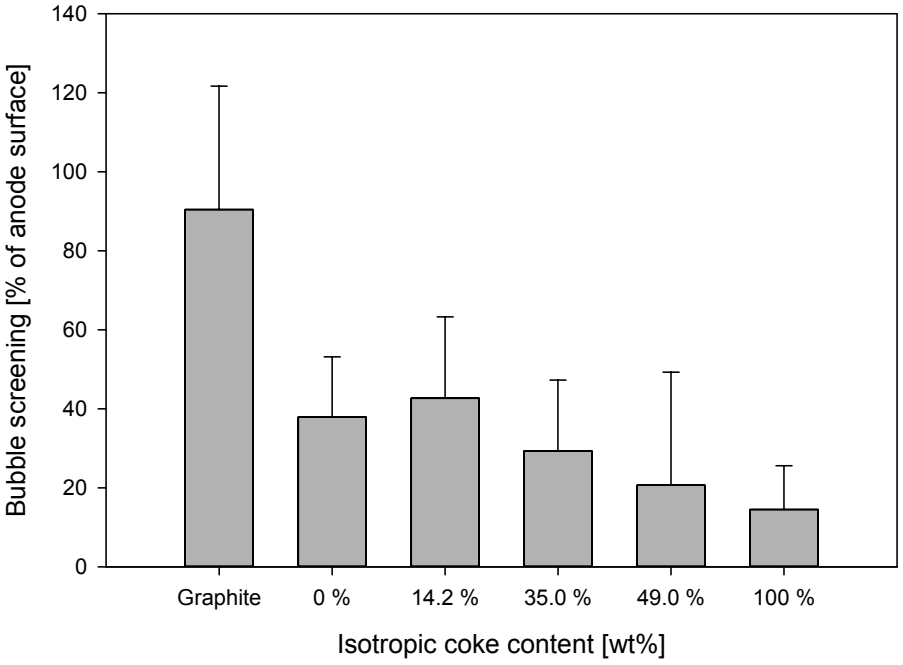

Figure 4.9: Percent of anode surface screened/covered by bubbles calculated from maximum and minimum current measured at constant voltage of 2.5 V. Error bars show one standard deviation, where n=4.

4.3.4 Wetting Properties of Polarised Anode Samples

Wetting properties between the anode and the electrolyte play an important role in the electrolysis cell, as better wetting gives a higher contact area between anode and electrolyte. The wetting properties of the pilot anode series, including graphite, were investigated using the immersion-emersion technique as described in [49, 54]. A four step experimental approach was used as described in the Materials and Methods section of this chapter. Figures 4.10-4.12 show examples of the raw data results from Steps 1-4 for one of the 0 % anodes. Figure 4.10 shows Steps 1 and 2 which are identical except that in step 1 the sample is a dry, virgin sample who has not been in contact with the electrolyte. As can be seen from Figure 4.10, the results from Step 1 and 2 are fairly similar. The various steps during the immersion-emersion sequence are described in the figure.

Figure 4.11 shows the immersion-emersion raw data during Step 3, where a current is applied for 10 s before the emersion. It is evident that the weight of the meniscus (m_σ) is higher in Step 3 compared with Steps 1 and 2 where the sample had not been polarised. Figure 4.12 shows a) raw data of Step 4, and b) corrected weight, m_m - m_t, of the sample during immersion where the weight in gas and the buoyancy effect has been subtracted as described in Equation 4.4. An arrow indicates the average m_m - m_t reported for each sample in Figure 4.13. The effect of the change in the meniscus length continues also in Step 4 as compared to Steps 1 and 2. This suggests that the change in wetting seen after polarisation is permanent due to adsorbed species as suggested by Solheim et al. [49].

Figure 4.13 shows a summary of the corrected weight and the calculated wetting angle from Equations 4.5 and 4.7. The reported values are average m_m-m_t values including one standard deviation of the horizontal region of the immersion as indicated with an arrow Figure 4.12 b). It is evident that there is a difference in the wetting conditions between the samples a) before and b) after polarisation, and for all samples the wettability of the anode towards the electrolyte is improved after polarisation. It is also evident that the wetting increases with isotropic coke content supporting the theory that wettability plays an active role in the bubble voltage response and bubble screening of the anode surfaces as seen in Figures 4.6 and 4.9, and also as described in [8, 54]. Einarsrud et al. [31] showed the importance in surface tension and wetting angle in order to fully describe the observed bubble behaviour in an experiment which was compared to modelled results. Better wetting between anode and electrolyte enhances the removal of gas from the anode surface.

The increased wettability for the 100 % isotropic coke anode compared with the 0 % anode and graphite was also found using the sessile drop technique [8], although, using the sessile drop technique gives different wetting angles when compared with this work. It has been argued that the immersion-emersion technique is more appropriate in order to describe the real wetting regime in electrolysis cells compared with sessile drop [54]. The reason for this is the larger size of the anode sample and the interface towards the electrolyte, and the fact that the sample used during sessile drop is flat with the electrolyte on top, making it an equilibrium measurement where the effect of velocity of the electrolyte is not taken into account. Lastly, during sessile drop experiments,

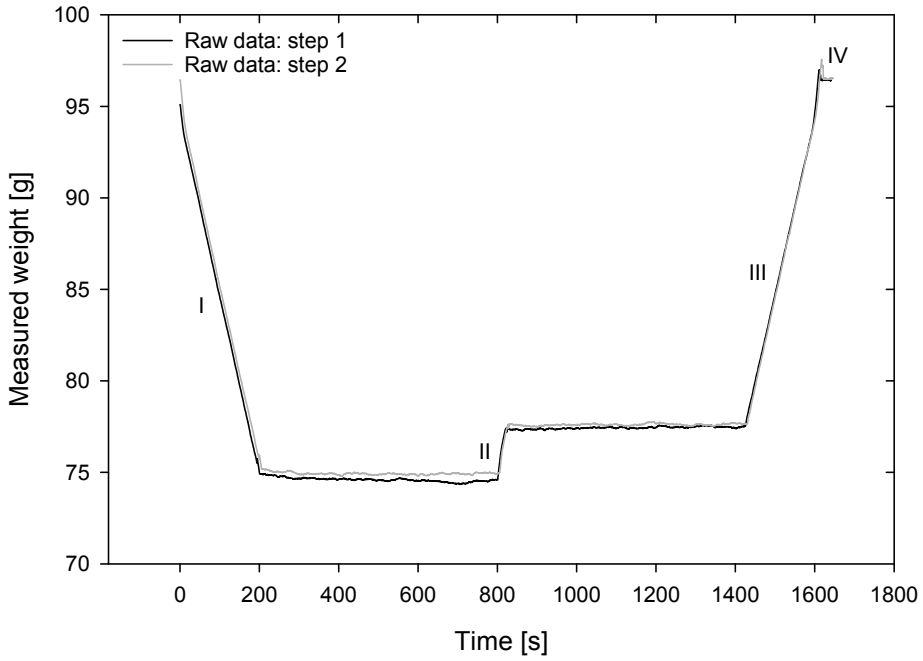

Figure 4.10: Example of raw data of measured weight *vs.* time for Step 1 (black) and Step 2 (grey) during the wetting test of a pilot anode showing I) immersion of the sample 40 mm into the electrolyte, II) changing the electrolyte height relative to the anode sample to 35 mm, III) emersion of the sample and IV) the observed meniscus that appeared when pulling the sample completely out of the electrolyte. Step 1 is when the dry anode is immersed into the electrolyte for the first time, and Step 2 is repeating Step 1 but now with "wet" sample. Samples are not polarised.

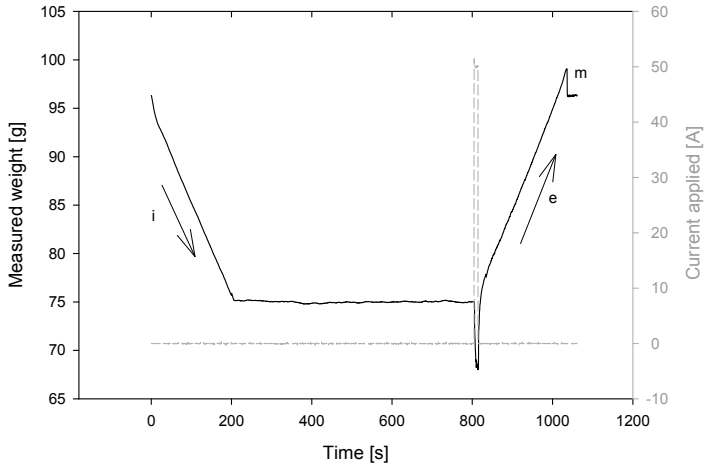

Figure 4.11: Example of raw data of measured weight *vs.* time for Step 3 (black) and current *vs.* time (grey) during the wetting test of a pilot anode where i=immersion, e=emersion and m=meniscus. A current of 50 A (0.7 A/cm^2) was applied for 10 seconds and the sample was subsequently pulled out of the electrolyte.

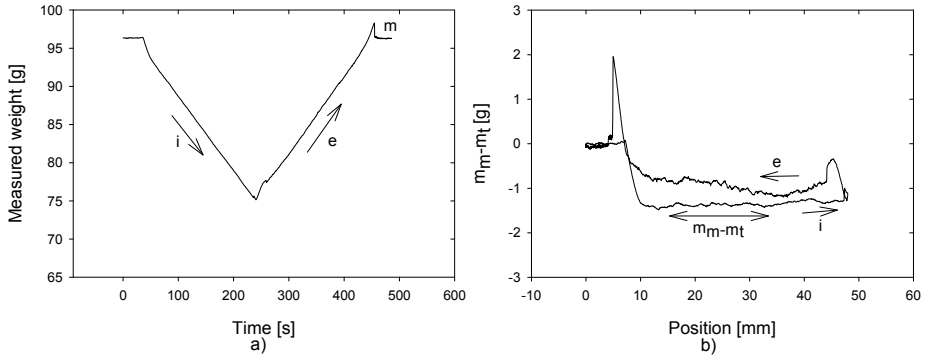

Figure 4.12: a) Example of raw data of measured weight *vs.* time for Step 4 during the wetting test of a pilot anode. b) The corresponding recorded weight (m_m) has been subtracted with the theoretical weight (m_t) *vs.* the position of the anode sample in the electrolyte for Step 4. In b), the part of the graph during immersion that has been used in order to report average m_m-m_t for the different anode samples in Figure 4.13 is indicated. i=immersion, e=emersion and m=meniscus.

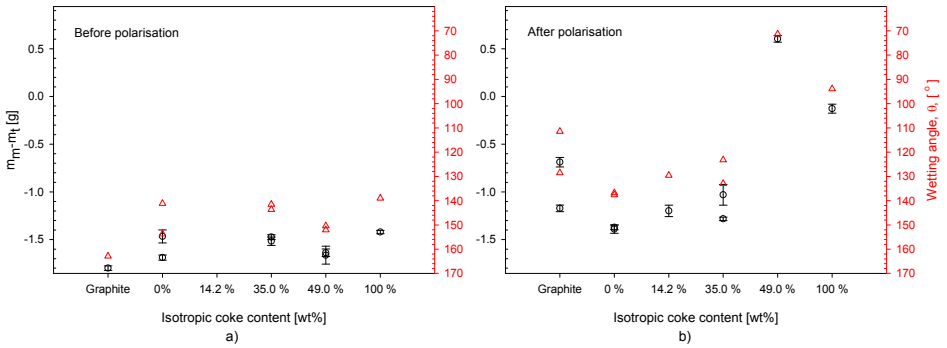

Figure 4.13: Difference between recorded weight, m_m, and theoretical weight, m_t, during immersion of the carbon samples into the electrolyte after polarisation at 0.7 A/cm^2 (50 A) (advancing angle of wetting) and calculated wetting angle from Equations 4.5 and 4.7, θ, *vs.* isotropic coke content. The reported values are average m_m-m_t values including one standard deviation of the horizontal region of the immersion as indicated with an arrow to the right in Figure 4.12.

the anode is also not polarised, making it a less relevant method for determining the real wetting conditions between anode and electrolyte. Nevertheless, the trends are essentially the same with both the sessile drop method and the immersion-emersion technique.

The sawtooth like bubble build-up pattern seen especially for the blended anodes in Figure 4.5, is caused by a reduction in screening before the bubbles are released. This may be explained either by bubbles being released from the anode surface before coalescing takes place or that the bubbles do coalesce, but the screening of the anodes are less due to the increased wetting observed for the anodes containing isotropic coke.

The effect of wetting between the anode:gas:electrolyte becomes increasingly important when the electrolyte is being depleted in Al_2O_3 when approaching the anode effect. These experiments were all performed in an electrolyte saturated in Al_2O_3, and it has been shown in literature that the wettability decreases with decreasing Al_2O_3 content [12, 49]. In further work it would be interesting to investigate the effect of isotropic coke content on the critical current density for the onset of the anode effect, to determine whether the anodes become less vulnerable to the anode effect due to the better electrolyte wettability of anodes containing isotropic coke as shown for high Al_2O_3 content.

4.4 Conclusion

Introduction of untraditional isotropic coke previously categorised as fuel grade coke, into carbon anodes has been shown to have positive effects on the amplitude of potential oscillations and on bubble screening of the anode surface in a laboratory cell with pilot anodes made from 0-2 mm aggregate. As the potential oscillations are reduced with only a small amount of isotropic coke blended in with a traditional anisotropic coke, potential energy savings can be made in the aluminium industry in terms of lower cell voltage (if these preliminary laboratory results can be confirmed in full scale operation). It is suggested that the porosity has some effect on the voltage response and bubble screening for the 100 % isotropic coke anode and the graphite anode. However, as the porosity patterns were similar for the rest of the pilot line (0-49.0 % anodes), the experimental results cannot be understood only as an effect of porosity, but should be related to the material properties. Differences in the observed potential oscillation amplitudes and the bubble screening for the anodes in the test series appear to correlate well with differences in wettability. Anodes containing isotropic coke showed better wettability between anode and electrolyte, and they also gave lower potential oscillation amplitudes and bubble screening compared to the anode entirely made from anisotropic coke. Upon introduction of isotropic coke in blends with various ratios to anisotropic coke, the very periodical voltage oscillation seen for both graphite and the pure anisotropic coke broke down. The bubble build-up pattern became more sawtooth-like, indicating a more irregular release of bubbles.

Acknowledgement

The work was financed by Hydro Aluminium and The Research Council of Norway through the research program called “HAL Ultra Performance Aluminium Cell”. Thanks are due to Aksel Alstad at the NTNU workshop for fabricating the experimental parts. Stein Rørvik, technicians at Hydro Aluminium Årdalstangen and Jannicke Kvello also deserve a thank you for help with various experimental techniques.

References

[1] K. Grjotheim and H. Kvande. *Introduction to Aluminium Electrolysis*. 2nd. Dusseldorf: Aluminium-Verlag, 1993.

[2] F. Nordmo and J. Thonstad. "On the anode effect in cryolite-alumina melts-IV. Gas composition and faradaic efficiency". *Electrochim. Acta* (1985), pp. 741–745.

[3] J. Thonstad, P. Fellner, G.M. Haarberg, J. Hives, H. Kvande, and Å. Sterten. *Aluminium Electrolysis: Fundamentals of the Hall-Heroult Process*. 3rd. Dusseldorf: Aluminium-Verlag, 2001.

[4] H. Kvande and W. Haupin. "Cell Voltage in Aluminum Electrolysis: A Practical Approach". *JOM* (2000), pp. 31–37.

[5] W. Haupin. "Interpreting the Components of Cell Voltage". *Light Metals* (1998), pp. 531–537.

[6] M. Cooksey, M.P. Taylor, and J.J.J. Chen. "Resistance Due to Gas Bubbles in Aluminum Reduction Cells". *JOM* (2008), pp. 51–57.

[7] R.J. Thorne, C. Sommerseth, A.P. Ratvik, S. Rørvik, E. Sandnes, L.P. Lossius, H. Linga, and A.M. Svensson. "Correlation between Coke Type, Microstructure and Anodic Reaction Overpotential in Aluminium Electrolysis". *J. Electrochem. Soc.* (2015), E296–E306.

[8] R.J. Thorne, C. Sommerseth, A.P. Ratvik, S. Rørvik, E. Sandnes, L.P. Lossius, H. Linga, and A.M. Svensson. "Bubble Evolution and Anode Surface Properties in Aluminium Electrolysis". *J. Electrochem. Soc.* (2015), E104–E114.

[9] C. Sommerseth, R.J. Thorne, A.P. Ratvik, E. Sandnes, L.P. Lossius, H. Linga, and A.M. Svensson. "Electrochemical Reactivity and Wetting Properties of Anodes Made from Anisotropic and Isotropic Cokes". *Light Metals* (2016), In press.

[10] J.A. Leistra and P.J. Sides. "Hyperpolarization at gas evolving electrodes-II. Hall-Heroult electrolysis". *Electrochim. Acta* (1988), pp. 1761–1766.

[11] R.J. Thorne, C. Sommerseth, A.M. Svensson, E. Sandnes, L.P. Lossius, H. Linga, and A.P. Ratvik. "Understanding Anode Overpotential". *Light Metals* (2014), pp. 1213–1217.

[12] H. Vogt. "Contribution to the interpretation of the anode effect". *Electrochim. Acta* (1997), pp. 2695–2705.

[13] A. Solheim, S.T. Johansen, S. Rolseth, and J. Thonstad. "Gas induced bath circulation in aluminium reduction cells". *J. Appl. Electrochem.* (1989), pp. 703–712.

[14] S. Fortin, M. Gerhardt, and A.J. Gesing. "Physical Modelling of Bubble Behaviour and Gas Release from Aluminum Reduction Cell Anodes". *Light Metals* (1984), pp. 721–741.

[15] K.E. Einarsrud and S.T. Johansen. "Modelling of bubble behaviour in aluminium reduction cells". *Prog. Comput. Fluid. Dy.* (2012), pp. 119–130.

[16] Y. Feng, M.P. Schwarz, W. Yang, and M. Cooksey. "Two-Phase CFD Model of the Bubble-Driven Flow in the Molten Electrolyte Layer of a Hall-Héroult Aluminum Cell". *Metall. Mater. Trans. B* (2015), pp. 1959–1981.

[17] R.J. Aaberg, V. Ranum, K. Williamson, and B.J. Welch. “The Gas under Anodes in Aluminium Smelting Cells. Part II: Gas Volume and Bubble Layer Characteristics”. *Light Metals* (1997), pp. 341–346.

[18] K. Zhang, Y. Feng, P. Schwarz, Z. Wang, and M. Cooksey. “Computational Fluid Dynamics (CFD) Modeling of Bubble Dynamics in the Aluminum Smelting Process”. *Ind. Eng. Chem. Res.* (2013), pp. 11378–11390.

[19] A.J. Simonsen, K.E. Einarsrud, and I. Eick. “The Impact of Bubble-Bubble Interaction on Anodic Gas Release: A Water Model Analysis”. *Light Metals* (2015), pp. 795–800.

[20] K.E. Einarsrud. “The Effect of Detaching Bubbles on Aluminum-Cryolite Interfaces: An Experimental and Numerical Investigation”. *Metall. Mater. Trans. B* (2010), pp. 560–573.

[21] K. Qian, Z.D. Chen, and J.J.J. Chen. “Bubble coverage and bubble resistance using cells with horizontal electrode”. *J. Appl. Electrochem.* (1998), pp. 1141–1145.

[22] Y. Wang, L. Zhang, and X. Zuo. “Fluid Flow and Bubble Behavior in the Aluminum Electrolysis Cell”. *Light Metals* (2009), pp. 581–586.

[23] L. Cassayre, G. Plascencia, T. Marin, S. Fan, and T. Utigard. “Gas Evolution on Graphite and Oxygen-Evolving Anodes during Aluminium Electrolysis”. *Light Metals* (2006), pp. 379–383.

[24] J. Xue and H.A. Øye. “Bubble Behaviour - Cell Voltage Oscillations during Aluminium Electrolysis and the Effects of Sound and Ultrasound”. *Light metals* (1995), pp. 265–271.

[25] Z. Zhao, Z. Wang, B. Gao, Y. Feng, Z. Shi, and X. Hu. “Observation of Anodic Bubble Behaviors using Laboratory Scale Transparent Aluminium Electrolysis Cells”. *Light Metals* (2015), pp. 801–806.

[26] B. Gao, H. Li, Z. Wang, and Z. Qiu. “A New Study on Bubble Behavior on Carbon Anode in Aluminum Electrolysis”. *Light Metals* (2005), pp. 571–575.

[27] L. Cassayre, T. Utigard, and S. Bouvet. “Visualizing Gas Evolution on Graphite and Oxygen-Evolving Anodes”. *JOM* (2002), pp. 41–45.

[28] H. Gudbrandsen, N. Richards, S. Rolseth, and J. Thonstad. “Field Study of the Anodic Overvoltage in Prebaked Anode Cells”. *Light Metals* (2003), pp. 323–327.

[29] Haupin W.E. “A Scanning Reference Electrode for Voltage Contours in Aluminum Smelting Cells”. *JOM* (1971), pp. 46–49.

[30] K.E. Einarsrud. “A Treatise on Interpolar Transport Phenomena”. PhD thesis. Norwegian University of Science and Technology, 2012.

[31] K.E. Einarsrud, I. Eick, P.J. Witt, A. Solheim, and Y. Feng. “Impact of Variable Bath Chemistry and Wetting on Gas Bubble Flow in Aluminium Electrolysis Cells”. *Light Metals* (2015), pp. 649–654.

[32] S.F. Jones, G.M. Evans, and K.P. Galvin. “Bubble nucleation from gas cavities - a review”. *Adv. Colloid. Interface* (1999), pp. 27–50.

[33] L.I. Kiss and S. Poncsák. “Effect of the Bubble Growth Mechanism on the Spectrum of Voltage Fluctuations in the Reduction Cell”. *Light Metals* (2002), pp. 217–223.

[34] J. Zoric and A. Solheim. “On gas bubbles in industrial aluminium cells with prebaked anodes and their influence on the current distribution”. *J. Appl. Electrochem.* (2000), pp. 787–794.
[35] K.E. Einarsrud, S.T. Johansen, and I. Eick. “Anodic Bubble Behaviour in Hall-Héroult Cells”. *Light Metals* (2012), pp. 875–880.
[36] R. Dorin and E.J. Frazer. “Operational characteristics of laboratory scale alumina reduction cells with wettable cathodes”. *J. Appl. Electrochem.* (1993), pp. 933–942.
[37] Z. Wang, B. Gao, H. Li, Z. Shi, X. Lu, and Z. Qiu. “Study on Bubble Behavior on Anode in Aluminum Electrolysis - Part I”. *Light Metals* (2006), pp. 463–466.
[38] B. Gao, X. Hu, J. Xu, Z. Shi, Z. Wang, and Z. Qiu. “Study on Bubble Behavior on Anode in Aluminum Electrolysis - Part II”. *Light Metals* (2006), pp. 467–470.
[39] K.E. Einarsrud and E. Sandnes. “Anodic Voltage Oscillations in Hall-Héroult Cells”. *Light Metals* (2011), pp. 555–560.
[40] T.M. Hyde and B.J. Welch. “The Gas under Anodes in Aluminium Smelting Cells. Part I: Measuring and Modelling Bubble Resistance under Horizontally Oriented Electrodes”. *Light Metals* (1997), pp. 333–340.
[41] E.W. Dewing. “The Chemistry of the Alumina Reduction Cell”. *Can. Metall. Quart.* (1991), pp. 153–161.
[42] D. Kasherman and M. Skyllas-Kazacos. “Effect of anode material and bath composition on bubble layer resistivity and gaseous volume fraction in an aluminium electrolysis cell with sloping anode and cathode”. *J. Appl. Electrochem.* (1991), pp. 716–720.
[43] G.J. Houston, M.P. Taylor, and D.J. Williams. “Predicting Bath Properties in Aluminium Smelting”. *Light Metals* (1988), pp. 641–645.
[44] N. Richards. “The Dynamics of Components of the Anodic Overvoltage in the Alumina Reduction Cell”. *Light Metals* (1998), pp. 521–529.
[45] C. Sommerseth, R.J. Thorne, S. Rørvik, E. Sandnes, A.P. Ratvik, L.P. Lossius, H. Linga, and A.M. Svensson. “Spatial Methods for Characterising Carbon Anodes for Aluminium Production”. *Light Metals* (2015), pp. 1141–1146.
[46] K. Kalgraf, M. Jensen, and T.B. Pedersen. “Theory of Bubble Noise, Bath Height and Anode Quality”. *Light Metals* (2007), pp. 357–361.
[47] M. Jensen, T.B. Pedersen, and K. Kalgraf. “Bubble Noise from Söderberg Pots”. *Light Metals* (2007), pp. 353–356.
[48] G.E. Totten and D.S. MacKenzie. *Handbook of Aluminum, Volume 2*. 1st. New York: Marcel Dekker, Inc., 2005.
[49] A. Solheim, H. Gudbrandsen, A.M. Martinez, K. Einarsrud, and I. Eick. “Wetting between Carbon and Cryolitic Melts. Part II: Effect of Bath Properties and Polarisation”. *Light Metals* (2015), pp. 671–676.
[50] R.G. Haverkamp. “An XPS study of the fluorination of carbon anodes in molten NaF-AlF_3-CaF_2”. *J. Mater. Sci.* (2012), pp. 1262–1267.
[51] R.G. Haverkamp and B.C.C. Cowie. “C K-edge NEXAFS study of fluorocarbon formation on carbon anodes in molten NaF-AlF_3-CaF_2”. *Surf. Interface. Anal.* (2013), pp. 1854–1858.

[52] L. Edwards, F. Vogt, M. Robinette, R. Love, A. Ross, M. McClung, R.J. Roush, and W. Morgan. “Use of Shot Coke as an Anode Raw Material”. *Light Metals* (2009), pp. 985–990.
[53] L. Edwards, N. Backhouse, H. Darmstadt, and M.-J. Dion. “Evolution of Anode Grade Coke Quality”. *Light Metals* (2012), pp. 1207–1212.
[54] A.M. Martinez, O. Paulsen, A. Solheim, H. Gudbrandsen, and I. Eick. “Wetting between Carbon and Cryolitic Melts. Part I: Theory and Equipment”. *Light Metals* (2015), pp. 665–670.
[55] W. Gebarowski, C. Sommerseth, A.P. Ratvik, E. Sandnes, L.P. Lossius, H. Linga, and A.M Svensson. “Interfacial Boundary between Carbon Anodes and Molten Salt Electrolyte”. *Light Metals* (2016), In press.
[56] A.D. McNaught and A. Wilkinson. *Compendium of Chemical Terminology*. 2nd. Oxford: IUPAC, 1997.
[57] L.P. Lossius, K.J. Neyrey, and L. Edwards. “Coke and Anode Desulfurization Studies”. *Light Metals* (2008), pp. 881–886.
[58] Micromeritics. *AutoPore IV 9500, Operator’s Manual V1.09*. Micromeritics, 2011.
[59] S. Rørvik and H.A. Øye. “A Method for Characterization of Anode Pore Structure by Image Analysis”. *Light Metals* (1996), pp. 561–568.
[60] K.N. Tran, A.J. Berkovich, A. Tomsett, and S.K. Bhatia. “Influence on Sulfur and Metal Microconstituents on the Reactivity of Carbon Anodes”. *Energy Fuels* (2009), pp. 1909–1924.
[61] Z. Kuang, J. Thonstad, and M. Sørlie. “Effects of Additives on the Electrolytic Consumption of Carbon Anodes in Aluminium Electrolysis”. *Carbon* (1995), pp. 1479–1484.
[62] L.P. Lossius, M. Lubin, L. Edwards, and J. Wyss. “Relationships between Coke Properties and Anode Properties - Round Robin 19”. *Light Metals* (2013), pp. 1183–1188.

5 The Effect of Baking and Mixing Temperatures on the Performance of Carbon Anodes for Aluminium Production

Abstract

Pilot scale anodes were produced using a coke aggregate consisting of a single source petroleum coke with a maximum grain size of 2 mm. These were used to investigate the effect of mixing temperatures and baking condition on physical parameters including density, specific electrical resistivity, air permeability, air and CO_2 reactivity, micro- and macroporosity, real surface area before and after electrolysis, morphology and structure of the electrode and electrochemical performance. The Mettler softening point of the coal tar pitch used was 119.1 °C and the mixing temperatures chosen were 150 °C and 210 °C. The equivalent baking temperatures chosen were 1150 °E (underbaking), 1260 °E (optimum baking) and 1350 °E (overbaking). Results show that a very low mixing temperature affects the anode quality to a large extent in terms of density, macroporosity, air permeability and specific electrical resistivity. The mixing stage was more critical for the anode quality than the baking temperature. At the lowest mixing temperature the anodes had a high number of large pores, due to insufficient wetting of the pitch towards the coke. It was shown that the electrochemically active surface area was slightly larger for the low mixing temperature anodes, even if the electrolyte does not penetrate into the largest pores. The overpotential measurements show little difference between anode samples. Hence, in small scale laboratory electrolysis experiments, the electrochemical performance of anodes made with varying baking and mixing temperature was similar even though the anodes vary in specific electrical resistivity.

5.1 Introduction

The aluminium industry utilises anodes produced from calcined petroleum coke and a coal tar pitch binder for production of aluminium by electrolysis. High quality anodes are crucial for maintaining stable production conditions in the electrolysis cells [1, 2]. Specific properties of high quality anodes are a high density, low electrical resistivity, low impurity level, low permeability and low air and CO_2 reactivity. Thus, optimization of the anode production is becoming more important. As discussed in several papers [1, 3–6], the quality of coke and pitch is changing and in the future it is expected that anodes will be produced from a wider range of coke qualities. In order to continue to produce high density anodes, the optimum baking, mixing and pitch levels have to be investigated and these parameters depend on the particular choice of coke and pitch. Decreasing anode density will affect electrical resistivity, permeability of the anodes, resistance to crack propagation and resistance to thermal shock [6]. Poor quality, low density, anodes will also cause excess carbon consumption and increase the risk of higher emission of greenhouse gases due to increased air and

CO_2 reactivity [7]. Furthermore, since the industry has moved towards increasing amperage in aluminium plants and increasing current density, the need for good quality anodes with a high apparent density is evident [6].

5.1.1 Mixing between Pitch and Coke

The first step when producing anodes is to mix coke, butts and pitch; anodes are then formed in the desired shape and finally baked at an elevated temperature. The mixing stage has been suggested to be the most critical step of the three production stages, as the initial interaction between coke and pitch has been shown to determine the final properties of the anode [8, 9]. These properties include thermal resistance, electrical resistivity, crushing and mechanical strength [9–11]. Also, according to Auguie et al. [12] a good anode is high in density, strong, low in specific electrical resistivity and has miniumum reactivity during electrolysis (CO_2). The authors state that an important factor for making high quality anodes is good cohesion of pitch towards the coke. In industrial scale anodes the target air permeability is usually well below 1 nPm [13]. At Dubal [14] anodes with an air permeability of 0.6 nPm have been demonstrated by optimising the mixing stage, coke blending and anode recipe, clearly showing the importance of these steps in anode production. High mechanical strength of the anode is a result of high bond strength between binder pitch and petroleum coke and, subsequently, good bond strength is a result of mechanical interlocking and adhesion of the pitch to the filler coke. To obtain good interlocking and adhesion, the pitch has to wet and penetrate pores of the coke well. Hence, the mixing and forming process is important for creating mechanically strong anodes [11]. However, quantitative studies on the effect of mixing temperature towards parameters like specific electrical resistivity, thermal resistance, density, mechanical strength and permeability are scarce in the open literature.

Currently in industry, the standard procedure is to mix the pitch binder and the calcined petroleum coke at a temperature ≈50°C above the softening point of the specific pitch used [7]. The wettability of the pitch is related to the softening point, surface tension and viscosity. A common method used for investigating the wettability between pitch and coke is by using the sessile drop test. This test measures the wetting angle between a coke substrate and a pitch droplet upon heating. There are some obvious shortcomings of this method. The coke substrate is fines only and the pitch droplet is very small. Also, the temperature regime during heating is different compared with the real mixing process.

Using the sessile drop method when investigating the pitch and coke wetting, it has been shown that a higher temperature than +50 °C above the pitch softening point may improve the wetting between the pitch and the coke giving a wetting angle much closer to 0° [9], and thereby achieve better coke-pitch interactions. At higher mixing temperatures, the viscosity of the pitch will be lower and the penetration and spreading of the pitch on the coke substrate is improved [9]. Mirchi et al. [5] and Rocha et al. [15] also found that when increasing the mixing temperature, the wettability between pitch and coke was increased. On the coke side the texture, particle size, porosity and

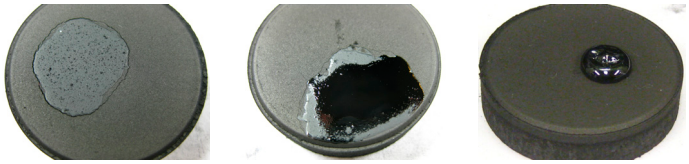

(a) (b) (c)

Figure 5.1: Examples of wetting of three different pitches towards a coke substrate a) Perfect wetting with penetration. b) Wetting but without penetration. c) No wetting - the Lotus effect. Images are courtesy of Hydro Aluminium.

chemical functional groups on the surface will affect the wettability [15]. Longer hold time at the mixing temperature is also beneficial in order to lower the contact angle between the pitch and the coke [9]. Increasing the mixing temperature also has the advantage that it enables a decrease of the pitch level in the anodes during anode production [16]. Figure 5.1 shows examples of pitch wetting toward a coke substrate with three different pitches, perfect wetting with penetration of the pitch towards the coke, wetting without penetration into the coke and poor wetting or the so-called Lotus effect where no wetting is seen between the coke and the pitch upon heating.

Rocha et al. [8, 15] and Couderc et al. [10] used a drop spreading test when investigating the wettability of pitch towards coke and it was found that the height of a pitch droplet towards a coke substrate decreases sharply upon heating, due to softening of the pitch, until it reaches a plateau. The temperature range at this plateau has been shown to vary between different pitch types. A plateau is reached as cohesive forces are greater than adhesive forces. When the temperature increases further, the adhesive forces become stronger and the pitch sample height then decreases sharply with temperature until full penetration of the coke is achieved. The softening of the pitch is determined by the pitch surface tension, and the pitch viscosity determines the penetration of the pitch into the coke particles [8, 15]. Sarkar et al. [9] found that a pitch containing high amounts of oxygen and nitrogen showed the best wetting properties. They concluded that the oxygen and nitrogen species present made the pitch more reactive towards coke.

The carbon substrate also plays a role towards the degree of penetration of pitch [17]. Sarkar et al. [9] found that high porosity cokes showed better wettability towards pitch, and that the chemical composition of the cokes played an important role in the bonding efficiency between the two phases. A coke rich in highly reaction oxygen and nitrogen surface groups such as CN, C-O and C=O, showed good wettability which was attributed to the ability to form new chemical bonds with the C-C/C=C components of the pitch. The coke that showed the poorest wettability towards pitch had high quantities of carbon-sulfur bonds. An explanation for this reduced wettability was that sulfur atoms on the surface of the coke can form intra or inter molecular hydrogen bonds which make them unavailable for hydrogen bonding with pitch [9].

Wilkening [6, 18] suggested that, in order to decrease the mixing time and also decrease the amount of crushing of large coke particles in the mixing process, a higher mixing temperature of up to 300-350 °C should be used. Additionally, the wetting of the pitch

on the coke substrate will be good at this temperature, and the end result will be better anodes with higher apparent density, higher strength, and up to 20 % lower electrical resistivity [6]. This will give better utilisation of the expensive pitch, and thus increase the anode production efficiency. By using high mixing temperature, Wilkening claims that a low mixing power will be needed.

5.1.2 Baking of Carbon Anodes

The carbonisation process of the pitch that takes place during the baking process increases the strength and electrical conductivity of the anodes [7, 19]. 2/3 of the pitch binder is transformed into coke, while 1/3 of the pitch is released as volatiles [13]. This carbonisation and volatilisation processes inevitably introduces porosity to the anode. However, the density and homogeneity of the anodes can be controlled by improved process control during the baking process. Good process control is achieved by designing baking furnaces with good temperature control, low ΔT throughout the furnace, and by reducing the heating rate [20, 21]. However, it is important to avoid overbaking in order to avoid desulfurisation of the anode [21]. Control of the baking heat treatment is not straight forward. Hydro uses the method of equivalent temperature as standard for measuring the baking temperature or baking level when producing anodes. Equivalent temperature (unit °E) is a measure of the level of calcination equivalent. The calcination equivalent is meausured in terms of the crystallographic parameter L_c, with a two hour heat treatment at a given temperature [22, 23]. Hence, the equivalent temperature is a function of both the temperature the sample sees, as well as the time it is exposed to this temperature. The method is described by the ISO standard (ISO 17499). L_c measurements of a reference coke that has been fired at various temperatures (e.g. 1050-1400 °E) for two hours provide a calibration curve for this specific reference coke [22]. Other anode producers may use other techniques like specific resistivity measurements, or multiple thermocouples to determine the baking level [20, 24].

Previously, the industry has experienced problems with anode quality (excess anode consumption and anode cracking) when increasing the amperage in the potroom [20, 25] and these problems could partly be solved through optimisation of the baking process. Jentoftsen et al. [26] observed a correlation between baking temperature, dust index and current efficiency in industrial electrolysis cells. An optimum baking temperature was determined to be approximately 1220-1250 °E. The anodic current efficiency dropped for anodes baked at low temperatures. However, Jentoftsen et al. do not mention whether any other changes took place in the production line in this specific time period e.g. mixing temperature alterations, pitch and coke quality.

The binder phase is thought to be more reactive to air and CO_2 than the coke phase, and means of reducing the reactivity of the anode are suggested by reducing the difference in reactivity between the binder phase and the coke phase [21, 27]. This can be obtained by using under-calcined coke, as a less ordered coke will also have a higher reactivity. Using under-calcined coke will give a more heterogeneous transition between coke and binder phase during the baking process, and a lower difference in reactivity

between the phases will be obtained. A more homogeneous anode is then produced and the tendency of the binder phase to be preferentially consumed during electrolysis decreases. One issue with using under-calcined coke is a reduction in anode density. However, industrial experiments showed that the carbon consumption (both air and CO_2 reactivity) of anodes produced with under-calcined coke was reduced compared with the reference anodes produced with standard calcined coke, despite the fact that the density of the baked anodes were slightly less [27].

5.1.3 The Effect of Sulfur Content in Carbon Anode Production

The sulfur content in petroleum cokes depends on the crude oil feedstock [28]. High-resin asphaltene feedstocks produce sponge cokes with a higher sulfur content compared to "honeycomb" coke. Most sulfur in coke structures mainly occurs in an organic form, bound to the carbon matrix, with thiophenes as the most likely abundant form [28, 29]. According to Ibrahim and Morsi [28], sulfur may exist as:

- Tiophenes bound to the organic carbon skeleton
- Naphtalenic or aromatic molecules attached to side chains
- Clustered molecules or between aromatic sheets
- Adsorbed, chemisorbed or condensed matter in coke pores or on the coke surface

At coke calcining temperatures up to 850 °C, sulfur in pores will be lost through desorption, and cracking of side chains. Between 850-1300 °C very little sulfur is lost. At temperatures above 1300 °C, decomposition of sulfur hydrocarbons such as thiophene start to occur [28, 29]. Desulfurisation will cause micropores (typically $<1\mu m^2$) to form, and this may give excessive carbon consumption through increased air reactivity [13, 31]. However, the critical temperature for desulfurisation of a coke is variable and it can be as high as 1400-1500 °C [29]. The initial sulfur concentration in the coke may determine the desulfurisation process and real density measurements of calcined coke indicate that high sulfur cokes show decreasing real density at calcining levels above 1600 K (so-called "puffing"), while low sulfur cokes show an increase in real density [28]. This indicates that low sulfur cokes do not necessarily see a "puffing" effect with increased microporosity due to desulfurisation even at these high temperatures.

For anodes, the rate of desulfurisation is generally constant, and a critical desulfurisation temperature is not seen. The desulfurisation process is also dependent on the hold time at the elevated temperature, and increasing hold time increases the rate of desulfurisation [29, 32]. Vogt, Ries and Smith [32] found that the resulting porosity of two anode samples varied with the baking process, even though the anodes had similar sulfur loss. One anode baked at 1150 °C with a holding time of 80 hrs lost 0.25 %

[2]Note that the IUPAC definition of porous materials deviate from the definition used in aluminium industry for microporosity: Microporous materials have pore diameter <2 nm, mesoporous materials have pore diameter in the range 2-50 nm and macroporous materials have pore diameters >50 nm [30]. This definition is not applied here. There is no consensus on the definition of microporosity within aluminium industry, although in the present work a definition for microporosity will include pores with diameter <1 μm, corresponding to the definition in [31].

sulfur compared with an anode baked at the same temperature but with a hold time of 20 hrs. The resulting porosity was 161 mm^3/g for the anode baked at 1150 °C and a holding time of 80 hrs. Another anode was baked at 1220 °C with a hold time of 20 hrs, also lost 0.25 % sulfur compared with the anode baked at 1150 °C and with a hold time of 20 hrs. However, the second anode had porosity of 155 mm^3/g. These results show that it is important how the sulfur is lost and not just the total amount of sulfur lost. Density measurements showed that shorter hold time at elevated temperatures lead to better anode properties irrespective of peak baking temperature [32]. Also, in general it has been found that the onset temperature for desulfurisation in high, normal and low sulfur cokes are the same, but the rate of desulfurisation is higher in high sulfur cokes than in normal and low sulfur cokes, respectively [29, 31]. Lossius et al. [31] found that for a low sulfur coke with 1 wt% sulfur hardly any desulfurisation was observed during baking. Edwards et al. [29] discusses that desulfurisation is a challenge for high calcined coke, as these cokes will desulfurise even more in the baking process compared to low calcined cokes. This was explained by sulfur-carbon structures being interrupted during the coke calcining process at high calcining temperatures. This will then cause further desulfurisation in the baking furnace.

As described above, the mixing temperature and the baking level (through desulfurisation and calcination and volatilisation of pitch) will affect the porosity of an anode. Higher porosity increases the real surface area of an anode. However, the real surface area is not necessarily the same as the electrochemically active surface area as has been shown qualitatively in Sommerseth et al. [33]. Here it was shown by X-ray computed tomography that even large pores in anodes were not penetrated with electrolyte when a frozen image of the electrode during electrolysis in a cryolitic melt was created, indicating that this internal pore surface area did not contribute to the electrochemically active surface area.

5.1.4 Purpose of this Work

In this work a range of anodes was prepared using the same recipe, and the same petroleum coke and industrial grade coal tar pitch. The factors varied during the pilot anode production were the equivalent baking temperature and the mixing temperature. Anodes were made with both a low mixing temperature of 150 °C compared to industrial standard (30 °C above the softening point of the pitch used) and a high mixing temperature of 210 °C (90 °C above the pitch softening point). The anodes were baked at various temperatures of 1150 °E, 1260 °E and 1350 °E. 1260 °E is the target equivalent baking temperature when producing anodes set by Hydro Årdalstangen for this specific coke. Thus, 1150 °E is defined as underbaked and 1350 °E is defined as overbaked where desulfurisation might be initiated [25, 31]. The purpose of the work was to investigate the effect of the mixing and baking temperature on the morphology and hence the physical properties of the anodes, like density and porosity. Furthermore, the electrochemical performance of the anodes was compared in lab-scale electrolysis experiments. Computed tomography was used for non-intrusive investigations of the internal morphology of the anodes before and after electrolysis, and similarly 3D optical microscopy was used to study changes in the surface morphology.

5.2 Materials and Methods

5.2.1 Pilot Anode Materials and Electrolyte

Pilot scale anodes (Ø = 130 mm, h = 180 mm) were produced by Hydro Aluminium from a single source industrial sponge type petroleum coke of anisotropic character and an industrial grade coal tar pitch. The particle size of the aggregate was 0-2 mm and this particle size was chosen to ensure a representative and fairly homogeneous surface of the area of the anode exposed in laboratory scale experiments. The recipe for producing the anodes was the same throughout the series and was based on combining 1-2 mm, 0-1 mm and a ball mill dust fraction. Two different mixing temperatures were used: 150 °C and 210 °C, and three different equivalent baking temperatures were used: 1150 °E, 1260 °E and 1350 °E. A graphite material from Svensk Specialgrafit AB (Ultrapure grade CMG) was used for comparison. The pitch binder used for production of the anodes had a Mettler softening point of 119.1 °C and a QI level of 7.8 %.

The electrolyte used when performing electrolysis was a cryolitic melt with a molar ratio of NaF to AlF_3 of 2.3 and saturated in aluminium oxide. The cryolite was a standard cryolite from Sigma Aldrich (>97 % purity) with an excess of AlF_3 of 9.8 wt% (industrial grade, sublimed in-house) and 9.4 wt% γ-Al_2O_3 from Merck. The same electrolyte composition was used in all electrochemical experiments.

5.2.2 Physical Analysis

The anodes were characterised using industry ISO methods for density (ISO 12985-1:2000), specific electrical resistivity (SER) (ISO 11713:2000), permeability (in house method at Hydro comparable to ISO 15906:2007) and coefficient of thermal expansion (ISO 14420:2005, but the temperature range was extended to 300-700 °C and a sample size of 20 mm diameter and 75 mm height). Air and CO_2 reactivity tests were performed using in-house methods developed at Hydro Aluminium similar to ISO 12989-1 and ISO 12988-1, respectively. Additionally, metal and sulfur impurities in the carbon anodes were characterised using X-Ray fluorescence (XRF). The methodology is described in ISO 12980:2000. All these tests were performed as part of routine characterisation at Hydro Aluminium Årdalstangen.

5.2.3 Porosity and Texture

A Micromeritics AutoPore IV 9500 Mercury Porosimeter was used in order to measure microporosity of the carbon anode samples. Bulk samples of ~2.2 g were filled with Hg at pressures 0.50-60000 psia ($3.45 \cdot 10^3$-$4.14 \cdot 10^8$ Pa) and the amount of intruded Hg was correlated to the microporosity ranging from 0.003-360 μm in pore diameter [34].

Porosity and microstructure of the anodes were also investigated through optical microscopy. 10 mm cores of anode samples were mounted in epoxy resin under vacuum (Epofix two-component epoxy with Epodye green fluorescent dye from Struers,

Denmark). When set, samples were ground and polished stepwise down to 1 μm and studied in an optical microscope. For porosity measurements a selective filter that only included wavelengths equal to blue light or shorter was used. A fluorescent light was produced when using this filter (named B5). The filter ensured a good contrast between the pores filled with epoxy resin and the carbon sample. 192 individual images of each sample was taken and then "stitched" together to give an image of the entire surface. The magnification of the measurement was x100. Custom written macros to the NIH image software were used and the procedure to analyse the porosity from fluorescent images followed the work of Rørvik and Øye [35].

When analysing the texture of the anodes another macro written for the NIH software was used in order to characterise the anodes in terms of both mosaic index and fiber index [36]. The mosaic index and fiber index can be related to the degree of isotropy and anisotropy. A magnification of x250 was used and a representative area of the samples (192 images stitched together) was investigated under polarised light.

5.2.4 X-Ray Computed Tomography

X-ray computed tomography (CT) was used to investigate qualitatively the pore distribution and structure on surface and interior of the anode samples. It was also used to investigate electrolyte distribution on the anode surface during electrolysis; a "frozen image" of the anode sample during electrolysis was created by pulling the sample out of the electrolyte with the current on (hot-pulling), and quickly cooled, before imaging. The method of hot-pulling has also been described elsewhere [33]. Multiple tomographs were recorded through cross-sections of the entire sample (height = 5 mm) creating a 3D image of the entire sample.

The anode design and the electrolysis cell used for CT scanned samples are shown in Figure 5.2. This experimental setup is similar to the one described elsewhere [37, 38]. The anodes were scanned before and after electrolysis at 1.0 A/cm^2 for 1800 s. The walls of the graphite crucible acted as the cathode and the bottom of the crucible was shielded using an alumina disk. This was done in order to ensure fairly straight current lines toward the crucible wall.

5.2.5 Confocal Microscopy for Surface Analysis

A simple rod shaped anode assembly was used for surface roughness investigations. Cores of 10 mm were drilled from the pilot anodes and the horizontal surface area was ground step-wise down to P#4000 using SiC paper. The horizontal circular surface area was investigated in terms of surface roughness using a confocal microscope (Infinitefocus from Alicona 3D). Multiple images were recorded and then "stitched together" in order to create one image of the entire sample. The instrument measured projected surface area and true area by including the area in voids and pores. The ratio between true area over projected area (TA/PA) was reported. The resolution was 410 nm and the total area scanned was 0.785 cm^2. Electrolysis was performed on the samples in an electrolyte, with the same composition as previously described, for

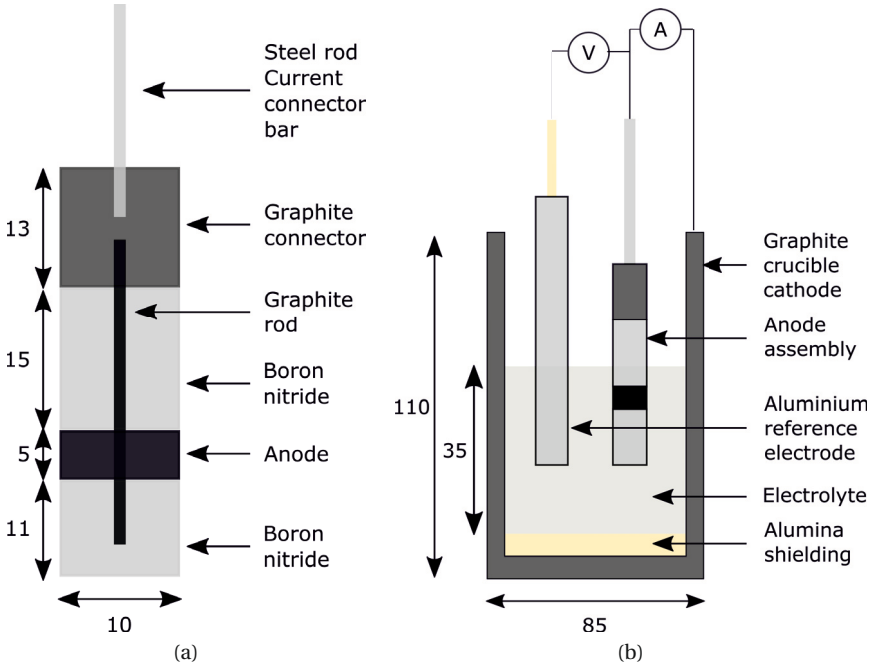

Figure 5.2: Electrochemical experimental setup used when electrolysing samples for CT scanning and during general electrochemical testing. All measures indicated in the figure are in mm. a) Vertical anode assembly. b) A principle sketch of the electrolysis cell used with the aluminium reference electrode, the graphite crucible acting as the cathode, the vertical anode assembly and the electrolyte.

25 mins at 1.0 A/cm^2. The remaining electrolyte on the anode surface was removed in a solution saturated in $AlCl_3$, and the horizontal end surface was then analysed in the confocal microscope to investigate the post-electrolysis surface roughness.

5.2.6 Electrochemical Measurements

All electrochemical tests were performed using a Zahner IM6 potentiostat with built in electrochemical impedance spectroscopy (EIS) module. The potentiostat had a PP201 20 A booster from Zahner-Elektrik.

The anodes were tested electrochemically by chronopotentiometry, EIS and cyclic voltammetry (CV). In all electrochemical experiments, the carbon anode was the working electrode, the graphite crucible walls acted as the counter electrode and potentials were measured towards an in-house produced aluminium reference electrode as described in [39]. The aluminium reference electrode is further described in Appendix A. All potentials in this chapter are quoted with respect to aluminium. The anode setup and laboratory electrochemical cell used are shown in Figure 5.2. The vertical anode setup will minimise bubble noise from CO_2 gas formed during

electrolysis, as previously shown [37]. The graphite connector, boron nitride (BN) shields and carbon anode were threaded on a Ø = 3 mm graphite rod that ensured electrical contact from the stainless steel current connector bar to the anode sample. The anodes were investigated by preconditioning by electrolysing at 1.0 A/cm^2 for 200 s. Then chronopotentiometry was performed at 1.0 A/cm^2 for 200 s and the data reported in this paper is the average of the potential response for the last 50 s. The potential has then been IR corrected using the series resistance (R_S), obtained by EIS at open circuit potential (OCP) and extracted from Nyquist plots (i.e. Z_{Re} at intercept when Z_{Im} is zero).

EIS spectra were collected for the anode materials at an applied voltage of 1.5 V (non-IR corrected) in the frequency range 100 000–0.1 Hz. The amplitude was 50 mV. The EIS spectra have been modelled using two circuits: the simple LR(CR) circuit and the more complex LR(Q(R(LR))) circuit as described by Harrington and Conway [40], except that the ideal double layer capacitance has been replaced by a constant phase element, Q (or often denoted as CPE). These circuits are further explained in Appendix C. In [40], this equivalent circuit was derived for a general reaction sequence involving intermediately adsorbed species. Introduction of the constant phase element is reasonable, since the anodes studied here have a relatively high surface roughness [41]. The simple LR(CR) circuit is used to extract data for the double layer capacitance (C_{dl}) directly, while the LR(Q(R(LR))) circuit was used to extract C_{dl} indirectly by approximating the effective capacitance on the surface ($C_{eff,surf}$) using Equation 5.1 below (same as Equation 15 in Orazem et al. [42], developed for faradaic systems).

$$C_{eff} = Q^{1/\alpha}\left(\frac{R_s(R_{CT_1}+R_{CT_2})}{R_s+R_{CT_1}+R_{CT_2}}\right)^{(1-\alpha)/\alpha} \tag{5.1}$$

In Equation 5.1, R_S, R_{CT_1} and R_{CT_2} are the series resistance, the first charge-transfer resistance and the second charge-transfer resistance, respectively. α is the dimensionless constant phase element exponent.

Cyclic voltammetry (CV) was performed at a slow scan rate of 100 mV/s. Three consecutive scans were recorded. Experience with the electrochemical setup has shown that the results obtained at this slow scan rate is comparable to polarisation curve measurements. The cyclic voltammograms may thus be assumed to provide information on the charge transfer resistance/electrochemical activity of the electrodes, as a supplement to the chronopotentiometric measurements.

5.3 Results

5.3.1 Physical Properties of the Anodes

Table 5.1 shows the physical parameters of the anode materials varying in baking and mixing temperatures. In Table 5.1 LM-HB, LM-MB, LM-LB-A and LM-LB-B denotes the anodes made with low mixing temperatures (LM, 150 °C) and high (1350 °E), medium (1260 °E) and low (1150 °E) baking temperatures, respectively. A and B are replicates of pilot anodes made with low mixing and baking temperatures. Similarly, HM-HB, HM-MB and HM-LB denote anodes made with high mixing temperature (HM, 210 °C) and high (1350 °E), medium (1260 °E) and low (1150 °E) baking temperatures. This labelling system will be used consistently throughout this paper.

Table 5.2 shows impurity levels for a baked anode made from the same coke and pitch as the anodes in this study determined by X-ray fluorescence (XRF). This anode was mixed at 168 °C and baked at 1230 °E (IM-MB).

Table 5.1: Physical properties of the anodes. SER = Specific el. resistivity, Perm. = Permeability, CTE = Coefficient of thermal expansion and CO_2 and air reactivity.

Anode	T_{baking}	T_{mix}	Density	SER	Perm.	CTE	R_{CO_2}	R_{Air}
	°E	°C	g/cm^3	$\mu\Omega$m	nPm	μm/mK	mg/cm^{2}h	mg/cm^{2}h
Graphite	N/A	N/A	1.771	12.7	0.20	N/A	2.5	0.3
LM-HB	1350	150	1.554	60.4	3.18	4.00	18.5	29.8
LM-MB	1260	150	1.526	65.1	5.31	3.93	17.5	46.3
LM-LB-A	1150	150	1.502	73.4	6.88	4.10	14.7	41.5
LM-LB-B	1150	150	1.552	64.3	4.09	3.96	12.1	37.5
HM-HB	1350	210	1.598	57.4	1.66	4.03	16.5	26.9
HM-MB	1260	210	1.576	59.7	1.40	4.07	15.0	47.9
HM-LB	1150	210	1.584	60.3	1.27	4.12	13.0	48.1

Table 5.2: Impurity levels obtained by XRF for graphite and a baked anode made from the same coke and pitch as the ones in this study (IM-MB).

Anode	Na	Si	P	S	Ca	V	Fe	Ni	Zn	Pb
	ppm	ppm	ppm	%	ppm	ppm	ppm	ppm	ppm	ppm
Graphite	9.5	10.0	1.0	0.0	11.0	1.0	25.0	3.0	1.0	1.0
IM-MB	55.5	108	11.0	0.9	24.5	69.5	287	44.5	5.0	7.0

5.3.2 Porosity and Texture

The porosity distribution in the anodes was measured by optical microscopy and Hg porosimetry. Figure 5.3 shows porosity images at a magnification of x100 obtained by optical microscopy of anodes with varying mixing and temperature regimes. 10 mm anode samples were mounted in fluorescent epoxy. The epoxy created a good contrast between the carbon sample and the voids of the pores, making the pores easily detectable by using a filter that enhanced this contrast. Black spots in the images represent closed pores that were not possible to fill with epoxy. The figure shows the anode samples with fluorescent epoxy resin filling the pores and it can be seen that LM-LB-A and LM-LB-B anodes have a large network of open porosity. Also the LM-HB and LM-MB anodes have a larger network of open porosity than the high mixing temperature anodes. Microporosity was measured using Hg porosimetry and the results from these tests shown in Figure 5.4. Figure 5.5 shows porosity measurements of the anodes *vs.* diameter of the pores obtained by optical microscopy.

Figure 5.6 shows fiber index and mosaic index of the anodes. Texture analysis of the samples was performed in the optical microscope by investigation of the samples under polarised light at a magnification of x250 and using the NIH software, modified by Rørvik et al. [36] to determine the texture. The average fiber index and mosaic index were measured as an average of 192 frames; these parameters relate to the alignment and fineness of optical domains. The 192 frames did not cover the entire surfaces of the samples, but tests have shown that the average fiber index and mosaic index do not change above 100 frames [36]. Hence, 192 frames give a representative texture image of the sample surface (total sample area of 4.6x4.6 mm^2 randomly spread out on the anode surface).

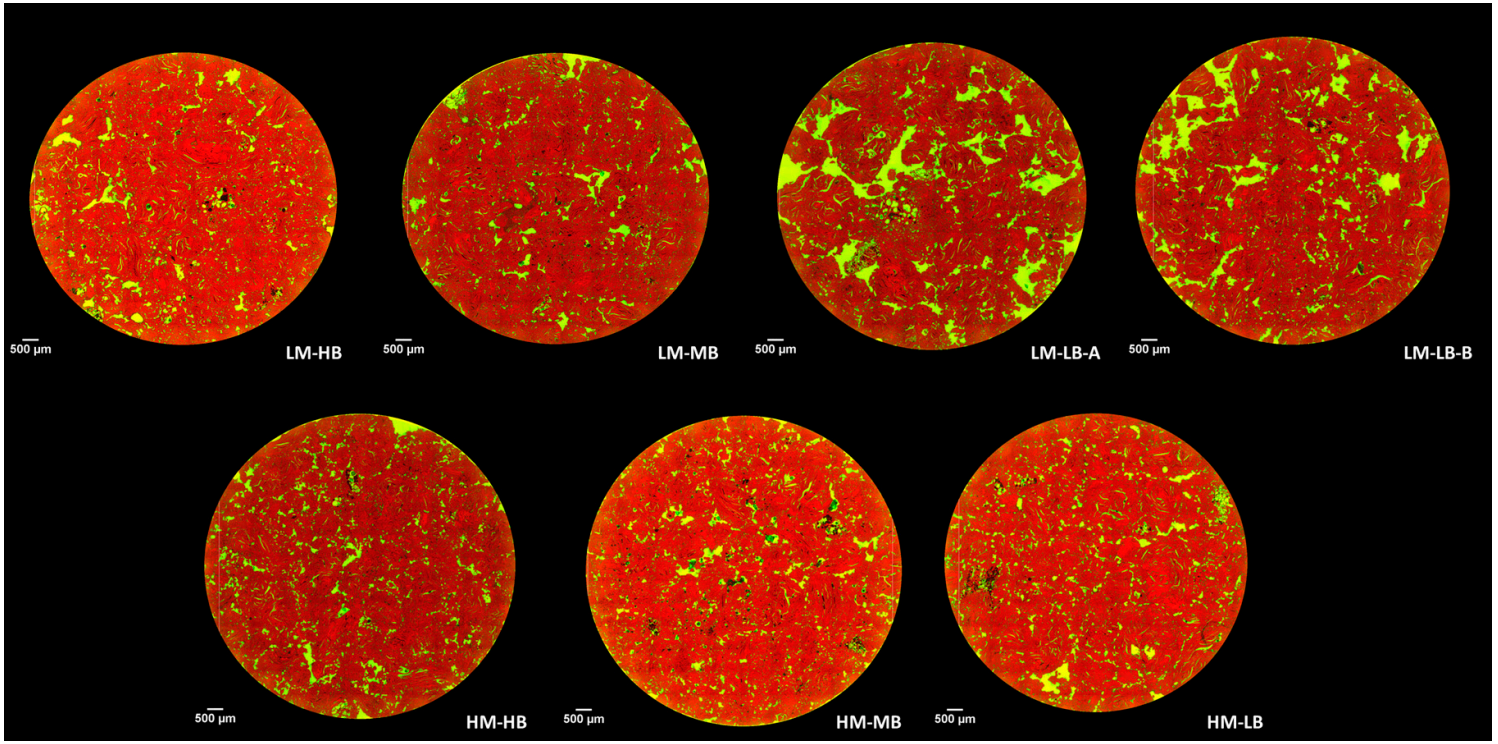

Figure 5.3: Optical microscopy images showing the porosity in the different anode materials.

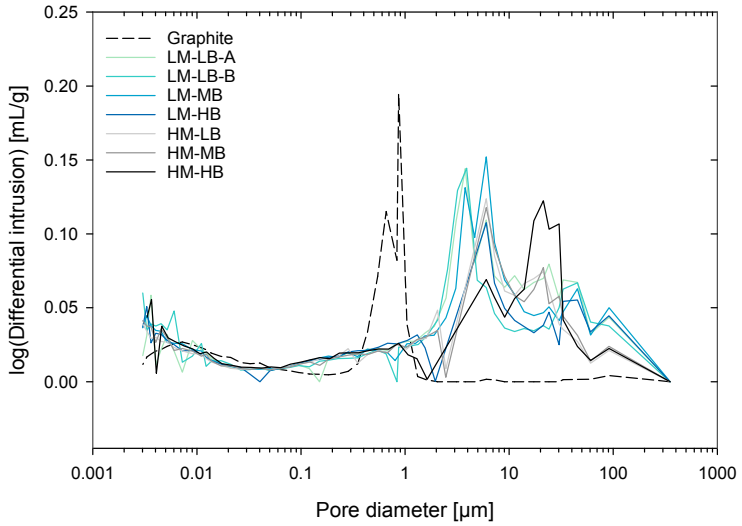

Figure 5.4: Differential intrusion of mercury into pores *vs.* pore size diameter. Results from one parallel per anode material, except for anode HM-HB where the average of the two parallels is shown.

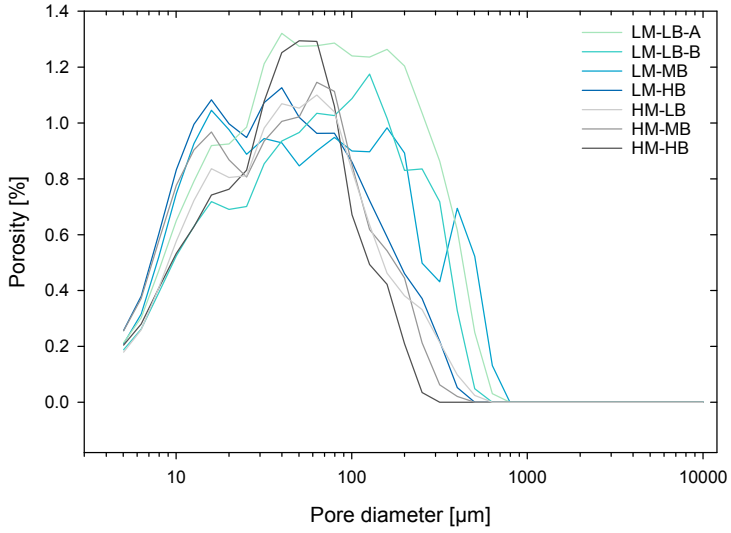

Figure 5.5: Porosity *vs.* pore diameter size obtained by optical microscopy. The results are averages between two or four parallels.

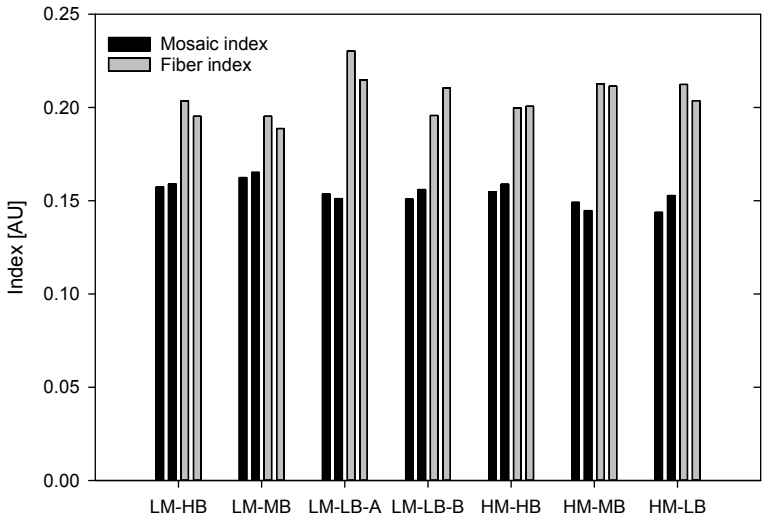

Figure 5.6: Mosaic index and fiber index of the anodes obtained by optical microscopy under polarised light. Results are shown for two parallels.

5.3.3 X-Ray Computed Tomography

The effects of mixing and baking temperature on the internal morphology of the anodes were studied by computed tomography (CT), and images of the anodes varying in baking and mixing temperature are shown in Figures 5.7-5.13. The images show the same cross-sections of the interior of the anodes before and after electrolysis for 1.0 A/cm^2 for 30 mins.

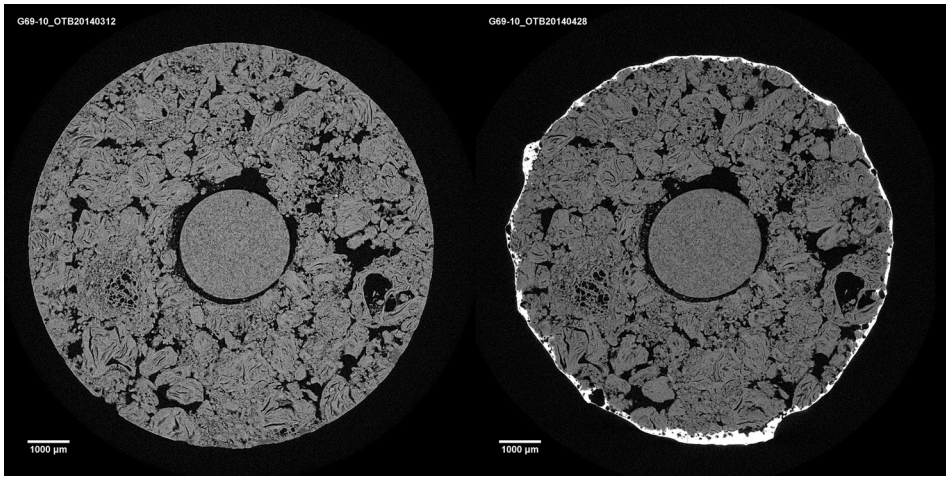

(a)

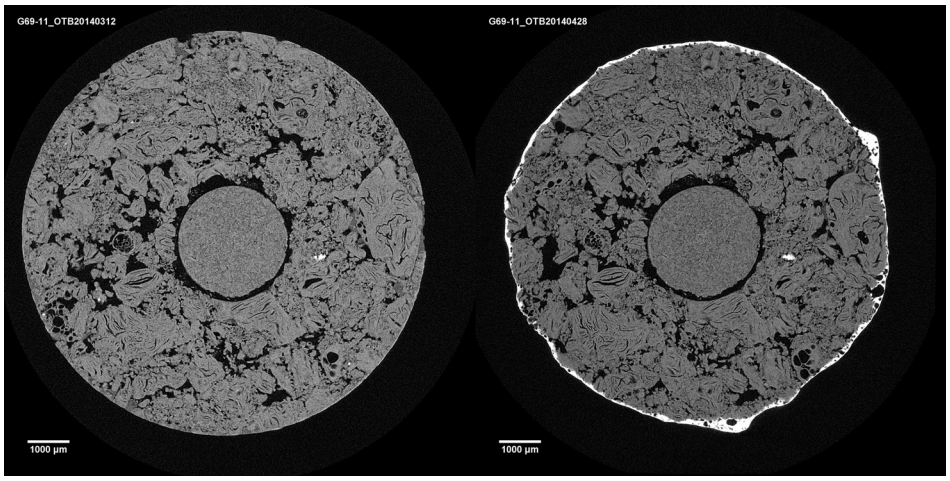

(b)

Figure 5.7: CT images of an interior cross-section of the anodes before and after electrolysis. a) and b) show anode LM-LB-A parallels 1 and 2, respectively.

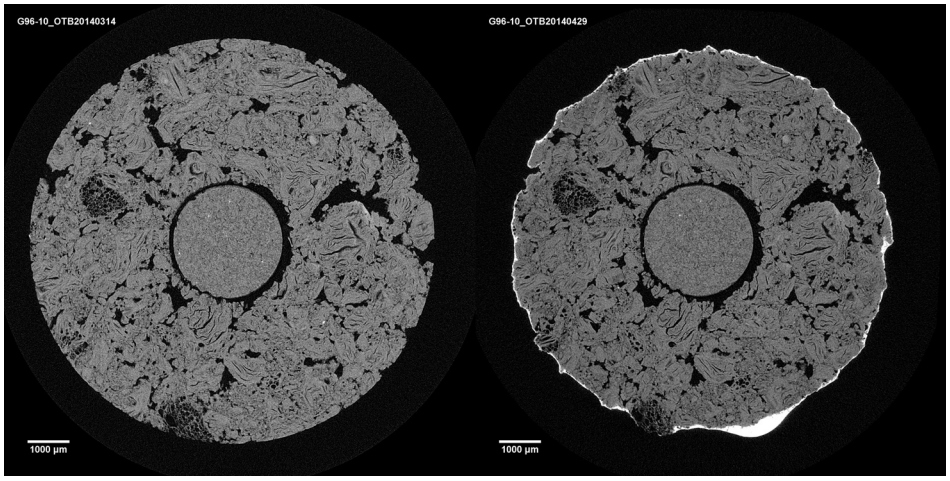

(a)

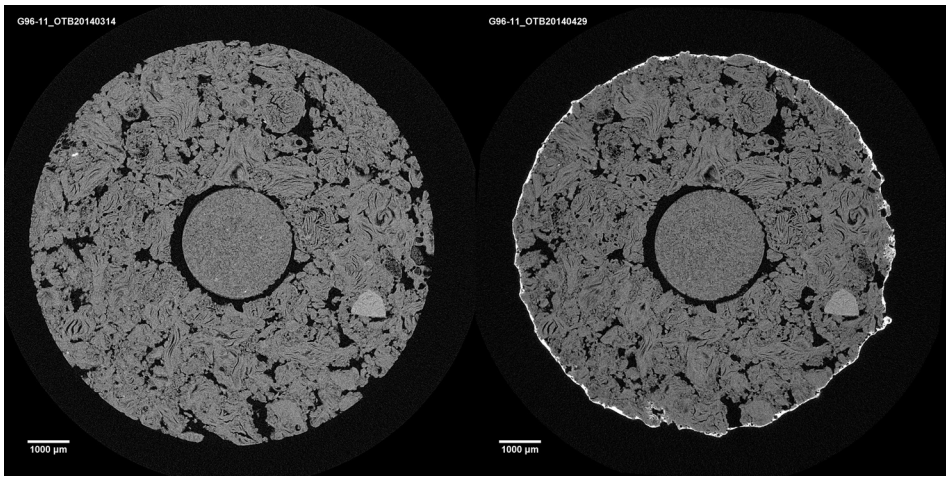

(b)

Figure 5.8: CT images of an interior cross-section of the anodes before and after electrolysis. a) and b) show anode LM-LB-B parallels 1 and 2, respectively.

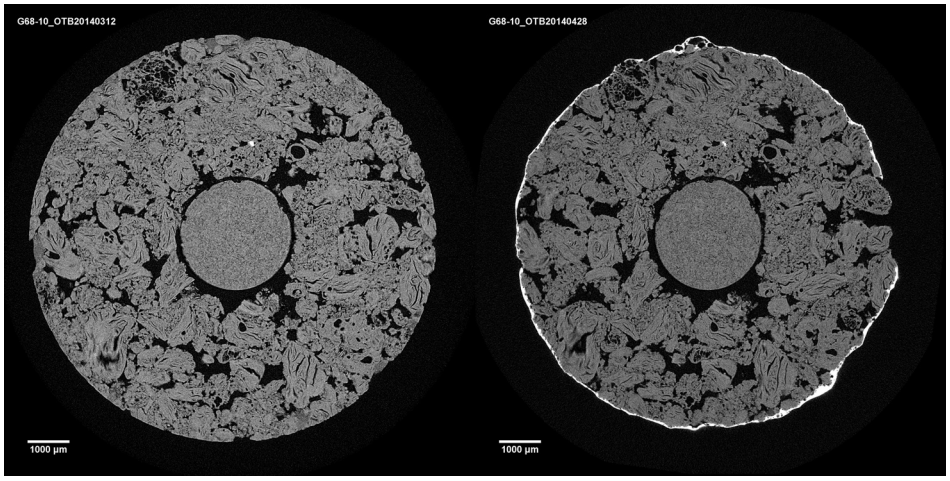

(a)

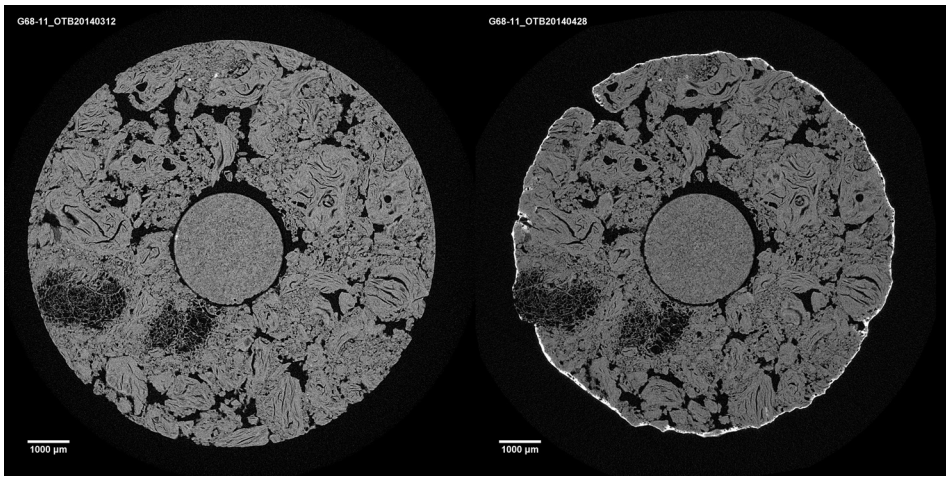

(b)

Figure 5.9: CT images of an interior cross-section of the anodes before and after electrolysis. a) and b) show anode LM-MB parallels 1 and 2, respectively.

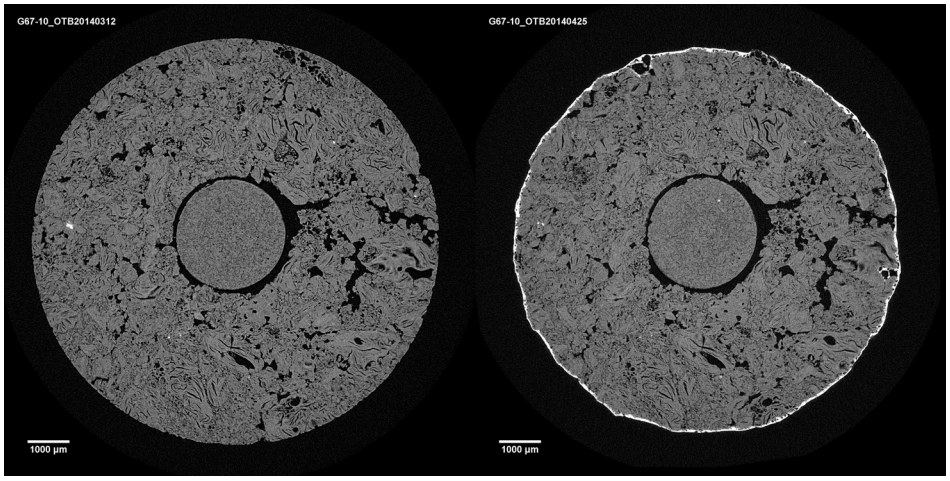

(a)

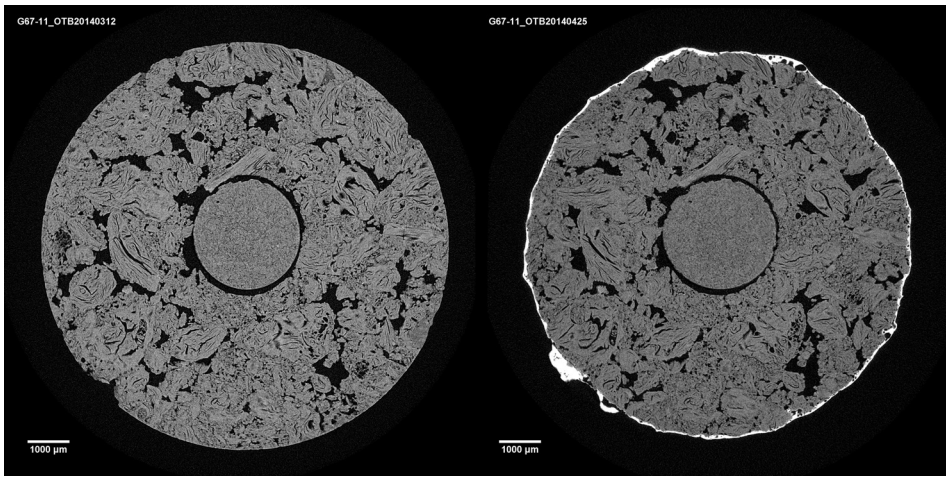

(b)

Figure 5.10: CT images of an interior cross-section of the anodes before and after electrolysis. a) and b) show anode LM-HB parallels 1 and 2, respectively.

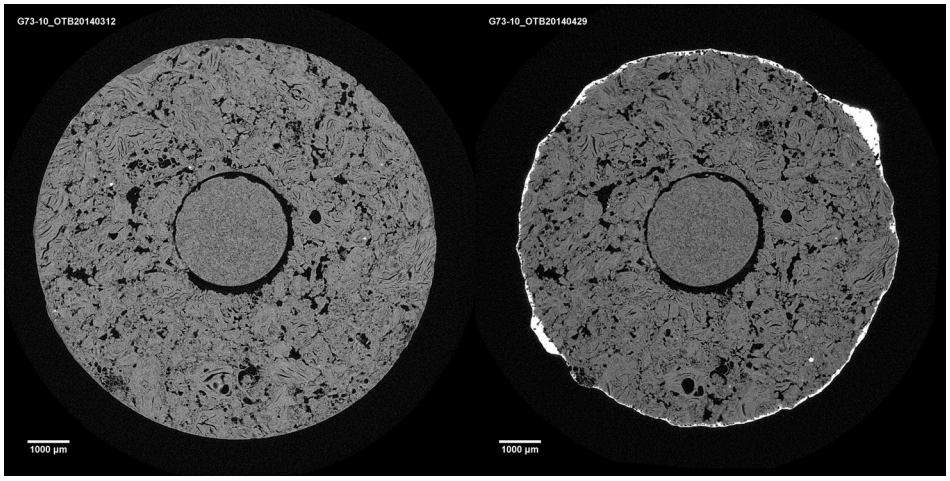

(a)

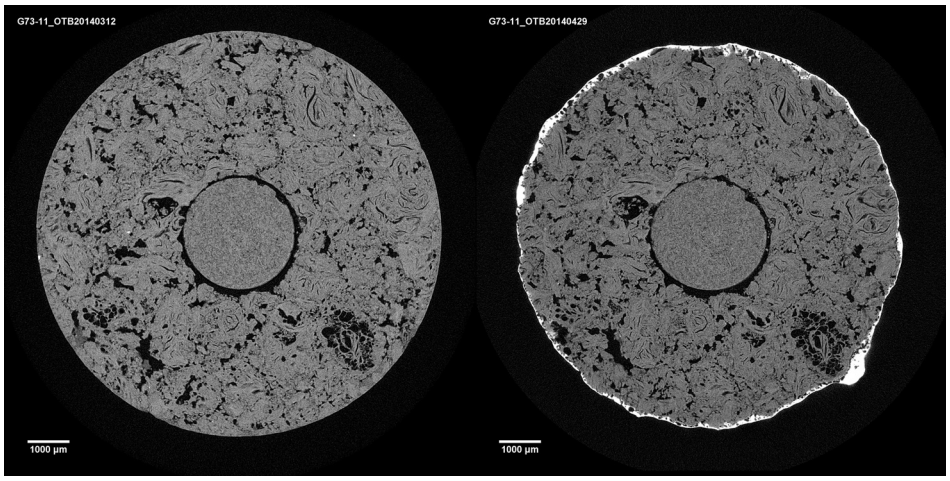

(b)

Figure 5.11: CT images of an interior cross-section of the anodes before and after electrolysis. a) and b) show anode HM-LB parallels 1 and 2, respectively.

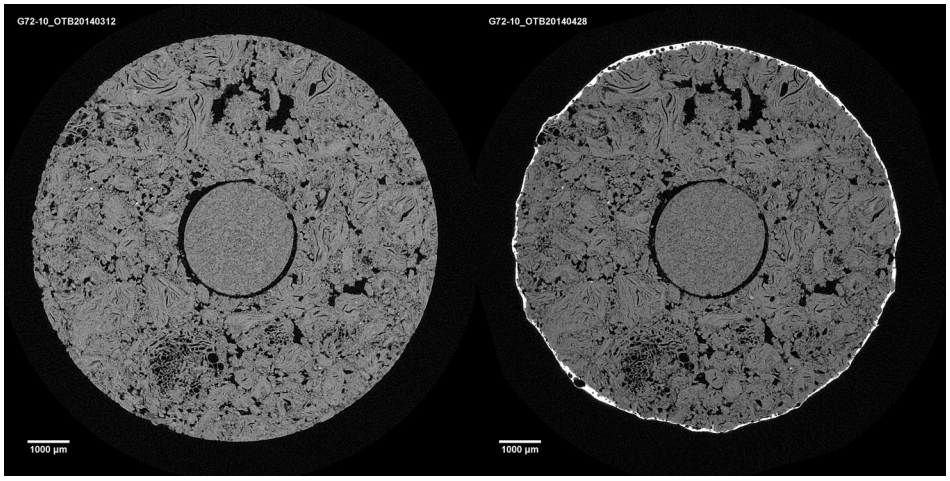

(a)

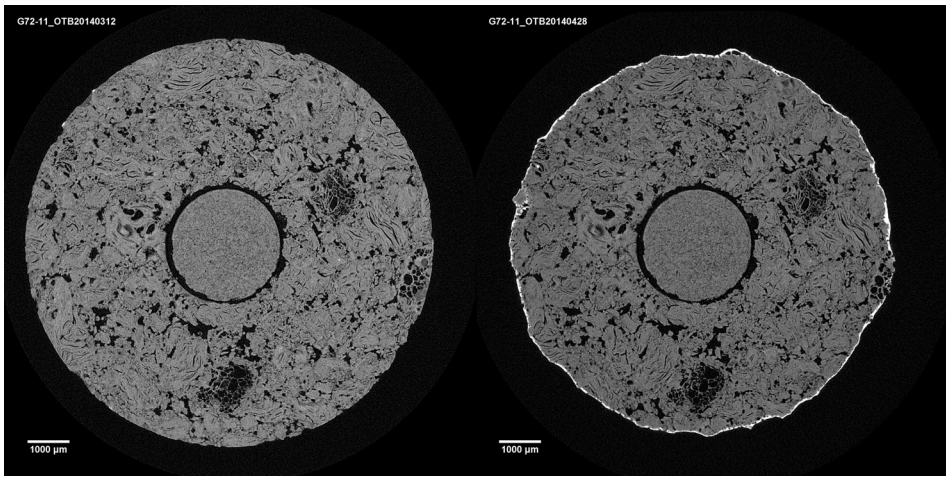

(b)

Figure 5.12: CT images of an interior cross-section of the anodes before and after electrolysis. a) and b) show anode HM-MB parallels 1 and 2, respectively.

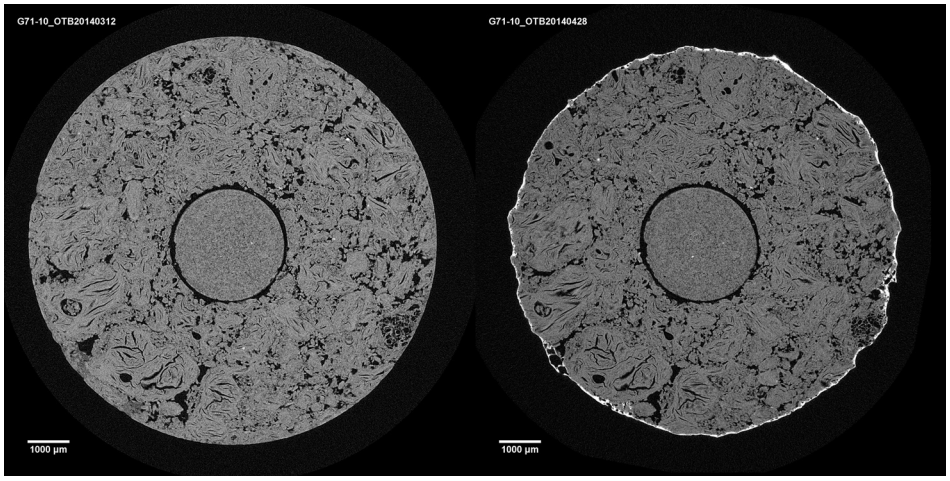

(a)

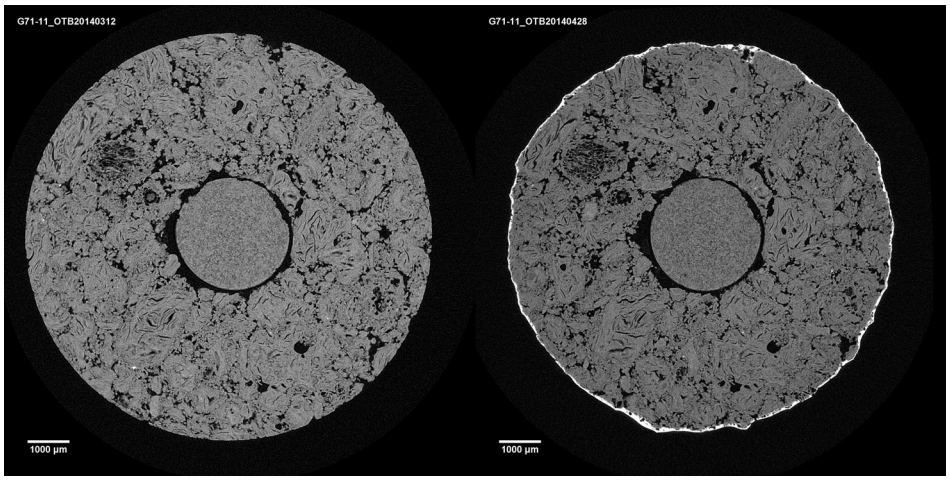

(b)

Figure 5.13: CT images of an interior cross-section of the anodes before and after electrolysis. a) and b) show anode HM-HB parallels 1 and 2,respectively.

5.3.4 Surface Roughness Determined by Confocal Microscopy

Figure 5.14 shows the ratio of true area over projected area (geometric 2D area) (TA/PA) for the anodes varying in baking and mixing temperature. The investigated area on the anodes was the horizontal circular area of cores of 10 mm that had been ground with SiC down to P#4000 (squares). Circle points show TA/PA on the same anode samples after they had been electrolysed for 25 mins at 1.0 A/cm^2 and the electrolyte had been removed by soaking in a solution saturated with $AlCl_3$. The true area/projected area measurement of one of the HM-HB sample after electrolysis is considered an anomaly.

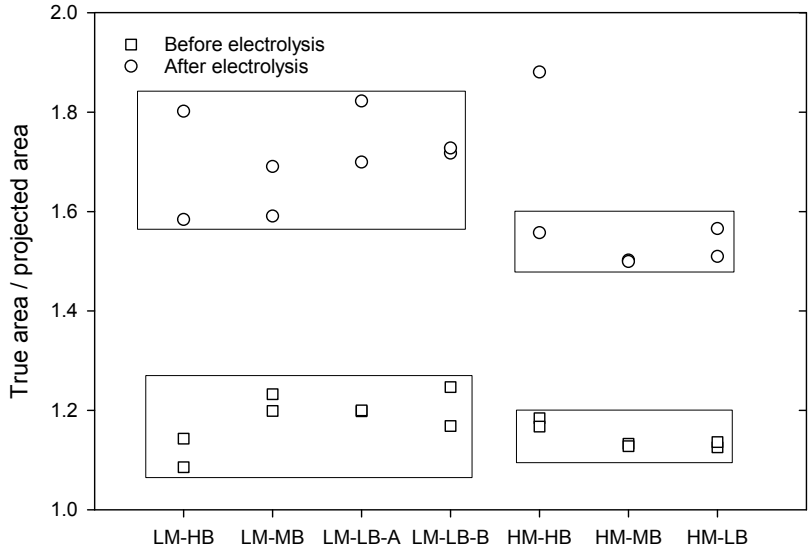

Figure 5.14: Ratio of true area over projected area obtained by confocal microscopy on freshly cut samples ground with SiC paper down to P#4000 (squares) and electrolysed samples (circles) at 1.0 A/cm^2 for 25 mins. The low and high mixing temperature anodes have been "boxed" together, respectively.

Figures 5.15 and 5.16 show some examples of images collected from the confocal microscope of anodes LM-MB and HM-MB, respectively. In both Figures 5.15 and 5.16, a) and c) show the before and after electrolysis images of the surface of the anode, parallel 1. The images are "stitched together" to show the entire surface of the anode (Ø=10 mm). b) and d) show contour images of the anode surface before and after electrolysis. Images e)-h) show the same as previously described for parallel 2.

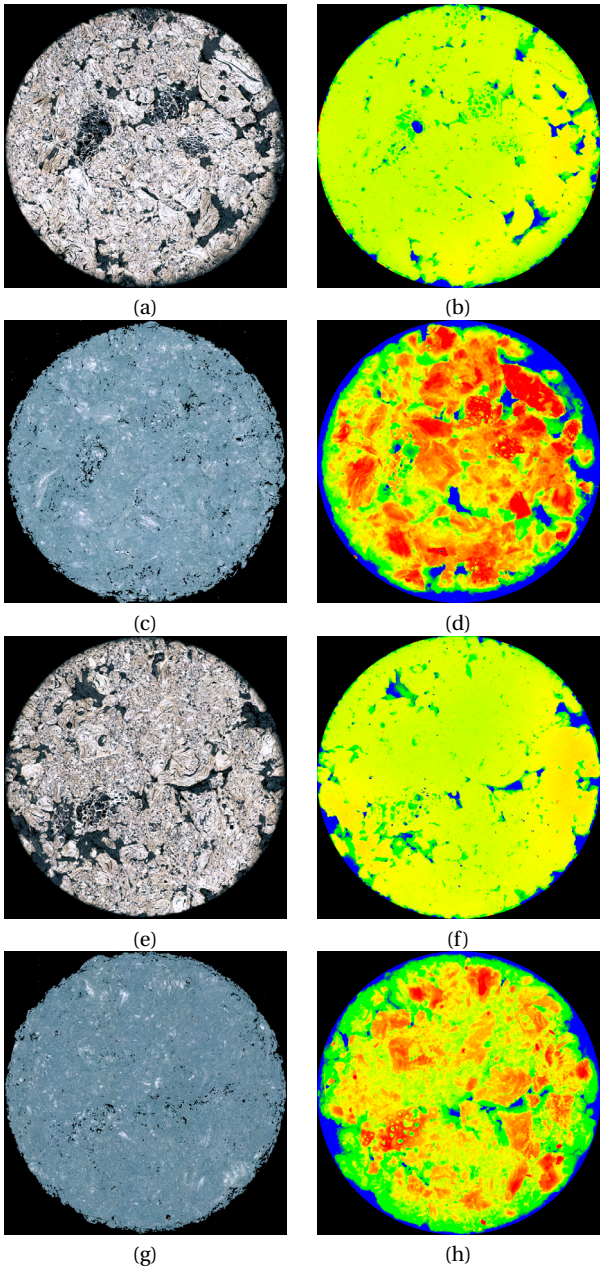

Figure 5.15: Confocal microscopy images for anode LM-MB. a) Microscopy image before electrolysis parallel 1. b) Contour image before electrolysis parallel 1. c) Microscopy image after electrolysis parallel 1. d) Contour image after electrolysis parallel 1. e) Microscopy image after electrolysis parallel 2. f) Contour image before electrolysis parallel 2. g) Microscopy image after electrolysis parallel 2. h) Contour image after electrolysis parallel 2.

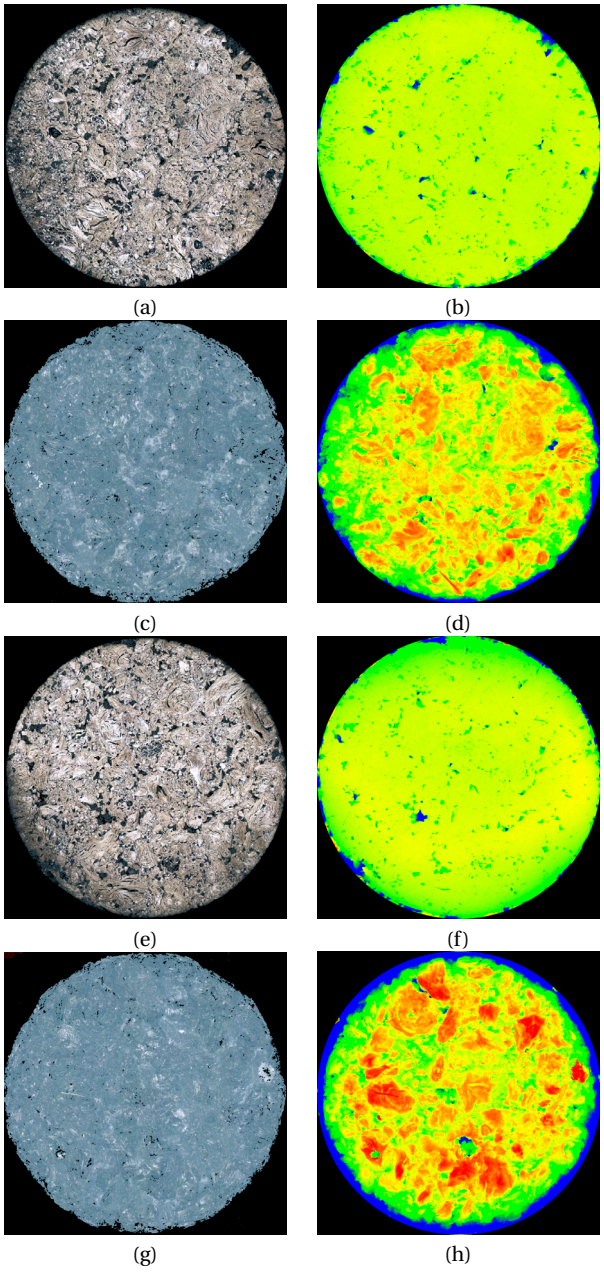

Figure 5.16: Confocal microscopy images for anode HM-MB. a) Microscopy image before electrolysis parallel 1. b) Contour image before electrolysis parallel 1. c) Microscopy image after electrolysis parallel 1. d) Contour image after electrolysis parallel 1. e) Microscopy image after electrolysis parallel 2. f) Contour image before electrolysis parallel 2. g) Microscopy image after electrolysis parallel 2. h) Contour image after electrolysis parallel 2.

5.3.5 Electrochemical Measurements

Figure 5.17 shows results from chronopotentiometry at 1.0 A/cm^2 measured for graphite and anodes LM-LB-B, HM-MB and HM-HB. The results are averages of the potential w.r.t. Al for the last 50 seconds of a 200 s measurement taken once the measurement had stabilised. Chronopotentiometry was performed on two parallels of each sample on the same melt in the same day. Figure 5.18 shows the second forward polarisation curves out of three consecutive forward and backward scans with a slow sweep rate of 0.1 V/s for the same anodes as shown in Figure 5.17. Figure 5.19 shows anode polarisation curves from a duplicate run of anodes LM-LB-A, LM-MB, LM-HB, HM-LB, HM-MB and HM-HB. It should be noted that the potentials were all lower in Figure 5.19 compared to the potentials reported in Figure 5.18, which is related to the use of a reference electrode which had been left in the melt for more than one day. The reference electrode was stable, but there is a shift in the potential related to changes in the electrode/electrolyte interface. Similar shifts in potential between days was found during reference electrode testing as described in Appendix A. Still, the relative differences between the anode may be assumed to be reasonable accurate.

Figure 5.20 shows the raw data from the electrical impedance spectroscopy (EIS) (black line and circles) together with the results from the fitting to the LR(CR) (red) and LR(Q(R(LR))) (blue) eqivalent circuits. For the fits to the LR(CR) circuit, only raw data in the frequency range 100000-39.53 Hz were included, excluding the inductive loop at the very low frequencies.

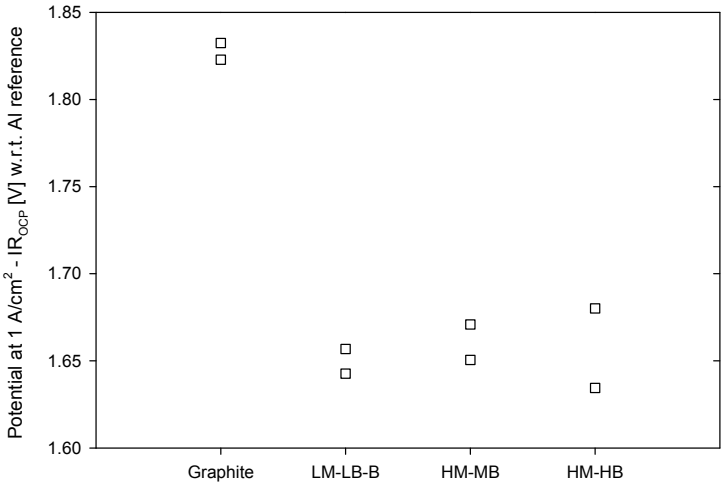

Figure 5.17: Chronopotentiometry measurements at 1.0 A/cm^2 for anodes varying in mixing and baking temperature. Graphite anodes were used as anode reference material.

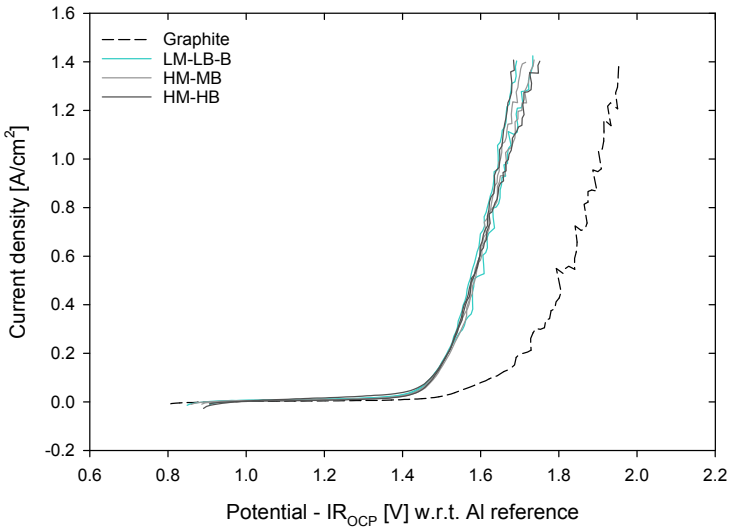

Figure 5.18: IR corrected polarisation curves of graphite and anodes LM-LB-B, HM-MB and HM-HB. The second forward scan of three consecutive forward and backward scans is shown for each anode.

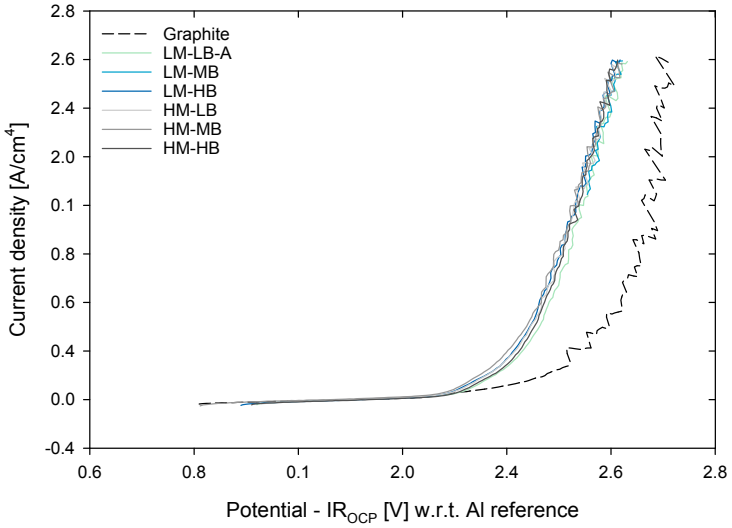

Figure 5.19: IR corrected polarisation curves of graphite and anodes LM-LB-A, LM-MB, LM-HB, HM-LB, HM-MB and HM-HB. The second forward scan of three consecutive forward and backward scans is shown for each anode.

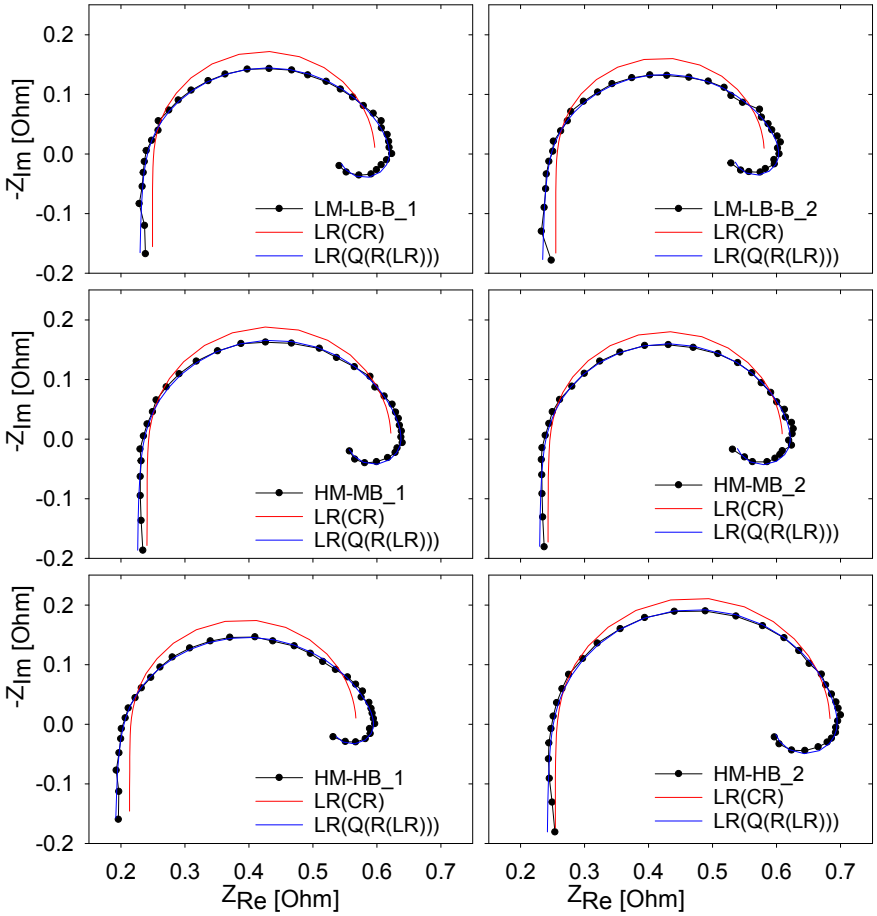

Figure 5.20: Raw data from EIS at 1.5 V (non-IR corrected) and LR(CR) and LR(Q(R(LR))) modelled circuits for the corresponding raw data.

Tables 5.3 and 5.4 show the parameters for inductance, L, series resistance, R_S, double layer capacitance, C_{dl}, charge transfer resistance, R_{CT}, constant phase element, Q, and the dimensionless constant phase element exponent, α, obtained when modelling the EIS equivalent circuits LR(CR) and LR(Q(R(LR))), respectively.

The impedance spectras were recorded at 1.5 V non-IR corrected, and the IR corrected potentials are slightly lower than 1.5 V. The small variations in current density will affect the charge transfer resistance (R_{CT}) to some extent, as can be seen in Tables 5.3 and 5.4.

In Table 5.5 the elevated capacitances based on the simple LR(CR) circuit and the more complex LR(Q(R(LR))) circuit are compared. Equation 5.1 was used to calculate the effective capacitance from the constant phase element, Q. Note that in Table 5.5 the double layer and effective capacitance have been divided by the area of the anode.

Table 5.3: The parameters obtained by fitting of the EIS results by the equivalent circuit LR(CR).

Anode	V IR corr. V	i A/cm^2	L H	R_S Ω	C_{dl} μF	R_{CT} Ω
LM-LB-B	1.47	0.10	$2.54\cdot10^{-7}$	0.25	371	0.35
LM-LB-B	1.46	0.11	$2.71\cdot10^{-7}$	0.25	369	0.33
HM-MB	1.47	0.09	$2.93\cdot10^{-7}$	0.24	279	0.38
HM-MB	1.47	0.10	$2.84\cdot10^{-7}$	0.24	269	0.37
HM-HB	1.47	0.10	$2.39\cdot10^{-7}$	0.21	341	0.35
HM-HB	1.47	0.09	$2.88\cdot10^{-7}$	0.25	213	0.43

Table 5.4: The parameters obtained by fitting of the EIS results by the equivalent circuit LR(Q(R(LR))).

Anode	V IR corr. V	i A/cm^2	L H	R_S Ω	Q μF	α	R_{CT_1} Ω	L_{ads} H	R_{CT_2} Ω
LM-LB-B	1.47	0.10	$2.80\cdot10^{-7}$	0.23	1928	0.80	0.32	$2.87\cdot10^{-3}$	0.09
LM-LB-B	1.46	0.11	$3.00\cdot10^{-7}$	0.23	2182	0.79	0.30	$2.40\cdot10^{-3}$	0.08
HM-MB	1.47	0.09	$3.13\cdot10^{-7}$	0.22	898	0.86	0.33	$2.91\cdot10^{-3}$	0.09
HM-MB	1.47	0.10	$3.03\cdot10^{-7}$	0.23	799	0.87	0.31	$2.69\cdot10^{-3}$	0.09
HM-HB	1.47	0.10	$2.70\cdot10^{-7}$	0.19	1976	0.79	0.34	$3.79\cdot10^{-3}$	0.07
HM-HB	1.47	0.09	$3.05\cdot10^{-7}$	0.24	511	0.90	0.36	$2.90\cdot10^{-3}$	0.10

Table 5.5: Capacitance results from electrical impedance spectroscopy using two different models: LR(CR) and LR(Q(R(LR))).

Anode	V IR corr. V	i A/cm^2	C_{dl} LR(CR) μF/cm^2	C_{eff} LR(Q(R(LR))) μF/cm^2
LM-LB-B	1.47	0.10	244	170
LM-LB-B	1.46	0.11	243	164
HM-MB	1.47	0.09	183	143
HM-MB	1.47	0.10	177	141
HM-HB	1.47	0.10	224	145
HM-HB	1.47	0.09	140	117

5.4 Discussion

The effect of mixing and baking temperature has been investigated by physical tests, porosity and electrochemical measurements. As shown in Table 5.1, density, specific electrical resistivity and permeability were strongly affected by the mixing temperatures. Higher density and lower electrical resistivity was obtained at higher mixing temperatures. The variation between samples with low mixing temperature is likely due to inhomogeneity caused by a too low mixing temperature. This is in good agreement with the results obtained by Wilkening who found that anode density affects properties of the anodes like electrical resistivity, air permeability, resistance to crack propagation and resistance to thermal shock [6, 18]. The air permeability is strongly reduced when the mixing temperature increases, although, the air permeability measured for the high temperature mixing anodes is still not up to industrial standard when comparing with literature values in e.g. [13, 14]. This is most likely due to a non optimised recipe for anode production in terms of pitch content and the ratio between coarse grains and fines. Baking temperature seems to have an effect on dust index and air and CO_2 reactivity as shown in Table 5.1. This is also in accordance with results reported in the literature [25, 26]. Air reactivity increases with decreasing baking temperatures while CO_2 reactivity shows the opposite trend. Coefficient of thermal expansion is not affected by production parameters, as CTE is rather affected by the raw materials [1]. Also, for the low mixing temperature anodes, the baking temperature appears to affect both the density, SER and air permeability. A higher baking temperature compensates to some extent for the poor mixing temperature. There is no effect of baking temperature for the high mixing temperature anodes.

Impurity levels obtained from X-ray fluorescence spectroscopy (XRF) analysis are shown in Table 5.2, and the results show that the anodes are low in almost every impurity commonly present in carbon anodes, including sulfur, vanadium, silicon and phosphorus. Worth noting is the low sulfur content of less than 1 %. XRF was performed on an anode produced at an intermediate mixing temperature (168 °C) and medium baking temperature (1260 °E), but only the level of sulfur could possibly be affected by the baking. The metallic impurities will remain in the anode under these conditions. Hg porosity measurements presented in Figure 5.4 indicate that very little

sulfur has been lost even for the high baking temperature anodes as these do not show an increase in microporosity (<1 μm) [31] compared with the other anodes baked at lower temperatures. This indicates that desulfurisation has not happened from this low sulfur coke to a large extent since no "puffing" effect and increased microporosity is observed, even at equivalent baking temperatures that are considered as overbaking (1350 °C) [28, 29]. The results here also support the findings in [31]. The slight increase in porosity seen for all samples in the range 0.003-0.01 μm in Figure 5.4 is most likely due to compression of the anode sample due to high pressure during experiment, rather than a real increase in porosity.

Both porosity analysis by optical microscopy and Hg porosimetry only detect open porosity. Any closed porosity is not reported. Porosity analysis by optical microscopy differs from Hg porosimetry as the software identifies the maximum diameter of each pore. Hg porosimetry on the other hand, is a "minimum pore" size analysis since it measures the pressure needed to penetrate into a pore [35]. If the pore has a large open volume, but a bottleneck entrance, a higher pressure is needed for pore penetration. This also explains why the results differ between the two porosity measurement methods, to a certain extent. Pores measured by Hg porosimetry on the anode samples will be underestimated and the peaks seen at about 4-7 μm are likely to correspond to the peaks at 15 μm in optical microscopy porosity analysis. These peaks correspond to the pores between fines. The peaks at 20-30 μm in Figure 5.4 and 30-100 μm in Figure 5.5 correspond to the calcining pores, appearing when volatiles are being released from pitch during baking and larger pores between fines. The peaks at about 100 μm (Figure 5.4) and 200-600 μm (Figure 5.5) are inhomogeneity pores appearing due to the non-ideal low mixing temperature. These peaks are much more evident for the low mixing temperature anodes, compared with the high mixing temperature anodes. It is not apparent why the two parallels of the HM-HB anode show a much larger peak at 20-30 μm in Figure 5.4 than the other samples. This finding is partly supported by the optical microscopy porosity analysis in Figure 5.5 where a rather high peak is observed for the HM-HB sample at 30-100 μm. The peaks seen at about 200-600 μm in Figure 5.5 are pores appearing due to non-ideal mixing temperatures which result in inhomogeneous anodes, as only the low mixing temperature anodes have these peaks. These pores are highly visible in the CT images and will be discussed further below.

In Figure 5.4 graphite is shown as the dashed line and appears to have pores only in the range of 0.4-1 μm. This is due to the way ultrapure graphite is produced: carbon particles are crushed down to a certain grain size, purified and then pressed together at such a high pressure that grains melt together. The pores present are those that arise between corners of each of these graphite grains and since these pores are fairly spherically shaped, the reported pore size is most likely very accurate. Porosity measurements were not performed on graphite by optical microscopy analysis due to difficulties in epoxy penetration of the very small pores in the graphite sample.

A summary of the texture analysis is shown in Figure 5.6 and it can be seen that the texture of the anodes were similar to each other throughout the entire anode series, as expected, as the range of baking temperatures applied are not likely to induce significant structural changes in the cokes.

X-ray computed tomography (CT) was used in order to investigate the anode/electrolyte interaction, as well as the interior of anode samples before and after electrolysis at 1.0 A/cm^2 for 30 mins. The anode samples were hot-pulled from the electrolyte with current still on and quickly cooled. This was done in order to create a frozen image of what the anode and electrolyte looked like during electrolysis. A selection of features of the anodes are shown in the tomographs presented in Figures 5.7-5.13. The tomographs show the non-electrolysed sample along with the same sample after electrolysis and at the same rotation. In general, it can be seen that the network of open porosity in the low mixing temperature anodes are much higher than the high mixing temperature anodes. The low mixing temperature anodes have larger pores and the pores appears to be connected to a larger extent than for the high mixing temperature anodes. These larger pores are also evident in the aforementioned porosity analysis (Figures 5.4 and 5.5). The high mixing temperature anodes are more homogeneous and the pores present are much smaller and not so interlinked. CT clearly shows qualitatively how the density, and hence parameters like SER and permeability are improved with a more optimised mixing temperature as already argued in several studies [6, 16, 18]. The larger pores in the low mixing temperature anodes are formed when coke particles are not well wetted with pitch. This is supported by the observation of pore walls appearing very rough for the low mixing temperature anodes. When the coke and pitch interactions are good, the pore walls are smooth. This can clearly be seen in Figures 5.7-5.13.

From the CT images it can be seen that this particular coke type has some coke particles that look like bubbles, previously termed "bubble coke" by Sommerseth et al. [33]. The bubble coke tends to stick out from the matrix after electrolysis, indicating that it is consumed at a lower rate than the regular coke texture. This is most likely due to higher electrical resistivity through these high porosity grains. Alternatively, it might be related to poor electrolyte wetting on these coke grains. It can also be seen in for example Figure 5.9 a) that electrolyte does not penetrate into large, open pores as seen to the right of the image. In Figure 5.9 b) a large pore or crack is seen at the upper left corner, and in the image after electrolysis it is evident that electrolyte has only penetrated halfway into this pore. Also, many pores do not show any penetration of electrolyte. In [33] it is shown that the pores have to be very large and/or of a convex character in order for the bath to penetrate into pores. This suggest that real surface area and electrochemically active surface area are not necessarily the same, and this will be discussed further below.

Investigations of the true surface area toward the projected or geometric surface area before and after electrolysis was performed by confocal microscopy. The anodes were first ground and then investigated in the confocal microscope. Then the samples were electrolysed at 1.0 A/cm^2 for 25 mins. The electrolyte left on the surface was removed by soaking in $AlCl_3$. This was done to be able to repeat the analysis of the sample surface area after electrolysis. Figure 5.14 shows the results of true area over projected area (TA/PA) for the entire anode series before and after electrolysis. An increase of TA/PA of about 40 % is seen for the anodes after electrolysis compared with the polished, non-electrolysed samples. This is in good agreement with Thonstad [43] who found by impedance measurements before and after electrolysis an increase

in double layer capacitance of 45 %. These experiments were performed on anode samples that had a well defined flat anode area, shielded by boron nitride. The samples were also tilted (about 120° compared with a horizontal setup) in order to facilitate gas bubble release. From CT images (Figures 5.7-5.13) it can be seen qualitatively that the electrolysed surfaces are rougher than the non-electrolysed samples, supporting the findings in both confocal microscopy and Thonstad's capacitance measurements [43].

For the low mixing temperature anodes there is a higher scatter of TA/PA between the anode samples and also between parallels than for the high mixing temperature anodes; both for non-electrolysed and electrolysed samples. The scatter is due to the presence of large pores and since the sample investigated is fairly small (10 mm diameter) some samples will have many large pores, while others may have fewer. As already shown with optical microscopy and CT-imaging, the high mixing temperature anodes are more homogeneous than the low mixing temperature anodes. Also, TA/PA is higher for the LM anodes than for the HM anodes of about 13 % after electrolysis. The images in Figures 5.15 and 5.16 are taken before and after electrolysis. Corresponding contour images of the LM-MB and HM-MB anodes are also shown. The images show multiple large pits in the LM-MB sample. There are less large pits in the HM-MB anode. This is also confirmed by CT image analysis. It is obvious that a higher total porosity will affect the density, permeability and electrical resistivity as Table 5.1 confirms. These pores are expected to influence the electrochemical active surface area. However, during CT it has also been shown how even large pores are not filled with electrolyte, implying that geometric surface area is not directly linked to the electrochemical active surface area. This will be further discussed below. The removal of electrolyte by soaking in $AlCl_3$ is a weak point of this experiment. It was not possible to remove all electrolyte on all samples, so the true area may be a little under-estimated. Also, removing electrolyte may detach some pieces on the anode surface making the area investigated by the confocal microscope not exactly the same area that was in contact with the electrolyte during electrolysis.

Figure 5.17 shows the average IR corrected potential output for the last 50 s, whilst applying 1.0 A/cm^2 for 200 seconds for the anode series (after the anode had been preconditioned at 1.0 A/cm^2 at 200 s). As can be seen from the results in the figure, baking and mixing temperatures do not affect the electrochemical potential output of the anodes. This finding is supported by the results shown in Figures 5.18 and 5.19 where a very slow CV scan was performed in two duplicate runs with a total of three parallels. The scans were slow (0.1 V/s), so it is reasonable to assume that they resemble polarisation curves. No large differences in potential output can be seen between the anodes varying in baking and mixing temperatures, and hence varying in apparent density (1.50-1.59 g/cm^3) and porosity. Jarek and Orman [44] found that overpotential increased with decreasing porosity. However, this was when comparing graphite to baked carbon anodes. The current work also shows increased overpotential for graphite samples compared with the baked carbon anodes, however, no significant differences can be seen between the baked carbon anodes. Jarek and Thonstad [45] found that the anodic overpotential on carbon anodes decreased slightly with increasing apparent density. In their work the apparent density ranged from 1.32-1.61 g/cm^3, which was a wider range and also gives more extreme porosity ranges

compared with the present work.

Figure 5.20 shows the raw data from impedance measurements at 1.5 V (non-IR corrected) for two parallels each of anode LM-LB-B, HM-MB and HM-HB along with the two equivalent electrical circuits: LR(CR) and LR(Q(R(LR))). It is evident that the curve fit for the latter model was much more accurate than for the former. For the LR(Q(R(LR))) circuit, Equation 5.1 had to be used to approximate the effective capacitance, giving rise to some uncertainty. The C_{dl} and C_{eff} parameters for the anodes are shown in Table 5.5. In the table the IR corrected potential for each measurement is given along with the recorded current density response. It can be seen that the current density varied a little between each experiment due to small variations in the ohmic potential drop. Both the C_{dl} and C_{eff} values shown are fairly consistent with the values obtained by Thonstad [46], although, the calculated C_{eff} values are slightly lower than the C_{dl}. Nevertheless, it is evident that the LM anodes show a higher C_{dl} and C_{eff} than the HM anodes. This is due to the increased surface area of the more porous LM anode. The increase of C_{eff} from the LM anodes to the HM anodes is ≈16 %, (considering the second HM-HB measurement anomaly). The difference of true area over projected area measured by confocal microscopy between the LM and the HM anodes after electrolysis was about 13 %. Hence, the effective capacitance and the TA/PA measurements are in good agreement. The difference between the LM and HM anodes was ≈35 % when the capacitance was determined using the LR(CR) circuit. It seems reasonable to assume that the LR(Q(R(LR))) eqivalent circuit provides a more realistic representation of the anode processes.

5.5 Conclusion

In this work the effect of two different mixing temperatures (150 °C and 210 °C) and three different equivalent baking temperatures (1150 °E, 1260 °E and 1350 °E) were investigated in terms of physical parameters, micro- and macroporosity and electrochemical performance. It has been shown that a non-ideal low mixing temperature affects physical parameters, including density, specific electrical resistivity and permeability, in a negative manner. The equivalent baking temperature affects air and CO_2 reactivity. It was shown that the low mixing anodes were not homogeneous, with many large pores distributed unevenly throughout the anode sample, most likely a result of insufficient wetting of the pitch. This was supported by CT images, as pitch could not be observed on the walls of the large pores. The high mixing anodes were more homogeneous, as shown by the imaging techniques. An increase in real surface area of about 40 % was observed between non-electrolysed samples and electrolysed samples. With confocal microscopy it was shown that the real surface area of the low mixing over the high mixing temperature anodes was about 13 % after electrolysis. Mixing and equivalent baking temperatures do not affect the electrochemical overpotential to any significant extent. The low mixing electrodes had slightly higher capacitance values after electrolysis compared to the high mixing electrodes, indicating a slightly larger electrochemically active surface area. The difference in electrochemically active area is however smaller than the corresponding differences in surface roughness after electrolysis, identified by optical microscopy. This could be understood by the CT

images, which also showed that the electrolyte does not generally penetrate into the pores on the surface, penetration will depend on the size and shape of the pore.

Acknowledgement

The work was financed by Hydro Aluminium and The Research Council of Norway through the research program called “HAL Ultra Performance Aluminium Cell”. Thanks are due to Aksel Alstad at the NTNU workshop for fabricating the experimental parts, Cristian Torres Rodriguez, technicians at Hydro Aluminium Årdalstangen, Ole Tore Buset, Wojciech Gebarowski and Jannicke Kvello for help with various experimental techniques.

References

[1] L. Edwards, N. Backhouse, H. Darmstadt, and M.-J. Dion. “Evolution of Anode Grade Coke”. *Light Metals* (2012), pp. 1207–1212.

[2] K. Grjotheim and H. Kvande. *Introduction to Aluminium Electrolysis*. 2nd. Dusseldorf: Aluminium-Verlag, 1993.

[3] S.S. Jones and E.F. Bart. “The Role of Primary Quinoline-Insolubles in Pitch-Coke Bond Formation in Anode Carbon”. *Light Metals* (1991), pp. 609–613.

[4] A.A. Mirchi, M. Collard, and G. Savard. “Interaction Study of the Paste Plant Production Parameters on VS Soderberg Anode Paste Fluidity and Baked Anode Performance”. *Light Metals* (2001), pp. 619–624.

[5] A.A. Mirchi, G. Savard, J.P. Tremblay, and M. Simard. “Alcan Characterisation of Pitch Performance for Pitch Binder Evaluation and Process Changes in an Aluminium Smelter”. *Light Metals* (2002), pp. 525–533.

[6] S. Wilkening. “Maintaining Consistent Anode Density using Varying Carbon Raw Materials”. *Light Metals* (2009), pp. 991–997.

[7] D. Kocaefe, A. Sarkar, S. Das, S. Amrani, D. Bhattacharyay, D. Sarkar, and Y. Kocaefe. “Review of Different Techniques to Study the Iteractions between Coke and Pitch in Anode Manufacturing”. *Light Metals* (2013), pp. 1045–1050.

[8] V.G. Rocha, C. Blanco, R. Santamaría, E.I. Diestre, R. Menéndez, and M. Granda. “An insight into pitch/substrate wetting behaviour. The effect of the substrate processing temperature on pitch wetting capacity”. *Fuel* (2007), pp. 1046–1052.

[9] A. Sarkar, D. Kocaefe, Y. Koceafe, D. Sarkar, and Bhattacharyay. “Coke-pitch interactions during anode preparation”. *Fuel* (2014), pp. 598–607.

[10] P. Couderc, P. Hyvernat, and J.L. Lemarchand. “Correlations between ability of pitch to penetrate coke and the physical characteristics of prebaked anodes for the aluminium industry”. *Fuel* (1986), pp. 281–287.

[11] J. Cao, A.N. Buckley, and A. Tomsett. “Re-examining the Pitch/Coke Wetting and Penetration Test”. *JOM* (2002), pp. 30–33.

[12] D. Auguie, M. Oberlin, A. Oberlin, and P. Hyvernat. “Formation of Thin Mesophase Layers at the Interphase between Filler and Binder in Prebaked Anodes. Effect of Mixing on Mesophase”. *Carbon* (1981), pp. 277–284.

[13] F. Keller and P.O. Sulger. *Anode Baking*. 2nd. Sierre: R & D Carbon Ltd., 2008.

[14] B. Ndjom, M.S. Malik, A.A. Marzouqi, T.K. Sahu, and S.A. Rabba. “Improving Anode Baked Density and Air Permeability through Process Optimization and Coke Blending”. *Light Metals* (2013), pp. 1105–1110.

[15] V.G. Rocha, C. Blanco, R. Santamaría, E.I. Diestre, R. Menéndez, and M. Granda. “Pitch/coke wetting behaviour”. *Fuel* (2005), pp. 1550–1556.

[16] K. Hulse, R.C. Perruchoud, W.K. Fischer, and B.J. Welch. “Process Adaptations for Finer Dust Formulations: Mixing and Forming”. *Light Metals* (2000), pp. 467–472.

[17] V.G. Rocha, C. Blanco, R. Santamaría, E.I. Diestre, R. Menéndez, and M. Granda. “The effect of the substrate on pitch wetting behaviour”. *Fuel* (2010), pp. 1373–1377.

[18] S. Wilkening. “Potentials in the Paste Plant”. *Light Metals* (1997), pp. 569–576.

[19] K. Azari, H. Alamdari, G. Aryanpour, D. Ziegler, D. Picard, and M. Fafard. “Compaction properties of carbon materials used for prebaked anodes in aluminum production plants”. *Powder Technol.* (2013), pp. 650–657.
[20] V. Piffer, P. Miotto, C. Kato, M. Meier, R. Perruchoud, and P. Sulger. “Process Optimization in Bake Furnace”. *Light Metals* (2007), pp. 959–964.
[21] B. Samanos and C. Dreyer. “Impact of Calcination Level and Anode Baking Temperature on Anode Properties”. *Light Metals* (2001), pp. 681–688.
[22] L.P. Lossius, I. Holden, and H. Linga. “The Equivalent Temperature Method for Measuring the Baking Level of Anodes”. *Light Metals* (2006), pp. 609–613.
[23] S. Rørvik, L.P. Lossius, and A.P. Ratvik. “Determination of Coke Calcination Level and Anode Baking Level - Application and Reproducibility of L-sub-C Based Methods”. *Light Metals* (2011), pp. 841–846.
[24] M. McClung, J.A. Ross, and G. Chovanec. “A Method to Determine the Optimal Baking Level of Carbon Anodes”. *Light Metals* (2000), pp. 473–479.
[25] L.P. Lossius, J. Chmelar, I. Holden, H. Linga, and M. Tkac. “Pilot Scale Anodes for Raw Material Evolution and Process Improvement”. *Light Metals* (2013), pp. 1177–1182.
[26] T.E. Jentoftsen, H. Linga, I. Holden, B.E. Aga, V.G. Christensen, and F. Hoff. “Correlation between Anode Properties and Cell Performance”. *Light Metals* (2009), pp. 301–304.
[27] J. Lhuissier, L. Bezamanifary, M. Gendre, and M.-J. Chollier. “Use of Under-Calcined Coke for the Production of Low Reactivity Anodes”. *Light Metals* (2009), pp. 979–983.
[28] H. Al-Haj-Ibrahim and B.I. Morsi. “Desulfurization of Petroleum Coke: A Review”. *Ind. Eng. Chem. Res.* (1992), pp. 1835–1840.
[29] L. Edwards, K.J. Neyrey, and L.P. Lossius. “A Review of Coke and Anode Desulfurization”. *Light Metals* (2007), pp. 895–900.
[30] A.D. McNaught and A. Wilkinson. *Compendium of Chemical Terminology*. 2nd. Oxford: IUPAC, 1997.
[31] L.P. Lossius, K.J. Neyrey, and L. Edwards. “Coke and Anode Desulfurization Studies”. *Light Metals* (2008), pp. 881–886.
[32] F. Vogt, K. Ries, and M. Smith. “Anode Desulfurization on Baking”. *Light Metals* (1995), pp. 691–700.
[33] C. Sommerseth, R.J. Thorne, S. Rørvik, E. Sandnes, A.P. Ratvik, L.P. Lossius, H. Linga, and A.M. Svensson. “Spatial Methods for Characterising Carbon Anodes for Aluminium Production”. *Light Metals* (2015), pp. 1141–1146.
[34] Micromeritics. *AutoPore IV 9500, Operator’s Manual V1.09*. Micromeritics, 2011.
[35] S. Rørvik and H.A. Øye. “A Method for Characterization of Anode Pore Structure by Image Analysis”. *Light Metals* (1996), pp. 561–568.
[36] S. Rørvik, M. Aanvik, M. Sørlie, and H.A. Øye. “Characterization of Optical Texture in Cokes by Image Analysis”. *Light Metals* (2000), pp. 549–554.
[37] R.J. Thorne, C. Sommerseth, A.M. Svensson, E. Sandnes, L.P. Lossius, H. Linga, and A.P. Ratvik. “Understanding Anode Overpotential”. *Light Metals* (2014), pp. 1213–1217.
[38] R.J. Thorne, C. Sommerseth, A.P. Ratvik, E. Sandnes, S. Rørvik, L.P. Lossius, H. Linga, and A.M. Svensson. “Correlation between Coke Type, Microstructure and

Anodic Reaction Overpotential in Aluminium Electrolysis". *J. Electrochem. Soc.* (2015), E1–E11.

[39] O.S. Kjos, T.A. Aarhaug, H. Gudbrandsen, A. Solheim, and E. Skybakmoen. "Fundamental studies of perfluorocarbon formation". *Proc. 10th AASTC* (2011). Ed. by B. Welch, G. Stephens, J. Metson, and M. Skyllas-Kazacos.

[40] D.A. Harrington and B.E. Conway. "ac Impedance of Faradaic Reactions Involving Electrosorbed Intermediates - I. Kinetic Theory". *Electrochim. Acta* (1987), pp. 1703–1712.

[41] M.E. Orazem and B. Tribollet. *Electrochemical Impedance Spectroscopy*. 1st. New Jersey: Wiley, 2008.

[42] M. Orazem, I. Frateur, B. Tribollet, V. Vivier, S. Marcelin, N. Pebere, A.L. Bunge, E.A. White, D.P. Riemer, and M. Musiani. "Dielectric Properties of Materials Showing Constant-Phase-Element (CPE) Impedance Response". *J. Electrochem. Soc.* (2013), pp. C215–C225.

[43] J. Thonstad. "Double layer capacity of graphite in cryolite-alumina melts and surface area changes by electrolyte consumption of graphite and baked carbon". *J. Appl. Electrochem.* (1973), pp. 315–319.

[44] S. Jarek and Z. Orman. "The Faradaic Impedance of the Carbon Anode in Cryolite-Alumina Melt". *Electrochim. Acta* (1985), pp. 341–345.

[45] S. Jarek and J. Thonstad. "Double-layer capacitance and polarization potential of baked carbon anodes in cryolite-alumina melts". *J. Appl. Electrochem.* (1987), pp. 1203–1212.

[46] J. Thonstad. "The Electrode Reaction on the C, CO_2 Electrode in Cryolite-Alumina Melts-II. Impedance Measurements". *Electrochim. Acta* (1970), pp. 1581–1595.

6 Conclusions

This work shows that there are both advantages and disadvantages related to blending of isotropic cokes in anodes. The most obvious positive effects are the lower potential oscillation amplitudes observed during bubble build-up and release. For anodes with blending ratios of isotropic to anisotropic coke of 7.2 %-49.0 %, the potential oscillation amplitude was reduced by ~0.19 V compared with an anode made from 100 % anisotropic coke. This reduction in potential oscillation amplitude is remarkably high and should be investigated further using larger anodes and a more industrial coke aggregate sizing. The improved wettability towards the electrolyte found for anodes containing isotropic coke by using the dedicated immersion-emersion apparatus compared with the purely anisotropic coke offers an explanation for this lowered potential oscillation magnitude. A slight reduction in reaction overpotential was also observed for anodes containing isotropic coke. Hence, isotropic coke appears to have some beneficial effects concerning electrochemical performance in the electrolysis cell.

However, the major drawbacks when considering use of isotropic cokes in anodes are the increased amount of impurities and the higher coefficient of thermal expansion. A threshold was observed for this pilot anode line between 14.2 % and 35.0 % isotropic coke content, in terms of anode cracking. The increased metal impurities in the coke will eventually report to the metal. Also, the increased sulfur content may raise problems in terms of keeping below authority limits for SO_2 emissions, unless an efficient wet scrubber facility is already present. The low porosity of isotropic coke will also affect the optimum pitch level. Care must be taken when producing anodes containing isotropic coke in order to avoid over-pitching.

The mixing temperature appeared to have a larger impact on the quality of the pilot anodes than the baking temperature. A too low mixing temperature proved to produce carbon anodes with a higher porosity, lower density, lower specific electrical conductivity and higher air permeability. The increased porosity of anodes produced with the lower mixing temperature was very visible when using X-Ray computed tomography. However, the reaction overpotential was not affected by the various mixing and baking temperatures. Nevertheless, the capacitance was observed to increase slightly with lower mixing temperatures. This was attributed to the higher surface roughness of anodes produced with a low mixing temperature.

The present work has clearly shown that it is extremely important to tune all production parameters during anode fabrication, including blending ratios of isotropic coke to anisotropic coke, pitch content, mixing temperatures and baking temperatures.

7 Topics for Further Research

Two paths are suggested for the further work where the first includes verification of the small laboratory scale experiments performed in this work:

- **Optimisation of anode recipes:** This includes optimising mixing temperature of pitch and coke, depending on the cokes used and optimising the granulometry of the coke fractions.
- **Larger anodes:** Electrochemical testing of anodes blended with isotropic coke with a coke recipe more similar to industrial scale anodes. This also means that the anode samples would have to be scaled up. Electrochemical testing of larger anodes has amperage limitations regarding potentiostats. However, bubble experiments can be performed using a power supply, and these experiments can give valuable information on the potential behaviour as bubbles build up and release on more upscale anodes.
- **Electrolyte composition I:** Electrochemical testing should be performed in electrolytes more similar to industrial conditions i.e. Al_2O_3 concentration of 3-4 % and additions of CaF_2.
- **Electrolyte composition II:** Electrochemical testing of anodes containing isotropic coke using an electrolyte depleted of Al_2O_3 in order to investigate the effect the high sulfur isotropic cokes have on anode effect.
- **Industrial measurements:** Measuring the bubble voltage fluctuations when bubbles build up and releases on industrial anodes containing isotropic coke *vs.* anodes not containing isotropic coke.

Further work building on this thesis can (and should) also look into the following:

- **See-through cell:** Repeat the bubble experiments using the pilot anodes (or similar) in a see-through cell, to investigate visually the bubble generation.
- **Surface investigations:** Investigate the anode surfaces after anode effect to determine if the increased sulfur content in isotropic coke will effect the degree of C-F bonding. High sulfuric cokes are expected to form COS to a greater extent than low sulfuric cokes. Will COS formation delay the COF_2 formation?
- **Wetting properties:** A further investigation as to why anodes containing isotropic coke show a higher wettability towards the electrolyte compared to anodes of aniostropic coke. What role does impurities play? What role does carbon structure play?

Appendices

A The Aluminium Reference Electrode

A stable reference electrode is crucial to the success of electrochemical measurements. The reference electrode is used for controlling and monitoring the potential when performing electrochemical experiments. The cryolite electrolyte represents a harsh environment due to the high temperature and the corrosive nature. A commonly used reference electrode in laboratory scale experiments is the aluminium reference. Various designs of aluminium reference electrodes have been described elsewhere [1–4]. The aluminium reference electrode is produced in-house, and a new reference has to be made for each experiment. A returning question when performing the electrochemical measurements for this thesis was the stability of the reference electrode. An experiment series for testing the reference electrode stability was performed in order to create an optimised procedure during electrochemical testing.

A.1 Reference Electrode Preparation

A sketch of the reference electrode is shown in Figure A.1. This reference electrode was essentially based on the reference electrode described in [1], with some minor alterations. As indicated in the figure, the reference electrode was made of a boron nitride tube ($Ø_{outer}$ = 10 mm, $Ø_{inner}$ = 5 mm). A hole (Ø = 1.5 mm) was drilled approximately 2.5 cm above the inner bottom of the BN tube. This hole allowed for the electrolyte to enter the reference electrode. 0.66 g pure aluminium was placed in the BN tube, giving a melted pool of aluminium at the bottom of the tube. The boron nitride tube was threaded onto a steel tube. A tungsten wire was threaded through an aluminium oxide (Alsint) tube (1.5 x 3 x 600 mm) and placed inside the steel tube. 1 cm of the tungsten wire was left unshielded by the Alsint tube and the tungsten wire was lowered into the pool of aluminium once the aluminium had melted (see Figure A.1).

Care had to be taken while lowering the Alsint tube and tungsten making sure that the tungsten wire did not slip inside the Alsint tube. Care also had to be taken in order to make sure that the boron nitride did not break when the tungsten wire hit the bottom of the tube as boron nitride is very brittle. Lastly, the reference electrode was lowered to the bottom of the carbon crucible holding the electrolyte, and then raised 1 cm from the bottom. After this step, the laboratory electrolysis cell was left for an hour to let electrolyte penetrate the hole in the reference electrode and let the system settle.

A.2 Reference Electrode Stability Testing

The reference electrode testing set out to investigate the stability of the reference electrode over time during one day and between days. The purpose was also to test

the effect of open circuit potential (OCP) on the output potential and series resistance, R_s, when current was applied. A long time period is observed until the open circuit potential stabilised during experiments. Two reference electrodes were made and placed in the laboratory cell. The potential output between the reference electrodes and the anode was logged with a datalogger. The datalogger was also used to log the current output during EIS measurements at various potentials in order to compare with the output current reported by the potentiostat.

Figure A.2 shows a sketch of the vertical anode setup used and the laboratory cell. Only one reference electrode is drawn in the sketch for simplicity. A current density of 1.0 A/cm^2 was applied and a Zahner IM6 potentiostat with a built in electrochemical impedance spectroscopy (EIS) module was used. The potentiostat had a PP201 20 A booster from Zahner-Elektrik. Ultrapure graphite was used as test material, since this material is highly uniform and homogeneous.

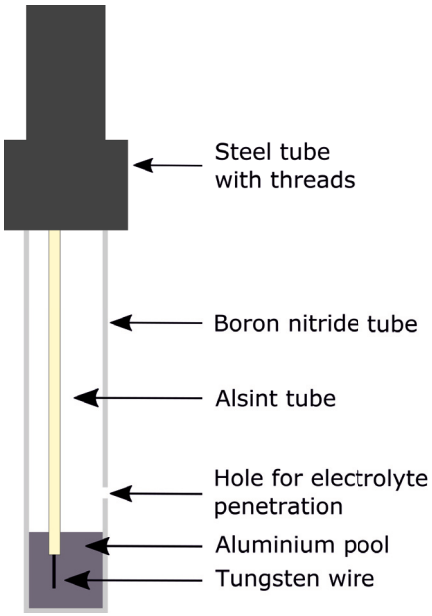

Figure A.1: Sketch of the reference electrode used.

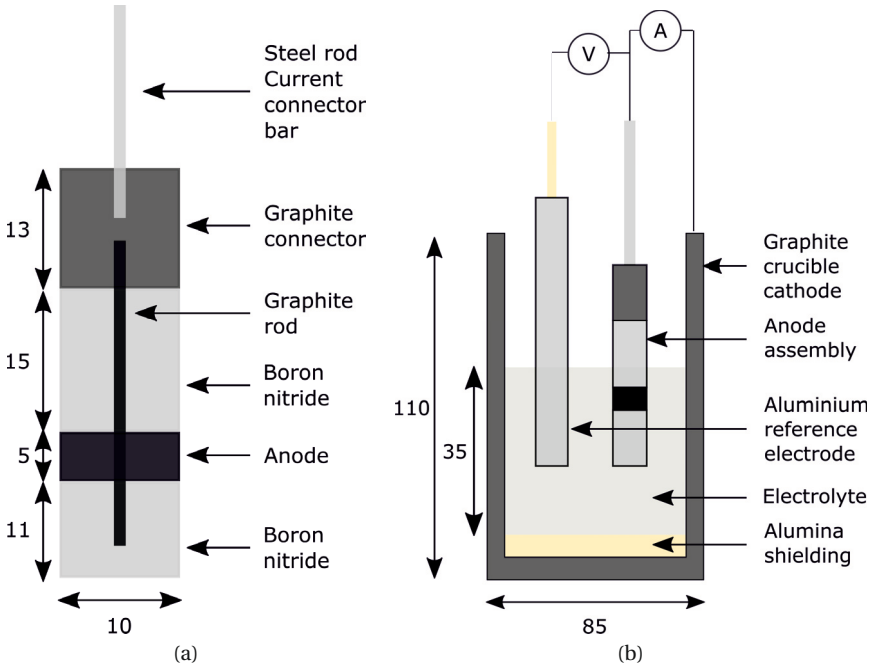

Figure A.2: Electrochemical experimental setup used during electrochemical testing. All measures indicated in the figure are in mm. a) Vertical anode assembly. b) A principle sketch of the electrolysis cell used with the aluminium reference electrode, the graphite crucible with the walls acting as the cathode, the vertical anode assembly and the electrolyte.

A.3 Results from Reference Electrode Testing

Figure A.3 a) shows the average potential output (not IR corrected) obtained at 1.0 A/cm^2. It is seen that reference 2 was more stable throughout the experiment of three days, especially when excluding the first anode. Instabilities for the first anode run in a fresh electrolyte are frequently observed. Reference 2 seems more stable during the first day compared with reference 2 according to Figure A.3 a).

Figure A.3 b) shows the potentials measured at 1.0 A/cm^2 at various OCP values. It is evident that a large variation in OCP does not have large effect on the potential. This is also seen in Figure A.5 b).

Figure A.4 shows the measured potential *vs.* time obtained in a different test. In Figure A.4 a rather large drift can be seen for reference 1 during the night between day 1 and day 2. This is also obvious when comparing the potential output (IR corrected) in Figure A.5 a) where a larger change in the potential outputs for reference 1 can be seen compared with reference 2 between the day 1 and day 2 current applications. When comparing Figure A.3 and A.5, a variation in the level of raw data potentials (not IR corrected - IR correction is typically 0.3 V) can be seen. For run 1 the potentials (non IR corrected) are observed in a range of 1.82-1.96 V while for run 2 the potentials are in the range of 2.05-2.20 V.

Table A.1 shows that R_s was not affected by the OCP value it was tested at.

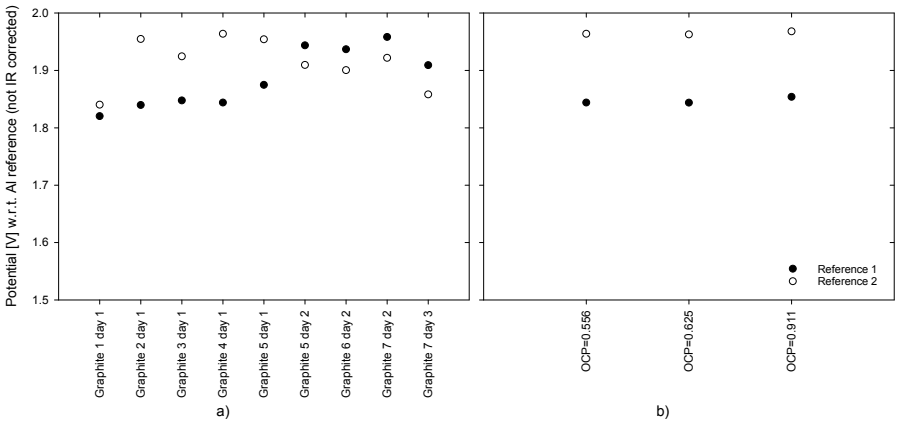

Figure A.3: a) Potential output for each anode at 1.0 A/cm^2, run 1 and b) potential output when varying OCP.

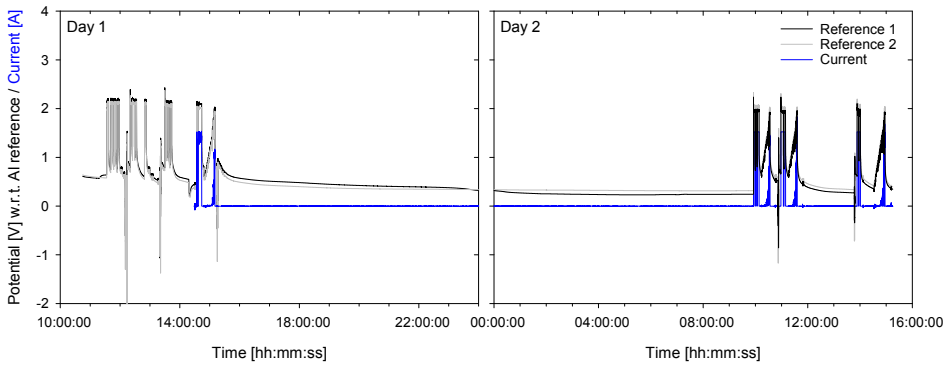

Figure A.4: Raw data from reference electrode stability testing, run 2. The potential is not IR corrected. Anode changes (i.e. disconnection of cables) can be observed as massive vertical potential jumps in both positive and negative voltage direction.

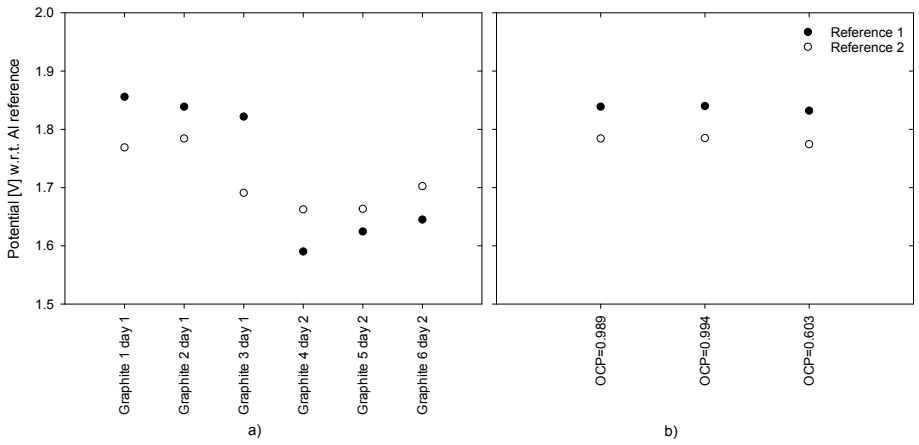

Figure A.5: a) Potential output for each anode at 1.0 A/cm^2, run 2 and b) potential output when varying OCP.

Table A.1: Series resistance measurements at various OCP.

Test run	Anode	OCP	R_s
		V	Ω
Test 2	Graphite 2	0.629	0.2230
Test 2	Graphite 2	0.534	0.2217

A.4 Conclusions from Reference Electrode Testing

The above results from the reference electrode stability testing provided the foundation for a standardised procedure during electrochemical testing of carbon anodes for this thesis:

- The tests were limited to one day only, due to the increased risk in drifting reference electrodes overnight.
- A dummy anode where a current of 1.0 A/cm^2 was applied was used first in every new electrolyte before the real electrochemical testing started.
- Graphite samples would be run first (but after the dummy sample) and last in every test sequence as a check on the reference electrode stability during the day.
- Two reference electrodes were made and used for every experiment in order to minimise the risk of a drifting reference electrode. A datalogger was used for simultaneous logging of the potential when applying 1.0 A/cm^2.
- Since variations in OCP values were not found to affect the output potentials and the ohmic resistance (R_s), it was decided to run the electrochemical testing without waiting for a certain OCP value. This was also beneficial in terms of time saving in the laboratory.
- Due to the variations in potential *between* electrochemical test runs, graphite was used as a reference, and all potentials for the pilot carbon anodes are reported relative to the graphite value of the day.

References

[1] O.S. Kjos, T.A. Aarhaug, H. Gudbrandsen, A. Solheim, and E. Skybakmoen. "Fundamental studies of perfluorocarbon formation". *Proc. 10th AASTC* (2011). Ed. by B. Welch, G. Stephens, J. Metson, and M. Skyllas-Kazacos.

[2] D. Sadoway. "Aluminium Reference Electrode". United States Patent 4,764,257. 1988.

[3] J.W. Burgman, J.A. Leistra, and P.J. Sides. "A Reference Electrode for Hall Cell Experiments". *Light Metals* (1986), pp. 463–472.

[4] J.W. Burgman, J.A. Leistra, and P.J. Sides. "Aluminum/Cryolite Reference Electrode for Use in Cryolite-Based Melts". *J. Electrochem. Soc.* (1986), pp. 496–500.

B Scanning Electron Spectroscopy and Energy Dispersive X-Ray Spectroscopy Images

Figures B.1-B.8 show SEM and EDS images of the horizontal surface of 10 mm anode cores as described in Chapter 3.3.2.

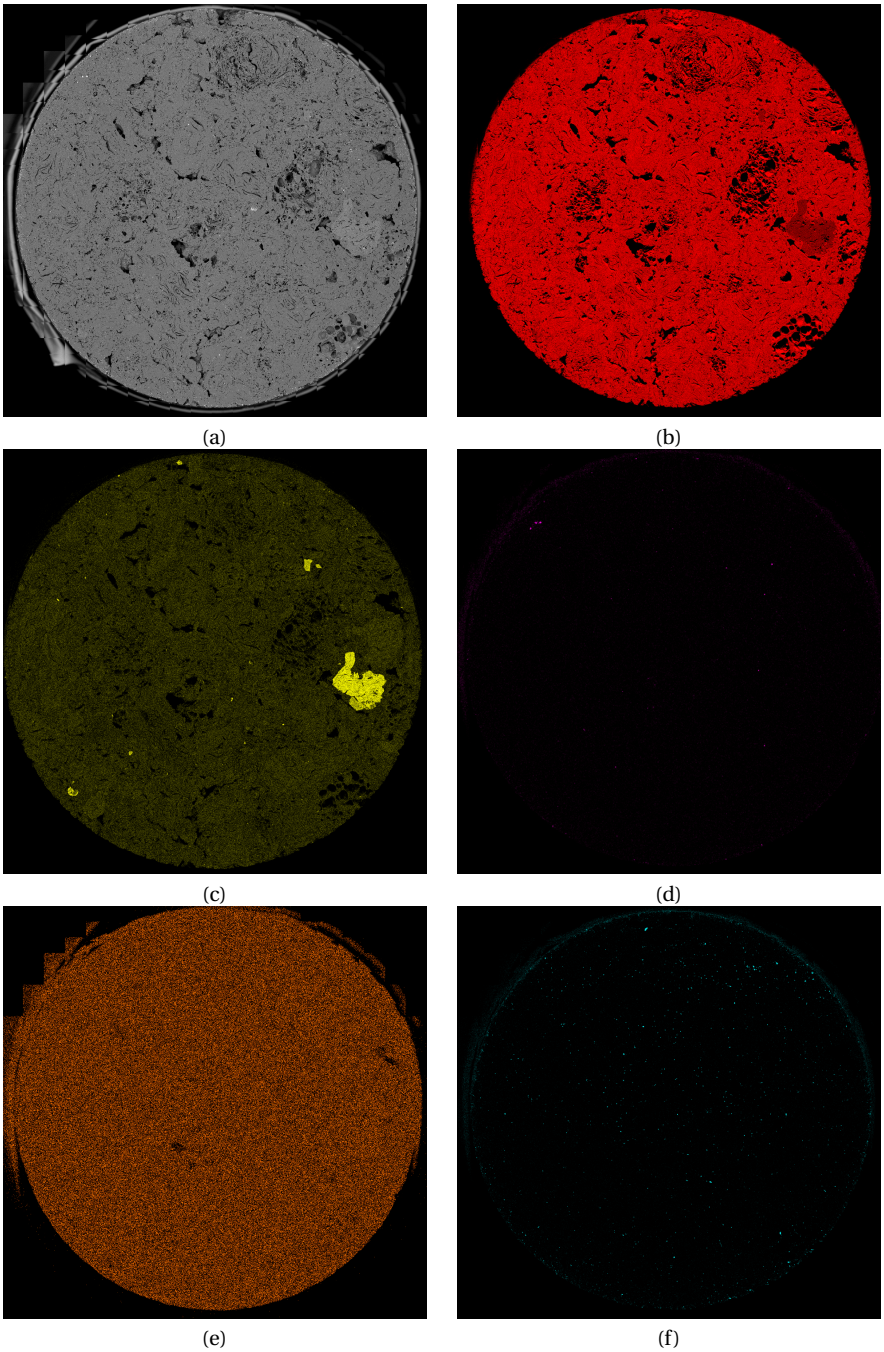

(a) (b) (c) (d) (e) (f)

Figure B.1: SEM/EDS pictures of the anode made of 100 % anisotropic coke, sample 1. a) SEM Surface map, b) Carbon element map, c) Sulfur element map, d) Iron element map, e) Vanadium element map and f) Silicon element map.

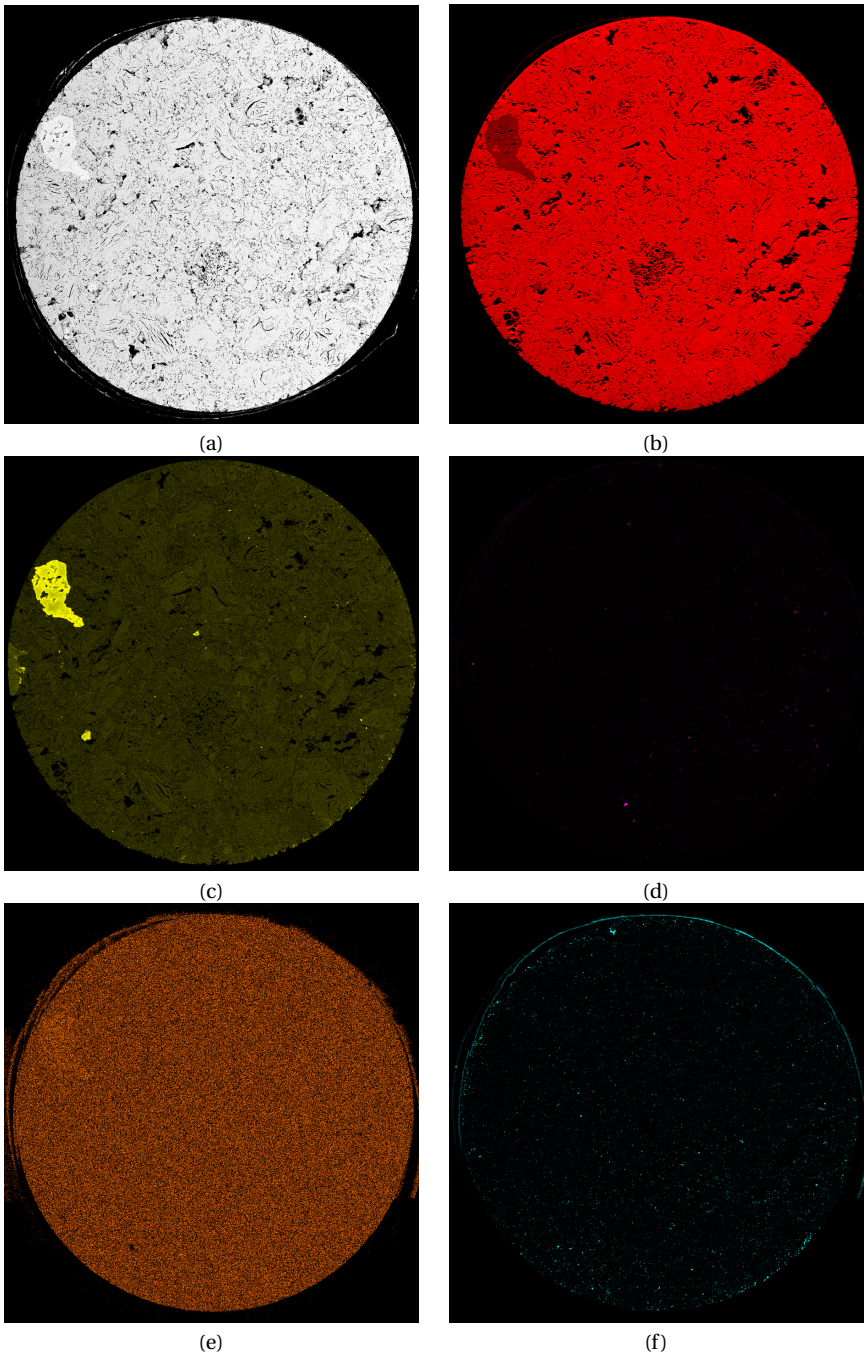

(a) (b) (c) (d) (e) (f)

Figure B.2: SEM/EDS pictures of the anode made of 100 % anisotropic coke, sample 2. a) SEM Surface map, b) Carbon element map, c) Sulfur element map, d) Iron element map, e) Vanadium element map and f) Silicon element map.

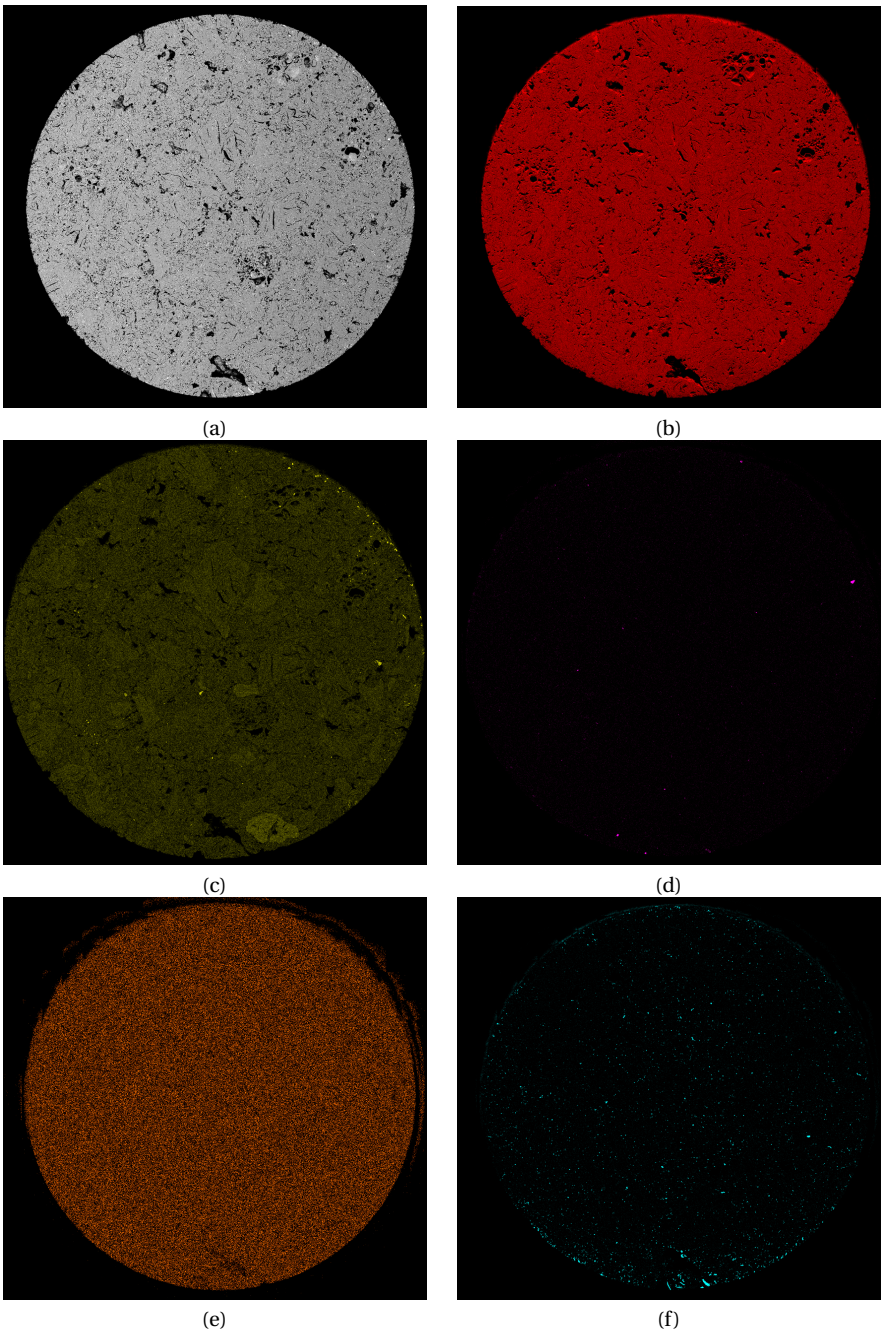

Figure B.3: SEM/EDS pictures of the anode made of 100 % anisotropic coke, sample 3. a) SEM Surface map, b) Carbon element map, c) Sulfur element map, d) Iron element map, e) Vanadium element map and f) Silicon element map.

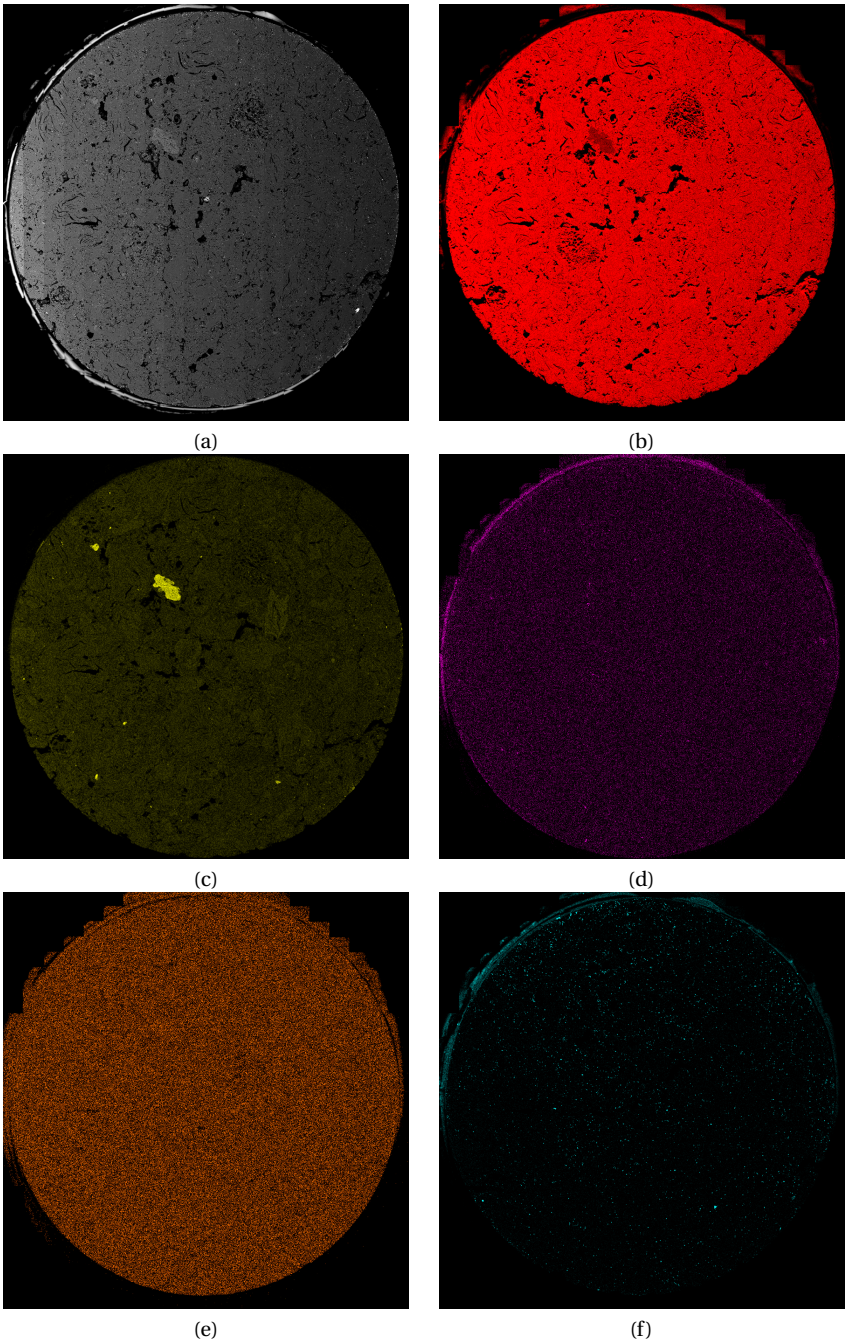

(a) (b) (c) (d) (e) (f)

Figure B.4: SEM/EDS pictures of the anode made of 100 % anisotropic coke, sample 4. a) SEM Surface map, b) Carbon element map, c) Sulfur element map, d) Iron element map, e) Vanadium element map and f) Silicon element map.

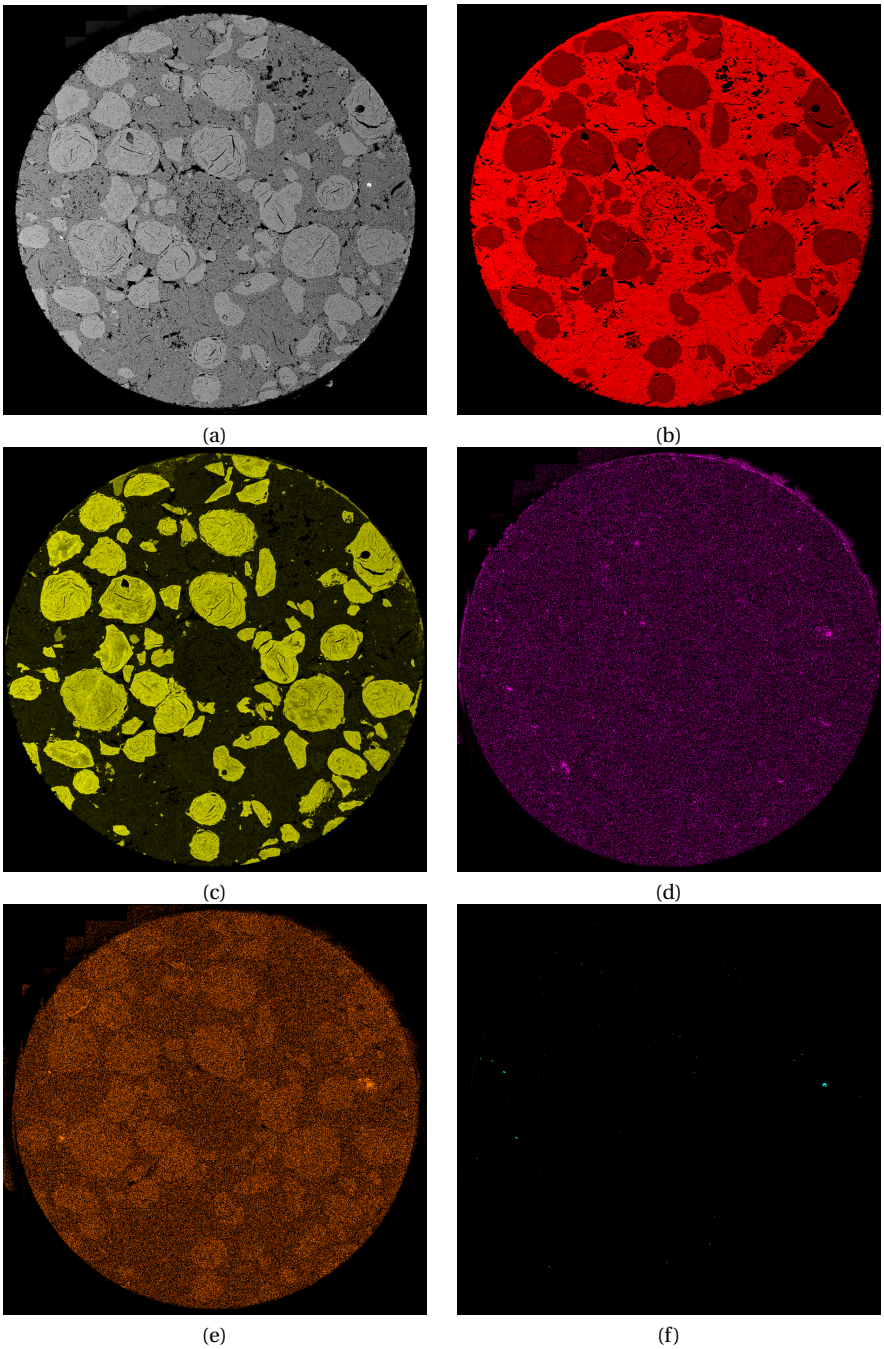

Figure B.5: SEM/EDS pictures of the anode made of 49 % isotropic and 51 % anisotropic coke, sample 1. a) SEM Surface map, b) Carbon element map, c) Sulfur element map, d) Iron element map, e) Vanadium element map and f) Silicon element map.

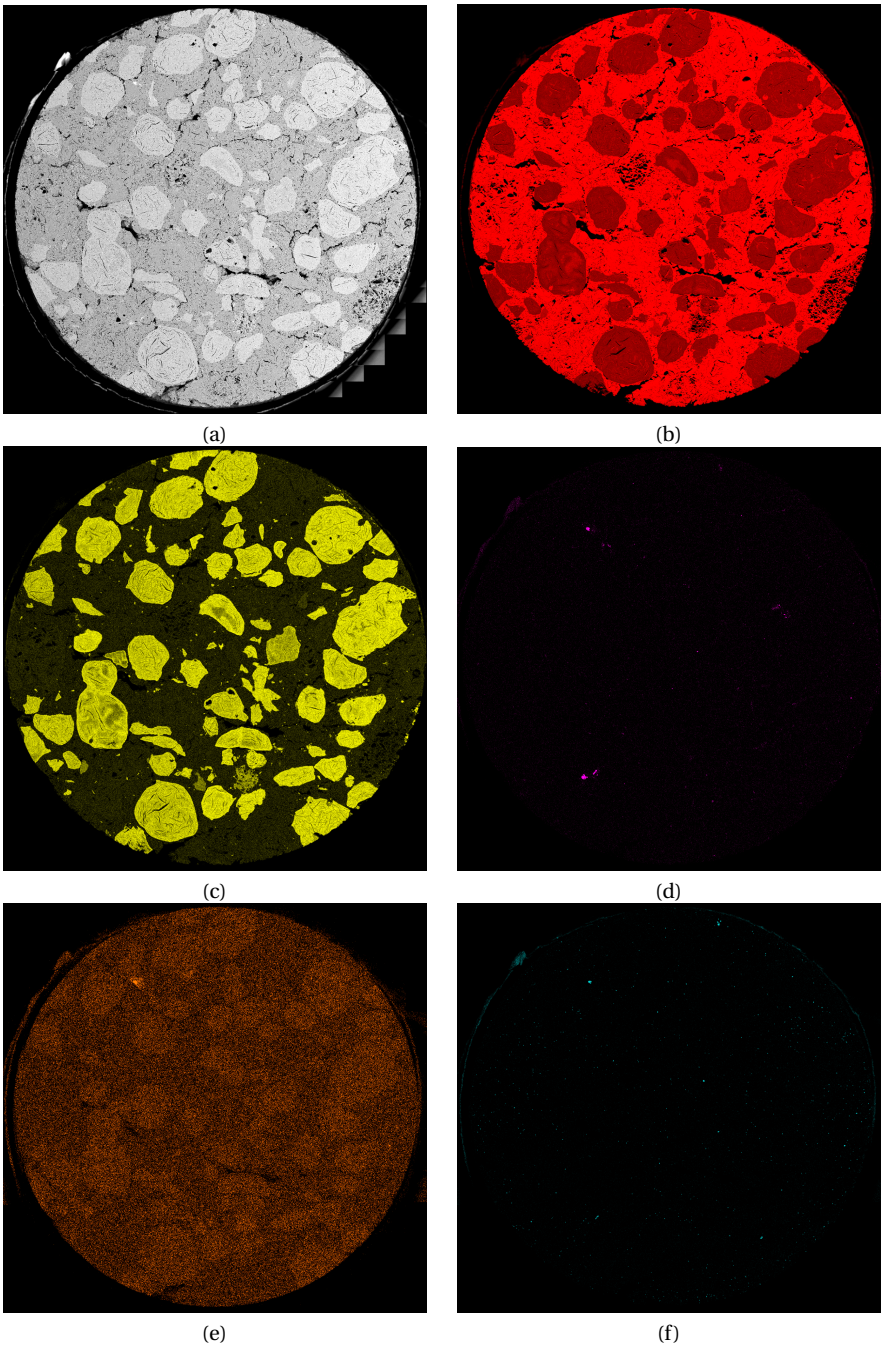

(a) (b) (c) (d) (e) (f)

Figure B.6: SEM/EDS pictures of the anode made of 49 % isotropic and 51 % anisotropic coke, sample 2. a) SEM Surface map, b) Carbon element map, c) Sulfur element map, d) Iron element map, e) Vanadium element map and f) Silicon element map.

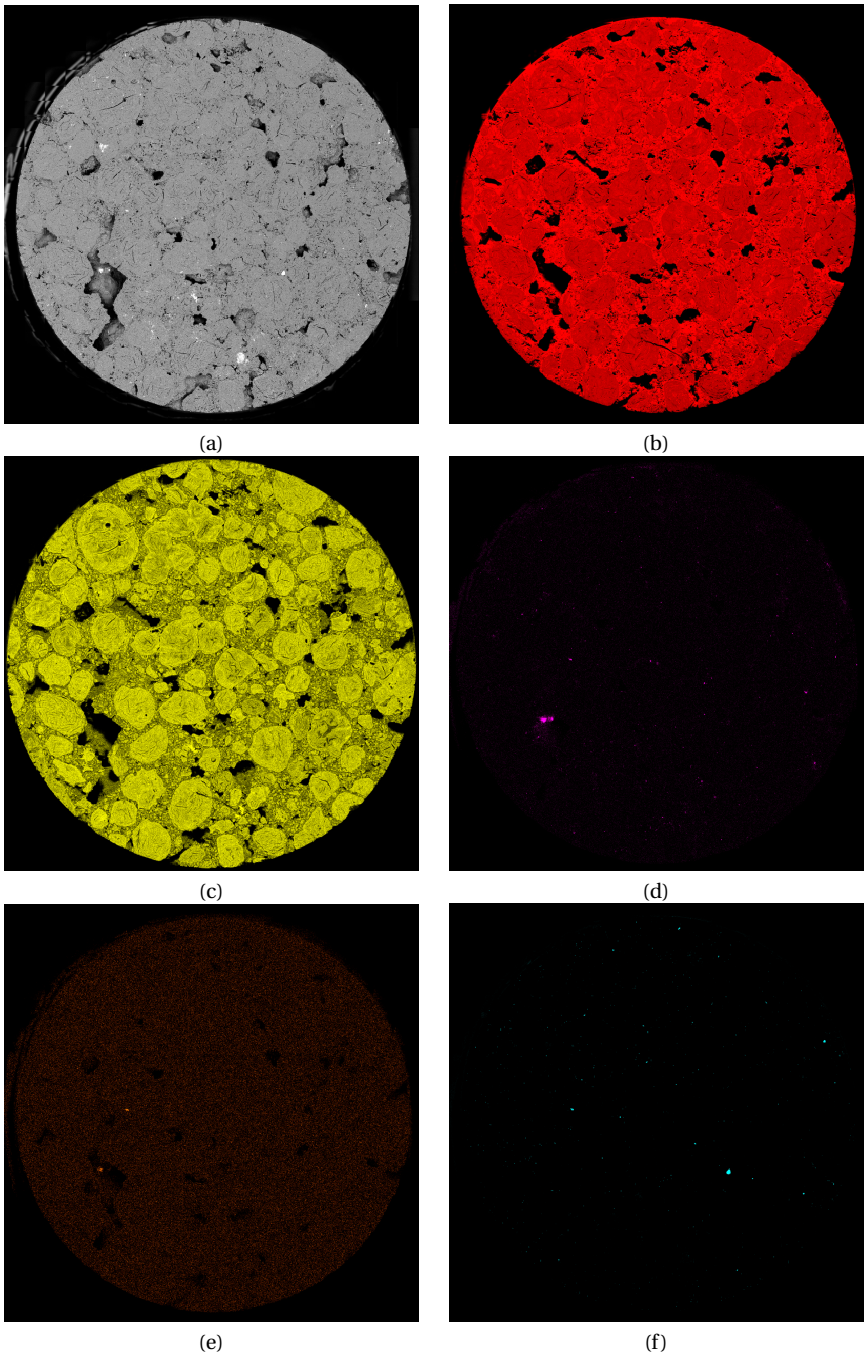

(a) (b) (c) (d) (e) (f)

Figure B.7: SEM/EDS pictures of the anode made of 100 % isotropic coke, sample 1. a) SEM Surface map, b) Carbon element map, c) Sulfur element map, d) Iron element map, e) Vanadium element map and f) Silicon element map.

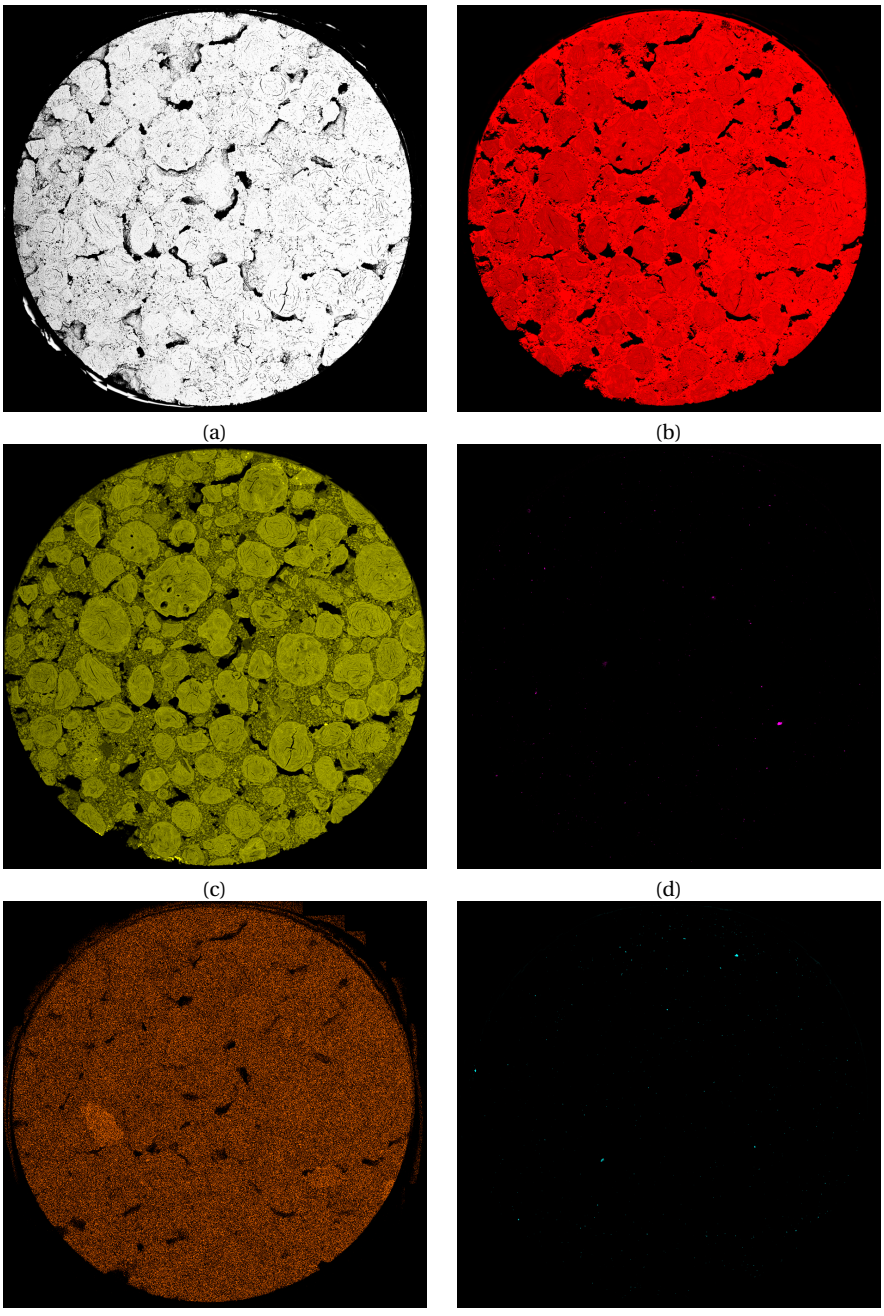

(a) (b) (c) (d) (e) (f)

Figure B.8: SEM/EDS pictures of the anode made of 100 % isotropic coke, sample 2.
a) SEM Surface map, b) Carbon element map, c) Sulfur element map, d) Iron element map, e) Vanadium element map and f) Silicon element map.

C Details on Equivalent Circuits, Capacitance and Electrochemical Impedance Spectroscopy

The in situ electrochemically active surface area can be measured by electrochemical impedance spectroscopy (EIS), by extracting the capacitance using a variety of equivalent electrical circuits [1]. The capacitance for a parallel-plate capacitor, C, given in Farads, F, is directly proportional to the area of the electrode by the expression in Equation C.1 [2].

$$C = \epsilon_r \epsilon_0 \frac{A}{d} \tag{C.1}$$

In the equation, ϵ_0 and ϵ_r are the dielectric constant in vacuum and the relative dielectric constant, respectively. d is the distance between the plates and A is the area of overlap between the plates.

Figure C.1 shows an example of a Nyquist plot obtained by EIS for one of the pilot anodes used in the present work. Some frequencies are indicated in the figure. The fitting of two relevant equivalent circuits are also indicated. The Nyquist plots were fitted to equivalent circuits using the software Zview 3.4e by Scribner Associates, Inc.. LR(CR) and LR(Q(R(LR))) are equivalent to the circuits shown in Figure C.2 a) and b), respectively. Common for both the LR(CR) and LR(Q(R(LR))) circuits is that the first L is attributed to inductance of cables and leads. The inductance is assumed to be dominating for the very high frequencies (i.e. ≥100000 Hz). The first R is attributed to the resistance of the electrolyte as well as the resistance through leads and cables. This resistance is known as the series resistance, R_S. Measured potentials can be IR corrected using the series resistance, R_S, as obtained from the high frequency intercept of the Nyquist plots. In the LR(CR) circuit the C and the R are the double layer capacitance, C_{dl} and the resistance to charge transfer, R_{CT}, respectively. As indicated in Figure C.1, the LR(CR) circuit is used to investigate the first semi-circle only.

For the LR(Q(R(LR))) circuit, Q is the constant phase element. The constant phase element is introduced since the semi-circle deviates from a perfect semi-circle as described in [1, 3] and as indicated in Figure C.1. The relatively high surface roughness of carbon anodes makes it reasonable to introduce a constant phase element. The second and third R in LR(Q(R(LR))) are the resistance to charge transfers for the first and second semi-circles, $R_{CT,1}$ and $R_{CT,2}$, as indicated in Figure C.2 b). Finally, the second L is the inductance of adsorbed species, L_{ads}, on the anode surface. This circuit was described by Harrington and Conway [4], except that the ideal double layer capacitance, C_{dl} has been replaced by a constant phase element, Q. This equivalent circuit was derived for a general reaction sequence involving intermediately adsorbed species.

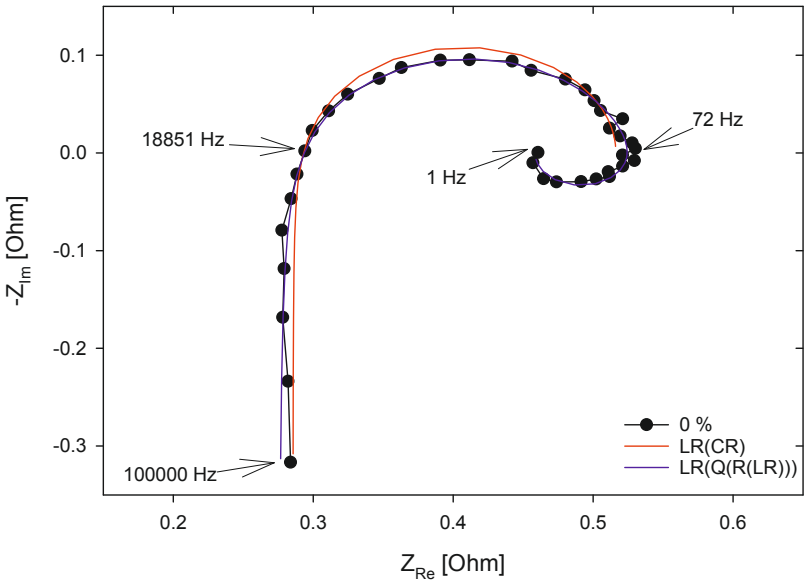

Figure C.1: Example of Nyquist plot.

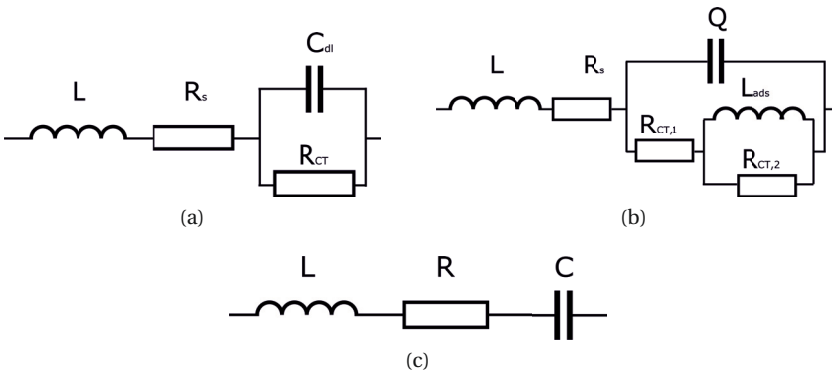

Figure C.2: a) The LR(CR), b) LR(Q(R(LR))) and c) LRC equivalent circuits, respectively.

The effective capacitance, C_{eff}, can be calculated from the constant phase element, Q, according to Equation C.2 (equivalent to Equation 15 in Orazem et al. [3] developed for Faradaic systems). The effective capacitance is also denoted interfacial capacitance and may be considered to be a good approximation for the double layer capacitance.

$$C_{eff} = Q^{1/\alpha}\left(\frac{R_S(R_{CT_1}+R_{CT_2})}{R_s+R_{CT_1}+R_{CT_2}}\right)^{(1-\alpha)/\alpha} \tag{C.2}$$

α is the dimensionless constant phase element exponent. The remaining symbols are described above.

Figure C.2 c) shows the LRC circuit. This circuit is used in the high frequency range in order to extract the double layer capacitance, C_{dl}. It is assumed that inductance of the wires is dominating for the horizontal part of the curve below the y-intercept in Figure C.1. For the present work, the inductance was extracted at 100000 Hz, according to Equation C.3.

$$L_{100000Hz} = \frac{Z_{Im,100000\,Hz}}{2\pi f} \tag{C.3}$$

In Equation C.3, f is the frequency and Z_{Im} is the imaginary impedance. The inductance was then used to calculate the capacitance using Z_{Im} for each frequency step according to Equation C.4.

$$C_{dl,high\,frequency} = \frac{1\cdot 10^6}{1.52\cdot 2\pi f(2\pi f L - Z_{Im})} \tag{C.4}$$

$C_{dl\,frequency}$ could then be plotted *vs.* frequency and from the graph a horizontal capacitance range is found in the high frequency region. This horizontal range can then be used to determine $C_{dl,high\,frequency}$. This method has also been described in [5–7].

References

[1] M.E. Orazem and B. Tribollet. *Electrochemical Impedance Spectroscopy*. 1st. Hoboken, New Jersey: Wiley, 2008.

[2] H.D. Young and R.A. Freedman. *University Physics*. 11th. San Francisco: Pearson Education, Inc., 2004.

[3] M. Orazem, I. Frateur, B. Tribollet, V. Vivier, S. Marcelin, N. Pebere, A.L. Bunge, E.A. White, D.P. Riemer, and M. Musiani. "Dielectric Properties of Materials Showing Constant-Phase-Element (CPE) Impedance Response". *Journal of the Electrochemical Society* (2013), pp. C215–C225.

[4] D.A. Harrington and B.E. Conway. "ac Impedance of Faradaic Reactions Involving Electrosorbed Intermediates - I. Kinetic Theory". *Electrochim. Acta* (1987), pp. 1703–1712.

[5] J. Thonstad. "The Electrode Reaction on the C, CO_2 Electrode in Cryolite-Alumina Melts-II. Impedance Measurements". *Electrochim. Acta* (1970), pp. 1581–1595.

[6] S. Jarek and J. Thonstad. "Double-layer capacitance and polarization potential of baked carbon anodes in cryolite-alumina melts". *J. Appl. Electrochem.* (1987), pp. 1203–1212.

[7] W. Gebarowski, C. Sommerseth, A.P. Ratvik, E. Sandnes, L.P. Lossius, H. Linga, and A.M Svensson. "Interfacial Boundary between Carbon Anodes and Molten Salt Electrolyte". *Light Metals* (2016), In press.

D Impedance Parameters for Equivalent Circuits LR(CR) and LR(Q(R(LR))) for Anodes Varying in Isotropic Coke Content

Tables D.1 and D.2 show the parameters (inductance, L, series resistance, R_s, double layer capacitance, C_{dl} and resistance to charge transfer, R_{ct}) obtained by modelling the impedance raw data with the equivalent electrical circuit, LR(CR), for the first anode parallel in the two duplicate runs. In the tables the IR corrected potential and the corresponding current density are also shown. Tables D.3 and D.4 show the parameters obtained when modelling the impedance raw data with the equivalent electrical circuit LR(Q(R(LR))) for the first parallel for the two duplicate runs, respectively. These parameters include inductance, L, series resistance, R_s, constant phase element, Q, the dimensionless constant phase element exponent, α, resistance to charge transfer, R_{CT_1} and R_{CT_2}, and inductance of adsorbed species on the electrode surface.

Table D.1: The parameters obtained by modelling the EIS results by the equivalent circuit LR(CR), run 1, parallel 1.

Anode	V IR corr. V	i A/cm^2	L H	R_S Ω	C_{dl} μF	R_{CT} Ω
Graphite	1.45	0.14	$1.78\cdot10^{-7}$	0.25	46	0.38
0 %	1.40	0.34	$2.15\cdot10^{-7}$	0.21	262	0.13
7.2 %	1.40	0.32	$2.59\cdot10^{-7}$	0.23	265	0.14
14.2 %	1.39	0.32	$2.58\cdot10^{-7}$	0.24	220	0.14
35.0 %	1.40	0.35	$2.90\cdot10^{-7}$	0.20	218	0.13
49.0 %	1.38	0.30	$2.51\cdot10^{-7}$	0.23	327	0.14
100 %	1.39	0.34	$2.51\cdot10^{-7}$	0.23	307	0.11

Table D.2: The parameters obtained by modelling the EIS results by the equivalent circuit LR(CR), run 2, parallel 1.

Anode	V IR corr. V	i A/cm^2	L H	R_S Ω	C_{dl} μF	R_{CT} Ω
Graphite	1.48	0.06	$3.69\cdot10^{-7}$	0.30	39	0.84
0 %	1.43	0.17	$4.99\cdot10^{-7}$	0.29	289	0.23
7.2 %	1.44	0.17	$5.45\cdot10^{-7}$	0.25	267	0.24
14.2 %	1.44	0.17	$5.19\cdot10^{-7}$	0.26	269	0.23
35.0 %	1.44	0.16	$4.40\cdot10^{-7}$	0.27	317	0.23
49.0 %	1.43	0.20	$4.97\cdot10^{-7}$	0.25	294	0.19
100 %	1.44	0.17	$4.85\cdot10^{-7}$	0.25	455	0.18

Table D.3: The parameters obtained by modelling the EIS results by the equivalent circuit LR(Q(R(LR))), run 1, parallel 1.

Anode	V IR corr. V	i A/cm^2	L H	R_S Ω	Q μF	α	R_{CT_1} Ω	L_{ads} H	R_{CT_2} Ω
Graphite	1.45	0.14	$2.23{\cdot}10^{-7}$	0.21	189	0.85	0.35	$2.39{\cdot}10^{-4}$	0.10
0 %	1.40	0.34	$2.25{\cdot}10^{-7}$	0.20	807	0.88	0.12	$1.59{\cdot}10^{-4}$	0.03
7.2 %	1.40	0.32	$2.65{\cdot}10^{-7}$	0.23	566	0.92	0.11	$2.46{\cdot}10^{-4}$	0.04
14.2 %	1.39	0.32	$2.69{\cdot}10^{-7}$	0.23	707	0.88	0.12	$1.33{\cdot}10^{-4}$	0.03
35.0 %	1.40	0.35	$3.07{\cdot}10^{-7}$	0.19	1116	0.82	0.12	$1.39{\cdot}10^{-4}$	0.04
49.0 %	1.38	0.30	$2.40{\cdot}10^{-7}$	0.26	1410	0.84	0.12	$2.73{\cdot}10^{-4}$	0.04
100 %	1.39	0.34	$2.63{\cdot}10^{-7}$	0.22	1476	0.83	0.10	$9.88{\cdot}10^{-5}$	0.02

Table D.4: The parameters obtained by modelling the EIS results by the equivalent circuit LR(Q(R(LR))), run 2, parallel 1.

Anode	V IR corr. V	i A/cm^2	L H	R_S Ω	Q μF	α	R_{CT_1} Ω	L_{ads} H	R_{CT_2} Ω
Graphite	1.48	0.06	$4.29{\cdot}10^{-7}$	0.25	119	0.88	0.67	$1.16{\cdot}10^{-3}$	0.25
0 %	1.43	0.17	$5.13{\cdot}10^{-7}$	0.27	897	0.87	0.18	$1.07{\cdot}10^{-3}$	0.07
7.2 %	1.44	0.17	$5.58{\cdot}10^{-7}$	0.24	727	0.89	0.18	$1.04{\cdot}10^{-3}$	0.07
14.2 %	1.44	0.17	$5.35{\cdot}10^{-7}$	0.24	934	0.86	0.19	$1.03{\cdot}10^{-3}$	0.07
35.0 %	1.44	0.16	$4.58{\cdot}10^{-7}$	0.25	1322	0.84	0.19	$1.18{\cdot}10^{-3}$	0.07
49.0 %	1.43	0.20	$5.12{\cdot}10^{-7}$	0.23	1195	0.84	0.16	$5.93{\cdot}10^{-4}$	0.05
100 %	1.44	0.17	$5.13{\cdot}10^{-7}$	0.22	5753	0.71	0.18	$8.69{\cdot}10^{-4}$	0.05

Capacitance parameters are shown in Tables D.5 and D.6 where the double layer capacitance, C_{dl} is extracted directly from the LR(CR) circuit and the effective capacitance is calculated using Equation 3.12 and the parameters obtained by modelling from the LR(Q(R(LR))) circuit (shown in Tables D.3 and D.4). The parameters for one parallel of each pilot anode from the two duplicate runs.

Table D.5: Capacitance results from electrical impedance spectroscopy using two different models: LR(CR) and LR(Q(R(LR))), run 1, parallel 1.

Anode	V IR corr. V	i A/cm^2	C_{dl} LR(CR) μF/cm^2	C_{eff} LR(Q(R(LR))) μF/cm^2
Graphite	1.45	0.14	30	20
0 %	1.40	0.34	172	142
7.2 %	1.40	0.32	174	156
14.2 %	1.39	0.32	145	119
35.0 %	1.40	0.35	143	102
49.0 %	1.38	0.30	215	173
100 %	1.39	0.34	202	158

Table D.6: Capacitance results from electrical impedance spectroscopy using two different models: LR(CR) and LR(Q(R(LR))), run 2, parallel 1.

Anode	V IR corr. V	i A/cm^2	C_{dl} LR(CR) μF/cm^2	C_{eff} LR(Q(R(LR))) μF/cm^2
Graphite	1.48	0.06	26	19
0 %	1.43	0.17	289	158
7.2 %	1.44	0.17	267	149
14.2 %	1.44	0.17	269	143
35.0 %	1.44	0.16	317	164
49.0 %	1.43	0.20	294	153
100 %	1.44	0.17	455	183

E Conferences and Publications

E.1 Primary Conferences and Publications

- "A Method for Comparing the HF Formation Potential of Aluminas with Different Water Contents", NMS (Norsk metallurgisk selskap), Trondheim, Norway, 2012. Oral presentation.
- Participation at TMS, San Diego, California, 2014.
- "Understanding Anode Performance", RMW9 (Reactive Metal Workshop), Caltech Pasadena, California, 2014. Poster presentation.
- "Spatial Methods for Characterising Carbon Anodes for Aluminium Production", TMS, Orlando, Florida, 2015. Publication in Light Metals 2015 and oral presentation.
- Participation at RMW10, MIT Boston, Massachusetts, 2015.
- "Electrochemical Reactivity an Wetting Properties of Anodes Made from Anisotropic and Isotropic Cokes", TMS, Nashville, Tennessee, 2016.

E.2 List of Secondary Publications - Co-Authorship

- "Electrochemical Characterization of Carbon Anode Performance", Rebecca Jayne Thorne, Camilla Sommerseth, Espen Sandnes, Ole Kjos, Thor Anders Aarhaug, Lorentz Petter Lossius, Hogne Linga and Arne Petter Ratvik. Light Metals, 2013.
- "Understanding Anode Overpotential", Rebecca Jayne Thorne, Camilla Sommerseth, Ann Mari Svensson, Espen Sandnes, Lorentz Petter Lossius, Hogne Linga and Arne Petter Ratvik. Light Metals, 2014. The paper won the "Subject Award – Electrode Technology for Aluminum Production" at TMS.
- "Bubble Evolution and Anode Surface Properties in Aluminium Electrolysis", Rebecca Jayne Thorne, Camilla Sommerseth, Arne Petter Ratvik, Stein Rørvik, Espen Sandnes, Lorentz Petter Lossius, Hogne Linga and Ann Mari Svensson. Journal of Electrochemical Society, 2015.
- "Correlation between Coke Type, Microstructure and Anodic Reaction Overpotential in Aluminium Electrolysis", Rebecca Jayne Thorne, Camilla Sommerseth, Arne Petter Ratvik, Stein Rørvik, Espen Sandnes, Lorentz Petter Lossius, Hogne Linga and Ann Mari Svensson. Journal of Electrochemical Society, 2015.
- "Interfacial Boundary between Carbon Anodes and Molten Salt Electrolyte", Wojciech Gebarowski, Camilla Sommerseth, Arne Petter Ratvik, Espen Sandnes, Lorentz Petter Lossius, Hogne Linga, Ann Mari Svensson. Light Metals, 2016.

E.3 From Light Metals Proceedings 2015

Light Metals 2015
Edited by: Margaret Hyland
TMS (The Minerals, Metals & Materials Society), 2015

SPATIAL METHODS FOR CHARACTERISING CARBON ANODES FOR ALUMINIUM PRODUCTION

Camilla Sommerseth[1], Rebecca Jayne Thorne[1], Stein Rørvik[2], Espen Sandnes[3], Arne Petter Ratvik[2], Lorentz Petter Lossius[3], Hogne Linga[3] and Ann Mari Svensson[1]

[1]Dept. of Materials Science and Engineering, Norwegian University of Science and Technology, NO-7491 Trondheim, Norway
[2]SINTEF Materials and Chemistry, NO-7465 Trondheim, Norway
[3]Hydro Aluminium AS, Årdal, Norway

Keywords: Carbon Anodes, Anisotropic Sponge Coke, Isotropic Coke, Carbon Consumption

Abstract

Pilot test anodes were designed by Hydro Aluminium for laboratory studies using controlled blends of <2 mm aggregate from two single source cokes. Spatial and imaging methods were used to characterise anode surfaces with respect to consumption, density, pore distribution and real active area before and after electrolysis. The methods include X-ray computed tomography (CT), confocal microscopy, scanning electron microscopy (SEM) and energy-dispersive X-ray spectroscopy (EDS). It was found that during electrolysis, the electrolyte does not completely wet the carbon inside large pores on the surface. Hence, even large pores do not contribute to the electrochemically active surface area. Large grains of isotropic cokes and anisotropic sponge cokes are consumed at approximately the same rate, and bubble coke in anisotropic sponge cokes are consumed at a slower rate than the bulk material. This is due to higher resistivity through the bubble coke.

Introduction

Producing stable and good quality anodes is critical for satisfactory performance of anodes during electrolysis. The industry is facing deteriorating coke quality, and previously rejected fuel grade cokes of isotropic character now have to be accepted as anode grade coke [1, 2]. These changes in coke quality will affect impurity levels, impurity elements and mixing and baking properties [3, 4]. Physical parameters like density, specific electric resistivity, air permeability, mechanical strength, coefficient of thermal expansion, thermal shock resistance, thermal conductivity, CO_2 and air reactivity and dusting are commonly used in the aluminium industry to characterise carbon anodes to evaluate their quality. These tests are done on non-electrolysed anodes before they have been used in cells, but there is not necessarily a good correlation between these properties and the anode performance during electrolysis.

When dealing with anodes and electrolysis to produce aluminium, one important factor is how the electrolyte wets the anodes. Wettability is an important factor for gas bubble growth, formation and release. Different coke types may affect wetting properties of anodes towards the electrolyte. Wetting tests have traditionally been done using the sessile drop method, where electrolyte is placed on an unpolarised anode surface, heated and the wetting angle measured when the electrolyte has melted. This gives an idea of the wetting conditions; although wetting conditions are thought to change during polarisation of the carbon surface. Poor wetting between electrolyte and anode is often said to cause the anode effect [5, 6], although this has been disputed by other researchers [7]. When performing the sessile drop method it has been found that the lower the alumina concentration, the poorer wetting [7].

Through powerful spatial imaging methods the understanding on how anodes are consumed during electrolysis can be improved. Wetting properties of the electrolyte toward the anode surface and pores in the anode structure can be investigated by CT scanning. Adams et al. [8] showed how CT scanning can be used to view interior of baked anodes. Picard et al. [3, 9] have demonstrated the use of CT scanning to determine apparent density and detect cracks in anodes. The method is non-destructive and enables reconstruction of the internal morphology of the samples, thus providing useful information about both pristine and electrolysed anodes. Confocal microscopy can be used to investigate the roughness of anode surfaces before and after electrolysis, and increases the understand-

ing of how anodes are consumed during electrolysis. The opportunity to create large area maps in SEM and create EDS elemental maps of larger areas also gives important information on the distribution of various impurity elements and coke grains, and how they might affect anode consumption locally.

In this work, wetting of the carbon anode during electrolysis, as well as possible preferential consumption of coke grains (anisotropic grains with and without high content of sulphur, bubble coke, and isotropic grains) has been investigated by CT scanning, SEM/EDS and confocal microscopy in order to better understand anode performance during electrolysis. Cracks in anodes formed during the baking process is also investigated by CT scanning.

Experimental

Pilot anodes were specially designed and made at Hydro Årdalstangen for these experiments. They were produced from industrial grade coke and pitch. The anodes were made of <2 mm coke aggregate from two different single source cokes and produced to a common sieving curve from ball mill product (fines <63 μm), 0-1 and 1-2 mm fractions. This was done to ensure a comparatively smooth and representative exposed surface area.

Three different anode materials were studied:

- Anode A = made from 100 % single source anisotropic sponge coke A (fines from sponge coke)
- Anode B = made from 100 % single source isotropic coke B (fines from isotropic coke)
- Anode C = 49 % isotropic coke B, 51 % anisotropic sponge coke A (fines from sponge coke)

The anodes were characterized by complementary image analysis techniques to investigate the pore distribution on the surface and interior in the anodes and electrolyte penetration into pores before and after electrolysis by using CT and investigating the pore structure in anodes before electrolysis by confocal microscopy. SEM/EDS were used to perform element mapping on large surface areas.

For the CT mapping an anode assembly similar to the one shown in Figure 1 in Thorne et al. [4] was used (Ø = 10 mm, height of anode sample = 5 mm). The anode test piece was covered with a BN piece on the top and bottom to create a horizontal anode surface area. A graphite rod in the middle served as electrical contact. The anodes were scanned both before and after electrolysis at 1.0 A/cm^2 for 1800 s in a cryolitic melt with cryolite ratio 2.3 and saturated in alumina. The anodes were withdrawn from the electrolyte with current still on (hot-pulled). CT was performed with a Nikon XT H225 ST. A molybdenum reflection target was used. Settings for the imaging were 110 kV and 200 μA. Integration time was 1 second, 1440 projections per revolution, distance from source to sample was 35.1 mm, distance from source to detector was 1124.8 mm and the voxel size (combination of "volume" and "pixel" to denote the resolution) was 6.2 μm. Three different software programs from Nikon Metrology were used to create the CT images: Inspect-X (used to control the x-ray generator, sample table and collecting images), CT Pro 3D (used to edit parameter files for reconstruction of CT images) and CT Agent (used for reconstruction of CT images). The images were exported as a stack of 2000 single 2D images sliced in the XY (transverse) direction. These were loaded and postprocessed in ImageJ by cropping, translating and rotating the images so that the after electrolysis scans matched the before electrolysis scans. The images were then merged into two side-by-side images allowing easy comparison of the before and after electrolysis scans. All these steps were done automatically by a custom written macro. The translation and rotation parameters were determined manually.

A different anode assembly was used for the confocal microscopy and SEM/EDS scans. The anodes were rods of Ø = 10 mm where the horizontal anode surfaces were grinded with SiC paper step-wise down to P#4000. The distribution of impurities on the anode surfaces was determined by SEM/EDS and the changes in topography before and after electrolysis was studied in an Infinitefocus from Alicona 3D confocal microscope. The resolution was 410 nm. The equipment used for the SEM/EDS large area image mapping was a low vacuum SEM, Hitachi S-3400N and the software used was Aztec by Oxford Instruments. The entire horizontal end piece area of the anode sample was investigated by creating over 400 small area maps with an overlap of 20 %. These maps were then stitched together to one large map using the Aztec software. 3D maps from confocal microscopy showed the surface roughness of the grinded

samples. Electrolysis was conducted for 1500 s at a current density of 1.0 A/cm^2, in a melt saturated with alumina, and with a cryolite ratio of 2.3. The electrolyte left on the anode samples after electrolysis, was removed using a solution of $AlCl_3$. Confocal microscopy measurements were repeated for the electrolysed samples in order to investigate changes in the surface roughness.

Results and Discussion

CT Imaging

Figures 1, 2 and 3 show two cross-sections before and after electrolysis through the core of two different anode parallels of the three anode materials (A-C), obtained by the CT method. The dense core in the middle is the graphite rod that the anode test piece is threaded around, in order to create electrical contact. The before and after images have been matched to fit the exact rotation and height in the anode piece and allows for identification of the electrolyte wetting of pores and carbon consumption on the surface. The CT images give a close to frozen view of the electrolyte-carbon surface interaction during electrolysis as the electrolyte freezes very quickly on the anode surface when it is taken out of the furnace.

In Figure 1, cross-sections of an anode (Ø = 10 mm) made of anisotropic sponge coke is shown. The single source coke used for anode A is inhomogeneous, with some small areas of bubble coke. Anode A is a well-mixed anode with few large pores. Figure 4 shows a zoom-in on an area of anode A parallel 2 with bubble coke and matrix before and after electrolysis. It is interesting to see that the bubble coke is consumed at a much lower rate than the bulk material. Also, the bubble coke appear to have poorer wetting towards the electrolyte, as the electrolyte layer is very thin. One explanation to why the bubble coke are consumed at a lower rate can be higher electronic resistivity through these high porosity grains. Another explanation can be that pores are filled with CO_2 gas, causing an overpressure that block the electrolyte from penetrating the pores. The former explanation seems more likely.

Anode B is displayed in Figures 2 (a) and (b). This anode is made from pure isotropic coke. The anode samples are full of large pores indicating potential for improved recipe, by changing the ratio between fines and larger coke grains. Even large pores are not filled with electrolyte, and the images suggest that the electrolyte forms a bridge at the neck of the pore. It is only when pores are convex (e.g. the pore of the left end of Figure 2 (b)) that the pore walls are wetted by electrolyte and contribute to the active surface area. In those cases an edge effect is seen and the surface is rounded off through electrolysis.

Images of scans of anode C are shown in Figure 3 (a) and (b). Anode C is a mixture of anisotropic (51 %) and isotropic coke (49 %). The isotropic coke grains are easily detectable as spheres in the anisotropic matrix. The anode is more porous than Anode A and long narrow cracks can be seen in the matrix close to the isotropic coke grains. Two enlarged pictures of anode B and C, shown in Figure 5, show that these narrow cracks can only be seen in the anodes of mixtures of coke A and B, not in anode B made of pure single cokes. The cracking probably occurs due to different thermal expansion of the coke types during baking. In Figure 3 (a) a white inclusion is seen in the non-electrolysed image in the upper left corner near the anode surface. After electrolysis, this inclusion is gone, and has left a void. It is reasonable to assume that this inclusion has been dissolved into the electrolyte. The electrolyte has not penetrated well into the void, suggesting poor wetting between the electrolyte and the anode when the anode is polarised. No preferred consumption between isotropic and anisotropic cokes can be seen.

Confocal Microscopy Images and SEM/EDS Maps

Figures 6 (a)-(x) show images from SEM/EDS investigations and confocal microscopy. EDS maps for other elements than sulphur have been excluded due to space limitations, although elements like Ca, Fe, Si and Zn were spread on the surface of the anode. Vanadium was not detected for anode A, but was found to "outline" the large spherical isotropic coke grains for anodes B and C. Figures 6 (d), (h) and (t) show contour images of the surfaces of anode A (both parallels) and anode C (parallel 1) after electrolysis, where the electrolyte has been removed using an $AlCl_3$ solution. On all those images it can be seen that bubble coke sticks out, suggesting low carbon consumption. The CT images support these findings. Also, there are indications that areas high in sulphur may have been consumed at a higher rate than the matrix. This can be due to different structure of the coke grains high in sulphur compared to the regular coke grains.

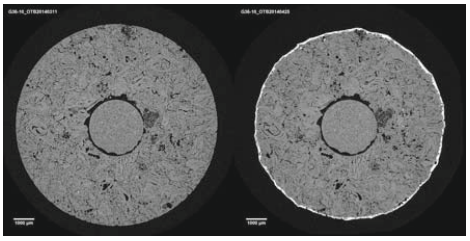

(a)

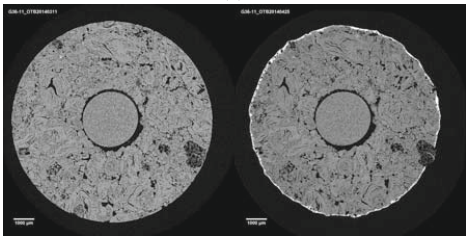

(b)

Figure 1: Anode A (a) Parallel 1. (b) Parallel 2.

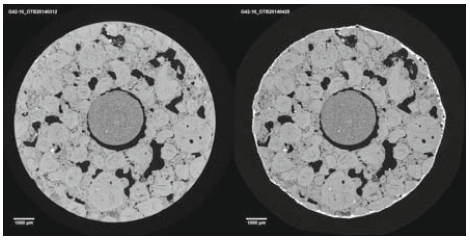

(a)

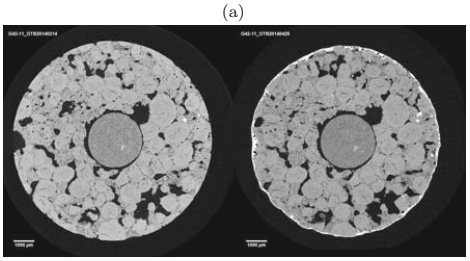

(b)

Figure 2: Anode B (a) Parallel 1. (b) Parallel 2.

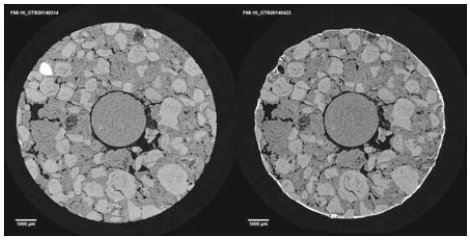

(a)

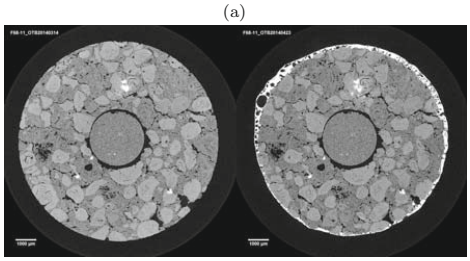

(b)

Figure 3: Anode C (a) Parallel 1. (b) Parallel 2.

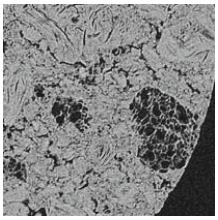

(a)

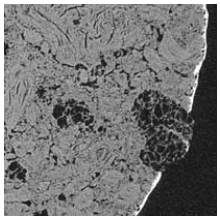

(b)

Figure 4: Anode A enlarged area, parallel 2 (a) Before electrolysis. (b) After electrolysis.

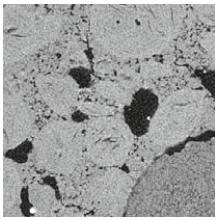

(a)

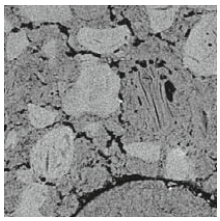

(b)

Figure 5: Enlarged area on anode cracks (a) Anode B. (b) Anode C.

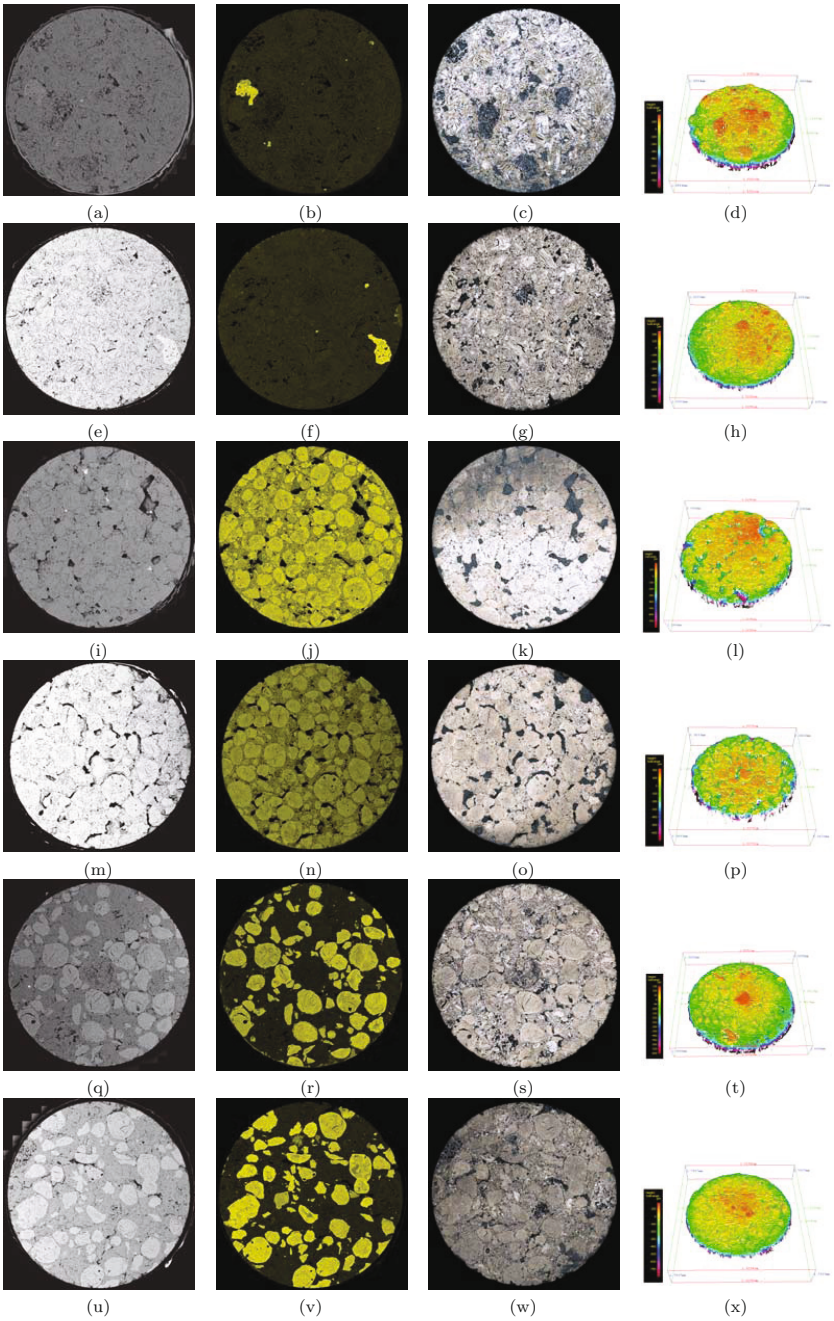

Figure 6: Anode A, parallel 1 ((a)-(d)) and parallel 2 ((e)-(h)). Anode B, parallel 1 ((i)-(l)) and parallel 2 ((m)-(p)). Anode C, parallel 1 ((q)-(t)) and parallel 2 ((u)-(x)). (a), (e), (i), (m), (q) and (u) are SEM surface maps. The pictures are stiched together of over 400 single pictures. (b), (f), (j), (n), (r) and (v) are sulphur element maps obtained by EDS. (c), (g), (k), (o), (s) and (w) are confocal microscopy images before electrolysis. (d), (h), (l), (p), (t) and (x) are 3D contour images obtained by confocal microscopy after electrolysis.

To verify this, more experiments need to be done, and possibly other methodologies need to be used. The removal of electrolyte by $AlCl_3$ is a weak point of the methodology of confocal imaging after electrolysis. Parts of the anode can detach when performing this cleaning procedure and the electrolyte proved difficult to remove from the anode despite being submerged into the $AlCl_3$ solution for a long time. Figures 6 (l) and (p) suggest that the fines have been consumed at a higher rate than the larger isotropic coke grains. However, the CT images do not support this, suggesting that removal of electrolyte on the carbon surface may have contributed to this observation. The CT images do not support any preferred consumption between the large isotropic coke grains and the fines and pitch binder. However, the fines in anode B were of isotropic character, whereas the fines in anodes A and C were of anisotropic character. Hence, Figures 6 (t) and (x) suggest that isotropic fines detach more easily from the anode surface when removing the electrolyte. This can be due to poor wetting between coke and pitch during anode fabrication.

Conclusion

CT imaging is a powerful and non-destructive method to investigate interior and structure (carbon porosity and coke grain distribution) of carbon anodes for aluminium production, both before and after electrolysis. The method gives valuable information on cracks and porosity, and can thus indicate ways to optimise baking and mixing temperature as well as pitch/coke interactions. CT also gives information on the consumption of the carbon surface when electrolysed. Large area mapping in SEM/EDS enables the investigation of relatively large anode surfaces in terms of elemental distribution of impurities and homogeneity. Confocal microscopy can be used to determine the real surface area including the pore surfaces. It can also be used to investigate the anode surface after electrolysis to a certain degree. The most important findings in this work is that during electrolysis there is no preferred consumption between large grains of anisotropic and isotropic coke. For sponge cokes, bubble coke are consumed at a slower rate than the matrix and electrolyte does not penetrate even larger pores unless they are of convex character.

Acknowledgement

This work was funded by The Norwegian Research Council and Hydro Aluminium AS through the research project Hal Ultra Performance. Funding and permission to publish is gratefully acknowledged. A great thank you is also sent to Aksel Alstad, Cristian Torres, Ole Tore Buset and Julian Tolchard.

References

[1] L. Edwards, N. Backhouse, H. Darmstadt, and M.-J. Dion, "Evolution of anode grade coke," *Light Metals*, pp. 1207–1212, 2012.

[2] L. Edwards, F. Vogt, M. Robinette, R. Love, A. Ross, M. McClung, R. Roush, and W. Morgan, "Use of shot coke as an anode raw material," *Light Metals*, pp. 985–990, 2009.

[3] D. Picard, J. Lauzon-Gauthier, C. Duchesne, H. Alamdari, M. Fafard, and D. Ziegler, "Automated crack detection method applied to CT images of baked carbon anode," *Light Metals*, pp. 1275–1280, 2014.

[4] R. Thorne, C. Sommerseth, A. Svensson, E. Sandnes, L. Lossius, H. Linga, and A. Ratvik, "Understanding anode overpotential," *Light Metals*, pp. 1213–1217, 2014.

[5] H. Vogt, "Effect of alumina concentration on the incipience of the anode effect in aluminium electrolysis," *J. Appl. Electrochem.*, pp. 779–788, 1999.

[6] H. Vogt, "The anode effect as a fluid dynamic problem," *J. Appl. Electrochem.*, pp. 137–145, 1999.

[7] P. Meunier, B. Welch, M. Skyllas-Kazacos, and V. Sahajwalla, "Effect of dopants on wetting properties and electrochemical behaviour of graphite anodes in molten Al_2O_3-cryolite melts," *J. Appl. Electrochem.*, pp. 837–847, 2009.

[8] A. Adams, O. Karacan, A. Grader, J. Mathews, P. Halleck, and H. Schobert, "The non-destructive 3-D characterization of pre-baked carbon anodes using x-ray computerized tomography," *Light Metals*, pp. 535–539, 2002.

[9] D. Picard, H. Alamdari, D. Ziegler, B. Dumas, and M. Fafard, "Characterization of pre-baked carbon anode samples using X-Ray computed tomography and porosity estimation," *Light Metals*, pp. 1283–1288, 2012.

E.4 From Light Metals Proceedings 2016

ELECTROCHEMICAL REACTIVITY AND WETTING PROPERTIES OF ANODES MADE FROM ANISOTROPIC AND ISOTROPIC COKES

Camilla Sommerseth[1], Rebecca Jayne Thorne[2], Arne Petter Ratvik[3], Espen Sandnes[1], Stein Rørvik[3], Lorentz Petter Lossius[4], Hogne Linga[4] and Ann Mari Svensson[1]

[1]Dept. of Materials Science and Engineering, Norwegian University of Science and Technology, NO-7491 Trondheim, Norway
[2]Norwegian Institute for Air Research, NO-2027 Kjeller, Norway
[3]SINTEF Materials and Chemistry, NO-7465 Trondheim, Norway
[4]Hydro Aluminium AS, Årdal, Norway

Keywords: Carbon Anodes, Anisotropic Coke, Isotropic Coke, Electrochemical Reactivity, Wetting Properties

Abstract

High quality anodes require stable raw materials. As the quality of the coke available for production of anodes is changing, future production will rely on cokes that are more isotropic with higher impurity levels than traditional raw materials. The purpose of this work was to improve the understanding of the electrochemical reactivity of different cokes. Anode:electrolyte wetting is a key factor towards determining electrochemical reactivity, which in turn is affected by anode properties, type of coke and polarization. Pilot anodes were fabricated from single source cokes; one anisotropic coke low in impurities, and one isotropic coke with significantly higher impurity levels. Electrochemical characterisation included chronopotentiometry, cyclic voltammetry and impedance spectroscopy. Wetting properties were studied on both unpolarised and polarised samples by a dedicated wetting apparatus, and indirectly by computed tomography (CT) images of frozen electrolyte films.

Introduction

The quality of anode grade coke has changed in the past decade due to shortage in supply of traditional anisotropic sponge coke, and cokes that were previously not regarded as anode grade coke are now accepted by the aluminium industry. These cokes are blended with more traditional anisotropic coke [1, 2].

An improved knowledge on how isotropic cokes influence the electrochemical behaviour of anodes is needed and has been investigated in [3, 4, 5]. The overpotential is a source of increased energy consumption. Equation 1 summarises the measured anodic potential, where E^{rev} is the reversible potential (1.187 V w.r.t. Al/Al^{3+} [6]), η_c is the concentration overpotential, and in a saturated melt this overpotential may be considered negligible. η'_r is the reaction overpotential which will depend on the anode material [4]. η_h is overpotential caused by hyperpolarisation due to bubbles on the surface. The last term in Equation 1 describes the increased ohmic resistance at the anode caused by bubble build-up: δR_s denotes the ohmic resistance due to bubbles blocking the anode surface and R'_s is the ohmic resistance with no bubbles screening the anode. Due to the vertical anode setup used, η_h, $I \cdot \delta R_s$ and $I \cdot R'_s$ are negligible. Thorne *et al.* found a slight reduction in reaction overpotential when using isotropic coke compared to anisotropic sponge coke in anodes [4].

$$E_{measured} = E^{rev} + \eta_c + \eta'_r + \eta_h + I(R'_s + \delta R_s) \quad (1)$$

Electrical impedance spectroscopy (EIS) can be used in order to investigate the capacitance of anodes, which is generally assumed to represent the wetting of the anode surface by the electrolyte [7]. An increase in capacitance of about 45 % was seen on a polarised anode sample compared with a fresh anode sample, and this capacitance increase was attributed to higher surface area exposed to electrolyte. Thonstad [7] measured a double layer capacitance range for pyrolitic graphite between 45-75 $\mu F/cm^2$ and a range for baked carbon between 150-600 $\mu F/cm^2$ using a horizontal anode setup. In this work, capacitance is used in order to determine the charge per anode area for the different anode materials used. Thorne *et al.* [4] found a slightly higher capacitance for an isotropic coke anode compared with an anisotropic coke anode, denoted as Anode 4 and Anode 1, respectively.

The wetting properties have been studied for various

electrolyte compositions and also for polarised *vs.* unpolarised samples [6, 8]. Solheim *et al.* [8] described how wetting properties change after polarisation of an anode surface compared with an unpolarised surface, using a specially constructed wetting apparatus for the immersion and emersion of a carbon anode cup. It was observed that the receding wetting angle during emersion changed when a crucible containing a cryolitic electrolyte was pulled away from an anode sample, before and after polarisation. CT imaging can also be used to investigate the frozen electrolyte image on an anode sample and is hence anticipated to reflect the wetting properties on the anode:electrolyte interface [9]. The sessile drop method was used in order to investigate the anode:electrolyte interface on an unpolarised anode surface by Thorne *et al.* [5]. It was found that for both graphite and the anisotropic coke materials, the anode:electrolyte wetting angles were of non-wetting character, i.e. θ>90°. The isotropic anode materials showed a wetted character between anode:electrolyte, i.e. θ<90°. The sessile drop method is an equilibrium measurement, where a very small electrolyte sample is placed on the anode surface. There are some sources of error with this method, including the small electrolyte sample on the very small anode surface area, the fact that the electrolyte:anode interface is stagnant, sensitivity to surface inhomogeneities and that no polarisation is applied.

In this work, the electrochemical reactivity of anodes towards a cryolitic electrolyte was investigated by reaction overpotential measurements and cyclic voltammetry. The wetting properties of the anode towards the electrolyte were investigated using three different methods. By capacitance measurements from EIS, by use of a dedicated wetting apparatus where the effect of polarisation was investigated, as explained in [8, 10] and finally, by CT imaging investigating the effect of the bathfilm thickness when pulling the anode out of the electrolyte with and without current on. The purpose of the work was to investigate correlations between electrochemically active surface area and the geometric surface area, as well as the electrochemical reactivity.

Experimental

Pilot anodes (Ø = 130 mm, h = 180 mm) were specially designed and made at Hydro Aluminium in Årdal for this experimental work. The anodes were produced from single source industrial grade cokes, one of anisotropic character: Anode A, and the other of purely isotropic character: Anode B. The same industrial grade pitch was used for both pilot anodes. Coke aggregate were produced to a common sieve curve from ball milled coke (fines <63 μm), 0-1 mm and 1-2 mm fractions. Fractions of <2 mm coke particles were chosen in order to maintain a representative exposed surface area during small scale electrochemical tests. For clarity, Anodes A and B in this work are identical to Anode A and B in Sommerseth *et al.* [9], also Anode A = Anode 1 and Anode B = Anode 4 in [3, 4, 5], however, new parallels samples have been made for all electrochemical tests. Ultrapure graphite (CMG grade) from Svensk Specialgrafit AB was used as reference carbon material.

During electrochemical tests an experimental setup and anode assembly similar to that described in Figure 1 by Thorne *et al.* [3] was used. The vertical anode assembly gave a well-defined, geometrical surface area of 1.52 cm^2 and negligible bubble noise. The surface area was not corrected for consumption of the anodes, however, the electrolysis time was kept to a minimum in order to avoid changes of the geometrical anode surface area. The electrolyte was a cryolite melt with a $NaF:AlF_3$ molar ratio of 2.3, corresponding to 9.8 wt% excess of aluminium fluoride, AlF_3. The cryolite was from Sigma-Aldrich (>97 %) and the AlF_3 was sublimed in-house for purification. The electrolyte was saturated in γ-Al_2O_3 (9.4 wt%) from Merck.

Electrochemical reactivity of anode A and B was determined by slow sweep-rate cyclic voltammetry (CV) at 0.1 V/s from open circuit potential (OCP) to 2.5 V and chronopotentiometry (CP) at 1.0 A/cm^2. Capacitance was measured by EIS at 1.5 V (non-IR corrected). Measurements were performed using a Zahner IM6 with built in EIS module and 20 A booster (PP201, from Zahner-Elektrik). Ohmic resistance was determined by taking the high frequency Z_{Re} intercept from the Nyquist plot obtained by EIS at OCP and this resistance was used to IR correct all electrochemical tests. An aluminium reference electrode was used and a new Al reference electrode was produced per duplicate run. Capacitance was extracted from Nyquist plots (EIS at 1.5 V) by three different methods: 1) modelling by the equivalent circuit LR(CR) and extracting the double layer capacitance (C_{dl}) directly, 2) modelling by the equivalent circuit LR(Q(R(LR))) and calculating the effective capacitance from Q according to Equation 13.10 in [11] and 3) extracting C_{dl} directly by extracting the

inductance directly at the highest frequency (100 000 Hz) and using the high frequency range of the Nyquist plot to determine the capacitance as described in [7].

Rod shaped anodes (Ø = 9.7 mm, h = 5 mm) were polarised for 1500 s at 1.0 A/cm^2 and electrolyte removed by soaking in saturated $AlCl_3$ solution until all remaining electrolyte on the surface was removed. The horisontal surface area was then investigated in a confocal microscope (Infinitefocus from Alicona 3D) in order to determine the surface roughness of the anode surface after polarisation. Based on data from the image analysis, the ratio of true area (including all voids and pores) to projected (geometrical) area of the horisontal surface was calculated. This true area over projected area was then used to normalise the capacitance for true surface area including all voids and pores.

The dynamic wetting angle for the anode:electrolyte interface was determined before and after polarisation at 0.7 A/cm^2 for 10 s, using the method described in [8] and [10]. This experimental setup was used with a slight modification: the anode cup samples in this work had an outer diameter of 30 mm and an inner diameter of 22 mm. The advancing wetting angles are reported here (during immersion of the anode sample into the electrolyte) due to more noisy recordings during the emersion of the sample.

The wetting properties of the anode:electrolyte interface for Anode A and Anode B were also investigated using CT imaging. Two test pieces of each Anodes A and B, respectively, were electrolysed for 2000 s, then one was pulled out of the furnace with current still on (hot-pulled) and the other was left in the electrolyte for 5 mins after current had been turned off and then pulled out (non-hot-pulled). The thickness of the bathfilm left on the sample surface was determined using the ImageJ software (from U. S. National Institutes of Health) where carbon and electrolyte were distinguished from each other by setting a threshold to the limit value of the density of the two different matters. Contour images of the bathfilm thickness were also produced. Methodology of CT imaging is thoroughly described in [9] and will not be described further here.

Results and Discussion

Figure 1 shows the IR corrected potentials corresponding to 0.6 A/cm^2, 0.8 A/cm^2 and 1.0 A/cm^2 extracted from CV curves and CP results at 1.0 A/cm^2. The

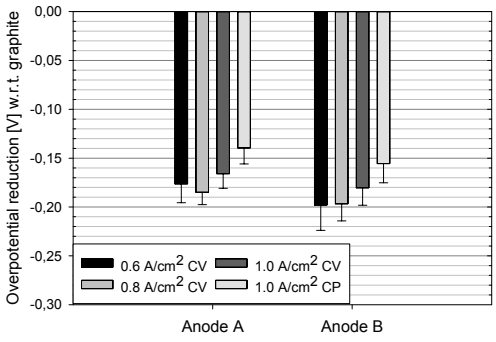

Figure 1: Overpotential reduction for Anode A and and Anode B w.r.t. graphite reference at three different current densities (0.6, 0.8 and 1.0 A/cm^2) obtained by CV curves and by CP at 1.0 A/cm^2.

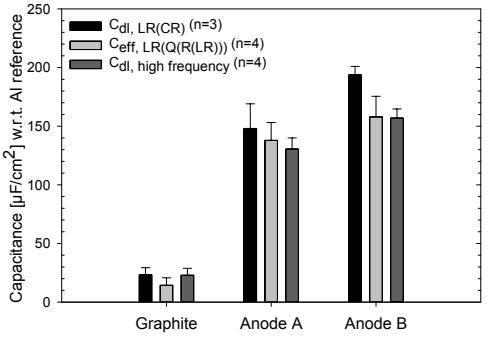

Figure 2: Capacitance for Graphite, Anodes A and Anode B obtained by running electrical impedance spectroscopy at 1.5 V (non-IR corrected).

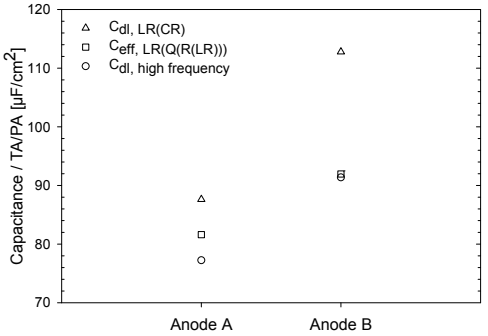

Figure 3: Surface area normalised double layer capacitance for Anode A and Anode B.

potential response was recorded with respect to Al reference and normalised with respect to graphite in order to compensate for some shifts in potential between duplicate runs with new reference electrodes. In general it can be seen that the purely isotropic coke based anode (Anode B), has a slightly lower reaction overpotential (η'_r) of about 15-20 mV, compared with Anode A, at all current densities and independent of measuring technique. This is in accordance with results found and reported elsewhere [4].

Figure 2 shows the capacitance for Graphite, Anode A and Anode B, extracted using three different methods, as described previously. For all three methods it is clear that Graphite has a very low capacitance at around 20 μF/cm^2 due to its non-porous and almost polished-like surface. The industrial anodes show higher capacitance where Anode A have values between 130-150 μF/cm^2 and Anode B have values between 155-195 μF/cm^2, depending on how the capacitance was extracted from the raw data. The Graphite values are somewhat lower than what Thonstad described [7], but this is probably due to the graphite materials used in the present work being non-identical to Thonstad's, as well as different instruments recording the spectras. Also, the industrial coke anodes are within the lower range to that Thonstad found for his baked carbon even though these materials are certainly not identical.

Confocal microscopy was used to determine the real surface area of the anode surfaces including all voids and pores, and this value was reported as true area over projected geometrical area (TA/PA). It was found that Anode B had a slightly higher TA/PA than Anode A. These area values were then used to determine if the higher capacitance for Anode B compared with Anode A, was merely due to increased surface area of Anode B. The capacitance was normalised in terms of TA/PA as seen in Figure 3. When normalising the capacitance values for surface area, capacitance values for Anode A and Anode B are still not equal. This indicates that there is a real capacitance difference between the two materials. It was also shown in [9] that pores had to be very large and of a concave form in order to be filled with electrolyte, with the conclusion that a surface area including all pores and voids is not necessarily equal to the electrochemical active surface area. Hence, when normalising capacitance values using TA/PA, the area effect may be over-estimated.

Figure 4 shows measured weight corrected for theoretical weight (m_m-m_t) when taking buoyancy into consideration and calculated wetting angle for Graphite, Anode A and Anode B using the immersion-emersion technique as described in [8], [10]. Before polarisation, the wetting difference between Anode A and Anode B is not so pronounced while Graphite shows a higher wetting angle. After polarisation, the wetting changes noticeably. For all anodes tested the wetting towards the electrolyte increases, but the shift is most prominent for Anode B, changing from a wetting angle of about 140° to nearly 90°. This change is highly relevant for the electrochemical reactivity of the anode, and is contrary with the finding in [8] where no difference between wetting angle before and after polarisation during immersion was found. Better wetting between anode and electrolyte probably means better anode performance in the potrooms.

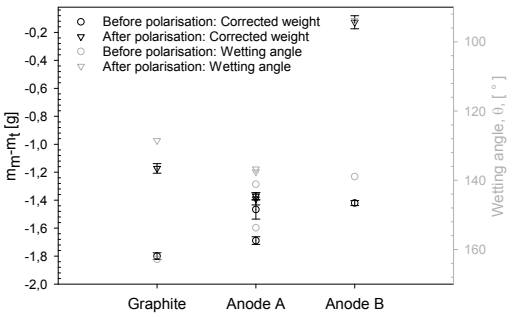

Figure 4: Corrected weight (black) and wetting angle (grey) before (circles) and after (triangle) polarisation.

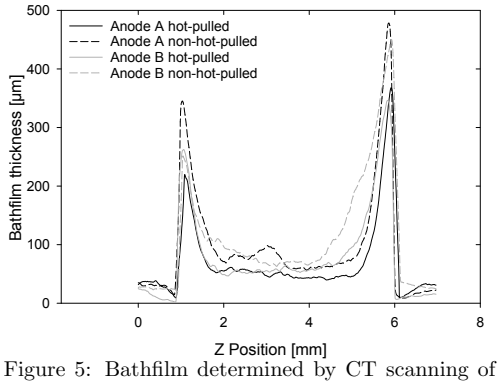

Figure 5: Bathfilm determined by CT scanning of hot-pulled and non-hot-pulled samples.

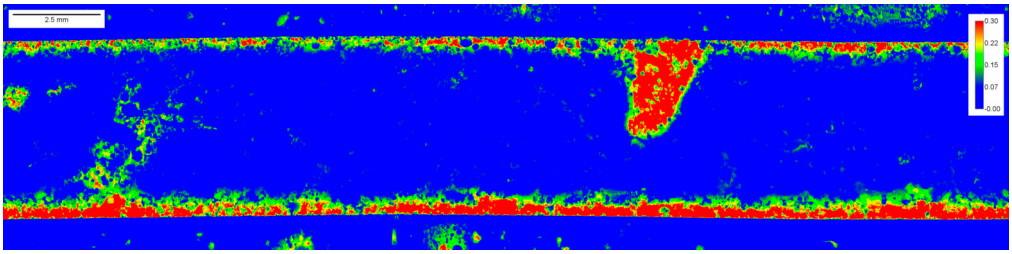

(a)

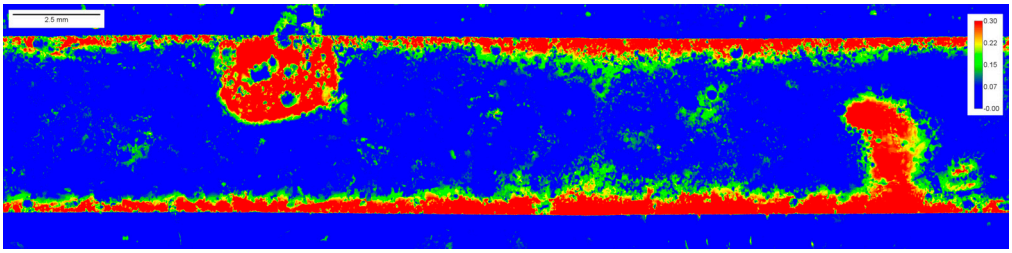

(b)

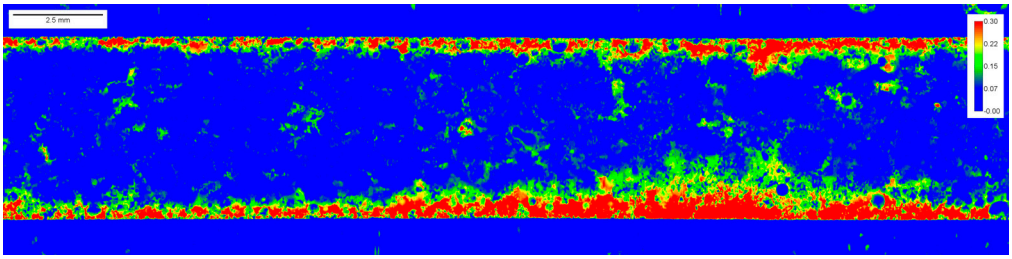

(c)

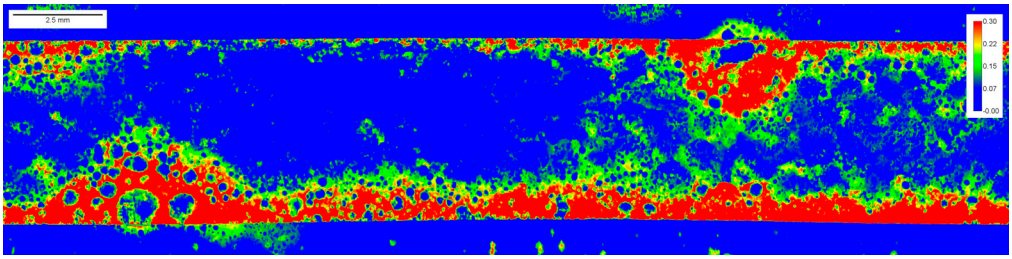

(d)

Figure 6: Contour plots of bathfilm obtained by CT. (a) Anode A hot-pulled, (b) Anode A non-hot-pulled, (c) Anode B hot-pulled and (d) Anode B non-hot-pulled.

Wetting behaviour of anode:electrolyte was also investigated by polarising the anodes at 1.0 A/cm^2, then either hot-pulling or not-hot-pulling. Then the anodes were investigated using CT to obtain the bathfilm thickness on the anode surfaces. Figure 5 shows the bathfilm thickness for Anode A and Anode B, both hot-pulled and non-hot-pulled. Anode B has a slightly thicker bathfilm both during hot-pulling and during non-hot-pulling compared with Anode A, supporting better wetting between Anode B and electrolyte after polarisation compared with Anode A. An edge effect is seen where the bathfilm is thicker towards both ends of the vertical anode sample. The thickness is largest at the bottom (to the right in Z position), as expected due to gravitational forces. Figure 6 shows corresponding contour images of the bathfilm thickness. Blue areas have thinner bathfilm, while red areas have thicker bathfilm. For Anode A, the large red areas are due to electrolyte around "bubble" coke, but on the bubble coke itself, the bathfilm is thin as was also found in [9]. During hot-pulling CO_2 gas bubbles will keep some of the electrolyte off the anode surface, and this is a likely explanation to why the hot-pulled anodes have a thinner bathfilm than the non-hot-pulled anodes. This work also supports the beneficial effects of hot-pulling anodes while changing anodes in the potroom as hotpulling will require less cleaning of butts.

Conclusion

Isotropic coke anodes showed both higher electrochemical reactivity in terms of lower overpotential and better wetting properties towards the electrolyte compared with an anode produced from anisotropic coke. The wetted surface area is not directly related to the geometric surface area, and thus wetting properties are material dependent.

Acknowledgement

This work was funded by The Norwegian Research Council and Hydro Aluminium AS through the research project Hal Ultra Performance. A great thank you is sent to Aksel Alstad, Cristian Torres, Ole Tore Buset and Julian Tolchard.

References

[1] L. Edwards, M. Robinette, R. Love, A. Ross, M. McClung, R. Roush, and W. Morgan, "Use of shot coke as an anode raw material," *Light Metals*, pp. 985–990, 2009.

[2] L. Edwards, N. Backhouse, H. Darmstadt, and M.-J. Dion, "Evolution of anode grade coke quality," *Light Metals*, pp. 1207–1212, 2012.

[3] R. Thorne, C. Sommerseth, A. Svensson, E. Sandnes, L. Lossius, H. Linga, and A. Ratvik, "Understanding anode overpotential," *Light Metals*, pp. 1213–1217, 2014.

[4] R. Thorne, C. Sommerseth, A. Ratvik, S. Rørvik, E. Sandnes, L. Lossius, H. Linga, and A. Svensson, "Correlation between Coke Type, Microstructure and Anodic Reaction Overpotential in Aluminium Electrolysis," *J. Electrochem. Soc.*, pp. E296–E306, 2015.

[5] R. Thorne, C. Sommerseth, A. Ratvik, S. Rørvik, E. Sandnes, L. Lossius, H. Linga, and A. Svensson, "Bubble Evolution and Anode Surface Properties in Aluminium Electrolysis," *J. Electrochem. Soc.*, pp. E104–E114, 2015.

[6] J. Thonstad, P. Fellner, G. Haarberg, J. Hives, H. Kvande, and . Sterten, *Aluminium Electrolysis*. Aluminium-Verlag, 3rd ed., 2001.

[7] J. Thonstad, "The Electrode Reaction on the C, CO_2 Electrode in Cryolite-Alumina Melts-II. Impedance Measurements," *Electrochimica Acta*, pp. 1581–1595, 1970.

[8] A. Solheim, H. Gudbrandsen, A. Martinez, K. Einarsrud, and I. Eick, "Wetting between carbon and cryolitic melts. Part II: Effect of bath properties and polarisation," *Light Metals*, pp. 671–676, 2015.

[9] C. Sommerseth, R. Thorne, S. Rørvik, E. Sandnes, A. Ratvik, L. Lossius, H. Linga, and A. Svensson, "Spatial methods for characterising carbon anodes for aluminium production," *Light Metals*, pp. 671–676, 2015.

[10] A. Martinez, O. Paulsen, A. Solheim, H. Gudbrandsen, and I. Eick, "Wetting between carbon and cryolitic melts. Part I: Theory and equipment," *Light Metals*, pp. 665–670, 2015.

[11] M. Orazem and B. Tribollet, *Electrochemical Impedance Spectroscopy*. Wiley, 1st ed., 2008.